IMPERIAL COLLEGE LONDON

Understanding and Improving environmental stability of lead triiodide perovskite films and solar cells

Thana Chotchuangchutchaval

Department of Chemistry

3/24/2018

Abstract

Organic-inorganic lead halide perovskite solar cells (PSCs) have generated considerable interest in recent years because of their high-power conversion efficiency. However, while converting solar light to electrical power has reported efficiencies exceeding 20 %, operational stability remains a concern, and therefore is preventing the widespread application of these devices. Several previously conducted studies have reported that perovskite solar cells such as those based on methyl ammonium lead iodide perovskite ($CH_3NH_3PbI_3$ or $MAPbI_3$) degrade rapidly when being operated under ambient operating conditions (e.g. in the presence of moisture and oxygen). The exact reason for the relatively poor stability of perovskite solar cells has yet to be fully elucidated. To better understand the reasons behind the poor stability and the rapid degradation of the PSCs in presence of moisture and oxygen, a new in-depth study was made and is the key focus of this thesis.

Oxygen and light induced degradation has recently been shown to be an important pathway for $CH_3NH_3PbI_3$ perovskite films. This oxygen-light degradation process involves the generation of highly energetic electrons while the films are exposed to both visible light and oxygen. These charges can then react with oxygen in the atmosphere generating a reactive oxygen species (superoxide, O^{2-}) which reacts with the methyl ammonium cation and causes $CH_3NH_3^+$ to deprotonate. The degradation and O^{2-} generation process is monitored from comparing Ultraviolet Visible Light Spectroscopy (UV-vis), Photoluminescence (PL) and Transient Absorption Spectroscopy (TAS) measurements with the exposure time. The results concluded from these three set of experiments indicate two main findings: 1.) oxygen induced degradation is an important loss pathway for both films and fully functioning devices and 2.) the drop rate in the yield of charge transfer at metal oxide / $CH_3NH_3PbI_3$ / hole transporting material HTM heterojunctions was found to be less when the $MAPbI_3$ was deposited on an electron accepting substrate; this was assigned to the presence of another kinetic pathway that can successfully compete with electron transfer to oxygen to form superoxide and therefore reduce the degradation rate.

After these two findings are established, the thesis aims to set a design criteria for electron accepting layer within heterojunction perovskite based solar cells to minimise light and oxygen induced degradation while the devices are functioned. The three main points addressed are:

1.) Improving air stability by maximising the electron acceptor-perovskite light absorber interface using mesoporous titiania (TiO_2) films.
2.) Slowing down light and oxygen induced degradation by using tin oxide (SnO_2) electron extraction layers; this being due to the low conduction band edge of SnO_2 as compared to TiO_2 and zinc oxide (ZnO).

3.) Applying (a) and (b) to a more oxygen-light stable lead trihalide perovskite photoabsorber, caesium formamidinium lead trihalide perovskite.

By incorporating the three above points to the lead trihalide perovskite solar cell, the optimised solar cell revealed itself to be over six times more stable than the controlled device while measured under identical conditions.

The studies also present an additional source of electron extraction process in order to improve light and oxygen induced degradation of perovskite films. This further stability enhancement of caesium formamidinium lead perovskite ($CsFAPbI_3$) films and solar cells was made by doping the absorber solution with $PC_{70}BM$. When an appropriate amount of $PC_{70}BM$ dopant (0.2 mg of $PC_{70}BM$ in 1 ml of DMSO) was blended with the absorber prior to the annealing process~~,~~ the dopant acts as an intermediate source to assist the harvested charges to be extracted from the absorber layer successfully. In addition, the optimised $PC_{70}BM$ doped $CsFAPbI_3$ device lasts over two times longer than the un-doped $CsFAPbI_3$ while having similar initial light harvesting performances (71 hours compared with 38 hours, respectively).

This effect of the post annealing temperature (up to 100 ^oC) was incorporated during the existing oxygen and light degradation experiment. Hence, the longevity of each perovskite based film and device consisted of $MAPbI_3$, $CsFAPbI_3$, or caesium formamidinium lead perovskite $CsFAPb(IBr)_3$ was compared. This study revealed that $CsFAPb(IBr)_3$ films exhibited the highest degree of photo-stability and thermal-stability compared to $CsFAPbI_3$ and $MAPbI_3$ films. When $CsFAPb(IBr)_3$ films were exposed to light and oxygen , $CsFAPb(IBr)_3$ films showed almost no changes in their absorbance, superoxide formation rate and hole recombination lifetime in $CsFAPb(IBr)_3$/spiro-OMeTAD over 120 hours. In addition, $CsFAPb(IBr)_3$ based solar cell devices exhibited higher initial power conversion efficiencies and better both oxygen-light and thermal stability compared to $CsFAPbI_3$ and $MAPbI_3$ devices. The operational time of $CsFAPb(IBr)_3$ is maximised with the appropriate amount of cation and anion substitutions.

Declaration of originality

This thesis represents my own contribution and works with some exceptions of some specific references that are made by others such as some figures, numbers or quotes. No part of my own work has been submitted to satisfy the fulfilment obligations of any other degree at this or any other university.

Thana Chotchuangchutchaval

2018, March

Declaration of Copyright

This thesis is produced by me, Thana Chotchuangchutchaval, the author and I reserve all of its copyright. This thesis is made available under a Creative Commons Attribution Non-Commercial No Derivatives licences. Researchers and my peers are free to quote, distribute or transmit the thesis under the condition that they attribute to it and they do not use it for any commercial contexts. In additions, they cannot alter or transform upon it. In the case of any reuse or re-distribution, researchers must refer to this thesis.

Acknowledgements

I would like to thank my friends and colleagues especially those who have contributed to my project and papers. I would like to especially mention Saif Haque, my supervisor, who is always cheerful, dependable, well-versed and enthusiastic. He has really helped and encouraged me with this project endlessly throughout my entire PhD. I have been able to and seek for his advice regardless however insignificant the issue may be. I am always feel gratitude towards him.

I also thank, everyone in my lab group who helped me improve my experimental skills and inspirations via informative group discussions that happened throughout my entire PhD. Namely, Luis Martinez, Niccholas Aristidou, Thomas Rath, Irene Sanchez-Molina, Ding Dong, Bu Xiangnan, Jason Rohr, Luis Lanzetta Lopez, Ali Afshar, Bowon Yoo, Robert Westbrook, MacLachlan, Flannan T. F. O'Mahony, Michael Brown, Ute Cappel and Andrew MacLachlan.

Also, I am grateful to my co-workers and paper collaborators that come from different area around the world; especially those who generously supplied many raw materials and essential lab equipment to me. Namely, Li Xiaoe , Pabitra Shakya Tuladhar, James Durrant, and Tim Albrecht.

Further, the Royal Thai Government who have supported my sponsorship and provided my living costs throughout my PhD project.

List of Publications

The Role of Oxygen in the Degradation of Methylammonium Lead Trihalide Perovskite Photoactive Layers Niccholas Aristidou*, Irene Sanchez-Molina, Thana Chotcuangchutchaval, Dr. Michael Brown, Dr. Luis Martinez, Dr. Thomas Rath, Saif A. Haque. (Angewandte Chemie International Edition · Volume 54, Issue 28, May 2015)

Light and Oxygen Induced Degradation Limits the Operational Stability of Methylammonium Lead Triiodide Perovskite Solar Cells Daniel Bryant*, Nicholas Aristidou, Sebastian Pont, Irene Sanchez-Molina, Thana Chotchuangchutchaval, Scot Wheeler, Jame R. Durrent, Saif A. Haque. (Energy & Environmental Science, 9, 1655–1660, April 2016)

Surface Passivation of Perovskite Films via Iodide Salt Coatings for Enhanced Stability of Organic Lead Halide Perovskite Solar Cells Xiangnan Bu*, Robert J. E. Westbrook, Luis Lanzetta, Dong Ding Thana Chotchuangchutchaval, Nicholas Aristidou, Saif A. Haque. (Solar RRL ,Volume 3, Issue 2, December 2018)

Conference

Print Photovoltaics: From Materials to Manufacture (Marriott Hotel, Swansea, UK ,20th April 2015)

PG Symposium (Queens Tower Rooms – Sherfield Building, 30th June 2015)

PG Symposium (Imperial College London, Core Lecture Theatre Huxley ,1st July 2016)

Contents

Abstract 2

Declaration of originality 4

Declaration of Copyright 5

Acknowledgements 6

List of Publications 7

Lists of Figures 12

Lists of tables 19

Lists of Abbreviations 20

1. Introduction: Available solar energy 24

2. Background, theory, aim and motivation 28

2.1. Photovoltaics (PV), semiconductors, discrete to continuous bands 28

2.2. Concept of p-n Junctions 32

2.3. Current density-Voltage measurement 35

2.4. Series and shunt resistance 37

2.5. Overview of photovoltaic technologies 39

2.5.1. Inorganic solar cells 40

2.5.1.1. Gallium Arsenide (GaAs) 40

2.5.1.2. Amorphous silicon (a-Si:H) 41

2.5.1.3. Micro and nano crystalline (μc/nc-Si) and polycrystalline silicon solar cells 42

2.5.1.4. Cadmium Telluride (CdTe)/Cadmium sulphide (CdS) 43

2.5.1.5. Copper Indium Gallium Selenide (CIGs) solar cells 43

Summaries for Pros and Cons for inorganic PV solar cells 44

2.5.2. Organic solar cell (OPV) 46

2.5.2.1. Donor materials 47

2.5.2.2. Acceptor materials 47

2.5.3. Dye-sensitized solar cells (DSSCs) 48

2.5.4. Perovskite solar cells 51

2.6. Factors that affect long term performances of perovskite films and solar cells 55

Known Factors that affect stability of the perovskite solar cells 55

2.6.3. Ultraviolet light (UV light) 55

2.6.4. Moisture 56

2.6.5. Temperature 58

2.6.6. Oxygen and light 60

2.7. Thesis layout 64

3. Experimental 67

3.1. Materials and processing 67

3.1.1. Materials 67

3.1.2. Cleaning glass substrates 67

3.1.3. Cleaning ITO pre-coated substrates 68

3.1.4. Synthesis of methylammonium iodide (MAI) 68

3.1.5. Synthesis of electron capping layer (c-TiO_2, c-SiO_2, c-ZiO) 68

3.1.6. Titanium (IV) chloride tetrahydrofuran complex ($TiCl_4$) treatment 69

3.1.7. Synthesis of mesoporous (mp) TiO_2 and Al_2O_3 69

3.1.8. Photoabsorber perovskite film fabrication 69

3.1.9. Spiro-OMeTAD films fabrication 70

3.1.10. Au electrode vapour deposition 70

3.2. Optical and Physical Characterisation 71

3.2.1. Ultraviolet-visible light Spectroscopy (UV-vis) 71

3.2.2. Photoluminescence Spectroscopy (PL) 71

3.2.3. X-Ray Diffraction, Energy-dispersive X-ray spectroscopy (EDX) 72

3.2.4. Scanning Electron Microscopy (SEM) 72

3.2.5. Atomic Force Microscopy (AFM) 72

3.2.6. Nuclear Magnetic Resonant (NMR) spectroscopy 72

3.2.7. Transient Absorption Spectroscopy (TAS) 73

3.2.8. JV measurements 74

4. Atmospheric Stability Assessment of Methylammonium Lead Triiodide Perovskite Photoabsorber 75

4.1. Abstract 75

4.2. Introduction 75

4.3. Experimental 77

4.4. Results and discussions 77

4.5. Conclusions 91

5. Establishment of an Electron Transporting Layer Design Guideline to Enhance Oxygen-light Stability for Lead Triiodide Perovskite Films and Solar Cells 92

5.1. Abstract 92

5.2. Introduction 92

5.3. Experimental 94

5.4. Results and discussions 95

5.5. Conclusions 115

6. Oxygen-light Stability Enhancement of $CsFAMAPbI_3$ Based Perovskite Films and Working Solar Cells with $PC_{70}BM$ Dopant 117

6.1. Abstract 117

6.2. Introduction 118

6.3. Experimental 119

6.4. Results and Discussions 119

6.5. Conclusions 127

7. Oxygen-light Stability Enhancement with Post Annealing Temperature Effect on Lead Trihalide Perovskite Films and Solar Cells 128

7.1. Abstract 128

7.2. Introduction 129

7.3. Experimental 130

7.4. Results and Discussions 131

7.5. Conclusions 141

8. Conclusions 142

9. Outlooks 145

10. References 146

SI sections 157

SI for Chapter 6 158

SI for Chapter 7 159

Lists of Figures

Figure 1: Average yearly solar radiation at the Earth's surface for the different locations around the earth (see labels). The solid green line represents the mean daily solar radiation around the earth which is 2.88 kWh/day. This graph is adapted from ITCA in 2008 [3]..... 24

Figure 2: (a) energy level diagram when 2 atoms interact with each other. Formation of bonding (σ) and anti-bonding molecular orbitals (σ*) are shown (b) the formation of a band of N molecular orbitals by accumulating atoms in 1 dimension. It is noted that this band retains finite width as N approaches infinite value. 29

Figure 3: Energy band diagram of a crystal material for (a) half-filled band in metal (b) overlapping conduction (CB) and valence band (VB) in a metal material (c) semiconductor material (d) insulator material. The half-filled band occurred when a metal contain only one valence electron per atom such as copper, gold and silver. The metal material containing 2 or more electrons in valence bands are shown in (b). ΔE_g represents bandgap energy [12]..... 30

Figure 4 : Schematic of metal and n-type semiconductor interface at zero bias. Schottky barrier is represented by ϕ_B which is the difference between conduction band energy (E_C) and Fermi level energy (E_F). In case of a p-type semiconductor, ϕ_B is the difference between valence band energy (E_V) and E_F [15]. 32

Figure 5: Schematic of a p-n junction of a photodiode with the energy diagram at p-n interface. Minority carriers are required to transfer to the depletion junction before photogenerated charges can be separated. E_{cn} and E_{vn} represents energy of the conduction band and valence band of the n-type semiconductor whereas E_{cp} and E_{vp} is the conduction band and valence band of the p-type semiconductor. hv is the light energy generated via electron hole recombination and ΔV is the difference between Fermi energy of n-type (E_{Fn}) and p-type (E_{Fp}) semiconductor [20]..... 33

Figure 6: A typical JV curve with and without illumination (blue and red curve, respectively) which contains three important index parameters: short circuit current (J_{sc}), open circuit voltage (V_{oc}) and maximum power point (P_{max}) which locates between these two extreme conditions. P_{max} is derived by multiplying current density at maximum power point (J_{mpp}) and voltage at maximum power point (V_{mpp}) together..... 36

Figure 7: Schematic of equivalent solar cell circuits. I_L is the photogenerated current, I_D is a diode current and I_{SH} is a leaked current through a shunt resistor. 37

Figure 8: Schematic of I-V curves showing (a) effect of increasing R_s (b) effect of decreasing R_{SH}... 38

Figure 9: Diagram displays free charge carrier formation after photoexcitation occurs at (a) donor material, (b) acceptor material. 46

Figure 10: Schematic for Typical DSSCs. Where TCO refers to transparent conductive oxide, I^-/I_3^- stands for the electrolyte redox couple and mp-TiO_2 is a mesoporous titiania which is a metal oxide scaffold [100]. 49

Figure 11: Illustration of electron transfer processes in a typical DSSCs (liquid state). 50

Figure 12: Schematic of crystal structure of typical organometallic halide perovskite. A refers to organic anion, B is metal cation and X represents halide. 51

Figure 13: Number of articles versus publication solar cell via Web of Science when the word 'perovskite solar cell' was input [117]. Approximately 1300 peer reviewed studies relating to perovskite solar cells were published in 2015 which were almost three times higher than the total publications in 2014 [117]. This graph was adapted from the data published by *Park, N.-G et al. Methodologies for high efficiency perovskite solar cells* [117]..... 53

Figure 14: Schematic diagram shows how transient absorption spectroscopy operates. The specimen is illuminated with a specific laser pulse (pump) while being continuously measured at microsecond time scales. The pulse is guided by a secondary specific probe wavelength via a monochromator to a detector unit. The detected probe light is measured with respect to incident light before the pulse interacts with the sample. The measured results reflect how long these generated charges 'live' before a recombination reaction takes place. During each measurement, each perovskite sample was flushed with a constant flow of nitrogen (1 lpm) to ensure no photodegradation was taking place. 73

Figure 15: Absorbance of eight $MAPbI_3$ films deposited on glass before and after (48 hours) dry air-light ageing in various testing conditions (see labels). The photographs of the films before (left) and after (right) the ageing were also shown next to each absorbance graph. This figure was adapted from the paper of Aristidou et al. [134]. * represents degraded $MaPbI_3$ films when they were subjected to dry air and AM 1.5 G illumination for 48 hours. 77

Figure 16: Normalised fluorescence intensity at 610 nm (excitation wavelength of 520 nm) of the superoxide HE probe (31.7 µM) mixed into dry toluene solution. $I_F(t)$ is the maximum PL intensity at time t while $I_F(t_0)$ is the background fluorescence intensity at probe at t = 0. The ratio between the two is the superoxide generation yield as the absorber film degraded under constant exposure of light and oxygen. Both PL emission trace were collected individually (see labels). Each film was submerged under (~20 $mWcm^{-2}$) and dry air (less than 10 ppm H_2O). Then the PL emission of toluene probe solution was tested over the course of 1 hour with 10 minute interval between each measurement. This figure was adapted from the paper of Aristidou et al. [133]. 78

Figure 17: Absorbance of $MAPbI_3$ deposited on top of two different metal oxide layers. Initial (black line) and 24 hours-aged (red line) absorbance spectra of each perovskite sample was measured. Without the combination of both light (~20 $mWcm^{-2}$ tungsten halogen lamp) and oxygen, there were no apparent changes observed in $MAPbI_3$ absorbance curves for any given experimental conditions. 79

Figure 18: Transient absorption kinetics as a function of ageing time probed at 1,600 nm for spiro-OMeTAD located of top $MAPbI_3$- metal oxide (see legend). All six film were aged either under 20 mW/cm^2 or under presence of constant flow of dry air (0.1 lpm). Laser photo excitation was done at 510 nm with an energy density of approximately 25 $\mu J/cm^2$. Without the combination of dry air and light, there are no apparent changes in the TAS absorption kinetic..... 80

Figure 19: UV-vis absorbance spectra of $MAPbI_3$ deposited on top of either mesoporous Al_2O_3 or TiO_2 (see legend) under different relative humidity conditions. Dry air contains 10 ppm or less H_2O content while open air contains approximately 60 percent relative humidity content. The samples were constantly bathed under 20 $mWcm^{-2}$ tungsten halogen lamp and (dry/open) air (see label). 81

Figure 20: 480 nm UV-vis trace of metal oxide/$MAPbI_3$ samples deposited on top of different metal oxide mesoporous substrate (see legends). This 480 nm UV-vis trace was derived from the Figure 19. 81

Figure 21: Transient absorption signal at 1600 nm of (a) Al_2O_3/$MAPbI_3$/spiro-OMeTAD and (b) TiO_2/$MAPbI_3$/spiro-OMeTAD films with (black) and without (red) HTM (spiro-OMeTAD). Transient absorption spectra of (c) Al_2O_3/$MAPbI_3$/spiro-OMeTAD and (d) TiO_2/$MAPbI_3$/spiro-OMeTAD films under N_2 (black) and dry air and light (red). Laser excitation energy density = 25 μJcm^{-2} at 510 nm. 82

Figure 22: Transient absorption kinetics as a function of ageing time probed at 1,600 nm of Al_2O_3/$MAPbI_3$/spiro-OMeTAD degraded under (a) open air or (b) dry air and TiO_2/$MAPbI_3$/spiro-

OMeTAD films degraded under (c) open air or (d) dry air. All films are aged under constant 20 mW/cm^2 illumination of halogen lamp and excess flow of dry air or open air. Laser photo excitation was done at 510 nm with an energy density of approximately 25 µJ/cm^2. 83
Figure 23: Normalised TAS decays at 10 µs versus oxygen-light ageing time taken from Figure 22 were shown (see labels). All films are aged under constant 20 mW/cm^2 illumination of halogen lamp and excess flow of dry air or open air. Laser photo excitation was done at 510 nm with an energy density of approximately 25 µJ/cm^2. 84
Figure 24: EDX/SEM spectra for $MAPbI_3$ deposited on two metal oxides. The inset shows the I:Pb atomic ratio of $MAPbI_3$ measured under air and light (see legend). 85
Figure 25: XRD patterns of (a) initial and 120 hours oxygen-light aged glass/$MAPbI_3$ and (b) initial and 120 hours oxygen-air aged mp-Al_2O_3/$MAPbI_3$ and mp-TiO_2/$MAPbI_3$. Both samples were either exposed under dry air (10 ppm H_2O) or open air (60 %RH) for 120 hr (see legends). 86
Figure 26: Top view SEM images of initial and 120 hours light-air aged mesoporous metal oxide/$MAPbI_3$ (see labels). 87
Figure 27: Current density-Voltage curve of (a) of ITO/c-TiO_2/mp-Al_2O_3/$MAPbI_3$/spiro-OMeTAD/Au devices (b) of ITO/c-TiO_2/mp-TiO_2/$MAPbI_3$/spiro-OMeTAD/Au devices. Both samples were illuminated under AM 1.5 G sunlight at approximately 100 mWcm^{-2} irradiance. In this case, a backward scan from 1.2 V to - 0.2 V was performed. It was noted that six different devices each of (a) and (b) were tested were exhibited identical JV performance when being subjected under the same environment. 88
Figure 28: (a) Steady-state photoluminescence spectra of $MAPbI_3$ based films along with a $MAPbI_3$ reference sample (with 485 nm excitation wavelength) (b) Normalised fluorescence intensity at 610 nm (with 520 nm excitation) of HE probe solution to detect the relative amount of superoxide generation within one hours. $I_F(t)$ is the probe fluorescence intensity maximum at time t whereas $I_F(t_0)$ is the background fluorescence intensity of the probe at t = 0. The $I_F(t)$: $I_F(t_0)$ hereafter refers to relative yield of superoxide generation (c) Normalised power conversion efficiencies (PCE) of $MAPbI_3$ based solar cells are measured under different conditions (see legends). The samples are measured under AM 1.5 G powered by equivalent white LED array equipped with UV blocking filter. Dry air comprised of approximately 20.95 % O_2 and 78.09 N_2. This data is adapted from the paper published by Bryant et al. [134]. 90
Figure 29: Energy level of $MAPbI_3$ as well as the HOMO and LUMO of three different compact electron transporting layer; namely zinc oxide (ZnO), titanium dioxide (TiO_2), tin oxide (SnO_2)..... 95
Figure 30: Absorbance spectra of glass/with and without ETL/$MAPbI_3$ samples (see labels) under constant exposure of a halogen tungsten lamp (~ 20 mWcm^{-2}) and dry air (less than 10 ppm H_2O). Three different ETLs were tested namely c-ZnO, c-TiO_2 and c-SnO_2. 96
Figure 31: PL emissions as a function of ageing time. Both reference and glass/ETL/$MAPbI_3$ samples were submerged in a mixture of dry toluene and hydroethedine (HE) probe solution (31.7 µM) under constant exposure of halogen light and excess dry air individually. Each PL emission of the toluene solution was measured at 10 minute interval over the course of one hour. 97
Figure 32: Microsecond transient absorption kinetic as a function of ageing time when each specimen (c-ETL/$MAPbI_3$/spiro-OMeTAD) was probed at 1,600 nm to trace the recombination lifetime of hole species in spiro-OMeTAD that deposited on each $MAPbI_3$ photoabsorber (see label). All samples were aged under constant 20 mWcm^{-2} illumination of a halogen lamp and excess flow of dry air (~1 lpm). The signal was probed at 1,600 nm for spiro-OMeTAD and the laser photo pulses excitation was at 510 nm with an energy density of approximately 25 µJcm^{-2}. 98

Figure 33: (a) 700 nm UV-vis trace of $MAPbI_3$ samples deposited on three different electron extraction layer (ETL) (see legend). (b) Superoxide measurement of hydroethedine probe (HE) which was highly emissive at 610 nm via excitation wavelength of 520 nm. $I_F(t)$ was the maximum PL intensity at time t while $I_F(t_0)$ was the background fluorescence intensity at the probe at t = 0. The ratio between the two represented the superoxide generation yield. Each specimen degraded under a dry environment and constant halogen light source (~20 $mWcm^{-2}$). (c) Normalised Transient absorption spectra trace at 10 µs as electron extraction layers are differed (see legend). All samples were aged under constant 20 $mWcm^{-2}$ illumination of a halogen lamp and an excess flow of dry air (~1 lpm). The signal was probed at 1,600 nm for spiro-OMeTAD and the laser photo pulses excitation was at 510 nm with an energy density of approximately 25 μJcm^{-2}..... 99

Figure 34: Schematic shows (a) $MAPbI_3$ (b) c-TiO_2/$MAPbI_3$ (c) c-TiO_2/mp-TiO_2/$MAPbI_3$ with overlayer (d) c-TiO_2/mp-TiO_2/$MAPbI_3$ without the overlayer. The absence of excess $MAPbI_3$ overlayer indicated that interfacial area between the absorber and mesoporous titiania was maximised.. 101

Figure 35: Absorbance curves of four $MAPbI_3$ based specimens as each metal oxide-photoabsorber interfacial area (between $MAPbI_3$ and mp-TiO_2) increased (a) $MAPbI_3$ (b) c-TiO_2/$MAPbI_3$ (c) c-TiO_2/mp-TiO_2/$MAPbI_3$ with an excess overlayer (d) c-TiO_2/mp-TiO_2/$MAPbI_3$ without excess overlayer (optimised). The absence of $MAPbI_3$ overlayer indicated that the interfacial area between the absorber and mp-TiO_2 was maximised. All 4 specimens were under constant exposure of a halogen lamp (20 $mWcm^{-2}$) and dry air (less than 10 ppm H_2O)..... 102

Figure 36: Superoxide measurements of toluene and hydroethedine probe solution which was highly emissive at 610 nm via the excitation wavelength of 520 nm. $I_F(t)$ was the maximum PL intensity at time t while $I_F(t_0)$ was the background fluorescence intensity at probe at t = 0. The ratio between the two represents the superoxide evolution yield as the absorber film degraded under a combination of constant halogen light (~20 $mWcm^{-2}$) and a dry environment (less than 10 ppm H_2O). 103

Figure 37: (a) absorbance trace at 750 nm of 4 different $MAPbI_3$ samples with different interfacial area between the $MAPbI_3$ and the mp-TiO_2 (see legend) (b) Superoxide generation traces at 610 nm of the mixture of toluene and hydroethedine probe (31.7 µM) with a 520 nm excitation wavelength (c) a steady state PL emission curves as the mp-TiO_2-$MAPbI_3$ interfaces was enhanced..... 104

Figure 38: Transient charge kinetic of $MAPbI_3$ based films (a) c-TiO_2/$MAPbI_3$/spiro-OMeTAD (b) c-TiO_2/mp-TiO_2/$MAPbI_3$-with excess overlayer/spiro-OMeTAD (c) c-TiO_2/$MAPbI_3$-without overlayer/spiro-OMeTAD (d) Normalised TAS decay at 1 µs versus oxygen-light ageing time .All samples are aged under constant 20 $mWcm^{-2}$ illumination from a halogen lamp and an excess flow of dry air or open air. The signal was probed at 1600 nm for spiro-OMeTAD. Laser photo excitation was at 510 nm with an energy density of approximately 25 μJcm^{-2}..... 105

Figure 39: (a) top view and (c) cross sectional SEM images of c-TiO_2/mp-TiO_2/$MAPbI_3$ with the excess overlayer. (b) top view (d) cross sectional SEM of the optimised c-TiO_2/mp-TiO_2/$MAPbI_3$..... 106

Figure 40: Absorbance curves of (a) $CsFAPbI_3$ (b) c-ZnO/$CsFAPbI_3$ (c) TiO_2/$CsFAPbI_3$ (d) c-SnO_2/$CsFAPbI_3$. All the samples were aged under constant illumination of halogen light (20 $mWcm^{-2}$) and dry air exposure (less than 10 ppm H_2O). 107

Figure 41: Superoxide measurement of mixture of dry toluene and hydroethedine (HE) probe solution (31.7 µM) after submerging each $CsFaPbI_3$ sample while each sample was exposed to a constant exposure of halogen light and excess dry air. The tested solution was highly emissive at 610 nm via an excitation wavelength of 520 nm upon superoxide formation. $I_F(t)$ is the maximum PL intensity at time t while $I_F(t_0)$ is the background fluorescence intensity at probe at t = 0. The ratio

between the two is the superoxide yield as the absorber film degrades under a constant light-oxygen environment. 108
Figure 42: (a) absorbance traces at 750 nm of $MAPbI_3$ and $CSFAPbI_3$ deposited on three difference compact layers of metal oxide (see legend) (b) Superoxide generation traces of the tested toluene mixed with HE probe solution (31.7 µM) at 610 nm with 520 nm excitation wavelength. Each c-ETL/$CsFAPbI_3$ contain three different compact metal oxides along with a reference $CsFAPbI_3$ sample (see legend) (c) raw steady state PL emission intensity of four different c-ETL/$CsFAPbI_3$. 109
Figure 43: Absorbance curves over ageing time of (a) c-ZnO/mp-TiO_2/$CsFAPbI_3$ (b) c-TiO_2/mp-TiO_2/$CsFAPbI_3$ (c) c-SnO_2/mp-TiO_2/$CsFAPbI_3$ .All the samples were aged under constant illumination of light (~20 $mWcm^{-2}$) and dry air exposure (less than 10 ppm H_2O). 110
Figure 44: Superoxide measurement of hydroethedine probe solution which was highly emissive at 610 nm while excitation wavelength was at 520 nm for each $CsFAPbI_3$ based samples (see legends). $I_F(t)$ is the maximum PL intensity at time t while $I_F(t_0)$ is the background fluorescence intensity at probe at t = 0. The ratio between the two is the superoxide yield as the absorber film degrades under a dry environment. Superoxide measurement of $MAPbI_3$ sample was included in (d) for comparison. 111
Figure 45: Transient charge kinetic of $MAPbI_3$ based films (a) c-ZnO/mp-TiO_2/$CsFAPbI_3$/spiro-OMeTAD (b) c-TiO_2/mp-TiO_2/$CsFAPbI_3$/spiro-OMeTAD /spiro-OMeTAD (c) c-SnO_2/mp-TiO_2/$CsFAPbI_3$/spiro-OMeTAD (d) TAS vertical trace at 10µs of its optical density of $CsFAPbI_3$ deposited on 3 different compact metal oxides. All samples were aged under constant 20 $mWcm^{-2}$ illumination of a halogen lamp and excess flow of dry air (less than 20 ppm H_2O). The signal was probed at 1,600 nm to track hole recombination lifetime in spiro-OMeTAD. Laser photo excitation was undertaken at 510 nm with an energy density of approximately 25 μJcm^{-2}. 112
Figure 46: (a) Normalised of UV-vis absorbance trace at 750 nm of c-ETLs/mp-TiO_2/$CsFAPbI_3$ (where ETL were namely ZnO, TiO_2 and c-SnO_2) (b) relative superoxide generation yield ($I_F(t)$:$I_F(t_0)$)at 610 nm of c-ETLs/mp-TiO_2/$CsFAPbI_3$ (c) raw steady state emission peak of c-ETLs/mp-TiO_2/$CsFAPbI_3$ (d) Transient absorption trace at 10 µs of of c-ETLs/mp-TiO_2/$CsFAPbI_3$/spiro-OMeTAD where each sample consisted of a different compact metal oxide (see legend). All of the optimised photoabsorbers were deposited on mesoporous titiania in order to maximise electron extraction at the absorber-mesoporous metal oxide interfaces. 113
Figure 47: JV curves of (a) ITO/c-TiO_2/mp-TiO_2/$MAPbI_3$/spiro-OMeTAD/Au (b) ITO/c-TiO_2/mp-ITO/TiO_2/$MAPbI_3$/spiro-OMeTAD/Au (c) ITO/c-SnO_2/mp-TiO_2/$CsFAPbI_3$/spiro-OMeTAD/Au (d) Normalised PCE for perovskite derived from (a), (b) and (c). Both samples are exposed under AM 1.5 G with approximately 100 $mWcm^{-2}$ irradiance powered by equivalent white LED array equipped with UV blocking. 114
Figure 48: (a) absorbance spectra trace at 750 nm of lead trihalide perovskite films (see legends) (b) Superoxide generation yield trace at 610 nm (with 520 nm excitation wavelength) of HE probe solution. 116
Figure 49: Absorbance spectra of c-TiO_2/mp-TiO_2/$CsFAPbI_3$ with and without $PC_{60}BM$/DMSO solution dopant (0.2 mg of $PC_{60}BM$ in 1 ml of DMSO). Each sample was doped with (a) 0 µl $PC_{60}PM$ (b) 10 µl $PC_{60}PM$ (c) 20 µl $PC_{60}PM$ (d) 30 µl $PC_{60}PM$ (e) 40 µl $PC_{60}PM$ doped dopant solution. 120
Figure 50: (a) UV-vis absorbance trace at 750 nm of c-TiO_2/$PC_{60}BM$-$CsFAPbI_3$ (b) steady state PL emission of c-TiO_2/PC60BM-$CsFAPbI_3$. Each CsFAPbI3 based film was doped with a different volume of the $PC_{60}BM$ DMSO solution. 120

Figure 51: (a) absorbance traces of c-TiO_2/mp-TiO_2/$CsFAPbI_3$ films doped with different amounts of $PC_{70}BM$ at 750 nm (see legend). All samples were degraded under constant exposure of illumination and dry air (less than 10 ppm H_2O). (b) steady state PL emission of 0-100 µl $PC_{70}BM$ doped $CsFAPbI_3$ based samples. Here, the amount of the dopant concentration corresponded with the photo-generated electron extraction capability at the $CsFAPbI_3$-mp-TiO_2 interfaces. (c) steady state PL emission of 120-200 µl $PC_{70}BM$ (0.2 mg in 1ml of DMSO) doped $CsFAPbI_3$ based samples. Here, the peak of PL emission of the heavily $PC_{70}BM$ doped sample started to become blue-shifted. (d) maximum PL intensity vs the normalised absorbance linier relation graph after 216 hours of a constant tungsten halogen light (~20 $mWcm^{-2}$) and oxygen ageing. The Raw UV-vis absorbance data is supplemented in the SI sections. 121

Figure 52: Transient charge kinetic of c-TiO_2/mp-TiO_2/$PC_{70}BM$ doped $CsFAPbI_3$spiro-OMeTAD as the dopant amount and oxygen-light ageing time was varied (see labels). All $CsFAPbI_3$ based samples were aged under constant 20 $mWcm^{-2}$ illumination with a halogen lamp and an excess flow of dry air. The signal was probed at 1,600 nm to track the hole recombination interaction in spiro-OMeTAD. Laser photo excitation was set at 510 nm with an energy density of approximately 25 μJcm^{-2} 123

Figure 53: XRD patterns of (a) initial c-TiO_2/ mp-TiO_2/$CsFAPbI_3$ with different $Pc_{70}BM$ dopant content (see legend) (b) 648 hours light-oxygen aged c-TiO_2/ mp-TiO_2/$CsFAPbI_3$ under constant exposure of dry air and illumination (~20 $mWcm^{-2}$). 124

Figure 54: Top view SEM images of c-TiO_2/mp-TiO_2/$CsFAPbI_3$ while $PC_{70}BM$ dopant solution (0.2 mg of $PC_{70}BM$ in 1 ml of DMSO) is varied (see legend). The dopant is dissolved in DMSO solution at 0.2 $mgml^{-1}$. The crystal size increases upon dopant addition. 125

Figure 55 : (a) JV curves of ITO/c-TiO_2/mp-TiO_2/$CsFAPbI_3$/spiro-OMeTAD/Au reference solar cells (b) ITO/c-TiO_2/mp-TiO_2/$CsFAPbI_3$-40 µl doped $PC_{70}BM$ (0.2 $mgml^{-1}$ in DMSO)/spiro-OMeTAD/Au from 0^{th} hour to 48^{th} hour under the testing conditions (c) The continuation of JV measurement over ageing time of the optimally doped $PC_{70}BM$-$CsFAPbI_3$ based solar cell under testing conditions from 49^{th} hour to 71^{th} hour (d) Normalised PCE traces of the undoped and optimally $PC_{70}BM$ doped-$CsFAPbI_3$ solar cells over ageing conditions. Both samples were exposed under constant exposure of dry air and AM 1.5 G with approximately 100 $mWcm^{-2}$ irradiance powered by equivalent white LED array equipped with UV blocking filter. Each JV curve was obtained via a backward JV scan from 1.2 V to -0.2 V. 126

Figure 56: (a) 750 nm of UV-vis absorbance traces of glass/c-TiO_2/mp-TiO_2/$MAPbI_3$ with a different post annealing temperature (see labels) for 30 minutes (b) 750 nm of UV-vis absorbance traces of glass/c-TiO_2/mp-TiO_2/$CsFAPbI_3$ with a different post annealing temperature (see labels) for 30 minutes (c) 750 nm of UV-vis absorbance traces of glass/c-TiO_2/mp-TiO_2/CsFAPb $(I_{0.8}Br_{0.2})_3$ with different post annealing temperature (see labels) for 30 minutes. All samples were subjected to constant exposure of a tungsten halogen lamp (20 $mWcm^{-2}$) and excess dry air flow (less than 10 ppm of H_2O). The insets shown in (b) and (c) emphasize the initial oxygen-light degradation period. The raw absorbance data of each individual perovskite sample is located at the SI section. 131

Figure 57: Superoxide measurement of three different set of lead trihalide perovskite based films: (a) glass/c-TiO_2/mp-TiO_2/$MAPbI_3$ (b) glass/c-TiO_2/mp-TiO_2/$CsFAPbI_3$ (c) glass/c-TiO_2/mp-TiO_2/CsFAPb $(I_{0.8}Br_{0.2})_3$. The superoxide generation yield on each sample was derived by tracking the evolution of luminescence hydroethedine (HE) probe solution that was highly emissive at 610 upon exposing it to the excitation wavelength of 520 nm. $I_F(t)$ was the maximum PL intensity at time t while $I_F(t_0)$ was the background fluorescence intensity at probe at t = 0. The ratio between the two

represented the superoxide generation yield in each perovskite photoabsorber layer. Each perovskite film was subjected to a different post annealing temperature for 30 minutes (see labels). All perovskite samples were submerged in HE probe solution while being exposed to a constant tungsten halogen light (20 mWcm^{-2}) and oxygen over the course of one hour. The raw data within this figure is supplemented in the SI section. 132

Figure 58: 10 µs of vertical trace of transient absorption spectra as a function of oxygen-light ageing time of (a) glass/c-TiO_2/mp-TiO_2/$MAPbI_3$ (b) glass/c-TiO_2/mp-TiO_2/$CsFAPbI_3$ (c) glass/c-TiO_2/mp-TiO_2/CsFAPb $(I_{0.8}Br_{0.2})_3$. Each perovskite film was subjected to a different post annealing temperature for 30 minutes (see labels). In addition, each sample was subjected to a constant tungsten halogen light (~20 mWcm^{-2}) and excess dry air flow (1 lpm). The signal was probed at 1,600 nm to track the hole recombination interaction in spiro-OMeTAD. Laser photo excitation was set at 510 nm with an energy density of approximately 25 µJcm^{-2}. Raw TAS data for every point is located in the SI sections. 133

Figure 59: XRD patterns of initial and fully oxygen-light aged c-TiO_2/mp-TiO_2/perovskite samples (see labels). All $MAPbI_3$, $CsFAPbI_3$ or CsFAPb $(I_{0.8}Br_{0.2})_3$ samples were subjected to constant exposure of a tungsten halogen lamp (~20 mWcm^{-2}) and dry air. In addition, 30 minutes of post annealing was imposed on each lead perovskite sample for 30 minutes from RTM to 100 °C (see legends). 135

Figure 60: Top view SEM images of c-TiO_2/mp-TiO_2/$MAPbI_3$ before subjecting to oxygen-light degradation. Each sample was post annealed at different temperature (see labels) for 30 minutes. 136

Figure 61: Top view SEM images of c-TiO_2/mp-TiO_2/$MAPbI_3$ after subjecting to oxygen-light degradation (120 hours). Each sample was post annealed at different temperatures (see labels) for 30 minutes. 136

Figure 62: Top view SEM images of c-TiO_2/mp-TiO_2/$CsFAPbI_3$ before subjecting to oxygen-light degradation. Each sample was post annealed at a different temperature (see labels) for 30 minutes. 137

Figure 63: Top view SEM images of c-TiO_2/mp-TiO_2/$CsFAPbI_3$ after subjecting to oxygen-light degradation (696 hours). Each sample was post annealed at a different temperature (see labels) for 30 minutes. 137

Figure 64: Top view SEM images of c-TiO_2/mp-TiO_2/CsFAPb $(I_{0.8}Br_{0.2})_3$ before subjecting to oxygen-light degradation. Each sample was post annealed at a different temperature (see labels) for 30 minutes. 138

Figure 65: Top view SEM images of c-TiO_2/mp-TiO_2/ CsFAPb $(I_{0.8}Br_{0.2})_3$ after subjecting to oxygen-light degradation (696 hours). Each sample was post annealed at a different temperature (see labels) for 30 minutes. 138

Figure 66: Normalised PCE traces over ageing conditions of (a) ITO/c-TiO_2/mp-TiO_2/$MAPbI_3$/spiro-OMeTAD/Au (b) ITO/c-TiO_2/mp-TiO_2/$CsFAPbI_3$/spiro-OMeTAD/Au (c) ITO/c-TiO_2/mp-TiO_2/ c-TiO_2/mp-TiO_2/ CsFAPb $(I_{0.8}Br_{0.2})_3$ /spiro-OMeTAD/Au. In addition, 30 minutes of post annealing to the perovskite photoabsorber was implemented during the device fabrication process (see legends). All samples were exposed under constant exposure of dry air and AM 1.5 G with approximately 100 mWcm^{-2} irradiance powered by equivalent white LED array equipped with UV blocking filter. Each JV curve was obtained via a backward JV scan from 1.2 V to -0.2 V. Each JV curve which represents each point for all lead trihalide bulk heterojunction devices, is plotted in the SI section. 139

Lists of tables

Table 1: (a) World total primary energy supply by fuel reported in 1973 and 2015 (measured in Mtoe, million tonnes of oil equivalent). (b) Solar photovoltaic (PV) electricity production reported in 2005 and 2017 (measured in Terawatt hour). OECD stands for Organisation for Economic Co-operation and Development while non-OECD Asia excludes China. The data in these 2 tables have been extracted from Statista 2018 (data taken in 2016) and Birol, F. Key World Energy Statistics 2017 [1,2]. 25

Table 2: Comparison table for inorganic single-junction terrestrial solar cells regarding state-of-the-art PV performances, toxicity and associated cost until 2016. The test solar cells were measured under AM 1.5 G spectrum (1,000 Wm^{-2}) at 25 °C. This table is adapted from the Solar cell efficiency table reported at 2015 and 2017 (version 45 and 49) [74,75]. 44

Table 3: I:Pb atomic ratio of initial, 120 hours light-air aged (under dry air or open air) derived from Figure 24. 85

Table 4: J_{sc}, V_{oc}, FF and PCE of Al_2O_3-$MAPbI_3$ and TiO_2-$MAPbI_3$ based solar cell devices before and the after two hours of oxygen-light degradation derived from Figure 27. Both samples were illuminated under AM 1.5 G sunlight at approximately 100 $mWcm^{-2}$ irradiance. In this case, a backward scan from 1.2 V to - 0.2 V was performed. The total of six identical devices from each category were being measured simultaneously. 88

Table 5: PV parameters of three different bulk heterojunction solar cells: ITO/c-TiO_2/mp-TiO_2/$MAPbI_3$/spiro-OMeTAD/Au, ITO/c-TiO_2/mp-TiO_2/$CsFAPbI_3$/spiro-OMeTAD/Au and ITO/c-SnO_2/mp-TiO_2/$CsFAPbI_3$/spiro-OMeTAD/Au. The total of six devices from each category were being measured simultaneously. 115

Table 6: Average crystal size of the $CsFAPbI_3$ upon $PC_{70}BM$ dopant addition (0.2 mg in 1 ml of DMSO). The average crystal sizes were maximised with 40 µl of the $PC_{70}CM$ dopant solution put into the $CsFAPbI_3$ precursor solution prior to the spin coating process of the photoactive layer. 125

Table 7: Relevant PV parameters for ITO/c-TiO_2/mp-TiO_2/$CsFAPbI_3$/spiro-OMeTAD/Au reference solar cell device and ITO/c-TiO_2/mp-TiO_2/$CsFAPbI_3$-40 µl doped $PC_{70}BM$ (0.2 mg/ml in DMSO)/spiro-OMeTAD/Au devices. Total of six identical devices from each category were being measured simultaneously. 127

Table 8: Relative atomic ratio of I:Pb for c-TiO_2/mp-TiO_2/$MAPbI_3$ samples before and after oxygen-light degradation (120 hours). Each EDX spectra is plotted in the SI section. 134

Table 9: Relative atomic ratio of I:Pb for c-TiO_2/mp-TiO_2/$CsFAPbI_3$ samples before and after oxygen-light degradation (840 hours). Each EDX spectra is plotted in the SI section. 134

Table 10: Relative atomic ratio of I:Pb for c-TiO_2/mp-TiO_2/CsFAPb $(I_{0.8}Br_{0.2})_3$ samples before and after oxygen-light degradation (840 hours). Each EDX spectra is plotted in the SI section 134

Table 11: PV parameters for three lead trihalide perovskite bulk heterojunction solar cells. Six identical devices from each category were measured simultaneously however only the best performing devices from each category were being shown. 140

Lists of Abbreviations

AM 1.5	Air Mass 1.5
AO	Atomic Orbital
a-Si	Amorphous Silicon
a-Si:H	Hydrogenated Amorphous Silicon
at. %	Atomic Percent
Au	Gold
$CaTIO_3$	Calcium Titanium Oxide
CB	Chlobenzene
CdS	Cadmium Sulphide
CdTe	Cadmium Telluride
CH_3NH_2	Methylamine
CH_3NH_3I, MAI	Methylammonium Iodide
$CH_3NH_3PbBr_3$, $MAPbBr_3$	Methyl Ammonium Lead Tribromide
$CH_3NH_3PbI_3$, $MAPbI_3$	Methyl Ammonium lead Triiodide
$CH_3NH_3PbX_3$	Methyl Ammonium Lead Halide
CIGs	Copper Indium Gallium Selenide
$CsFAPbBr_3$	Caesium Formamidium Lead Tribromide
$CsFAPbI_3$	Caesium Formamidium Lead Triiodide
CsI	Caesium Iodide
c-Si	Crystalline Silicon
$Cu(In_xGa_{1-x})Se_2$, CIGS	Copper Indium Gallium Diselenide
Cu_2ZnSnS_4, CZTS	Copper Zinc Tin Sulfide
CVD	Chemical Vapor Deposition
DMSO	Dimethyl Sulfoxide
DSC	Differential Scanning Calorimetry
DSSC	Dye-Sensitized Solar Cell
EA	Electron Affinity
E_c	Conduction Band Energy
EDX	Energy Dispersive X-ray Spectrometry
E_F	Fermi Level Energy
EQE	External Quantum Efficiency
ETL	Electron Extraction layer
E_v	Valence Band Energy
FAI	Formamidinium Ammonium Iodide
FF	Fill Factor
GaAs	Gallium Arsenide
GBL	ɣ-butyrolactone
HAAD TEM/XRD	High-Angle Annular Dark-field Scanning Transmission Electron Microscopy TEM/XRD

HE	Hydroethedine
HI	Hydroiodic acid
HOMO	Highest Occupied Molecular Orbital
I_{MPP}	Current at Maximum Power Point
IPA	Propan-2-ol
IPCE	Incident Photon Conversion Efficiency
ITO	Indium Tin Oxide
J	Joule
J_{sc}	Short Circuit Current Density
L_{ex}	Exciton Diffusion Length
Li-TFSI	Bis(triluoromethane)-Sulfonamide Lithium Salt
lpm	Litre Per Minute
LUMO	Lowest Unoccupied Molecular Orbital
MBE	Molecular Beam Epitaxy
M_n	Number Average Molecular Weight
MO	Molecular Orbital
MOCVD	Metal Organic Vapor Phase Deposition
mp	Mesoporous
Mtoe	Million Tons of Oil Equivalent
M_w	Weight Average Molecular Weight
Ø	Work Function
O_2	Oxygen
O^{2-}	Superoxide
OECD	Organization for Economic Co-operation and Development
OPV	Organic Solar Cell
P3HT	3-hexylthiophene
$PbBr_2$	Lead Bromide
PbI_2	Lead Iodide
$PC_{60}BM$	Phenyl-C61-Butyric acid methyl ester
$PC_{70}BM$	[6,6]-Phenyl-C71-butyric acid methyl ester
PCE	Power Conversion Efficiency
PDI	Poly Dispersity Index
PECVD	Plasma Enhanced Chemical Vapor Deposition
PES	Photoelectron Spectroscopy
PL	Photoluminescence
ppm	Part Per Million
PSC	Perovskite Solar Cell
PTFE	Polytetrafluoroethylene
PV	Photovoltaic
rpm	Round Per Minute
rtm	Room Temperature
R_S	Series Resistance
R_{SH}	Shunt Resistance
SEM	Scanning Electron Microscopy

SnO_2	Tin Oxide
Spiro-OMeTAD	2,2',7,7'-Tetrakis[N,N-di(4-methoxyphenyl)amino]-9,9'-spirobifluorene
SWE	Staebler–Wronski Effect
TAS	Transient Absorption Spectroscopy
TBP	4-tert-butylpyridine
TCO	Transparent Conductive Oxide
TEM	Transmission Electron Microscopy
$TiCl_4$	Titanium (IV) Chloride Tetrahydro-furan Complex
TiO_2	Titanium dioxide or Titania
UV-vis spectroscopy	Ultraviolet-Visible Light Spectroscopy
V	Volt
V_{MPP}	Voltage at Maximum Power Point
V_{oc}	Open Circuit Voltage
W	Watt
Woc	Bandgap-Voltage Offset
wt. %	Weight Percent
XRD	X-Ray Diffraction
ZnO	Zinc Oxide
ΔOD	Change in Optical Density
ε_r	Dielectric Constant

1. Introduction: Available solar energy

At present, fossil fuel energy is still a predominant form of energy that is required to satisfy our demand in everyday life activities. In direct relationship with this forever increasing demand, the total fuel consumption data collected by the international Energy Agency in 2017 reported that the unit price for the petrol has started to become unaffordable for most middle class populations [1,2]. To make the matter worse, hydrocarbon wastes produced from fossil fuel combustion are causing a significant rise in the atmosphere temperature globally. Thus, there is a huge drive to develop more affordable and cleaner forms of energy to replace the current fossil fuel sources. Some forms of clean energy are for example obtained from the movement of the tides, wind power to rotate wind mills or even nuclear sources. However, no renewable source is as commonly available, safe and consistent as the sun.

While it may be true that there is no model that can fully portray the actual global warming that has been taking place until now, the mean diffuse Solar radiation graph shown in Figure 1 provides a good estimation on how much energy the sun can provide to the earth.

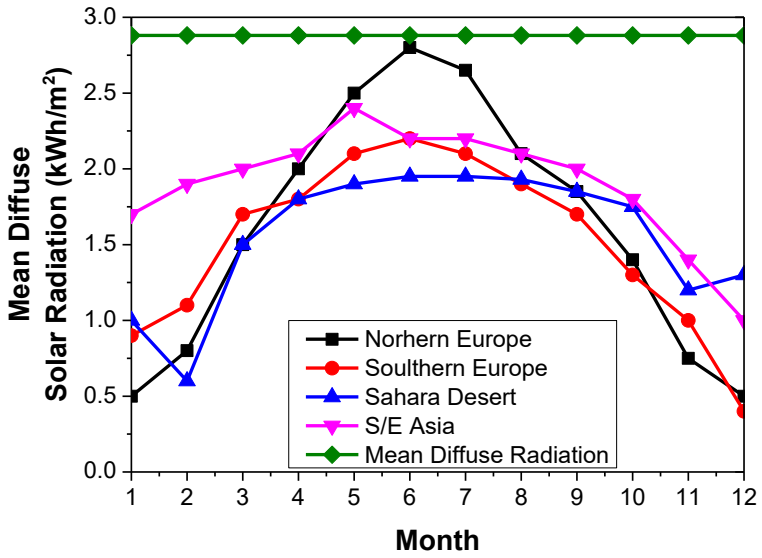


Figure 1: Average yearly solar radiation at the Earth's surface for the different locations around the earth (see labels)**.** The solid green line represents the mean daily solar radiation around the earth which is 2.88 kWh/day**.** This graph is adapted from ITCA in 2008 [3].

According to the average daily solar radiation reported in Global Development in 2008 posted by ITACA. [3], the average daily radiation for people in this world is approximately 2.88 kWh per day (green line in Figure 1) [3]. By integrating the previous number over the course of one year, the average yearly solar irradiance reaches over 6 GJm^{-2} which is equivalent to the energy of one barrel of oil, 140 m^3 of natural gas and 200 kg of coal [4]. Hence, the earth receives power from the sun of over 108 GW per

year [4]. Even with an assumption that 0.1 % of this available solar energy would be harvested at 10 % efficiency, it would still be four times greater than the world's energy generating capacity (approximately 3,000 GW) [4]. By the year of 2015, Table 1(a) shows that the total global energy consumption had been rising rapidly over decades and eventually reached a new record of over 13,647 Mtoe. [1,2]

Table 1: (a) World total primary energy supply by fuel reported in 1973 and 2015 (measured in Mtoe, million tonnes of oil equivalent). (b) Solar photovoltaic (PV) electricity production reported in 2005 and 2017 (measured in Terawatt hour). OECD stands for Organisation for Economic Co-operation and Development while non-OECD Asia excludes China. The data in these 2 tables have been extracted from Statista 2018 (data taken in 2016) and Birol, F. Key World Energy Statistics 2017 [1,2].

(a)

Sources	Year	
	1973 (Mtoe)	**2015 (Mtoe)**
Oil	2818.7	4326.1
Coal	1494.7	3834.8
Natural gas	976.2	2947.8
Nuclear	54.9	668.7
Hydro	109.8	341.2
Biofuel and waste	640.6	1323.8
Others	6.1	204.7
Sum	**6101**	**13647**

(b)

Sources	Year	
	2005 (TWh)	**2015 (TWh)**
OECD	3.64	183.52
Non-OECD EU and Euasia	0.00	0.00
Middle East	0.00	4.69
China	0.08	45.20
Non-OECD Asia	0.22	9.88
Non-OECD Americas	0.05	0.99
Africa	0.01	2.72
Sum	**4.00**	**247.00**

Importantly, a majority portion of the total energy production is still governed by non-renewable energy sources such as crude oil, coal, natural gas and bio fuel [1,2]. The total fuel consumption report in 2015 has increased over double of what it was reported to be back in 1973 (6101 Mtoe) [1,2]. Meanwhile, Table 1(b) compares the total solar photovoltaic electricity production between 2005 and 2015 which shows a massive improvement of over sixty times (4 TWh compared with 247 TWh) [1,2].

Even still, 247 TWh is still far less than the total demanded energy which is equivalents to 13,647 Mtoe. To cope with these demands, further photovoltaic researches and developments are desperately required.

The main viable option for mass commercial production of photovoltaic solar cells currently are crystalline silicon based solar cells which have been thoroughly developed over the past decade and thus limit the scope for any further developments. In addition, this photovoltaic technologies involve an energy intensive and time consuming production method which may not justify their cost-efficiency trade off. On this basis, the investigations of far more affordable materials and processing methods while minimising other associated costs are proposed. One of the ways to move away from silicon production technology is to use versatile solution-based methods such as spin coating or roll to roll printing in order to lower the production cost while offers high mechanical flexibility and lighter weight to solution-processed solar cells compared to their pure inorganic counterparts. Thus, this motivation has led many researchers, including myself, to look into solution processable materials such as organic /small molecules polymers, dye-sensitized solar cells, solution processable inorganic semiconductors or a more complicated hybrid systems where both inorganic and organic components are incorporated.

Regardless, these alternative usages of starting materials and production methods create new challenges for design criteria of photovoltaic systems. Currently, the performance gap between the traditional crystalline silicon solar cells and other solution processable solar cells are still huge. In order to diminish the difference in their performances, further understanding of how these alternative solar cell technologies operate as well as comprehending the factors is desired. The thesis aims to go through relevant solar cell technologies one by one while comparing each of their advantages and disadvantages along the way. In addition, the relevant parameters that govern photovoltaic device performances are also defined.

In particular, the doctoral thesis focuses heavily on addressing the environmental susceptibility of organic-inorganic lead trihalide perovskite photoabsorber films and solar cells. Especially since 2013, lead trihalide perovskite solar cells (PSCs) have generated considerable research attention due to their fast pace growth in power conversion efficiency[5] .By the year of 2016, and the certified efficiencies of the perovskite solar cell reported by Natural Renewable Energy Laboratory reached 21 % [6]. However, PSCs easily malfunction when they are subjected to many external factors such as ultra-violet and visible light, moisture, high processing temperature and oxygen from ambient. Even though some of these factors can be excluded by using glass as a barrier layer or using UV-coating on a glass surfaces, it is almost impossible to completely separate oxygen, visible light and/or moisture from the actual

fabrication process to PSCs. Therefore, the effect of atmospheric stability of organo-inorgano lead trihalide perovskite based films and solar cells under subjection to constant exposure of visible light and oxygen is of significant importance and will be addressed throughout this thesis. In addition, the oxygen-light stability improvement of these lead trihalide based films and solar cells are proposed.

2. Background, theory, aim and motivation

2.1. Photovoltaics (PV), semiconductors, discrete to continuous bands

In general, two requirements are necessary for a material to function as an effective photovoltaic (PV) device: 1.) ability to efficiently absorb sunlight in order to convert it into free charge carriers 2.) ability to transfer and collect these charges at appropriate storing units where it can do work later on. In order to make a 'good' PV device, harvested charges must flow coherently and systematically through the created circuit with a minimum resistance.

The electronic properties of semiconductors allow the above phenomenon to be realised. According to its definition, a semiconductor is "a material which exhibits electrical conductivity in the range between metals and insulators in which the charge carrier density can be changed by external means" (10^{-6} $\Omega^{-1}cm^{-1}$ - 10^{4} $\Omega^{-1}cm^{-1}$) [7]. Around each atom, electrons have to 'stack' at some sets of distance away from the atom while contain different spins individually in each electron orbital [8,9]. Hereafter, this orbital region is called the atomic orbital (AO). On a bigger picture, the interaction of two atoms leads to the formation of the molecular orbital (MO) [10]. Crucially, the energy level of newly occupied orbitals comprise of a lower value than those of the individual atoms. This phenomenon is called bonding molecular orbitals (σ) [10]. On the contrary, the anti-bonding molecular orbital (σ*) which contains higher energy levels than the individual atoms is also formed. More molecular orbitals join together when accumulation of atoms is made in larger molecules. The largest scale of these interaction is located in a crystal where there are numerous molecular orbitals joined together so that their energy levels appear to be continuous 'bands' of energy level [11].

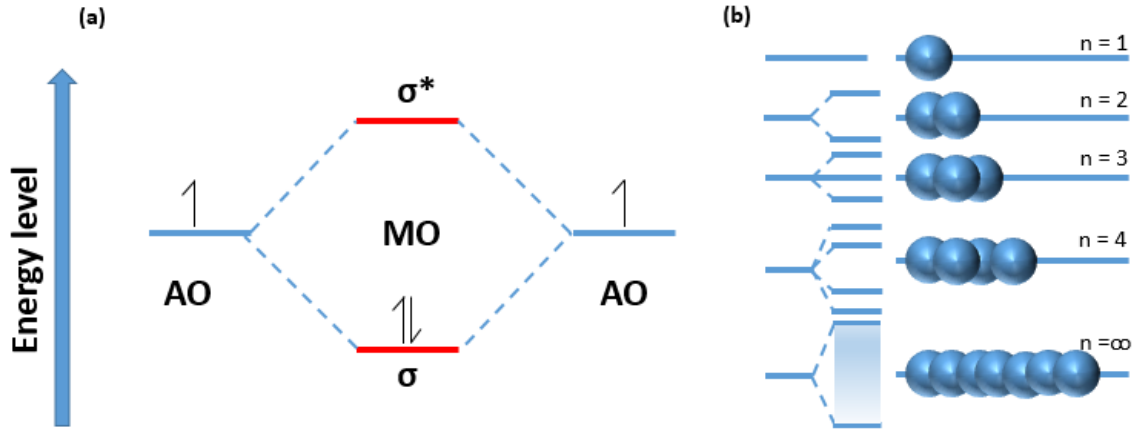


Figure 2: (a) energy level diagram when 2 atoms interact with each other. Formation of bonding (σ) and anti-bonding molecular orbitals (σ*) are shown (b) the formation of a band of N molecular orbitals by accumulating atoms in 1 dimension. It is noted that this band retains finite width as N approaches infinite value.

The highest energy band edge that is occupied with electrons is the valence band (VB) while the lowest energy band that is vacant at absolute zero is called the conduction band (CB). The remaining electrons that are not directly involved in binding molecules together are free to move within crystals. For a metal material, its VB and CB are located either relatively close or overlap naturally which in turn cause excitation of electrons to the unoccupied band to occur readily [12]. This intrinsically introduces an electronic conduction property to a metal material. If there is an energy gap (ΔE_g) between CB and VB in a material, it is classified as either a semiconductor or insulator material. Typically, semiconductor material has its ΔE_g from 0.5 to 3 eV whereas insulator material contains ΔE_g more than 5.5 eV [12]. To further simplify the categorization analysis, only the valance electrons are of interest whereas the core electrons are bound to the atom and are not allowed to move freely in the material. Thus four different possible scenarios are showed via Figure 3 [12].

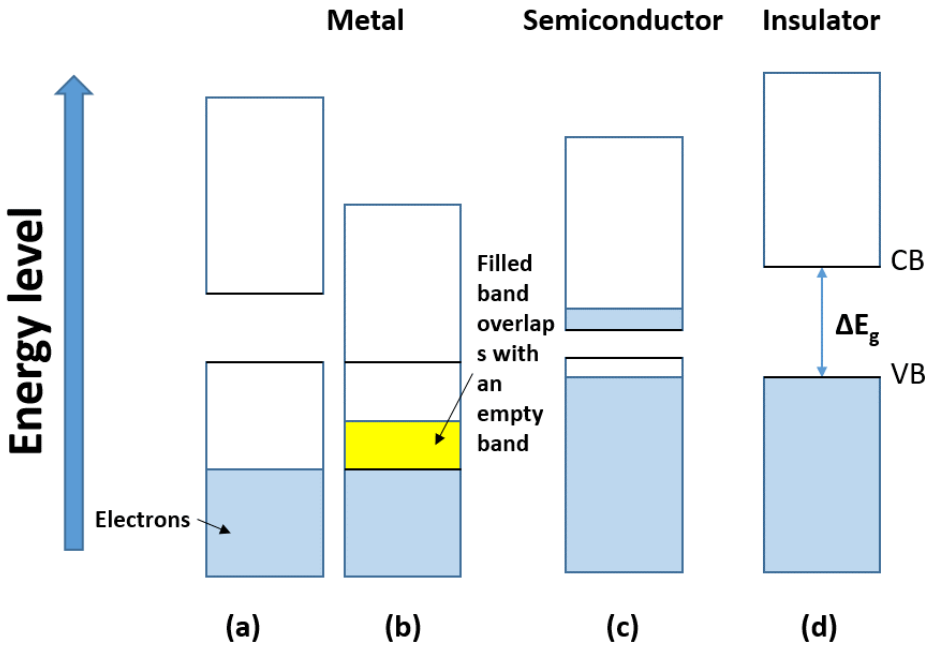


Figure 3: Energy band diagram of a crystal material for (a) half-filled band in metal (b) overlapping conduction (CB) and valence band (VB) in a metal material (c) semiconductor material (d) insulator material. The half-filled band occurred when a metal contain only one valence electron per atom such as copper, gold and silver. The metal material containing two or more electrons in valence bands are shown in (b). ΔE_g represents bandgap energy [12].

Figure 3(a) illustrates a half-filled band which occurs in a metal material consisted of atoms with one valance electron per atom whereas Figure 3(b) demonstrates an overlapping between a filled band and an empty band which happens with a metal material containing two or more electrons in valance bands [12]. Figure 3(c) and 3(d) represents an energy diagram of a semiconductor and an insulator material, respectively when the separation between its CB and VB becomes bigger which makes its energy gap (ΔE_g) starts to increase. As the results, it becomes harder to promote electrons to the CB [12]. For an insulator material, it is almost impossible to guide an electron from its VB to CB in order to make such material conductive whereas for the semiconductor material, limited conductivity is plausible as a few electrons in its VB can energetically process sufficient energy to be promoted into its CB by overcoming ΔE_g via an external energy source provided such as heat or light [12]. Similarly, holes in VB can be considered as positive charges free to drift in the opposite direction of electrons as electrical potential is applied [12]. With increasing ΔE_g, the possibility of any given material to become conductive intrinsically decreases. By a given electrical field (Ɛ), drift velocity (v) per given electric field can be measured. This is defined as mobility (μ) which is widely used parameter to classify responsively to conduct charges in metal, semiconductor and insulators.

$$\mu = \frac{|v|}{\mathcal{E}} \tag{1}$$

The most stable electrical state happens at absolute zero temperature where electrons process no kinetic energy and thus sit at their lowest available energy level. The potential energy which is the energy difference between highest and lowest energy level in such conditions is called the Fermi-energy level (E_F) [13,14]. As stated previously, as the external temperature increases, electrons are excited into a higher unoccupied energy level [13,14]. Eventually at the equilibrium state, the probability function at any given T temperature by Fermi-Dirac distribution occurs [13,14]:

$$f(E, E_f, T) = \frac{1}{e^{\left(\frac{E-E_f}{k_B T}\right)} + 1} \tag{2}$$

Where k_B is the Boltzmann's constant, T is the temperature, E is the energy of a single particle state and E_f is the total chemical potential, E_F is the Fermi energy level at absolute zero [13,14].

2.2. Concept of p-n Junctions

The mechanism of using semiconductors to convert sunlight into electricity is quickly realised with a promotion of ground state electrons from the valence band to the conduction band via photoexcitation energy that is equal or greater than the bandgap of any given semiconductor material (opposite is also true for holes). In working PV solar cells, photoexcited electrons and holes are bonded with strong columbic force that must overcome to separate from one another and harvest into appropriate storing units before they are recombined and disappeared. To enforce this phenomenon, an additional driving force is required. Luckily, by introducing asymmetry (which is known later as 'junction') at the interface of two different types of semiconductors (or semiconductor and metal), an electric field is generated which causes each charge species to drift in an opposite direction and subsequently separate from one another. This is a fundamental concept of a Schottky junction.

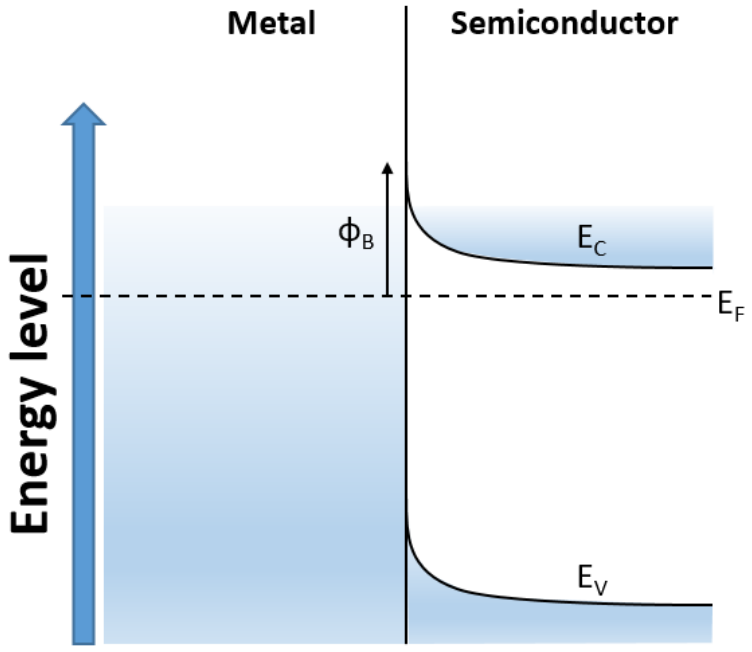


Figure 4 : Schematic of metal and n-type semiconductor interface at zero bias. Schottky barrier is represented by ϕ_B which is the difference between conduction band energy (E_C) and Fermi level energy (E_F). In case of a p-type semiconductor, ϕ_B is the difference between valence band energy (E_V) and E_F [15].

Figure 4 shows that when two different conductive materials are attached to each other, electrons are transported from lower to higher work function material until the thermal equilibrium state is achieved. In other words, the charge transfer reaction ceases when the E_F of those two different conductive materials are levelled. Since charge carriers' density is finite, this introduces a built-in electric field that generates near the junction [15]. Therefore, this creates a 'barrier' for any further charge to be transported in an original direction. Hence, the Schottky Barrier (ϕ_B) is formed [15].

After the Schottky heterojunction is utilised for semiconductor-metal to function as a PV system, the amount of generated photovoltage from such system is very limited [16–18]. In contrast, there is a more efficient method by attaching an n-type semiconductor with a p-type semiconductor which is called p-n homojunction is soon realised. Unlike a semiconductor-metal interface, a p-n homojunction between two differently doped semiconductors lacks a physical material boundary which eliminates undesirable interfaces that may act as electron-hole recombination sites. This concept was first introduced back in 1950s by PV researchers in New Jersey [19]. They demonstrated the first working solar cell which is still widely used as a foundation for many of the most efficient PV devices to date [19]. The Schematic of p-n junction with the energy diagram at p-n interface is showed in Figure 5 [20].

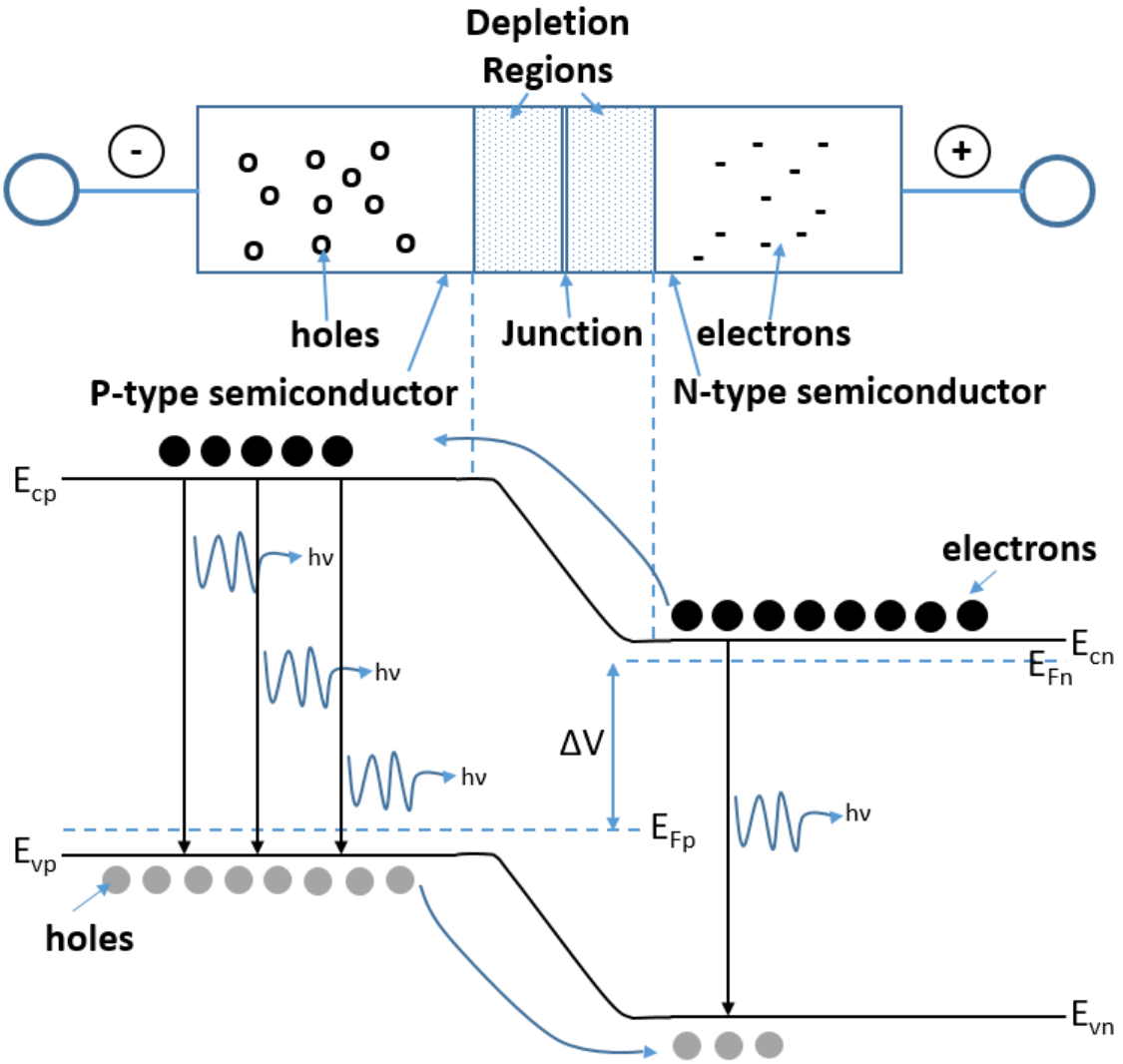


Figure 5: Schematic of a p-n junction of a photodiode with the energy diagram at p-n interface. Minority carriers are required to transfer to the depletion junction before photogenerated charges can be separated**.** E_{cn} and E_{vn} represents energy of the conduction band and valence band of the n-type semiconductor whereas E_{cp} and E_{vp} is the conduction band and valence band of the p-type semiconductor. hv is the light energy generated via electron hole recombination and ΔV is the difference between Fermi energy of n-type (E_{Fn}) and p-type (E_{Fp}) semiconductor [20].

Figure 5 shows that when two differently doped semiconductors are attached to one another, electrons flow from a p-type semiconductor to an n-type semiconductor until their Fermi-level are equilibrated and a depletion region forms at the contacted interface. Thus, a built-in electric field across these two semiconductors is established and a p-n junction is formed. Unlike the previous case with a semiconductor-metal junction shown in Figure 4, the depletion region expand across the whole interface and efficiently functions as a diode. When the device is exposed under illumination, this allows minority carriers (electrons in a p-type and hole in an n-type semiconductor) from each side of the semiconductor material to be swept across the established junction. The depth of the depletion region depends largely on the doping concentration and dielectric permittivity. After that, electron-hole pairs are formed at the assembly interface, and subsequently split via either an external or intrinsic built-in electric field. The latter can only be achieved after minority carriers need to reach the depletion region to prevent the charge carrier recombination process. This acts as one of the limiting factors during photogeneration reaction [21]. In crystalline silicon, which is one of the most well studied and practically used semiconductors in p-n junction materials, ultra-pure crystal purity of silicon is required to keep their number of recombination sites at minimum and in turn maximise their minority carrier diffusion lengths.

2.3. Current density-Voltage measurement

In section 2.3, each step on how photodiode converted sunlight into electricity via the usage of p-n junctions will be briefly described. This section discusses each important operator which determines how efficient each photodiode can be.

The most common interpretation of the effectiveness of each PVs solar cell's performs is to gauge the power output (P_{out}) with respect to its input (P_{in}). Simply put, the ratio between power of electrical output per incident power

$$\mathrm{PCE} = \frac{\mathrm{P_{out}}}{\mathrm{P_{in}}} = \frac{\mathrm{V_{oc}J_{sc}FF}}{\mathrm{P_{in}}} \tag{3}$$

A proper photodiode should behave as a diode in the dark and only allow current to flow when forward bias is applied, not in reverse. At open circuit conditions, the rate of charge recombination is equal with to the charge separation rate and no net current flow is observed. Here, the devices reach their maximum voltage (V_{oc}). On the other hand, short-circuit current (J_{sc}) is reached when $V_{oc} = 0$. Between these two extreme conditions, a point where maximum power output (P_{max}) is reached can be found. The ratio between P_{max} and the theoretical value of P_t is defined as the fill factor (FF). P_t is derived by multiplying V_{oc} and J_{sc} together which represents the power output when no loss recombination occurs.

$$\mathrm{FF} = \frac{\mathrm{P_{max}}}{\mathrm{P_t}} = \frac{\mathrm{V_{mpp}J_{mpp}}}{\mathrm{V_{oc}J_{sc}}} \tag{4}$$

Where V_{mpp} and J_{mpp} is the voltage and current density is at maximum power point. The graphical demonstration is drawn in Figure 6 which includes all important parameters.

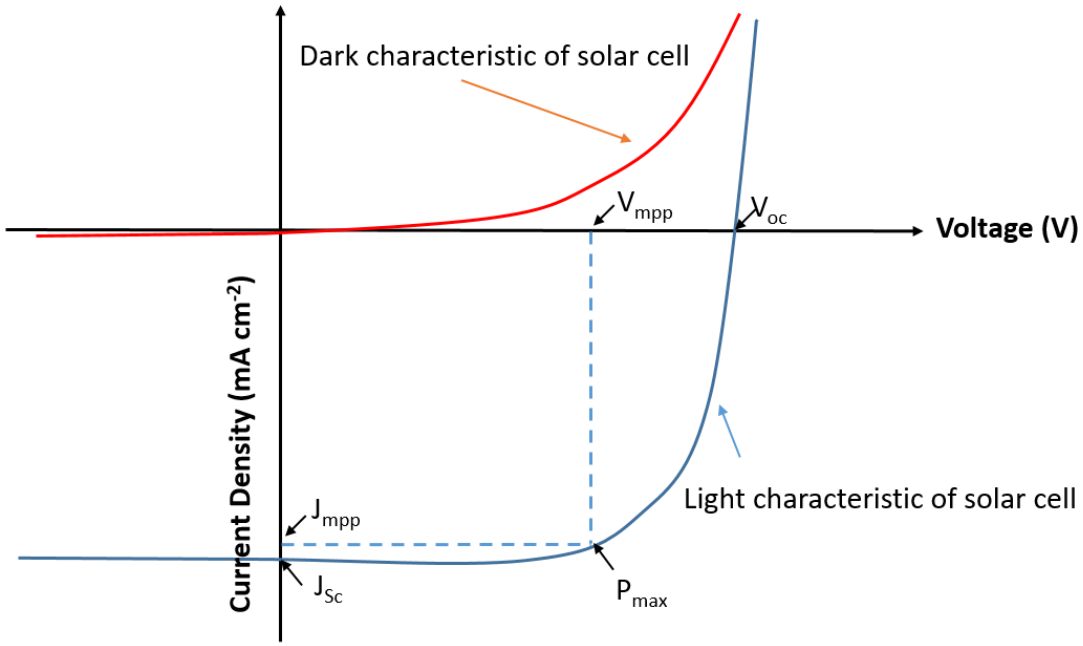


Figure 6: A typical JV curve with and without illumination (blue and red curve, respectively) which contains three important index parameters: short circuit current (J_{sc}), open circuit voltage (V_{oc}) and maximum power point (P_{max}) which locates between these two extreme conditions. P_{max} is derived by multiplying current density at maximum power point (J_{mpp}) and voltage at maximum power point (V_{mpp}) together.

Perhaps, the most important index is the external quantum efficiency (EQE) which is the ratio between the numbers of collected charges from the short circuit current (J_{sc}) and the monochromatic photon from the incident light absorbed. It is noted that EQE is a wavelength dependent parameter.

$$\mathrm{EQE} = \frac{1240\mathrm{J_{sc}}(\lambda)}{\lambda \mathrm{P_{in}}(\lambda)} \mathrm{x}\ 100\ \% \tag{5}$$

Where 1240 is derived from the responsivity which is the function of the photon wavelength (hc/e). h refers to the Boltzmann constant, c refers to speed of light in a vacuum and e refers to electrical charge of an electron.

2.4. Series and shunt resistance

Practically, most PV solar cells suffer heavily from dissipation of power via imperfect morphology within the devices or imperfect flows from the harvested charges at the generation point to the storage units. This introduces parasitic resistances and leakage current. The series resistance (R_S) of the PV devices is mostly reflected by the amount of resilience of the harvested charges transported from photoabsorber to contacts. On the other hand, shunt resistance (R_{SH}) refers to an intrinsic resistance to current loss via alternate pathways (i.e. at grain boundaries or imperfect sites). These effects are illustrated in an equivalent circuit diagram via series and parallel resistor, respectively. In the ideal case, R_S should exhibit a really low value and R_{SH} should be infinite. In other words, the harvested current should not be lost at the diode-electrode interfaces or alternative transporting pathways. Increasing values of R_s and R_{SH} cause JV response shape to be altered as illustrated in Figure 7 [22].

The less steep gradient of the JV curve near V_{oc} is an indication that series resistance within the device increases. As a result, the FF value of such device is heavily taxed. The V_{oc} is unaffected by R_s as current flow is prohibited in the device. According to Ohm's law, as R_s increases, J_{sc} can be altered.

A reduction in the R_{SH} value causes a reduction in the gradient near J_{sc} in the JV curve (Figure 8). Simply put, harvested current is able to bypass the diode and allows it to flow under a reverse bias. Consequently, the current is 'leaked' [23]. For the device with low R_{SH}, its V_{oc} decreases. At short circuit condition, V_{oc} = 0 V which means there is no resistance apart from R_s for photocurrent. Therefore, J_{sc} is unaffected by the effect of R_{SH} [23].

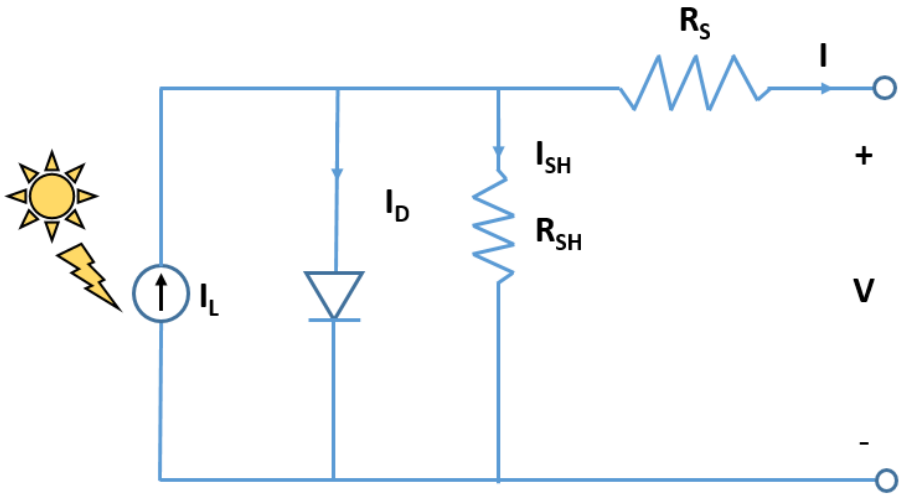


Figure 7: Schematic of equivalent solar cell circuits. I_L is the photogenerated current, I_D is a diode current and I_{SH} is a leaked current through a shunt resistor.

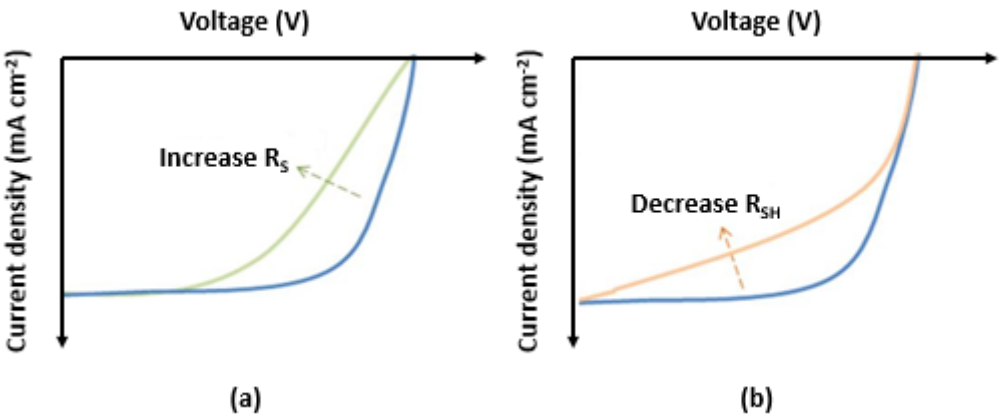


Figure 8: Schematic of I-V curves showing (a) effect of increasing R_s (b) effect of decreasing R_{SH}**.**

2.5. Overview of photovoltaic technologies

Perhaps, the first experimental demonstration of PV was demonstrated by Edmond Becquerel back in the 1839. Much later in 1883, Charlas Fritts made the first successful attempt to separate the charge from the p-n junction of the PV device which had just over 1 % PCE. The cell was made of selenium coated with a thin gold (Au) electrode. Knowledge of how the solar cell operated still remained not fully understood for more than half century later. In 1905, the photoelectric effect was proposed by Albert Einstein in order to clarify the photo induced charge carrier process. Based on this knowledge, the first generation of silicon PV device was first born in 1954. After the Second-World War, a 6 % PCE p-n silicon solar cell was introduced [19]. However, due to the high manufacturing cost along with slow PCE improvement over the course of two decades, the initial application of this PV only surfaced in space development as equipped on the outer surface of satellite providing electricity support for spaceships without modifying the power system. Presently, there are several types of solar cells that are constantly being developed as a renewable energy generation source instead of a finite source like a combustion fuel.

Solar cells can be divided according to their intrinsic chemical composition. For example, Inorganic solar cell which composes of inorganic components or organic solar cell which is functioned by pairing two different types of organic materials. Each type of solar cell is discussed.

2.5.1. Inorganic solar cells

Currently, there are many different types of inorganic solar cells. Some of these inorganic solar cells are expanded upon briefly below.

2.5.1.1. Gallium Arsenide (GaAs)

Gallium arsenide (GaAs) is one of the most widely used III-V semiconductor for photovoltaic applications [24–26]. This is attributed to its high electron mobility (8,500 $cm^2V^{-1}s^{-1}$), its direct band gap (1.4 eV at 300K) and highly reproducible growth mechanisms [27,28]. Therefore, GaAs single junction devices have rapidly become a reference system for thin film solar cells. The world record power conversion efficiency (PCE) of the Gallium arsenide based solar cell was reported to be at 28.6 % [24]. To achieve high efficiency in GaAS thin film devices, the crucial step is the synthesis of highly crystalline GaAs absorber on GaAs substrate. Typically, Chemical Vapour Deposition (CVD) [29–33], metal organic vapour phase epitaxy (MOCVD)[34–38] or Molecular Beam Epitaxy (MBE) [39–41] is used to achieve such possibility . CVD refers to a class of fabrication methods in which a solid source is grown by reaction of gaseous source material yielding a product effluent gas. Some examples of GaAs deposition methods can be found below [24,27,28,38,42]:

CVD : $\mathbf{2Ga + 2\ AsCl_3 \rightarrow\ 2\ GaAs + 3Cl_2}$

MOCVD : $\mathbf{Ga(C_2H_5)_3 \downarrow + AsH_3 \downarrow \rightarrow GaAs + 3C_2H_6 \uparrow}$

MBE : $\mathbf{4\ Ga + As_4 \rightarrow 2\ Ga +\ As_2 + 2GaAs \rightarrow 4GaAs}$

Where ↓ is designated for a gas that adsorbs on the substrate surface prior to chemical vapour deposition reaction and ↑ indicates a by-product that is left from the reaction.

CVD and MBE allow multifunction and tandem GaAs solar cells to be made possible such as AlGaAs/Si [43–45], AlGaAs/GaSb tandem [46–48] and GaAs/InGaP [45,49,50]. However, there are a number of limitations of GaAs thin film solar cells. Firstly, GaAs sources need to be ultra-pure because CVD is susceptible to any impurities. These impurities may disturb the deposition rate of gallium or arsenide plasma and thus lower its PV performances. Secondly, all three of GaAs deposition techniques require a pumping system: pressure within the CVD chamber is typically kept below 10^{-6} Pa (or approximately 10^{-8} Torr) [30,31,33], while MOCVD requires moderately low pressure within the deposition chamber (10 to 750 Torr) [35–37] and MBE takes place in ultra-high vacuum (10^{-8}-10^{-12} Torr) [51]. Regardless of whichever deposition techniques is used, the pumping process is considered to be a bottle neck which slows down the fabrication process of GaAs solar cells. Thirdly, all three GaAs deposition processes are rather wasteful and expensive. In order to create uniform plasma or ionised gas flumes of gallium and

arsenide, super pure starting materials are needed and a lot of those materials are wasted during the deposition processes. In addition, Gallium in itself is scarce and expensive to mine or refine (17 ppm in the Earth crust) compared to silicon (28 % in the Earth crust) [52].

2.5.1.2. Amorphous silicon (a-Si:H)

Amorphos silicon (a-Si:H) has a wide absorption range within the visible spectrum (1.7 eV - 1.5 eV of direct and indirect band gap, respectively) [53]. Silicon also has a very high absorption coefficient (approximately 10^5 cm^{-1}) [54,55]. In addition, silicon can be doped as an n-type or a p-type material which is a required characteristic for p-i-n type solar cells [56].

Silicon based solar cells have a number of advantages over GaAs solar cells. For example, silicon is plentiful and economical to process in the form of silicate minerals. In addition, the foundation of the silicon industry is well-established and well-grounded much earlier than GaAs technologies thereby hindering the adoption of GaAs [46,57]. Up until the 2010, many billions of pounds had been invested globally to develop amorphous Si (a-Si:H) technologies for example 'Golden-Sun Program [58,59]. Perhaps, the underlying reason for this investment was to even attempts replacing multi-crystalline or microcrystalline silicon (µc-Si). This gave rise to numerous innovations such as cell integration, grade gap and multi-junction light trapping which all contributed to the improvement in the cell performance [60,61]. In 2015, Matsui et al. reported a-Si:H single junction solar cells achieved PCE of 10.11% [61] via plasma enhanced chemical vapour deposition (PECVD). Realistically, average single junction a-Si:H solar cells degrade down upon continuous usage to around 5-7 % depending on how these are used [61].

At present, a-Si:H solar cell researches and developments still face many limitations in order to gain more market share; this includes a-Si:H intrinsic properties and the chemical vapour deposition method that is used [62].

1.) High energy cost with CVD/PECVD and sputtering method: both the CVD and sputtering method does still involve using a high electric current and a moderately low pressure in the deposition chamber (milliTorr to a few Torrs) in order to form uniform a Si reactive plasma.
2.) Poor a-Si:H morphology: a-Si:H has poor morphology compared with other inorganic solar cells. With its poor morphology, any harvested charges of a-Si:H solar cells arrive at their correspondence electrodes at much slower paces than the extracted charges from highly crystalline solar cells such as poly crystalline (µc-Si), resulting in a much lower PCE.
3.) A typical 10-30 percent PCE drop from its initial efficiency within the first 6 months of constant light exposure: This phenomenon is also known as the Staebler-Wronski Effect (SWE) [63]. Upon

constant light exposure to a-Si solar cells, more defect density within a-Si:H is formed, thus increasing recombination current which in turn lower PCE of a-Si:H based solar cells [63].

2.5.1.3. Micro and nano crystalline (μc/nc-Si) and polycrystalline silicon solar cells

Micro and nano crystalline silicon (multi-crystalline or μc/nc-Si which is also known as micromorph a-Si:H) has small grains of crystalline Si imbedded in amorphous Si phase which makes μc/nc-Si based solar cells contain a higher PCE compared to a-Si:H based solar cells [62]. The highly crystalline structure along with a lower band gap property (1.1 eV) cause the c-Si layer to be able to absorb red and infrared light which in turn enhances its overall PCE. The combination of μc/nc-Si and a-Si:H layers are made to form tandem solar cells where their energy offset is created at multi-crystalline - amorphous interfaces. In contrast, polycrystalline silicon consists solely of highly oriented silicon grains. As a results, polycrystalline silicon based solar cells exhibit higher PCE compared to μc/nc-Si solar cells In 2016, Kaneka Corporation reported the PCE of 26.33 % in practical size 180 cm^2 polycrystalline silicon rear junction solar cell [64–66] while at 2015, Weiwei deng et al. reported a 20.6 % PCE for multi-crystalline silicon solar cell (156mm x 156mm) [67,68].

Nonetheless, the fabrication processes of μc/nc-Si and polycrystalline Si involve using a higher vacuum compared to a-Si:H solar cells. This translates to a higher production cost for μc/nc-Si and polycrystalline solar cells.

2.5.1.4. Cadmium Telluride (CdTe)/Cadmium sulphide (CdS)

Cadmium telluride (CdTe) is one of the materials that is used to replace Si solar cells. Theoretical efficiency of CdTe based solar cells is higher than that for silicon (30% [69] compared with 29.1% [65]). Perhaps, the initial motivation in CdTe solar cells comes from the fact that it is possible for CdS and CdTe based solar cells to be produced via the solution processes [69,70]. In general, it can be classified as a colloidal quantum dot solar cell which mostly involves depositing photosensitive p-type quantum dot onto a semi-transparent electrode such as fluorine tin oxide/titiania (TiO_2) which generates built-in electric field. This electric field is generally used to separate photogenerated charges. Quantum dot CdTe and CdS acts as both photoabsorber and conductor. Recently, the world record efficiency of lab CdTe solar cells reached over 21 % [69,71,72], although, there are a number of concerns toward CdTe and CdS solar cell development. For example:

1.) Toxicity in cadmium source. Some environmental concerns have been raised regarding cadmium toxicity and the likelihood of contaminating the surrounding environment where such devices are manufactured.
2.) Telluride sources become harder to obtain. Further CdTe/CdS researches and developments are stagnated which is responsible for a decrease in the likelihoods of an up-scaling industrialisation.

2.5.1.5. Copper Indium Gallium Selenide (CIGs) solar cells

Copper Indium Gallium Selenide (CIGs) solar cells incorporate four elements allowing sophisticated band gap engineers to suit many PV applications. CIGs can be made via co evaporated-CVD, spray deposition or screen printing. In 2013, the most efficient CIGs solar cell was reported by Reinhard et al. to be 20.3 % and 18.7% when deposited on rigid glass and polyamide flexible substrate, respectively [73].

Similarly to CdTe limitations, CIGs researches and developments face comparable issues. For example:

1.) Indium and Gallium starts to become harder to acquire.
2.) Complex synthesis process and the sophisticated control required during the fabrication process; this makes upscaling become costly compared with that of other inorganic solar cells. In addition, low reproducibility of CIGs normally take place due to these complex methods.
3.) Toxicity: CdS is normally added during CIGs solar cell fabrication processes; this implies higher production cost via encapsulation.

Summaries for Pros and Cons for inorganic PV solar cells

The summary of all inorganic solar cells lists above are compared in Table 2 whereby their PV performances, toxicity and availability are taken into accounts.

Table 2: Comparison table for inorganic single-junction terrestrial solar cells regarding state-of-the-art PV performances, toxicity and associated cost until 2016. The test solar cells were measured under AM 1.5 G spectrum (1,000 Wm^{-2}) at 25 °C. This table is adapted from the Solar cell efficiency table reported at 2015 and 2017 (version 45 and 49) [74,75].

Materials	PCE (%)	Advantages	Limitations	Test centre, date and references
GaAs (thin film)	28.8 ± 0.9	1. Direct band gaps. 2. Allow sophisticated band gap engineering. 3. p-i-n junctions possible. 4. Tandem possible. 5. Thermally and environmentally stable, suitable for high temperature application.	1. Gallium start to become harder to find. 2. CVD and other vapour deposition method are slow and costly. A lot of starting materials are wasted. 3. The deposition techniques are susceptible to impurities. 4. Limited laboratory lab size production. Hinder upscaling.	Alta Devices. NREL (5/12) [24,71]
Si (a-Si:H) (cell)	10.2 ± 0.3	1. Easy to handle silicate. 2. Nontoxic 3. Readily available.	1. Indirect band gap materials, 2. Slow manufacturing process (similar to GaAs) 3. Lack of cell's stability.	AIST.AIST (7/14) [61]
Si (µc/nc-Si)	21.3 ± 0.4	1. Cheap material costs. 2. Nontoxic. 3. Readily available. 4. Longer device stability than a-Si.	1. More expensive to purify and process than a-Si. 2. Slower production process. 3. Indirect band gap.	Trina Solar. FhG-ISE (11/15) [67,68]

Si(crystalline)	26.3 ± 0.5	1. Intermediate material costs. 2. Non-toxic. 3. Readily available. 4. Higher PV performances than a-Si and µc/nc-Si	1. Even slower production process. 2. Even more expensive. 3. Approach theoretical efficiency limit of 29.1 % [65]	Kaneka rear junction FhG-ISE (11/16)[64–66]
CdTe (cell)	21.0 ± 0.4	1. Direct band gap. 2. Fast production speed. 3. Solution processable	1. Highly Toxic. 2. Expensive in both material (Te in particular)and high pre/post production cost	Kaneka rear junction, FhG-ISE (7/16) [69,71,72]
CIGS (cell)	21.0 ± 0.6	1. High flexibility to adjust its band gap to suit desired properties. 2. Solution processable.	1. Toxic. 2. Expensive in both material and pre/post .production cost. 3. Large batch-to-batch variation.	Solibro, pn glass. FhG-ISE (4/14) [71,73]

2.5.2. Organic solar cell (OPV)

PV based organic solar cells have attracted intense attention since the first organic solar cell with PCE of over 1 % was invented back in 1977 by incorporating energy band offset of electron donor and acceptor organic semiconductors [76,77]. In contrast with the more rigid structure of inorganic solar cells, organic photovoltaic (OPV) provides not only higher manufacturing flexibility (i.e. possibility of depositing PV on the flexible polyamide substrate) to suit a boarder range in PV applications, but also enabling other upscaleable production techniques like roll-to-roll and doctor blading for large area solar cell devices. To date, many actual OPVs devices can already be found in many small to medium scale applications which mostly exist in the form of solar curtains or sheets integrated within buildings and electronic consumer products [78–83].

Despite the great advancement in the OPV technologies [84–87], the operating mechanism of OPV still need further clarifications. Similar to inorganic solar cells, upon the photo excitation process, OPV forms an excited state, termed as exciton (electron-hole pairs) which has a finite lifetime. For inorganic materials, they mostly contain relatively high dielectric constant (ε_r ~ 1000), thus any harvested light energy is converted to free charge feasibly. However, OPV materials have lower dielectric constant (ε_r ~ 3) in general. In other words, electrons and holes in OPVs are bounded by strong columbic forces and are unable to separate naturally. Before the recombination process of electrons and holes can take place, the thermodynamic energy offset is required to overcome the exciton binding energy and subsequently convert exciton into free charge carriers. This energy offset can be found at the electron donor (p-type) and acceptor (n-type) interface. At the n-p junction, electrons gain extra kinetic energy as they travel from the lowest unoccupied molecular orbital (LUMO) of the electron donor to highest occupied molecular orbital (HOMO) acceptor material, whereas holes travel via the opposite direction. Therefore, the driving force for interfacial charge separation and exciton diffusion length are two main limiting factors to determine how efficiency of each OPV device [88].

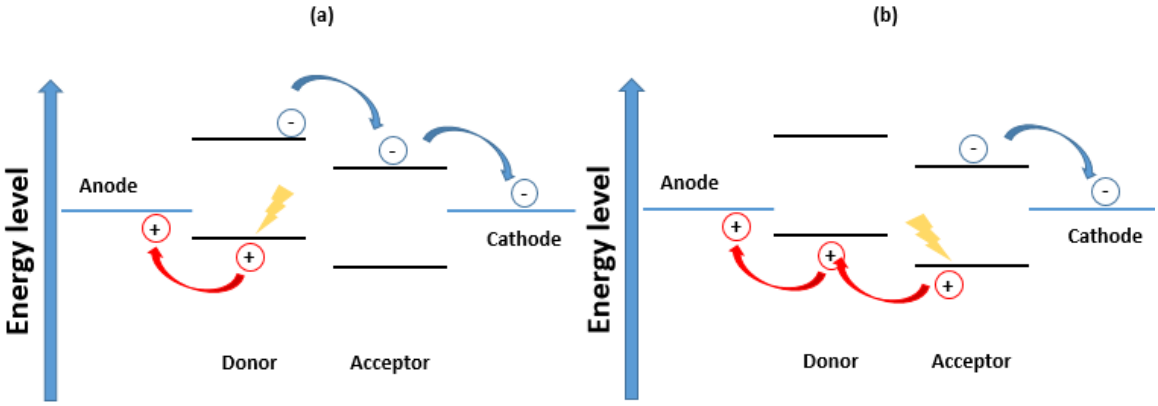


Figure 9: Diagram displays free charge carrier formation after photoexcitation occurs at (a) donor material, (b) acceptor material.

2.5.2.1. Donor materials

In terms of PCE of OPVs, Schrber et al. suggested that a 10 % solar cells can be fabricated if the ideal conditions are met [88]. They stated that an ideal donor material should have an LUMO below -3.92 eV with a band gap less than 1.74 eV when measured in vacuum [88]. This aim was made possible recently by Heliatek who set a world record efficient OPV measured to be at 13.2 % in 2016 [89].

The most commonly used electron donor material seems to be 3-hexylthiophene (P3HT). Typically, P3HT has its LUMO and HOMO at -3.3 eV and -5.2 eV, respectively [90]. P3HT also contains relatively high hole mobility ($10^{-4}m^2V^{-1}s^{-1}$) and exhibits high environmental stability [91]. Nevertheless, the large band gap in P3HT may be considered to be a limiting factor for the amount of solar spectrum absorbed.

2.5.2.2. Acceptor materials

Usually, fullerene derivative materials such as Phenyl-C61-butyric acid methyl ester ($PC_{60}BM$) or [6,6]-Phenyl-C71-butyric acid methyl ester ($PC_{70}BM$) are commonly used as electron acceptor in OPVs. $PC_{60}BM$ and $PC_{70}BM$ as both have suitable LUMO and HOMO level to create sufficient energy offset with P3HT or other donor polymers ($PB_{60}CM$ has HOMO and LUMO at -6.1 eV and -3.7 eV while $PC_{70}BM$ has HOMO and LUMO levels at -5.9 and -3.9 eV, respectively). In addition, both $PC_{60}BM$ and $PC_{70}BM$ is highly soluble in chlobenzene which is a necessary requirement for printable solar cells [92].

Nonetheless, there are a few drawbacks of using fullerene derivative as an n-type material in OPV solar cells. For example:

1.) Both $PC_{60}BM$ and $PC_{70}BM$ have a very limited degree of solubility in common environmental friendly solvents such as isopropanol or ethanol [93,94]. This often increase post production cost for OPVs for large scale solar cell devices significantly.
2.) Fullerene itself is expensive. Approximately 250 g of C_{60} (>99.5 %) plus reagent could easily cost more than 1.2k dollars according to SES research in 2017 [95].
3.) Fullerene might affect the morphology of OPV solar cells due to its bulky size.
4.) Fullerene intrinsically contains high electron density within its molecule which may chemically react with other nearby polymers and drastically reduce the OPV operational lifetime.
5.) Fullerene is not a good visible light absorber candidate. In OPV solar cells, only p-type polymer material functions as a photoabsorber, which in turn potentially limits the total number of generated exciton.

2.5.3. Dye-sensitized solar cells (DSSCs)

Back in the 1880s, Moser first introduced the concept of the dye-sensitized solar cell (DSSCs) by using it along with halogenated silver plate to enhance photocurrent [96]. However, light harvesting and charge separation processes in DSSCs were not fully explained until much later in 1976 where the first real attempt was made to address at these 2 aspects [97]. Since then, many more extensive studies and researches were made in order to push DSSCs maximum PV performances. In 1991, a big leap in power conversion efficiency (PCE) spike of approximately 7 % was reported by Gratzel and O, Regan [98]. This PCE breakthrough was made possible via a combination of the electrolyte iodide/triiodide (I^-/I_3^-) redox shuttle and the mesoporous titiania (TiO_2). The proposed design involves using a large interface area betweenTiO_2 and the tri-iodide electrolyte complex to supress harvest charge recombination and help generate free charge carriers. In addition, these large surface area enhance light absorption for DSSCs [98]. In 2014, Simon Mathew et al. reported a world record PCE of DSSC of 13 % via molecular engineering of porphyrin sensitizers (dye code SM315) coupled with cobalt redox shuttle in order to maximise visible light absorption [99].

Dye-sensitized solar cells (DSSCs) are considered a cost effective PV solar cell device because not only the starting materials are very affordable, but typical DSSCs has plain and simple fabrication design. Furthermore, DSSCs can be operated under a wide range of temperatures or in an easily contaminated environment. All these advantages in DSSCs make mass industrialisation very possible. A typical DSSCs consists of a metal oxide scaffold such as titanium dioxide or titiania (TiO_2) acting as an electron extractor component and hole conductor layer which can take the form of liquid electrolyte such as an iodide/triiodide redox couple (I^-/I_3) or solid state hole transporting material. Furthermore, a thin dye absorber layer is normally used to ensure photon absorption that takes place near a hole-electron transporting interfacial area. This dye-sensitizer removes another prerequisite for exciton diffusion to

occur at the hole-electron transporting layer interface [100]. Figure 10 illustrates electron generation and transfer within the DSSCs [100].

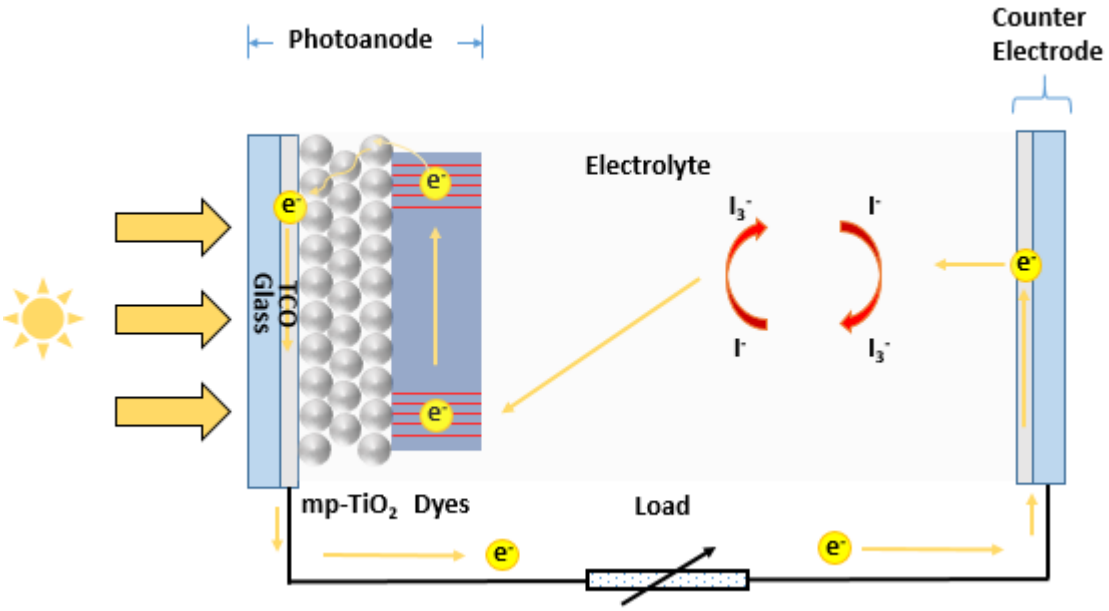


Figure 10: Schematic for Typical DSSCs. Where TCO refers to transparent conductive oxide, I^-/I_3^- stands for the electrolyte redox couple and mp-TiO_2 is a mesoporous titiania which is a metal oxide scaffold [100].

Under illumination, the dye-sensitizer generates excitons and then subsequently injects electrons to titiania which acts as an electron transporting material while the holes are transported via a hole conductor or liquid iodide/tri-iodide redox couple. The interfacial charge separation causes the (quasi) Fermi energy level of electrons and holes in the systems to split which in turn creates photovoltage [100]. The free charge carriers are transported and extracted to an appropriate electrode in order to produce photocurrent [100]. During all these chare extraction processes, the recombination process at the dye-sensitizer, electron-hole transporting layer interface are also taking place and compete with the charge extraction processes kinetically [100]. The effectiveness of the charge extraction processes over charge recombination processes determines how 'good' each DSSCs is in PV aspect. For instance, electron injection from the dye-sensitizer needs to occur before the exciton recombine, which means its excited state will convert back into the ground state and render harvest energy useless and holes in the iodide/tri-iodide redox couple need to successfully be transported to the appropriate electrode before they can recombine with an opposing carrier. Under the condition where no extracted current is found, for the open-circuit condition, the forward and reverse charge harvest rate are equal which creates a steady state population of separated charge within a device. This point in time defines the open-circuit voltage (V_{oc}). The energy diagram shown in Figure 11 summarises the electron

transporting processes in DSSCs. It is noted that hole transportation process occurs from the dye-sensitizer to redox electrolyte couple.

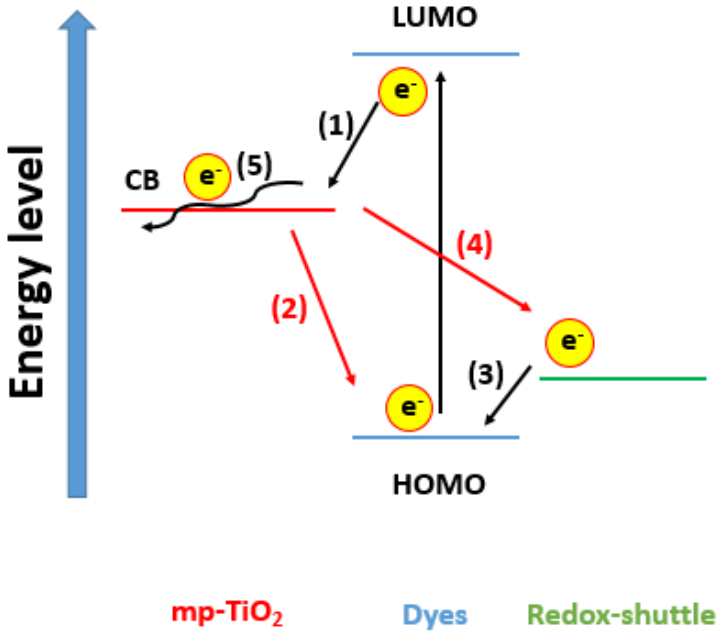


Figure 11: Illustration of electron transfer processes in a typical DSSCs (liquid state).

1.) Electron injection from the dye sensitizer into the conduction band (CB) of mesoporous titiania (mp-TiO_2) after the photoexcitation process.
2.) 1st possible electrons (from mp-TiO_2) and holes (from the dye-sensitizer) interfacial recombination process.
3.) The redox couple regeneration at the dye-sensitizer. Or hole transfer from the dyes to redox shuttle.
4.) 2nd possible electrons-hole interfacial recombination process between the titiania and redox electrolyte, respectively.
5.) Electron extraction process from mp-TiO_2 to the transparent conductive electrode (TCO).

However, most triiodide redox shuttles have relatively high concentration in order to suppress interfacial recombination within TiO_2 nano-crystals and the dye sensitizers which generates a high possibility for the redox electrolyte to erode any adjacent capsulated components within DSSCs. This problem became the primary driving factor for the development of solid state DSSCs by replacing the liquid electrolyte with a solid state HTM. In the 1998s, U. Bach et al. demonstrated a usage of *2,2',7,7'-Tetrakis[N,N-di(4-methoxyphenyl)amino]-9,9'-spirobifluorene,* which is widely known as spiro-OMeTAD ,as a replacement for a liquid electrolyte for DSSCs [101]. Since then, the research fields involving solid state dye-sensitized solar cells have begun to gain their momentum.

2.5.4. Perovskite solar cells

The perovskite structure was discovered way back in the 19th century. The term "perovskites" refers to a group of specific crystal structures by the general formula ABX_3. The most common example of perovskite structure is calcium titanium oxide ($CaTIO_3$). The A-site contains organic cation, B-site is a metal centre cation and X refers to halide anion. Each metal cation is bounded by a halide octahedral cage. The most commonly studied perovskite in PV fields is organometallic halide perovskite (which is normally referred to general as perovskite), in particular, methyl ammonium lead trihalide perovskite ($CH_3NH_3PbI_3$ or $MAPbI_3$). In this case, $CH_3NH_3^+$ is the organic component, lead or Pb is the metal cation and iodine or I^- is the halogen anion [102]. The schematic of crystal structure of organometallic halide perovskite is drawn in Figure 12.

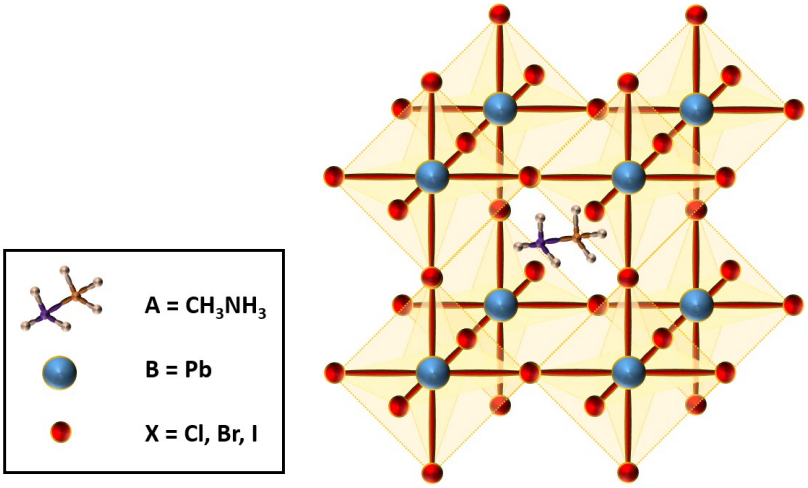


Figure 12: Schematic of crystal structure of typical organometallic halide perovskite. A refers to organic anion, B is metal cation and X represents halide.

The perovskite layer process has various desirable advantages as a photoabsorber material. Firstly, the perovskite layer can be deposited via solution process methods such as spin coating and screen printing [103–106]. Roldan-Carmona et al. and Schmidt et al. reported the design guideline to fabricate perovskite solar cells on top of flexible substrates [107,108]. Secondly, perovskite itself contains a relatively high absorber coefficient all across visible wavelength regions meaning only thinner absorber layer is sufficient in order to constructing a decent solar cell. Thirdly, the non-radiative recombination of perovskite is rather low. Thus, this reduces bandgap-voltage offset (W_{oc}) which in turn , allows high V_{oc} for perovskite solar cells [109]. Typically, many studies for perovskite solar cells show V_{oc} exceeding 1 V [110,111]. Moreover, perovskite contains high carriers mobility as well as long diffusion length [112].

$$W_{oc} = \frac{E_g}{q} - V_{oc} \tag{6}$$

The main device construction of perovskite solar cells was developed based on DSSC technology. As explained previously, the main DSSC building blocks consisted of mp-TiO_2, dye-sensitizer and liquid

electrolyte. Originally, perovskite such as methyl ammonium lead tri-iodide ($CH_3NH_3PbI_3$ or $MAPbI_3$) and methyl ammonium lead tri-bromide ($CH_3NH_3PbI_3$ or $MAPbBr_3$) were used as alternative resources for dye materials [113]. Perovskite sensitizer solar cells had a moderate success of approximately 3.8% in terms of their device PCE in 2009 [113]. Not long after in 2011, the peak PV efficiency of perovskite sensitizer solar cells of 6.5 % was achieved by Jeong-Hyeok and Park et al. [114]. However, the major problem of this kind of technology involves the intrinsic instability of the dissolution of perovskite absorber into the organic electrolyte component. Hence, research attentions were majorly shifted towards solid state solar cells by replacing liquid parts with solid state p-type hole transporting materials such as *2,2',7,7'-Tetrakis[N,N-di(4-methoxyphenyl)amino]-9,9'-spirobifluorene* (spiro-OMeTAD). By following this notion, Park et al. managed to gain another massive PCE improvement exceeding 9 % [115] for perovskite based solar cells . In the meantime, Snaith et al. had demonstrated that a substitution of aluminium dioxide (alumina or Al_2O_3) over TiO_2 in an organometallic lead halide perovskite can lead to yet another PV performance enhancement of approximately 10.9 % [116]. For mp-TiO_2/lead halide perovskite solar cells, the metal scaffold is normally used as a photoanode which functions similarly to that of DSSCs while the perovskite acts as a visible light absorber and photo-electron transporting layers into the CB of mp-TiO_2. On the other hand, photo-electron injection from the perovskite to mp-Al_2O_3 is absent as the CB of Al_2O_3 is higher when compared with regard to the excited state of the perovskite. This shows that the perovskite material is capable of not only acting as photoabsorber, but also as the photo electron-hole pair dissociation layer without needing the underlying mp-TiO_2 [112]. The dissociation take place within the perovskite layer due to its sufficiently long electron-hole diffusion length which exceeds 1 µm [112]. In other words, the perovskite layer can transport both electrons and holes simultaneously. Ever since, solid state perovskite solar cell technology has been categorised in its own unique class of solar cell alongside others'.

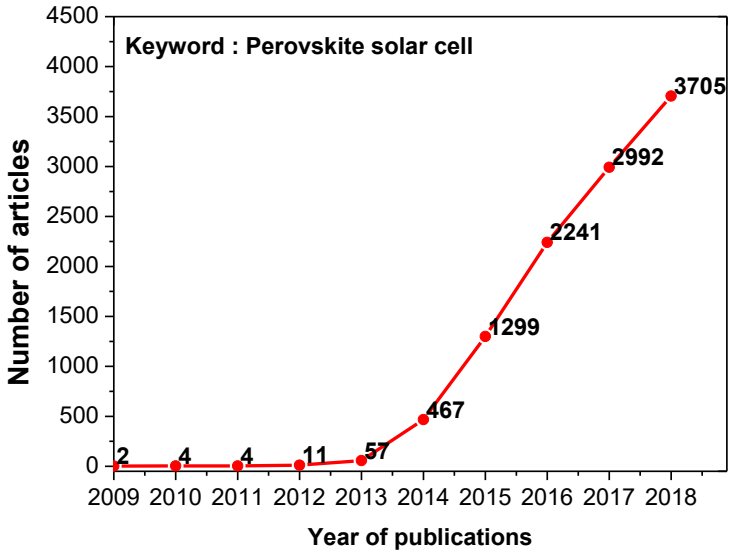


Figure 13: Number of articles versus publication solar cell via Web of Science when the word 'perovskite solar cell' was input [117]. Approximately 1300 peer reviewed studies relating to perovskite solar cells were published in 2015 which were almost three times higher than the total publications in 2014 [117]. This graph was adapted from the data published by *Park, N.-G et al. Methodologies for high efficiency perovskite solar cells* [117].

Even though organometallic trihalide perovskite solar cell technologies are derived from DSSCs, the perovskite solar cells contain higher photocurrent (J_{sc}) compared to DSSCs which normally translate to a higher capability to capture visible light. In particular, the absorption spectrum of typical organometallic trihalide perovskite covers not only the entire visible light region but also extends partially into the near infrared regime. Furthermore, the absorption coefficient of organometallic trihalide perovskite has about one order of magnitude higher than typical organic dyes. In regard to open circuit voltage of perovskite based solar cells, it largely depends on the energy offset between the HOMO of the hole transporting layer such as spiro-OMeTAD and the perovskite rather than that in the semiconductor layers of the photoanode. Thus, the high level of electron (quasi) Fermi level in the perovskite in open circuit condition verifies the reason why organometallic based perovskite solar cells normally contain relatively high V_{oc} exceeding 1 V [110,111].

At present, an impressive world record efficiency for thin film perovskite solar cell was set over 22 % by Yang et al in 2015 [118]. It was made possible with the use of formamidium lead iodide perovskite which absorbs a boarder solar spectrum range than traditional $MAPbI_3$ and an intramolecular exchange reaction between dimethylsulfoxide (DMSO) molecules and formamidinium iodide [118].

In order to mass produce cheap and efficient perovskite solar cells, the solar cell manufacturers must be able to ensure the long term stability of their products typically more than 20 years without losing

more than 80 % of the PV initial performances [56,119]. At present, perovskite solar cell technologies are making a sudden improvement in terms of their PCE. However, the perovskite material itself has a serious problem with environmental stability. There are a number of external and internal factors that may cause perovskites to stop functioning as a solar absorber layer. Thus, these factors must be addressed. Perhaps, the first review to attempt to pinpoint the factors that influence operational life time of perovskite solar cell was made by Niu et al. [120]. Multiple studies including Niu et al. have pinpointed four factors that affect operational lifetime of perovskite material: moisture, oxygen, UV/visible light and thermal effects [102,111,120]. Ever since, many researchers including myself have shifted their attention to further explore this issue in detail. In section 2.6, the known environmental factors that affect stability of organo-inorgano lead trihalide perovskite photoabsorbers are reviewed. In addition, the aims and objectives of this thesis are provided.

2.6. Factors that affect long term performances of perovskite films and solar cells

In section 2.6, four primary factors which affect operational lifetime of lead trihalide perovskite material are addressed. Section 2.6 also discusses a current understanding of each of these factors affecting the operational lifetime of perovskite based solar cells. The aim of this thesis is to study two of these factors in particular, oxygen and visible light, and prolong the operational lifetime of lead trihalide perovskite solar cells while retaining their excellent PV performances under the subjection of these two factors.

Known Factors that affect stability of the perovskite solar cells

2.6.3. Ultraviolet light (UV light)

Many previous studies report that long term exposure of UV light may cause degradation of the absorber layer including perovskite solar cells [121–123]. Not long after in 2013, some researchers such as Leijtens et al. demonstrated and rationalised how UV light induced instability in perovskite solar cells [124]. Both encapsulated and non-encapsulated perovskite solar cell samples were exposed to standard one sun Air mass (AM) 1.5 G illumination with and without a UV filter. Without the presence of a UV filter, they observed more rapid degradation to take place in encapsulated devices compared with non-encapsulated devices [124].

They theorised that UV light caused photoexcited electrons to trap in deep lying unoccupied sites in mp-TiO_2 and thus made TiO_2 less conductive to act as an electron transporting layer [124]. To avoid such interaction between UV light and TiO_2, they proposed three solutions [124]:

1.) Pacify the trap sites.
2.) Ensure minimum contact of UV light with TiO_2 layer.
3.) Replace TiO_2 with alternative materials.

It is important to note that this paper was published back in 2013.Therefore, the earlier suggestions serve as a milestone that will be implemented in this doctoral thesis to further enhance environmental stability of perovskite solar cells.

2.6.4. Moisture

In 2013, Niu et al. proposed the perovskite degradation mechanism when exposed under a presence of water, light and air [120]:

$$CH_3NH_3PbI_3 \overset{H_2O}{\Longleftrightarrow} CH_3NH_3I_{(aq)} + PbI_{2(s)}$$

$$CH_3NH_3I_{(aq)} \Leftrightarrow CH_3NH_{2(aq)} + HI_{(aq)}$$

$$4HI_{(aq)} + O_2 \overset{H_2O}{\Longleftrightarrow} 2I_{2(s)} + H_2O$$

$$2HI_{(aq)} + O_2 \overset{h\nu}{\Leftrightarrow} 2I_{2(s)} + H_2O$$

In summary, water acted as a catalytic component in this water assisted degradation mechanism to cause a series of irreversible reactions to lead triode perovskite.

Soon after, the water assisted degradation mechanism of perovskite material was illustrated further by J Frost et al. [125] . The main problem with their proposed reaction was that its by-products such as HI and PbI_2 were soluble in water and were considered as highly toxic substances.

Yang et al. attempted to determine upper relative humidity (RH) regimes where the moisture content began to decompose the $CH_3NH_3PbI_3$ films rapidly [126]. The RH-regulator chamber was made to monitor such changes. While RH within the regulating chamber is varied, the absorbance of each $CH_3NH_3PbI_3$ was measured within the RH-regulating chamber. As RH contents increased, a reduction absorption at short wavelength (less than 500 nm) as well as reduction in band edge of the perovskite sample was observed [126]. This degradation reaction was accelerated at fast pace when the RH within the chamber is above 98 %, in which its absorption became half within 4 hour after the initial moisture exposure [126]. On the other hand, the same degradation pathway took place but at much slower pace (above 10,000 hours) when the perovskite samples were to exposed with less than 20 % RH [126]. They also observed a hydrated by-products of $CH_3NH_3PbI_3$ when the sample was subjected to 80 %RH exposure for approximately 2.5 hours. They attribute this hydrated by-product to be $(CH_3NH3)_4PbI_6.2H_2O$ [126]. However, this presence of hydrate stage somewhat contradicts the proposed degradation reaction of Niu et al. [120].

Christian et al. also supported the presence of the intermediate hydrated by-product phase of $CH_3NH_3PbI_3$ via XRD patterns [127]. The XRD patterns of the decomposed hydrated films matched with XRD peaks of $(CH_3NH_3)_4PbI_6.2H_2O$ synthesis compound that Christian et al. synthesised themselves [127]. The presence of this intermediate hydrated compound caused a severe instability in the film

absorbance [127]. Christian et al. suggest that strengthening the organic cation and metal halide is the key to enhance the perovskite resistance to moisture [127].

Regardless, to date the actual water assisted degradation pathway is not fully established. The suggestion from Christian et al. in particular served as one of my motivation to further explore how moisture plays a role in the degradation mechanism of $CH_3NH_3PbI_3$ films.

2.6.5. Temperature

Temperature is one of the crucial factors that may influence operational lifetime of perovskite solar cells drastically as the perovskite layer requires annealing after each perovskite solution is deposited on a designated substrate. Many researchers suggest that perovskite annealing temperature should not exceed 100 °C [120,128,129]. In particular, Philippe et al. investigated the effect of annealing temperature to $CH_3NH_3PbI_3$ films in more detail [128]. They used photoelectron spectroscopy (PES) as the characterisation technique allowing them to identify relative chemical content without relying on crystallinity of the annealed films. Each perovskite film was annealed at different temperature (up to 200 °C) and time (up to 120 minutes) in a vacuum chamber to exclude air and water from the outside atmosphere. PES tracked I:Pb and N:Pb ratio of each annealed sample for the sake of comparison. For Pb: I case, 3:1 ratio represented highly temperature stable sample while 2:1 sample referred as degraded samples while N:Pb case, 1:1 and 1:0 ratio represent stable and non-stable temperature of annealed perovskite samples [128].

They showed that the $CH_3NH_3PbI_3$ film becomes thermally unstable when the sample was heated beyond 100 °C for 20 minutes as indicated with I:Pb and N:Pb[128]. Further annealing temperature accelerated formation of degraded species of the $CH_3NH_3PbI_3$. This is a strong indication for a presence of PbI_2. Philippe et al. then suggested the temperature induced degradation mechanism of $CH_3NH_3PbI_3$ [128]:

$$CH_3NH_3PbI_3 \xrightarrow{\Delta} PbI_2 + CH_3NH_2 \uparrow + HI \uparrow$$

While sufficient elevated temperature enables decomposition reaction of the perovskite films, further exploration for more complex situations with the presence of elevated temperature together with the presence of water and air are required. I decide to take this aspect of such study as an inspiration on my thesis which will be discussed later on.

Conings et al. applied the earlier study of pseudo perovskite solar cell devices (ITO/TiO_2/ $CH_3NH_3PbI_3$) [130]. Essentially, the hole transporting layer and gold electrode were omitted in order to focus their attention to understand how isolated $CH_3NH_3PbI_3$ degraded with the presence of other underneath layers [130]. The specimens were heated up to 85 °C for 24 hours under various environmental conditions.

When the pseudo $CH_3NH_3PbI_3$ solar cells were subjected under air and elevated temperature of 85 °C continuously for 24 hours, most severe changes occurred within the perovskite layer [130]. Such degree

of decomposition of $CH_3NH_3PbI_3$ at a relatively low temperature of 85 ^oC is particularly worrisome. Therefore, chapter seven will be dedicated to improve thermal stability of lead trihalide perovskite.

2.6.6. Oxygen and light

Over the last few years, environmental stability has become a key challenge for methylammonium lead triiodide ($CH_3NH_3PbI_3$ or $MAPbI_3$) perovskite solar cells. Many researchers such as Tomas et al. demonstrated promising operational stability of the encapsulated $CH_3NH_3PbI_3$ perovskite solar cell devices [124]. The devices were kept under an inert atmosphere using some form of physical barrier (i.e glass) to segregate the photoabsorber layer with outer environment specially to water and/or oxygen molecules. As mentioned earlier, UV light [124], annealing temperature [120,128,129] and moisture [120,125] can lower the operational lifetime of $CH_3NH_3PbI_3$ perovskite solar cells. Crucially, it is largely accepted as common knowledge that moisture is a dominant factor that affects the perovskite solar cell's stability [127,131].

However, $CH_3NH_3PbI_3$ perovskite solar cells show a sign of photo-instability even when moisture content around the devices is absent [132–134]. O'Mahony et al. reported that a $CH_3NH_3PbI_3$ photoactive layer could potentially degrade when it was exposed under a combination of oxygen and visible light [132].

In 2013, Snaith et al. showed that a substitution of aluminium dioxide (alumina or Al_2O_3) over TiO_2 block electron injection from $MAPbI_3$ to the mesoporous layer [116]. Not long after, O'Mahony et al. demonstrated a more rapid drop in absorbance spectra of mp-Al_2O_3/ $MAPbI_3$ films than that for mp-TiO_2/$MAPbI_3$ samples when both samples were subjected to a constant exposure of visible light and oxygen [132]. In addition, the microsecond TAS experiment probed at 1,600 nm showed that the hole recombination lifetime at the HTM of mp-Al_2O_3/ $MAPbI_3$/spiro-OMeTAD films decayed much faster than the hole recombination lifetime of the HTM in mp-Ti_2O_3/ $MAPbI_3$/spiro-OMeTAD films. Both findings were attributed to the higher conduction band (CB) of alumina compared with titiania. Thus, this trapped photo-generated electrons within the photoabsorber layer and increased the likelihood of it triggering the decomposition reaction of the $MAPbI_3$ under constant exposure of dry air and visible light [132].

Via the oxygen-light degradation apparatus that the author has established, Aristidou et al. proposed one of the decomposition pathways of a $CH_3NH_3PbI_3$ perovskite photoactive layer under a combination of oxygen molecules and visible light without the presence of moisture in the ambient condition [133]. Here, it was concluded that superoxide played a major part for decomposition of $CH_3NH_3PbI_3$ films when exposed to a combination of 'dry' air (less than 10 ppm of moisture content) and visible light [133]. The proposed degradation pathway was triggered initially via visible light absorption of the perovskite layer and generated highly energetic electrons in the process [133]. Then these highly energetic electrons interacted with oxygen in the outer atmosphere, and formed superoxide (O_2^-) [133]. This superoxide

caused a deprotonation reaction of the organic cation ions ($CH_3NH_3^+$ or $MeNH_3^+$) from $CH_3NH_3PbI_3$ along with other by-products such as PbI_2 and most importantly water molecule. These water molecules later triggered a water-assisted degradation mechanism and further accelerated the decomposition of $CH_3NH_3PbI_3$ into PbI_2 [133]. As a result, the $CH_3NH_3PbI_3$ samples turned from black to yellow visually. The oxygen induced degradation pathway of $CH_3NH_3PbI_3$ is located below [133].

$$\mathrm{MAPbI_3} \xrightarrow{\text{light, moisture-free}} \mathrm{MAPbI_3^*}$$

$$\mathrm{O_2} \xrightarrow{\text{light, moisture-free}} \mathrm{O_2^-}$$

$$\mathrm{MAPbI_3 + O_2^-} \xrightarrow{\text{Deprotonation}} \mathrm{MeNH_2 + PbI_2 + \frac{1}{2} I_2 + H_2O}$$

The above oxygen-light degradation mechanism was supported by the following two observations:

1. **Evolution of related by-products of the proposed oxygen-light degradation reaction in $MAPbI_3$ films**

In conjunction with the earlier finding with regard to the evolution of superoxide within toluene solution, other related by-products such as iodine and lead iodide (PbI_2) were detected via Ultraviolet Visible Light Spectroscopy (UV-vis) and XRD patterns [133].

The first by-product that was detected from degrading the mp-Al_2O_3/$MAPbI_3$ sample was found to be iodine [133,135]. Iodine is versatile at room temperature. This might cause the change in coverage of the $MAPbI_3$ sample as ageing time of the absorber increased. This was proven by degrading the $MAPbI_3$ film when immersed in dry toluene under a constant flow of dry air and illumination. It was shown in the paper that after approximately 72 hours of constant exposure to light and dry air, the colour of $MAPbI_3$ film changed from black to yellow while the toluene solution turned light pink [133]. This finding was attributed to the formation of iodine. UV-vis absorbance of the pink solution confirmed the evolution of iodine in the toluene solution [133]. Furthermore, an additional test by putting sodium thiosulfate into the solution also took place. Sodium thiosulfate reduced iodine to iodide and turned the toluene solution from light pink to colourless [133,135]. This finding further supports the presence of the product as iodine.

Secondly, a mixture of hexagonal and rhombohedral phase of PbI_2 was shown in XRD patterns of the degraded $MAPbI_3$ sample [133]. The peak positions of the degraded $MAPbI_3$ matched well with PbI_2 XRD peaks for methylammonium lead iodide according to literature data [136,137].Lastly, the detachment interaction of methylammonium cation ion ($CH_3NH_3^+$) from the $MAPbI_3$ perovskite was proposed. Both reference solution and the solution of the submerged $MAPbI_3$ were tested via nuclear magnetic

resonance (NMR). The model reaction was set up by dissolving methylammonium iodide (MAI) in dry ethanol and potassium superoxide (KO_2) [133]. Some deuterated acetone was added in order to calibrate the NMR spectrum properly. The tested solution converted from colourless to orange. NMR spectra showed protons shift up field upon addition of the KO_2 probe solution which verified a deprotonation interaction of the methylamine group ($MeNH_2$) from the perovskite sample [133]. Thus, all three by-products in the earlier proposed reaction were detected.

2. Different superoxide generation yield when the $MAPbI_3$ photoabsorber was deposited on different metal oxide mesoporous substrate

Aristidou et al. were able to relate photodegradation susceptibility of the mp-Al_2O_3/ $MAPbI_3$ and mp-TiO_2/$MAPbI_3$ films at constant exposure of dry air and visible light with their superoxide formation rates via the use of Photoluminescence (PL) [133]. The experiment involved submerging both mp-TiO_2/$MAPbI_3$ and mp-Al_2O_3/ $MAPbI_3$ films into dry toluene solution (which is insoluble with water) to ensure a constant moisture-free and illumination environment [133]. This is a test that was performed to confirm the presence and formation progression of superoxide in both toluene solutions [133]. The amount of superoxide in each toluene solution was related by tracking the PL emission data of the hydroethedine (HE) solution probe over the course of a one hour with 10 minute intervals [133]. The HE probe was highly emissive at a specific wavelength of 610 nm with an excitation wavelength of 520 nm upon exposure to the superoxide radial anion allowing us to compare the relative superoxide generation yield of both samples within one hour period after the decomposition of $MAPbI_3$ in both sample start to trigger [133]. After the experimental period, there was an obvious evolution in PL emission of toluene 610 nm for both mp-TiO_2/$MAPbI_3$ and mp-Al_2O_3/ $MAPbI_3$ films [133].

The PL trace at 610 nm for both mp-Al_2O_3/$MAPbI_3$ and mp-TiO_2/$MAPbI_3$ films clearly showed in the paper that the mp-Al_2O_3/ $MAPbI_3$ film produced more superoxide than the mp- TiO_2/$MAPbI_3$ film over the course of one hour after the decomposition of the photoabsorber began to take place [133]. This finding served as a strong indicator to support the earlier proposition of oxygen and light degradation pathway of $MAPbI_3$ under a moisture-free environment [133].

At present, it is important to note that the direct connections between a drop in absorbance, a drop in superoxide evolution and the charge recombination lifetime of $MAPbI_3$ based film have not yet been made despite the fact that all these experiments reflect a degree of environmental stability in $MAPbI_3$ photoabsorber layers. In addition, the direct comparison of oxygen-light stability between bulk heterojunction mp-Al_2O_3/MAPbI3/spiro-OMeTAD based solar cells and mp-TiO_2/$MAPbI_3$/spiro-

OMeTAD based solar cells have yet to be completed. Thus, this serves as an initial focus for this doctoral thesis which will be discussed in section 2.7.

2.7. Thesis layout

As discussed in section 1 in this thesis, it is emphasised that solar cells will ease a fair portion of our basic needs to providing power at present and for future generations. The core message of the background section 1 is that the converging goal of those attempting research in the area of photovoltaics is the progression in understanding the fundamental science that will lead to more efficient and sustainable yet cheaper solar cells. The aim of this doctoral thesis is to tackle the environmental stability aspect of the organometallic trihalide perovskite solar cell which is classified as one particular type of solar cell that has emerged recently alongside other types of PV devices.

Organic-inorganic lead halide perovskite solar cells (PSCs) in particular have generated considerable research attention as of late due to their fast pace growth in terms of power conversion efficiency surpassing 20 percent. However, their operational stability still cannot satisfy a strict condition for mass production. Recently, a main approach to separate key factors that decompose PSCs such as encapsulation is employed to enhance their operational lifetime. Unfortunately, some of those key factors such as moisture, oxygen and light cannot be completely isolated from PSCs. In fact, it was shown in section 2.6 how oxygen and light induces degradation pathways to $CH_3NH_3PbI_3$ perovskite via reactive oxygen species known as superoxide formation within the photoabsorber layer. This superoxide reacts with methylammonium cation, deprotonates the organic component from the perovskite and subsequently decomposes the photoabsorbers. Hence, an in-depth study was made as a key motivation of this thesis in order to improve environmental stability of organometallic lead trihalide perovskite photoabsorber under the presence of moisture, oxygen and light.

One of the key methods to gain a better understanding and determine relative environmental stability of each lead trihalide perovskite sample is to track any relative changes in their spectroscopies via UV-vis, PL and TAS over time individually and then compare each of them side by side. Using these spectroscopies to probe photophysics of lead trihalide perovskite occupies a significant portions in this thesis. The exact detail of operation modes and basic principles of each spectroscopy along with the characterisation techniques used throughout this thesis is written in chapter three.

Oxygen and light induced degradation has recently been shown to be an important pathway of $CH_3NH_3PbI_3$ perovskite films. This process involves the generation of highly energetic electrons while the films are exposed to both visible light and oxygen. These charges can then react with oxygen in the atmosphere generating a reactive oxygen species (superoxide, O^{2-}) which reacts with the methyl ammonium cation and causes $CH_3NH_3^+$ to deprotonate.

Chapter four of this thesis focuses on establishing the interrelations among three different spectroscopic trends when $CH_3NH_3PbI_3$ based films and solar cells were subjected to the constant oxygen-light ageing via three main spectroscopies techniques mentioned earlier. Results emerge from this work: 1.) the drop in absorbance of $CH_3NH_3PbI_3$ based films and hole recombination lifetime in $CH_3NH_3PbI_3$-spiro-OMeTAD based films over the function of oxygen-light ageing time were minimised when less superoxide was formed 2.) these three spectroscopic changes mentioned in 1.) were at minimum when the electron accepting substrate such as mp-TiO_2 was deposited along with $MAPbI_3$; this was assigned to the presence of another charge kinetic pathway that can successfully compete with electron transfer to oxygen to form superoxide and therefore reduce the oxygen-light degradation rate 3.) bulk heterojunction TCO/c-TiO_2/mp-TiO_2/$CH_3NH_3PbI_3$/spiro-OMeTAD/Au solar cells exhibited higher tolerance to the oxygen-light degradation than the TCO/c-TiO_2/mp-Al_2O_3/$CH_3NH_3PbI_3$/spiro-OMeTAD/Au solar cells.

The work in chapter five concerns the introduction of the electron extraction layer (ETL) design guidelines in order to enhance the operational lifetime of organic-inorganic lead trihalide films and fully functioning devices upon the findings from chapter four. The results in chapter five indicate the potential role of an electron accepting layer (inserted within the device stack) in slowing down light and oxygen induced degradation of $MAPbI_3$. Specifically, the second part of this chapter focuses on investigating the effects of electron extraction on materials and device stability; it more precisely elucidates the key design criteria required for electron layers in perovskite based layers to minimise light and oxygen induced degradation. The three main points addressed are:

1.) Improving air stability by maximising the electron acceptor-perovskite light absorber interface using mesoporous titiania (TiO_2) films.
2.) Slowing down light and oxygen induced degradation by using tin oxide (SnO_2) electron extraction layers; this being due to the low conduction band edge of SnO_2 as compared to TiO_2 and zinc oxide (ZnO).
3.) Applying (a) and (b) to caesium formamidinium lead trihalide perovskite photoabsorber which exhibit more tolerance to the oxygen-light degradation.

The three points mentioned above show that the stability of a range of different perovskite could be improved by tuning the properties of the electron acceptor layer. By incorporating the three above points to the $MAPbI_3$ solar cell, the optimised $MAPbI_3$ solar cell reveals itself to be over six times more stable while measured under identical conditions.

Chapter six of this thesis focuses on the use of alternative electron acceptor materials such as $PC_{60}BM$ and $PC_{70}BM$ to improve light and oxygen induced degradation of perovskite films. The further stability enhancement of caesium formamidinium lead perovskite ($CsFAPbI_3$) films and solar cells was made by doping the photoabsorber layer with $PC_{60}BM$ and $PC_{70}BM$. When an appropriate amount of $PC_{70}BM$ dopant was blended with the absorber prior to the annealing process, the light and oxygen induced degradation was stagnated. This deceleration occurred because the $PC_{70}BM$ acted as an additional source to assist mesoporous TiO_2 to further extract highly energetic electrons during the charge transfer processes at the absorber-metal oxide interfaces. It was also observed in TAS that the initial shape of hole recombination lifetime of all $PC_{70}BM$ doped $CsFAPbI_3$/spiro-OMeTAD films are nearly identical with an initial TAS signal of a reference $CsFAPbI_3$ film. Therefore, the $PC_{70}BM$ dopant does not hinder the charge separation and transfer process at $CsFAPbI_3$-TiO_2 interfaces but actually acts as an intermediate source to assist charges to be extracted successfully. At the end of this chapter, the optimised $PC_{70}BM$ doped $CsFAPbI_3$ device lasts over two times longer than the un-doped $CsFAPbI_3$ while having similar initial light harvesting performances.

Chapter seven focuses on the effect of post annealing temperature of $MAPbI_3$, $CsFAPbI_3$, caesium formamidinium lead perovskite $CsFAPb(IBr)_3$ films on photo-stability. The effect of the temperature was simulated by varying their post annealing temperature from room temperature to 100 ^oC in increments. This study revealed that $CsFAPb(IBr)_3$ films exhibited the highest degree of photo-stability and thermal-stability compared to $CsFAPbI_3$ films and $MAPbI_3$. In addition, when exposed to light and oxygen conditions $CsFAPb(IBr)_3$ films showed almost no changes in their absorbance, superoxide formation rate and microsecond TAS decay over 120 hours. At the end of this chapter, it was shown that $CsFAPb(IBr)_3$ devices exhibited higher initial power conversion efficiencies and better photo-stability compared to $CsFAPbI_3$ and $MAPbI_3$ devices. The operational lifetime of $CsFAPb(IBr)_3$ based solar cells was maximised with the appropriate amount of cation and anion substitutions.

Chapter eight draws main conclusions and finally chapter nine discusses future work at the end of the thesis.

3. Experimental

Throughout this thesis, photoabsorber of $MAPbI_3$ thin films were prepared via a consecutive three step spin coating process coupled with anti-solvent polishing (4,000 r.p.m, 500 r.p.m and 4,000 r.p.m for 10, 5 and 30 seconds, respectively) according to the literature reported by Nam Joong et al. [138]. The PbI_2 was weight with respect to MAI was approximately 3:1 mole ratio.

Whereas $Cs_{0.17}FA_{0.83}PbI_3$ thin films were constructed according to the study made by Jin-Wook Lee et al. with 7:3 volume ratio of DMF:DMSO [139]. While $Cs_{0.17}FA_{0.83}Pb(I_{0.8}Br_{0.2})_3$ photoabsorber films were modified from the study made by Michael et al. [140].

Similarly, $Cs_{0.17}FA_{0.83}Pb(I_{0.8}Br_{0.2})_3$ photoabsorber films were prepared according to Saliba et al.[140].

3.1. Materials and processing

3.1.1. Materials

All chemicals were used as received, including 99 % of lead(II) iodide (PbI_2, Sigma-Aldrich), caesium iodide (CsI, Sigma-Aldrich), lead(II) bromide (>98 % $PbBr_2$, Sigma-Aldrich), methylammonium iodide (MAI, Sigma-Aldrich), formamidinium ammonium iodide (FAI, Sigma-Aldrich), hydroiodic acid (HI, 57 % in water, Sigma-Aldrich), methylamine (CH_3NH_2, 52 %wt in absolute ethanol, Sigma-Aldrich), Titanium diisopropoxide bis(acetylacetonate) (IPA, 97 %wt in isopropanol, Sigma-Aldrich), *2,2',7,7'-Tetrakis[N,N-di(4-methoxyphenyl)amino]-9,9'-spirobifluorene* (spiro-OMeTAD, Lumtec, Dyesol), *Bis(triluoromethane)-sulfonimide lithium salt* (Li-TFSI, Sigma-Aldrich), *4-tert-butylpyridine* (TBP, Sigma-Aldrich), 97%wt Titanium (IV) chloride tetrahydro-furan complex ($TiCl_4$, Sigma-Aldrich), diethyl ether, acetone, ethanol (Sigma-Aldrich), isopropanol (Sigma-Aldrich), ethanolamine (Sigma-Aldrich), 2-methoxyethanol (Sigma-Aldrich), chlobenzene (Sigma-Aldrich), ɣ-butyrolactone (GBL, Sigma-Aldrich), TiO_2 paste (Dyesol DSL 30 NR-D 30nm), aluminium oxide paste (Al2O3 with < 50 nm particle size, 20 %wt in isopropanol, Sigma-Aldrich), Terpineol, hydroethedine (HE), toluene (Sigma-Aldrich), Dimethyl Sulfoxide (DMSO, Sigma-Aldrich), acetonitrile, silver conductive paste (Ag, Sigma-Aldrich), detergent, deionized Water.

3.1.2. Cleaning glass substrates

1.2 cm x 1.2 cm pieces of glass were cut and rinsed with acetone. .The washing series were performed as follows – five minutes in acetone, and five minutes in IPA, respectively.

3.1.3. Cleaning ITO pre-coated substrates

1.2 cm x 1.2 cm ITO pre-coated slides were labelled and rinsed in acetone for one minute to wash away organic photoresist that was coated on top of the ITO substrates. After that, the following washing sequences were took place:

1. Detergent diluted deionised water for five minutes
2. Deionised water for five minutes x three times.
3. Acetone for five minutes x two times.
4. Isopropanol for five minutes x two times.

3.1.4. Synthesis of methylammonium iodide (MAI)

The MAI powder synthesized methods followed the study made by Wang et al. [141]. MAI used for the first result chapter was self-synthesized by reacting approximately 24 ml of CH_3NH_2 and 10 ml of HI in a 500 ml round bottom flask in a cold bath (0 °C) for approximately two hours. The solution with precipitate was then filtered through a rotary evaporator and carefully removed liquid solvent components at 50 °C. The precipitated products were then re-dissolved in 80 ml absolute ethanol and then re-precipitated with an additional 300 ml diethyl ether. This procedure was repeated twice before the final MAI product was dried at 60 °C overnight under a vacuum before the collection. However, for later result chapters, results from EDX/SEM showed that there was still an excess iodide relative content with respect to lead atoms in $MAPbI_3$ films within the MAI synthesized sources. Therefore, MAI was later purchased from Sigma-Aldrich.

3.1.5. Synthesis of electron capping layer (c-TiO_2, c-SiO_2, c-ZiO)

The c-TiO_2 layer was made via spin coating its precursor solution which was made in the same fashion as O'Mahony et al. [132]. The solution comprised of 70 µl of titanium diisopropoxide bis(acetylacetonate), 55 µl of ethanolamine and 1 ml of 2-methoxythanol. Prior to usage, the solution was left to stir at room temperature for 30 minutes, then filtered with a 0.2 µm Polytetrafluoroethylene (PTFE) syringe filter. The solution was then pipetted and spun onto preferable substrates while each substrate was vacuumed on top of the spin coater. A Laurell Technologies WS-650MZ-23NPP Spin Coater was used to fabricate all c-TiO_2 films throughout this thesis (including mp-TiO_2, photoabsorber and spiro-OMeTAD layers). Each c-TiO_2 film was spun at 6,000 rpm, 2,000 $rpms^{-1}$ for 30 seconds. The films were then heated in a furnace at 450 °C for 30 minutes.

The precursor solution of c-ZnO was prepared according the literature reported by Hau et al. [142]. The precursor solution (mixture of 160 gl^{-1} of zinc acetate solution in 96 % 2-methoxy ethanol and 4 % ethanolamine) was left stirring at room temperature overnight before being filtered through a 0.2 µm

PTFE filter. The c-ZnO solution was then pipetted onto a designated substrate before spin coating in air at 4,000 rpm, 4,000 $rpms^{-1}$ for 30 seconds. The spun films were annealed under air at 150 °C.

c-SnO_2 precursor solution (0.1 M of $SnCl_2$ in 5ml of ethanol) was made according to the study made by Govindhasamy et al. [143]. The precursor solution was filtered with a 0.2 µm (PTFE) membranes and pipetted onto either a glass or ITO pre-coated substrate. The solution was spun at 2,000 rpm, 2000$rpms^{-1}$ for 30 seconds.

3.1.6. Titanium (IV) chloride tetrahydrofuran complex ($TiCl_4$) treatment

230 mg of $TiCl_4$ powder was weighed and mixed into 30 ml of deionised water. The mp-TiO_2 films were then submerged into this solution and heated at 70 °C for 30 minutes. The treated films were then rinsed with deionised water and dried with a nitrogen gun. Subsequently, they were annealed at 450 °C for another 30 minutes.

3.1.7. Synthesis of mesoporous (mp) TiO_2 and Al_2O_3

Mesoporous titiania (mp-TiO_2) was made via spin coating from its precursor solution. The precursor was made by mixing a Dyesol TiO_2 paste containing <30 nm TiO_2 particle sizes into ethanol 1:2.5 weight ratio (30 nm TiO_2 paste : solvent ratio). The 1.2 cm x 1.2 cm glass substrates (or ITO pre-coated substrates) were rinsed in detergent (only for the pre-coated substrates), IPA, acetone, and distilled water, respectively. The cleaned substrates were then dried via N_2 air gun and spun-coated with the diluted precursor solutions. Each mp-TiO_2 was spun at 6,000 rpm, 2,000 $rpms^{-1}$ for 30 seconds, then preheated at 90 °C for approximately one minute before heated at 450 °C for one hour in the furnace. The mp-TiO_2 films were then transferred out from the furnace and left to cool down at room temperature for 10 minutes.

Mesoporous alumina (mp-Al_2O_3) on the other hand, was made by mixing aluminium dioxide solution (< 50 nm particle sizes in IPA) with isopropanol (IPA) in 2:1 volume ratio. The precursor solution was then left to stir at room temperature for 30 minutes prior to the spin coating process. 45 µl of mp-Al_2O_3 precursor solution was then pipetted out on each designated clean substrate before spin-coating at 4,500 rpm, 2000 $rpms^{-1}$ for 45 seconds. After that, mp-Al_2O_3 films were annealed at the hotplate at 150 °C for 30 minutes.

3.1.8. Photoabsorber perovskite film fabrication

$CH_3NH_3PbI_3$ or $MAPbI_3$ precursor solution was prepared by weighing 0.25 g of MAI powder and 0.78 g of PbI_2 powder (1:1 mole ratio) dissolved in 1.4 ml of anhydrous GBL and 0.6 ml DMSO (7:3 volume ratio). The precursor solution was left to stir at 60 °C overnight. The solution was then filtered through

a 0.2 µm PTFE syringe filter and pipetted into three consecutive spinning steps under a nitrogen atmosphere in a glovebox. The spinning cycles were at 4,000 rpm, 4,000 $rpms^{-1}$ for 10 seconds followed by 500 rpm, 500 $rpms^{-1}$ for 5 seconds and 4,000 rpm, 4,000 $rpms^{-1}$ for 30 seconds. During the 2nd steps of the consecutive spinning coating, each substrate was chemically polished via a drop casting process with an anti-solvent of 500 µl anhydrous toluene. Each $MAPbI_3$ film was then annealed at 100 °C for 10 minutes. The colour of the films was changed from yellow to brown immediately upon annealing. It is noted that it is entirely possible that each sample came in contact with moisture in the open atmosphere. To minimise this effect, the samples are kept in a closed container filled with excess drying agents underneath after the spin coating processes.

Similarly, $Cs_{0.17}FA_{0.83}PbI_3$ precursor solution was made by mixing 44.2 mg of CsI powder ,461 mg of PbI_2 and 155 mg of FAI into a mixture solvent of 71 µl of DMF and 636 µl of DMSO (7:3 volume ratio). The precursor solution was left to stir at 60 °C for 30 minutes before filtering with a 0.2 µm PTFE syringe filter. After that, the filtered solution was pipetted onto each designate substrate and spun in the same spinning sequences for $MAPbI_3$ films. However, dry chlobenzene was used as an anti-solvent to polish the $Cs_{0.17}FA_{0.83}PbI_3$ films. Each polished film was spun and annealed at 70 °C for five minutes and 100 °C for five minutes under a nitrogen environment.

$Cs_{0.17}FA_{0.83}Pb(I_{0.8}Br_{0.2})_3$ photoabsorber films were prepared by mixing 137.62 mg $PbBr_2$ powder, 461 mg of PbI_2, 44.2 mg of CsI and 155 mg of FAI into a mixture solvent of 71 µl of DMF and 636 µl of DMSO (7:3 volume ratio). The spinning and annealing processes of $Cs_{0.17}FA0_{.83}Pb(I_{0.8}Br_{0.2})_3$ films were kept in a similar fashion to that of $Cs_{0.17}FA0_{.83}PbI_3$ films.

3.1.9. Spiro-OMeTAD films fabrication

The spiro-OMeTAD solution was prepared with respect to the study made by Bryant et al. [134]. The HTM solution was made by dissolving 72 mg of spiro-OMeTAD powder in anhydrous 1 ml of chlobenzene. For the study concerning lead trihalide perovskite based solar cell devices, additional of µl of Li-TFSI precursor solution (175 mg of Li-TFSI powder in 1 ml of acetonitrile) and 10 µl of 4-tert-butylpyridine (TBP)) was added in the spiro-OMeTAD solution. The solution was left to stir for 30 minutes and filtered with a 0.2 µm PTFE membrane filter. After that, the solution was pipetted onto the designated substrate and spun at 4,000 rpm, 4,000 $roms^{-1}$ for 40 seconds. The films were then exposed under dark with excess dry air overnight.

3.1.10. Au electrode vapour deposition

The Au counter electrode was deposited on top of the spiro-OMeTAD via chemical vapour deposition. Au plasma was formed within a thermal evaporation chamber under a pressure of 5 x 10^{-6} Torr. The

active area of each solar cell was 0.25 cm^2.The fabricated device pictured from bottom to top: ≈ 150 nm of ITO electrode, ≈ 500 nm of mp-TiO_2/perovskite photoabsorber, 100nm of the perovskite overlayers, ≈ 550 nm of spiro-OMeTAD (overlapping with the mp-TiO_2 thickness) and ≈70-100 nm of gold electrode.

3.2. Optical and Physical Characterisation

3.2.1. Ultraviolet-visible light Spectroscopy (UV-vis)

The UV-vis spectra has relevant parameters such as transmittance (T), absorbance (A(λ)) and extinction coefficient Ɛ(λ). UV-vis is one of the most commonly characterised methods used to study how photoabsorber specimens interact with light from UV to visible light ranges. In some cases, the observed wavelength can be extended into the infrared region.

The term transmittance is defined by the equation shown below.

$$T = \frac{I}{I_0} \tag{7}$$

Where T is the transmittance, I refers to transmitted light, and I_0 is the incident light before it is shined on the sample.

On the other hand, absorbance is denoted as a function of transmittance of some sort which is dependent on a specific wavelength. The function can be described according to Beer-Lambert's law.

$$A(\lambda) = -\log T(\lambda) = cl\varepsilon(\lambda) \tag{8}$$

Where c stands for the concentration of the tested molecule in solution, l is the optical path length and Ɛ is the extinction coefficient.

Throughout this thesis, Uv-vis absorbance measurements were carried out using a UV-vis spectrometer (PerkinElmer Lambda 750 UV-vis-n-IR absorption spectrometer fitted with an integrating sphere) in a wavelength range from 400 nm to 900 nm with a scan speed of 480 nm per minute with 1 nm data intervals and cycle time of 1 second. The slit width was set as 1.0 nm.

3.2.2. Photoluminescence Spectroscopy (PL)

3.2.2.1. Steady-state Photoluminescence Spectroscopy

Photoluminescence emission spectra were measured at room temperature using a Horiba Jobin Yvon Flurolog-3-spectrometer. The perovskite based films were scanned from 550nm to 800 nm with 520 nm excitation wavelength with 1 nm interval. The slit width was set as 10 nm.

3.2.2.2. Superoxide probe testing

Superoxide probe testing was achieved by dissolving 10 ml of stock solution (31.7 µM) of the hydroethedine (HE) probe in 10 ml dry toluene. Sonication was used to facilitate miscibility. Perovskite films were submerged into this solution. Photoluminescence spectra were recorded with excitation wavelength of 520 nm and slit width of 10 mm on a Horiba Jobin-Yvon Fluorolog-3 spectrofluorometer. Each perovskite film was illuminated by a visible light source through a 400 nm long pass optical filter throughout the experiment. The illumination was provided by a tungsten halogen lamp. The light intensity was approximately 20 $mWcm^{-2}$.

3.2.3. X-Ray Diffraction, Energy-dispersive X-ray spectroscopy (EDX)

X-ray diffraction patterns were obtained from a PANalytical X'Pert ProMRD diffractrometer using Ni filtered Cu K_α radiation at 40 keV and 40 mA. SEM-EDX measurements were performed on a JEOL 6400 scanning electron microscope operated at 20 kV. The samples were sputtered coated with approximately 10 nm chromium prior to the measurement in order to enhance their surface conductivity.

3.2.4. Scanning Electron Microscopy (SEM)

SEM images were acquired on a LEO 1525 Field Emission Scanning Microscope operated at 5kV using an In Lens detector. Similarly, the samples were coated with approximately 10 nm of chromium prior to the SEM measurement.

3.2.5. Atomic Force Microscopy (AFM)

AFM is a technique that reflects topography of the test subjected by tracking an atomic tip needle that is traced along each sample surface. Generally, the needle vibrates vertically as it is dragged along the tested surface. This is known as contact mode. For the soft surface where it is easily scratched, tapping mode is employed in order to minimise contacts between the tip and the sample surface.

AFM measurements were employed to obtain the surface profile of each perovskite based film. The measurements were obtained in air at room temperature with Agilent 5500 AFM/SPM (Agilent Technologies) operating under both contact tapping modes with an atomic sharp silicon tip.

3.2.6. Nuclear Magnetic Resonant (NMR) spectroscopy

The NMR spectra were recorded on a 400 MHz Bruker spectrometer using Topspin software. The test solution was set up by dissolving methylammonium iodide (MAI) in dry ethanol and potassium superoxide (KO_2) [133]. Some deuterated acetone was added in order to calibrate the NMR spectrum properly. [133].

3.2.7. Transient Absorption Spectroscopy (TAS)

Transient absorption spectroscopy is the time-dependent pump probe technique that is used to investigate the interaction of short-lived charge species of tested subjects. The samples are excited via a short specific laser pulse resulting in a generation of these excited electronic species. They are then guided via secondary probe light while having their absorbance measured before and after the excitation (ΔOD, optical density). ΔOD is described via Beer Lambert's law, as stated earlier with either positive or negative value. Positive values of ΔOD represent a photo-absorption of the specimen while negative ΔOD mean the sample is photo-bleached which typically results in a depopulation of the ground state in that specimen. It is entirely possible that wavelength regions of the positive and negative value of ΔOD overlap. Thus, careful control measurements are required to track individual contributions of each component within tested solar cells. Commonly, polarons and triplet excited states are tracked with micro-second TAS [113,144–146]. Figure 14 shows schematic of micro-second TAS along with two operational modes used to monitor changes in polaron concentration of each perovskite based sample.

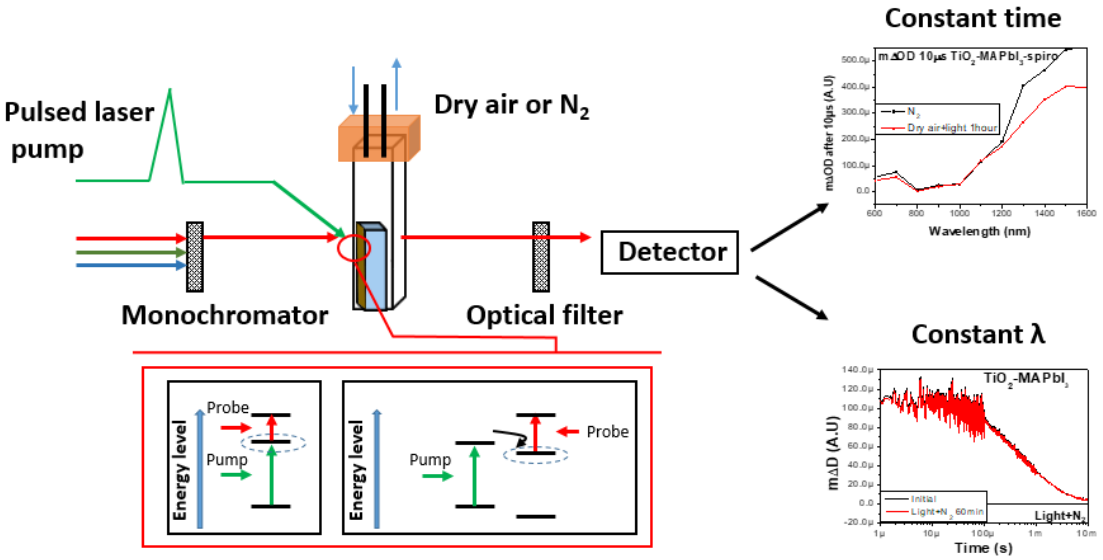


Figure 14: Schematic diagram shows how transient absorption spectroscopy operates. The specimen is illuminated with a specific laser pulse (pump) while being continuously measured at microsecond time scales. The pulse is guided by a secondary specific probe wavelength via a monochromator to a detector unit. The detected probe light is measured with respect to incident light before the pulse interacts with the sample. The measured results reflect how long these generated charges 'live' before a recombination reaction takes place. During each measurement, each perovskite sample was flushed with a constant flow of nitrogen (1 lpm) to ensure no photodegradation was taking place.

Generally, there are two operational modes in TAS [147]: 1.) oscilloscope with a continuous probe beam to measure the transient absorption spectrum (constant time) 2.) a specific probe beam with a time-resolved delay (constant λ).

For polarons species in organic component within perovskite based films, their decay mechanism happens right after these polarons generate via laser pulse. They travel through random walk from one molecule to another until they encounter an opposite charged polaron and subsequently recombine. The charge decay in microsecond TAS is described by the equation shown below:

$$\frac{\partial \mathrm{p}}{\partial \mathrm{t}} \propto \mathrm{np} = \mathrm{k}.\,\mathrm{np} = \mathrm{kp}^2 \tag{9}$$

k refers to a constant, n refers as anion concentration and p denotes polaron concentration. Under the assumption that opposite pairs recombination is the only loss process and polarons are generated by the dissociation of excited state via laser pulse, n_i=p_i (known as the charge neutrality rule).

TAS allows the rate of change of the polarons concentration to be monitored. By integrating the equation above, the relationship between ΔOD and time after the excitation can be found.

Throughout this thesis, TAS measurements were performed with a 510 nm dye and a GL-301 dye laser (Photon Technology International, TSI) through an oscilloscope (TG330 Function generator with 3 MHz-Generator, 120 MHz counter/sweep). The frequency of the laser pulse was 4 Hz. The pulse was generated with a light source (Bentham IL 1 illuminator) and a voltage of approximately 12.3 V (Bentham 605). The signal size was filtered with a long pass filter monochromator (Thorlabs) and an optical shielding filter. Each measurement was measured at 10 ms time scales for 64 averages for ten times with a pulse power of 25 μJcm^{-2}. The aged sample was illuminated against the tungsten halogen lamp (Thorlabs) with an approximate power of 20 mWcm^{-2} with a 400nm long pass optical filter throughout the experiments. Each sample was also purged with dry compressed air (< 10 ppm moisture) during the ageing conditions.

3.2.8. JV measurements

JV curves were obtained by placing the samples in the measuring chamber to isolate each sample from the atmosphere. The unit was then measured using a 2400 series source meter (Keithley Instruments) under AM. 1.5G sunlight at approximately 100 mWcm^{-2} irradiance. In this experiment, a backward scan starting from 1.2 V to -0.2 V was performed on all perovskite solar cells. The scan direction and scan range during each JV measurement needs to be kept consistent due to the presence of the hysteresis caused by positive mobile ions.

4. Atmospheric Stability Assessment of Methylammonium Lead Triiodide Perovskite Photoabsorber

4.1. Abstract

In chapter two, it was discussed that combination of oxygen and light was required to decompose methylammonium lead triiodide ($CH_3NH_3PbI_3$, or $MAPbI_3$) perovskite film via superoxide formation and deprotonation reaction of organic cation. In this chapter, studies are performed to improve the fundamental understanding of this degradation pathway through the interrelationships among three spectroscopy techniques namely: Ultraviolet-visible light (UV-vis) spectroscopy, Photoluminescence (PL) emission and microsecond transient absorption (TAS) spectroscopy. These spectroscopy measurements were performed while each perovskite photoabsorber was deposited on an either an electron insulating or electron transporting mesoporous metal oxide layer (mp-Al_2O_3 and mp-TiO_2, respectively) as the series of environmental conditions were varied. It was found that

1.) Increasing superoxide formation in the $CH_3NH_3PbI_3$ based films caused both of their absorbance and the hole recombination lifetime in $CH_3NH_3PbI_3$ –spiro-OMeTAD to drop. In particular, a drop in TAS signal of the non-stable lead trihalide perovskite based films began to surface upon contact of the films with oxygen and light much earlier than a drop in the absorbance.

2.) mp-TiO_2 supressed superoxide formation within $CH_3NH_3PbI_3$ film. Subsequently, the photoabsorber exhibited less drop in its absorbance spectra when the samples were subjected to a constant oxygen-light ageing. In addition, a longer hole recombination lifetime was found in the spiro-OMeTAD of the mp-TiO_2/ $CH_3NH_3PbI_3$/spiro-OMeTAD sample than that with mp-Al_2O_3/ $CH_3NH_3PbI_3$/spiro-OMeTAD.

3.) The presence of moisture surrounding the $CH_3NH_3PbI_3$ samples could be treated as a catalyst which does not severely alter either light harvesting performance or charge recombination lifetime as long as it is kept between 10 ppm and 60 %RH.

Towards the end of this chapter, JV measurements were performed for the bulk heterojunction $CH_3NH_3PbI_3$-spiro-OMeTAD solar cells. The drop in the PCE of the device with an insulating mesoporous alumina reinforced the (ii) findings.

4.2. Introduction

With the absence of moisture , it was stated in chapter two that combination of oxygen and light are two primary factors that decompose $CH_3NH_3PbI_3$ into PbI_2 along with other volatile by-products such as iodine via superoxide formation and organic cation deprotonation [133]. In addition, an alternative

method was undertaken in order to showcase that it is possible for $CH_3NH_3PbI_3$ based solar cell devices to degrade under the dark as long as electrons were forcefully injected into the device together with oxygen [134]. Both works pinpoints the same conclusion that superoxide is the main cause that needs to be minimised in order to enhance air and light stability of the $CH_3NH_3PbI_3$ photoabsorbers. However, to date, the interrelationship of decomposition rate of the photoabsorber, its superoxide formation rate and its changes in charge recombination lifetime still remain unexplored despite the fact they interplay closely with one another. Understanding these interrelations would lead us to be able to extend the operational lifetime without compromising the effectiveness of the charge carrier lifetime of $CH_3NH_3PbI_3$ films.

Based on this idea, three spectroscopy techniques namely UV-vis, PL and TAS were employed to monitor the relative changes in the $CH_3NH_3PbI_3$ films when photoelectron extraction capability within each photoabsorber differed. More specifically, the electron extraction capability at the photoabsorber/ETL interface was altered with different mesoporous metal oxides such as mesoporous titiania or alumina. Mesoporous alumina acted as an electron insulator layer that hindered photogenerated electrons from being transported out of the perovskite layer whereas mesoporous titiania allowed these photogenerated electrons to be extracted out of the system and thus lower the probability of them reacting with oxygen and light to generate superoxide within the photoabsorber. It was found that mp-TiO_2/ $CH_3NH_3PbI_3$ samples exhibited a more constant trend in their absorbance, superoxide formation and charge carrier lifetime compared with those found in mp-Al_2O_3/ $CH_3NH_3PbI_3$ samples over time when exposed to oxygen and light. These findings led to the conclusion that mesoporous titiania helped to minimise the superoxide generation rate without shortening the recombination pathways of photogenerated electrons. As a result, mp-TiO_2/ $CH_3NH_3PbI_3$ films were more air and light stable than mp-Al_2O_3/ $CH_3NH_3PbI_3$ samples. The PCE measurements of mp-Al_2O_3 and mp-TiO_2 based $CH_3NH_3PbI_3$ perovskite solar cells also converged towards the same conclusion. Towards the end of chapter four, three spectroscopy measurements were repeated with the photoabsorber samples exposed under air, light and surrounding moisture (~60 %RH). These measurements were then compared to the previous set of experiments. The absorbance spectra comparisons between these two sets of experiments showed that the drop in absorbance of both set of sample under the subjection of oxygen and light was similar while more noticeable drops, yet perhaps insignificant in TAS signals, were measured for the lead trihalide perovskite based samples exposed under air, light and surrounding moisture. It was then concluded that between the ranges of ~10 ppm-60 %RH, relative moisture content could affect hole recombination lifetime of the metal oxide/$CH_3NH_3PbI_3$/spiro-OMeTAD films to some extent but do not affect them to the point that their decolouration and their absorbance would differ significantly.

4.3. Experimental

Three spectroscopy techniques namely UV-vis, PL and TAS were employed to mesoporous metal oxide/ $CH_3NH_3PbI_3$ samples under different environmental exposure conditions to confirm that the combination of oxygen and light affected the operational lifetime of the photoabsorbers. In particular, spiro-OMeTAD was used as HTM on top of each photoabsorber in the TAS experiments in order for photogenerated holes to be generated, transported and monitored. The experiments were then repeated under constant exposure to moisture, light and oxygen. The surrounding relative moisture (RH) for the testing site was 60 %RH. The illumination source used for the oxygen-light degradation reaction to all perovskite films was roughly 20 $mWcm^{-2}$. However, the AM 1.5 G light sources were used to measure PV performances for each $CH_3NH_3PbI_3$ based solar cell. The full details each spectroscopy and characterization techniques was stated in chapter three.

4.4. Results and discussions

The oxygen-light degradation to $MAPbI_3$ films

Eight identical glass-$MAPbI_3$ samples were degraded under different surrounding conditions. This degradation experiment were performed while presence of oxygen, illumination exposure and presence of moisture were differed among each sample for 48 hours[134]. Each absorbance against wavelength curve of all eight sample were plotted in Figure 15.

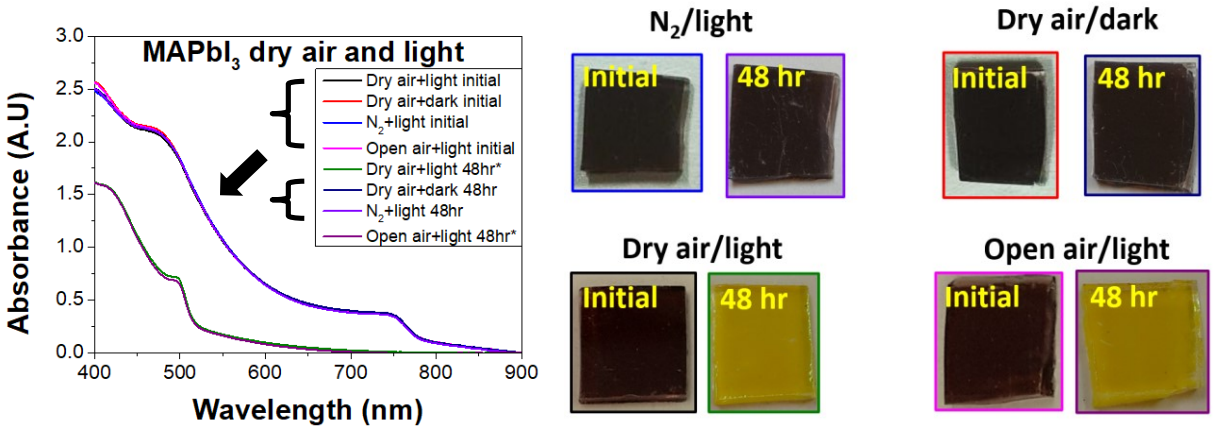


Figure 15: Absorbance of eight $MAPbI_3$ films deposited on glass before and after (48 hours) dry air-light ageing in various testing conditions (see labels). The photographs of the films before (left) and after (right) the ageing were also shown next to each absorbance graph. This figure was adapted from the paper of Aristidou et al. [134]. * represents degraded $MaPbI_3$ films when they were subjected to dry air and AM 1.5 G illumination for 48 hours.

The complete photodegradation reaction of $MAPbI_3$ film was observed only when combination of oxygen and visible light was present (green and dark purple lines marked with * in Figure 15). However, considerably less time was required for PSCs to malfunction and cease to work as a

photodiode. Hence, TAS was used as a monitoring tool to track the charge interactions at hole-electron extraction interfaces. The intensity of the experimental light source was also dropped down to ~20 mW/cm^2 from here onwards.

Superoxide measurements

Figure 16 demonstrated that superoxide formation on the $MAPbI_3$ layer could be suppressed when mp-TiO_2 was deposited underneath the photo-absorption layer [133]. Based on this finding, interrelation of this trend with the change in TAS decays and UV-vis absorbance were investigated.

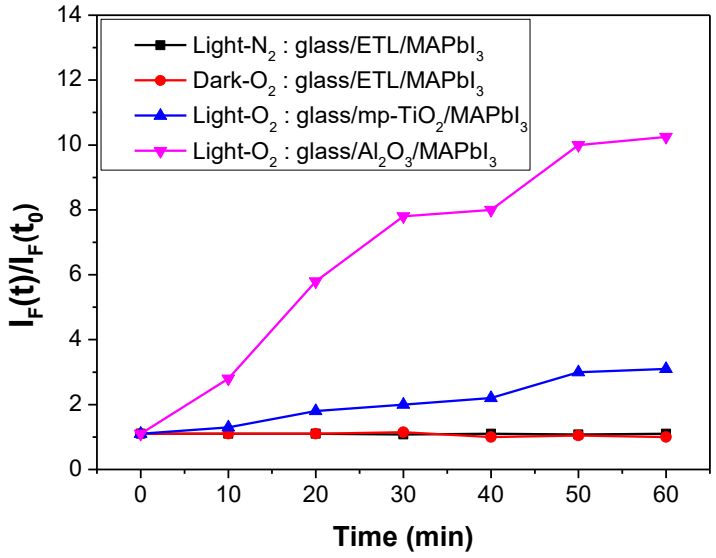


Figure 16: Normalised fluorescence intensity at 610 nm (excitation wavelength of 520 nm) of the superoxide HE probe (31.7 µM) mixed into dry toluene solution. $I_F(t)$ is the maximum PL intensity at time t while $I_F(t_0)$ is the background fluorescence intensity at probe at t = 0. The ratio between the two is the superoxide generation yield as the absorber film degraded under constant exposure of light and oxygen. Both PL emission trace were collected individually (see labels). Each film was submerged under (~20 mWcm^{-2}) and dry air (less than 10 ppm H_2O). Then the PL emission of toluene probe solution was tested over the course of 1 hour with 10 minute interval between each measurement. This figure was adapted from the paper of Aristidou et al. [133].

Control experiment

The initial UV-vis spectra of six c-TiO_2/mesoporous metal oxide/ $CH_3NH_3PbI_3$ (black line in Figure 17) were measured before being exposed to either constant illumination of a tungsten light source (~20 mWcm^{-2}) or dry air (less than 10 ppm of H_2O) for 24 hours. Then, their degraded UV-vis spectra were acquired (red line in Figure 17) and compared with each of their initial UV-vis spectrum under the same identical testing conditions. The UV-vis results confirm that without combination of both light and oxygen, $CH_3NH_3PbI_3$ films remained stable.

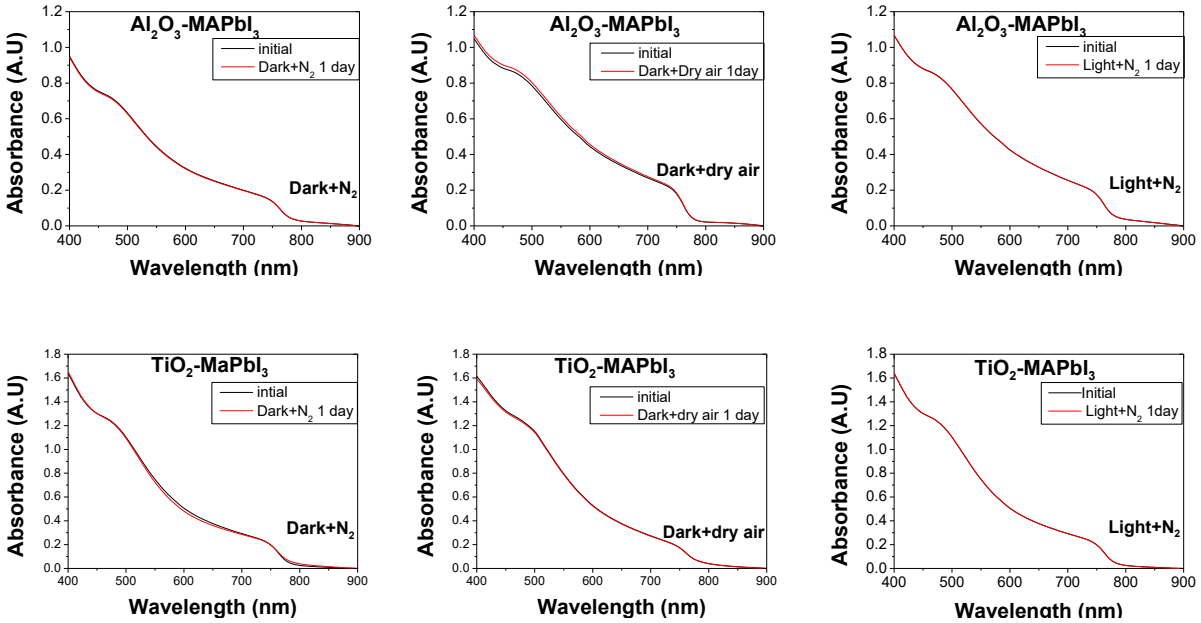


Figure 17: Absorbance of $MAPbI_3$ deposited on top of two different metal oxide layers. Initial (black line) and 24 hours-aged (red line) absorbance spectra of each perovskite sample was measured. Without the combination of both light (~20 $mWcm^{-2}$ tungsten halogen lamp) and oxygen, there were no apparent changes observed in $MAPbI_3$ absorbance curves for any given experimental conditions.

The similar set of experiments was performed while having their initial and one hour-light or dry air aged TAS signal measured (Figure 18~~)~~. Each sample was photoexcited via 510 nm laser pulse with an energy density of approximately 25 μJcm^{-2} under an excess dry air flow (0.1 litre per minute). It was found that TAS decays of all $MAPbI_3$ samples were not altered without the combination of dry air and light.

It was noted that each set of samples used for UV-vis and TAS were not identical. An additional layer of spiro-OMeTAD is required on top of the absorber in order to ensure charge transfer at the interfaces of the electron-hole extraction layer.

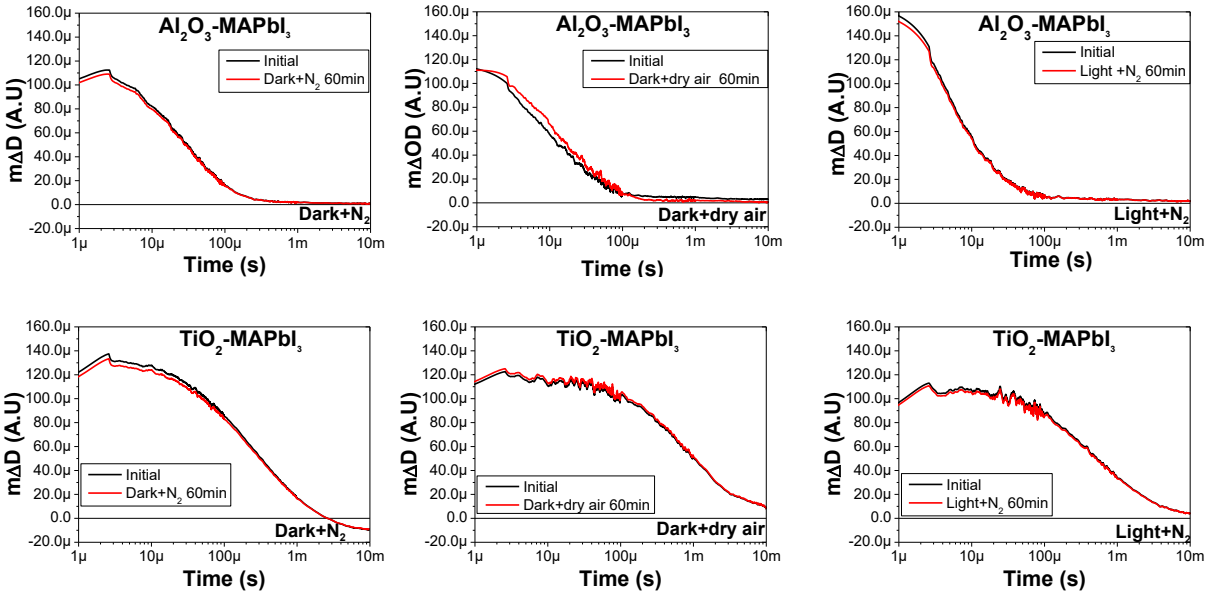


Figure 18: Transient absorption kinetics as a function of ageing time probed at 1,600 nm for spiro-OMeTAD located of top $MAPbI_3$- metal oxide (see legend). All six film were aged either under 20 mW/cm^2 or under presence of constant flow of dry air (0.1 lpm). Laser photo excitation was done at 510 nm with an energy density of approximately 25 $\mu J/cm^2$. Without the combination of dry air and light, there are no apparent changes in the TAS absorption kinetic.

The unchanged TAS and UV-vis signals after light or dry air ageing ensured us that the presence of both light and oxygen were required in order to degrade lead trihalide perovskite photoabsorber films.

Combination of light-oxygen $MAPbI_3$ degradation with/without moisture

Moisture was included as another value along with the light-oxygen degradation process. Each $MAPbI_3$ samples were exposed to two opposite extreme of relative moisture content alongside light and oxygen exposure. The condition that lacks relative moisture is called the 'dry air' condition (<10 ppm H_2O) while the other condition where moisture is readily available is called 'open air'. Approximately, the relative humidity during UV-vis and TAS measurement were kept at 60 % relative humidity (RH).

Figure 19 showed that when combination of (both dry and open) air and light was exposed to the $CH_3NH_3PbI_3$ films, a signal drop in UV-vis was found (see label). For the sake of comparisons, a vertical 480 nm trace of UV-vis was plotted in Figure 20.

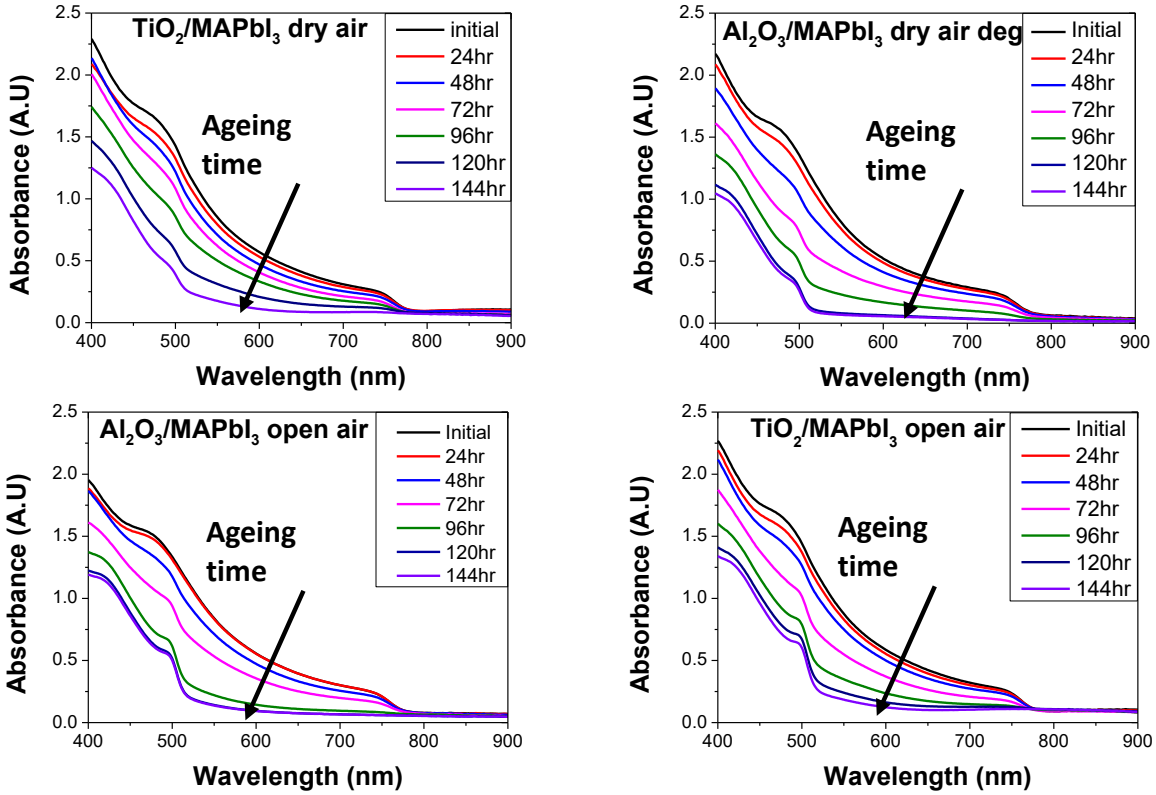


Figure 19: UV-vis absorbance spectra of $MAPbI_3$ deposited on top of either mesoporous Al_2O_3 or TiO_2 (see legend) under different relative humidity conditions. Dry air contains 10 ppm or less H_2O content while open air contains approximately 60 percent relative humidity content. The samples were constantly bathed under 20 $mWcm^{-2}$ tungsten halogen lamp and (dry/open) air (see label).

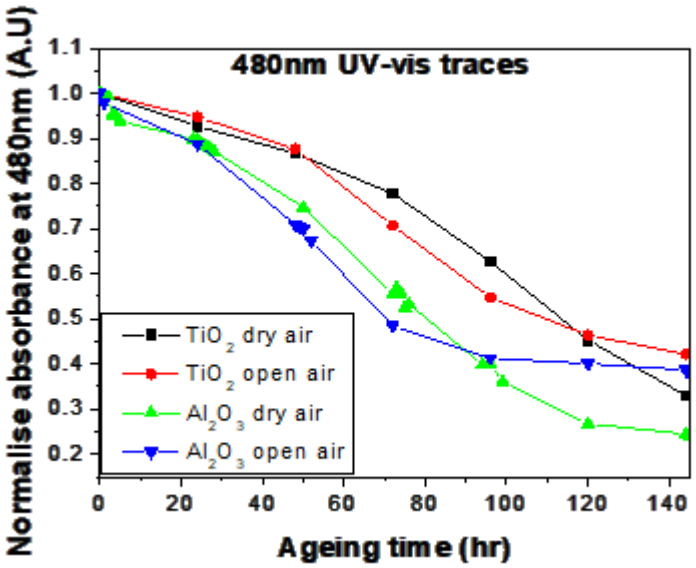


Figure 20: 480 nm UV-vis trace of metal oxide/$MAPbI_3$ samples deposited on top of different metal oxide mesoporous substrate (see legends). This 480 nm UV-vis trace was derived from the Figure 19.

The 480 nm UV-vis trace showed that the mp-TiO_2/ $MAPbI_3$ samples were visually more stable when being exposed under air and light compared with those of mp-Al_2O_3/ $MAPbI_3$ films regardless of the amount of relative moisture surrounding all $MAPbI_3$ samples. Similarly, a drop in TAS signals was monitored while each metal oxide/$MAPbI_3$ sample was subjected to the same environmental conditions for the UV-vis experiment shown previously. Here, both TAS decays (fix probe wavelength while vary the decay time as shown in Figure 21a and 21b) and TAS spectra (vary probe wavelength while fix decay time as shown in Figure 21c and 21d) were plotted. The TAS spectra indicated hole transfers within spiro-OMeTAD via the laser pump excitation. The TAS decays became more noticeable when mp-TiO_2/$MAPbI_3$ were subjected to combination of light, oxygen with or without presence of moisture. This implied the difference in relative moisture content could affect the hole recombination lifetime in $MAPbI_3$/spiro-OMeTAD. However, within the range of 10 ppm to 60 %RH, the UV-vis absorbance spectra of the photoabsorber remain relatively unchanged.

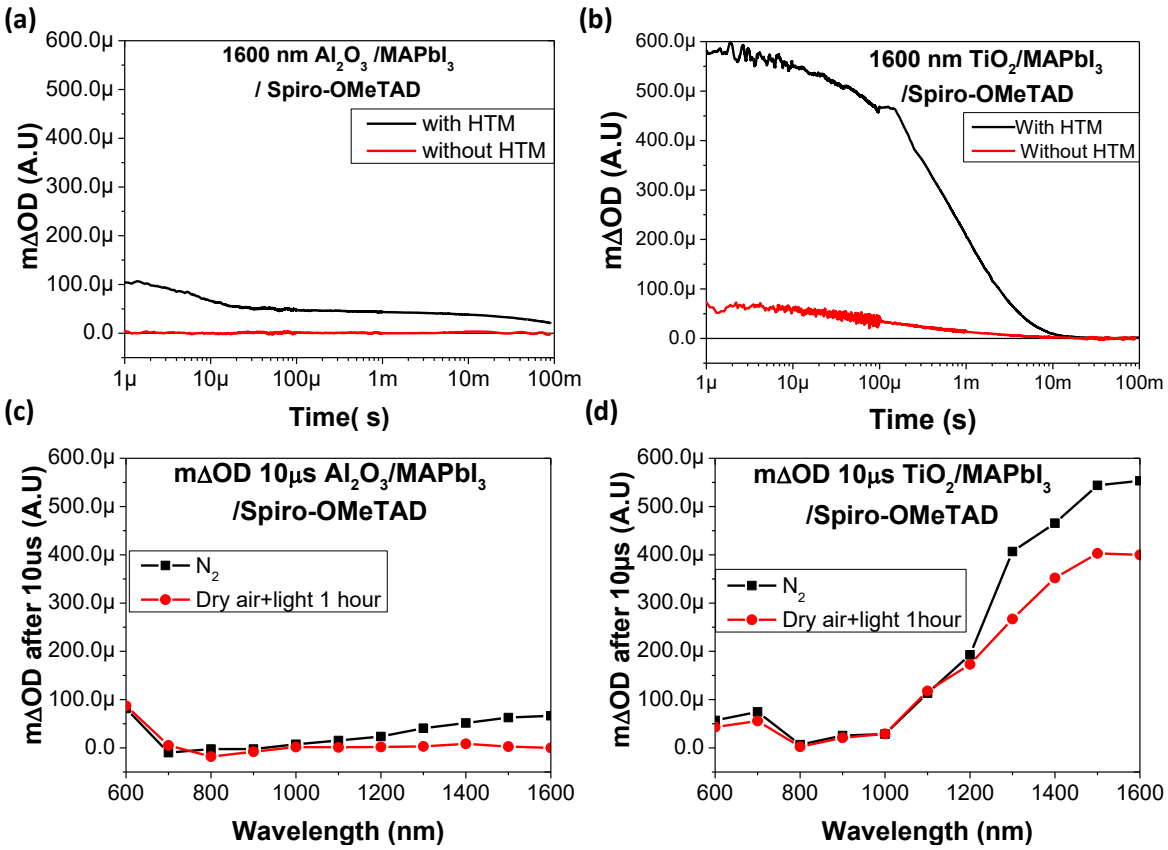


Figure 21: Transient absorption signal at 1600 nm of (a) Al_2O_3/$MAPbI_3$/spiro-OMeTAD and (b) TiO_2/$MAPbI_3$/spiro-OMeTAD films with (black) and without (red) HTM (spiro-OMeTAD). Transient absorption spectra of (c) Al_2O_3/$MAPbI_3$/spiro-OMeTAD and (d) TiO_2/$MAPbI_3$/spiro-OMeTAD films under N_2 (black) and dry air and light (red). Laser excitation energy density = 25 μJcm^{-2} at 510 nm.

It was established in Figure 22 that oxygen-light stability of $MAPbI_3$ can be accessed by comparing TAS decay (probed at 1600 nm) plotted against ageing time. TAS decay experiment were carried out on identical set of $MAPbI_3$ UV-vis samples (shown in Figure 22). Then, all normalised TAS signal at 10 µs of these $MaPbI_3$ samples was plotted in Figure 23 to compare its oxygen-light stability among each other. Figure 23 indicated that the longer operational lifetime of the $MAPbI_3$ photoabsorber deposited on the electron extraction layer (mp-TiO_2) than that for the electron insulator layer (mp-Al_2O_3). The conclusion further enhanced the theory that the presence of suitable metal oxide could slow down the oxygen-light degradation rate of $MAPbI_3$ which will be addressed in chapter five.

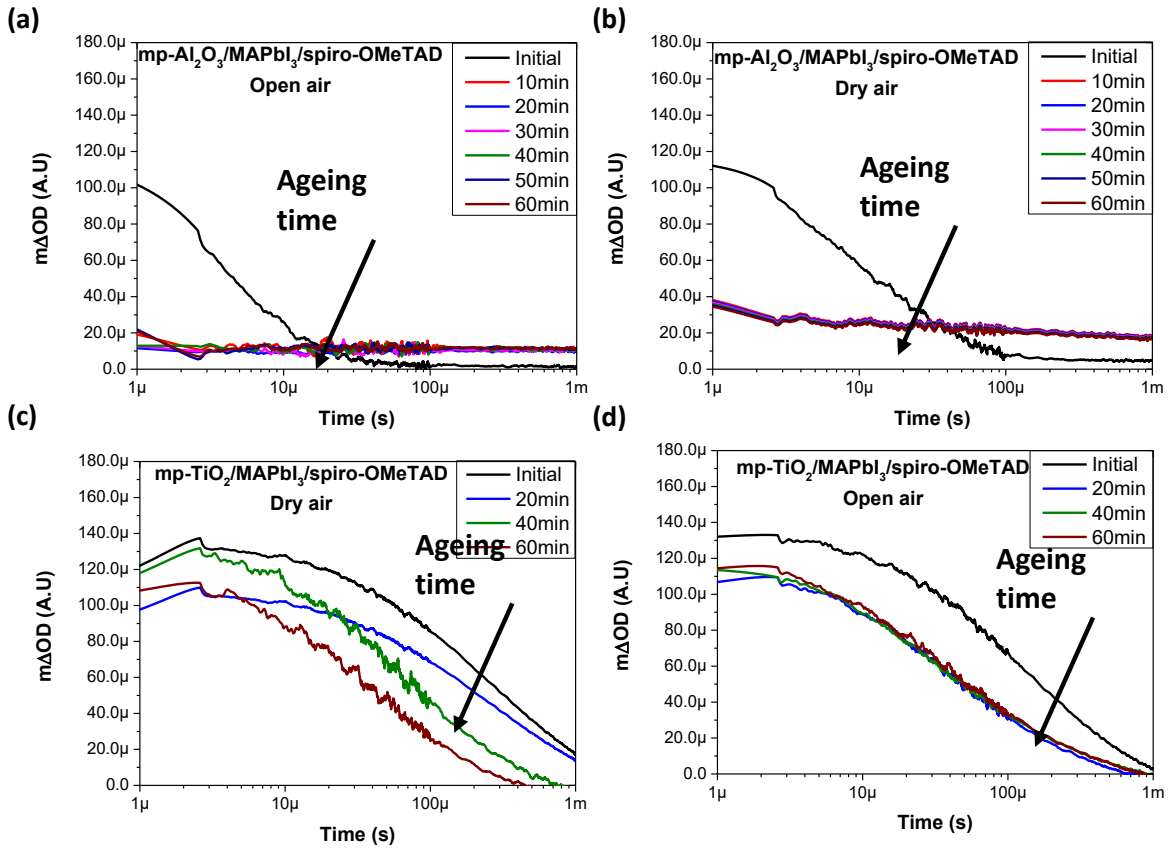


Figure 22: Transient absorption kinetics as a function of ageing time probed at 1,600 nm of Al_2O_3/$MAPbI_3$/spiro-OMeTAD degraded under (a) open air or (b) dry air and TiO_2/$MAPbI_3$/spiro-OMeTAD films degraded under (c) open air or (d) dry air. All films are aged under constant 20 mW/cm^2 illumination of halogen lamp and excess flow of dry air or open air. Laser photo excitation was done at 510 nm with an energy density of approximately 25 µJ/cm^2.

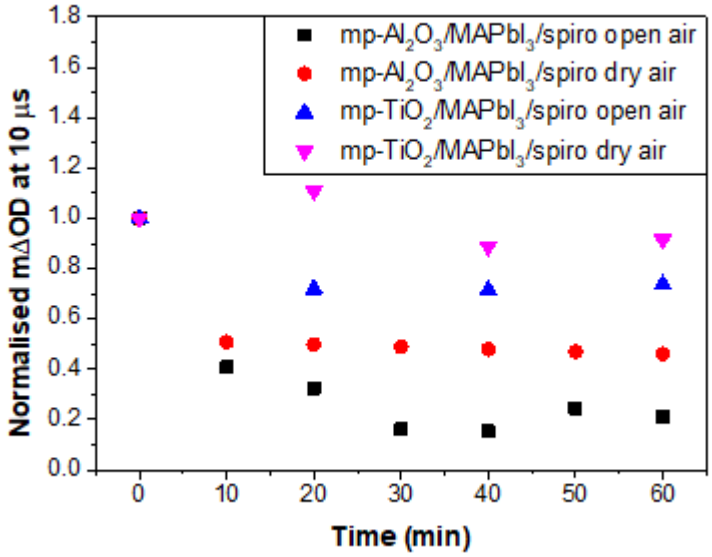


Figure 23: Normalised TAS decays at 10 µs versus oxygen-light ageing time taken from Figure 22 were shown (see labels). All films are aged under constant 20 mW/cm^2 illumination of halogen lamp and excess flow of dry air or open air. Laser photo excitation was done at 510 nm with an energy density of approximately 25 µJ/cm^2.

Section 4.4 also focuses on identifying the oxygen-light degradation by-products after $MAPbI_3$ completely cease to function as a photoabsorber. Thus, various characterisation techniques such as EDX, XRD and SEM are employed.

Energy-dispersive X-ray spectroscopy (EDX)

EDX was performed as another characterisation technique used to ensure that both mp-Al_2O_3/$MAPbI_3$ and mp-TiO_2/$MAPbI_3$ samples experienced the same photodegradation pathways. EDX/SEM spectra (Figure 24 and Table 3) showed the change of atomic I:Pb ratio before and after the degradation of both metal oxide samples. The I:Pb atomic ratio in all samples changed from ~3.5 to ~2.2 on averages. This strongly indicated the presence of PbI_2 which was one of the photo-degraded by-products of $MAPbI_3$.

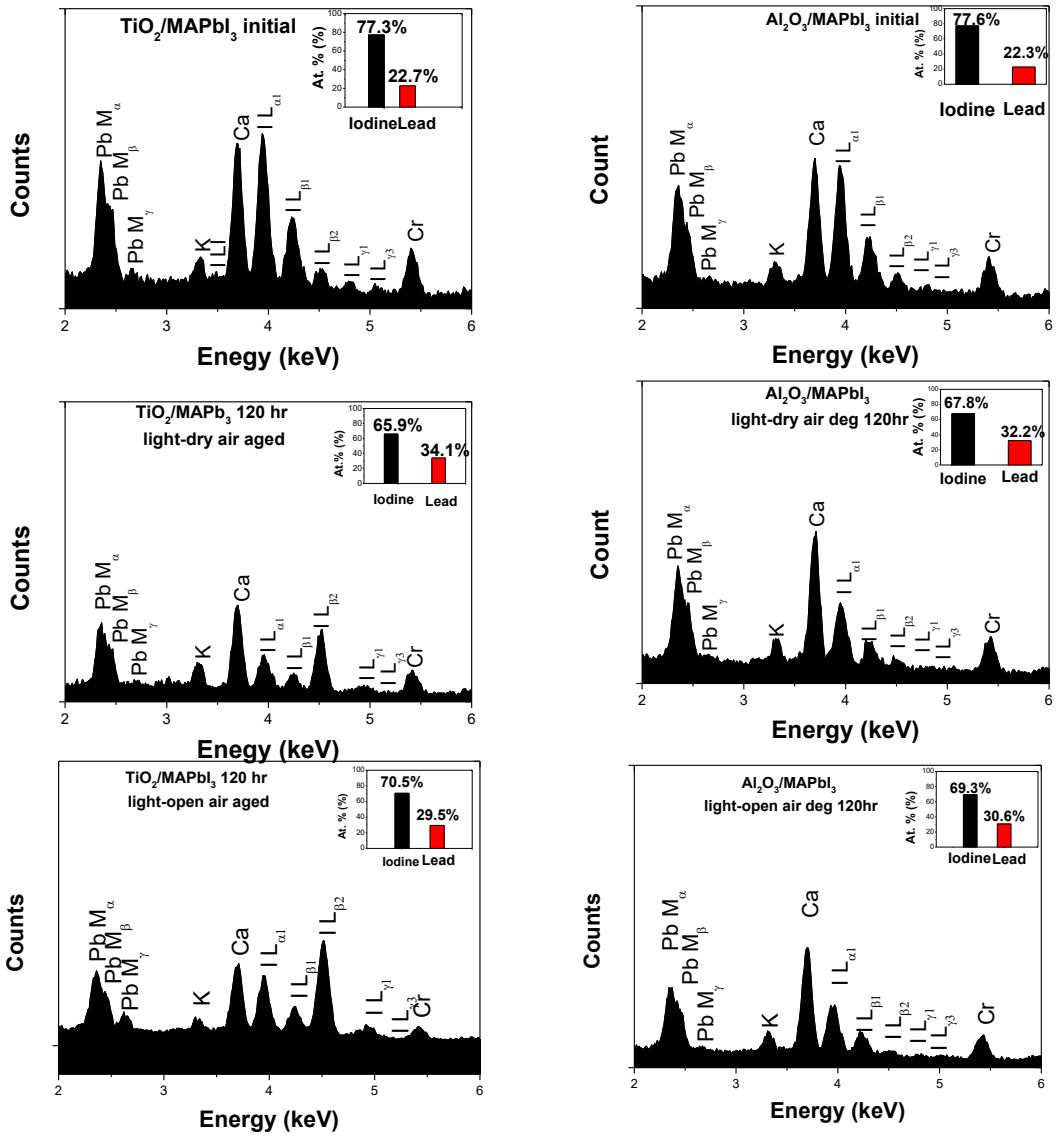


Figure 24: EDX/SEM spectra for $MAPbI_3$ deposited on two metal oxides. The inset shows the I:Pb atomic ratio of $MAPbI_3$ measured under air and light (see legend).

Table 3: I:Pb atomic ratio of initial, 120 hours light-air aged (under dry air or open air) derived from Figure 24.

Samples	I/Pb atomic ratio	
	Dry air-light	**Open air-light**
$MAPbI_3$initial	3.41 ± 0.08	3.48 ± 0.08
Degraded mp-Al_2O_3/$MAPbI_3$	2.11 ± 0.07	2.26 ± 0.08
Degraded mp-TiO_2/$MAPbI_3$	1.93 ± 0.08	2.39 ± 0.04

EDX spectra indicated the change in atomic level as $MAPbI_3$ degrades under air and light and both Al_2O_3-$MAPbI_3$ and TiO_2-$MAPbI_3$ photo-degraded films (for both dry air and open air cases) implied that moisture content surrounding the photoabsorber did not alter the degradation pathway for $MAPbI_3$.

X-ray diffraction spectroscopy

X-ray patterns which were plotted in Figure 25 showed no apparent changes in the light and oxygen aged sample of $MAPbI_3$ regardless of relative moisture content presented. A mixture of rhombohedral and hexagonal PbI_2 was one of the final products of the $MAPbI_3$ degradation pathway. The XRD patterns further reinforced that the moisture content did not alter the photodegradation pathway of $MAPbI_3$. Furthermore, XRD patterns of both Al_2O_3 based films were more scattered than mp-TiO_2/$MAPbI_3$ samples when aged under dry air or open air. This was attributed to less remaining PbI_2 material on top of the mp-Al_2O_3 layer compared to that for the TiO_2 layer. To verify this hypothesis, top view SEM images of these 4 samples were performed.

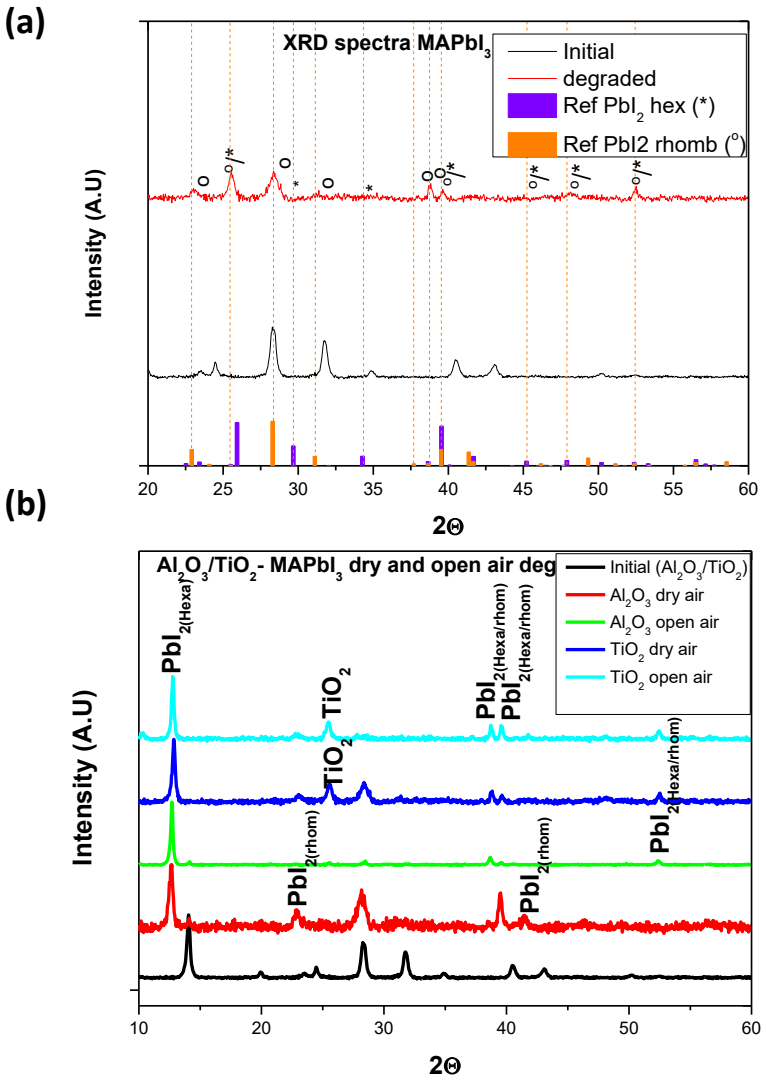


Figure 25: XRD patterns of (a) initial and 120 hours oxygen-light aged glass/$MAPbI_3$ and (b) initial and 120 hours oxygen-air aged mp-Al_2O_3/$MAPbI_3$ and mp-TiO_2/$MAPbI_3$. Both samples were either exposed under dry air (10 ppm H_2O) or open air (60 %RH) for 120 hr (see legends).

Scanning Electron Microscopy (SEM)

Top view SEM images of $MAPbI_3$ were also shown in Figure 26. There was less coverage of metal oxide/$MAPbI_3$ photo-degraded samples exposed under dry air than under open air for 120 hours. Perhaps, some of the by-products such as $I_{2(g)}$ escaped from the mesoporous surfaces.

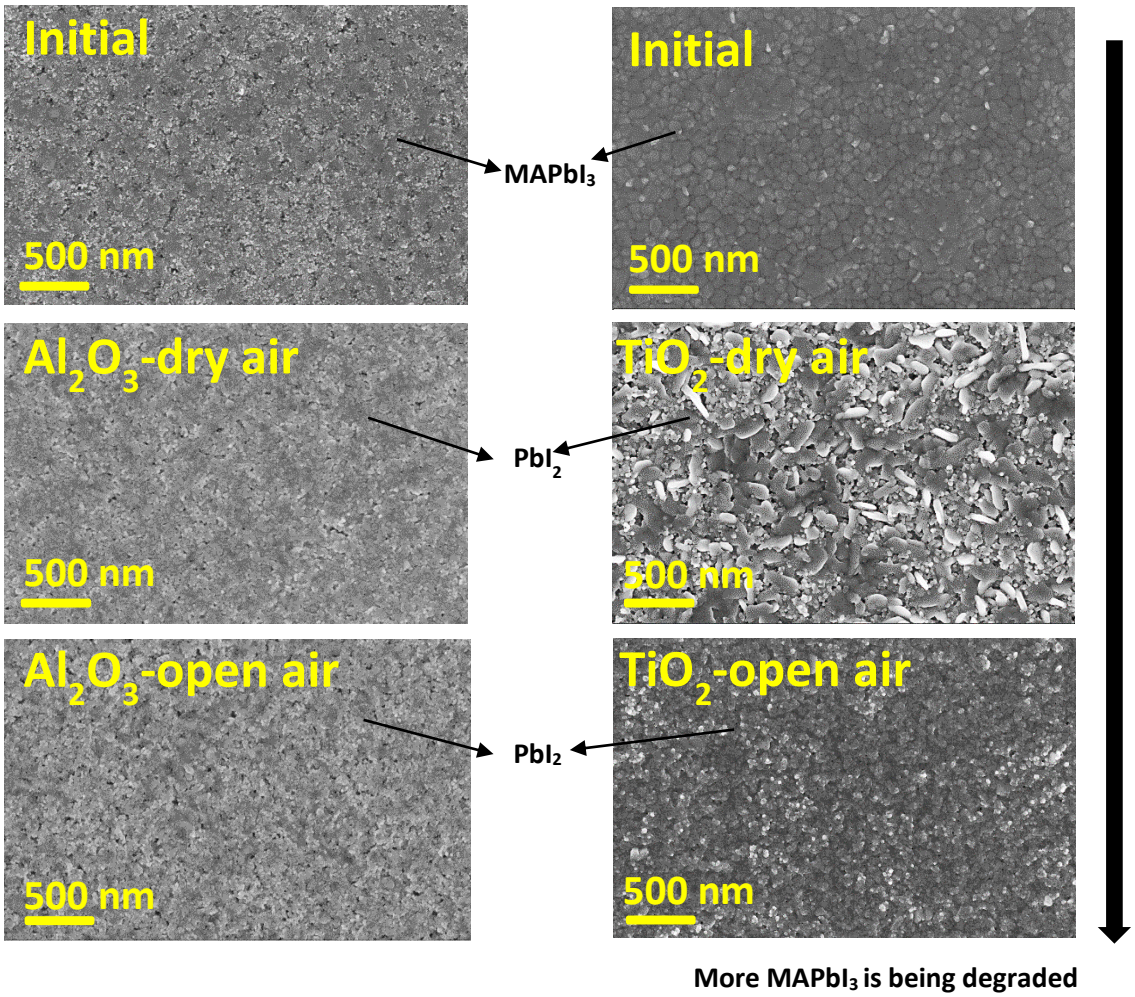


Figure 26: Top view SEM images of initial and 120 hours light-air aged mesoporous metal oxide/$MAPbI_3$ (see labels).

On aged $MAPbI_3$, there were more islands or clusters of $MAPbI_3$ over layers on top of each metal oxide layer. This led to the hypothesis that the presence excess $MAPbI_3$ overlayer accelerated its light-oxygen degradation pathway.

Chapter four ends with the PCE comparison study between two bulk heterojunction solar cells with different mesoporous metal oxide layer (ITO/c-TiO_2/mp-metal oxide /$MAPbI_3$/spiro-OMeTAD/Au). Both mp-Al_2O_3/$MAPbI_3$ based and mp-TiO_2/$MAPbI_3$ solar cells were exposed under constant and AM 1.5 G illumination and dry air.

JV-measurements

The criticality of the photo-stability of $MAPbI_3$ perovskite was even more crucial on the functioning solar cell device perspective. Each Initial metal oxide/$MAPbI_3$ based devices was tested simultaneously to ensure the same environmental conditions of both samples. After two hours of constant illumination of AM 1.5 G and dry air (less than 10 ppm of H_2O), the PCE of the ITO/c-Al_2O_3/mp-Al_2O_3/$MAPbI_3$/spiro-OMeTAD/Au (Al_2O_3-$MAPbI_3$) device decreased rapidly and ceased to function as a working solar cell while the PCE of ITO/c-TiO_2/mp-TiO_2/$MAPbI_3$/spiro-OMeTAD/Au (TiO_2-$MAPbI_3$) solar cell still exhibited a similar value under the same conditions (Figure 27 and Table 4).

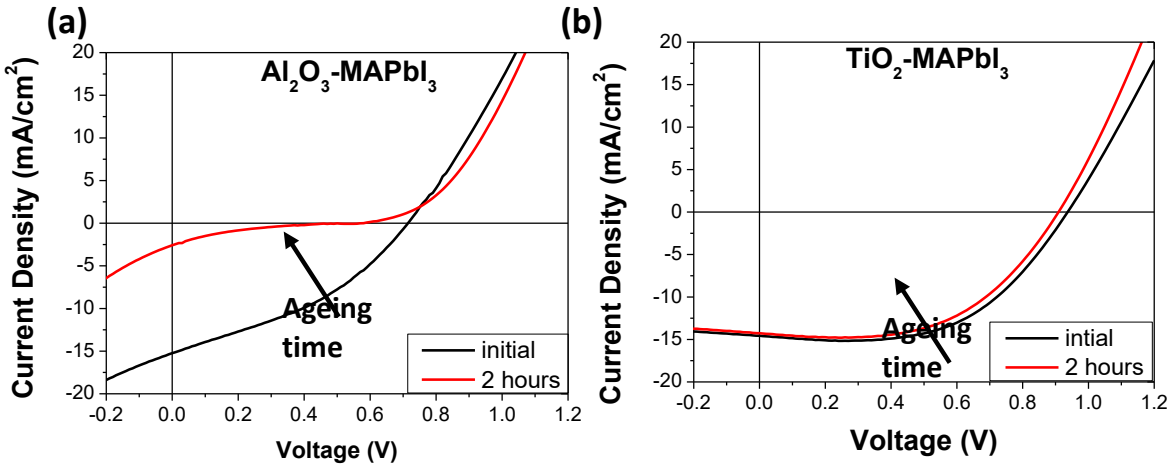


Figure 27: Current density-Voltage curve of (a) of ITO/c-TiO_2/mp-Al_2O_3/$MAPbI_3$/spiro-OMeTAD/Au devices (b) of ITO/c-TiO_2/mp-TiO_2/$MAPbI_3$/spiro-OMeTAD/Au devices. Both samples were illuminated under AM 1.5 G sunlight at approximately 100 $mWcm^{-2}$ irradiance. In this case, a backward scan from 1.2 V to - 0.2 V was performed. It was noted that six different devices each of (a) and (b) were tested were exhibited identical JV performance when being subjected under the same environment.

Table 4: J_{sc}, V_{oc}, FF and PCE of Al_2O_3-$MAPbI_3$ and TiO_2-$MAPbI_3$ based solar cell devices before and the after two hours of oxygen-light degradation derived from Figure 27. Both samples were illuminated under AM 1.5 G sunlight at approximately 100 $mWcm^{-2}$ irradiance. In this case, a backward scan from 1.2 V to - 0.2 V was performed. The total of six identical devices from each category were being measured simultaneously.

	Al_2O_3		TiO_2	
	Initial	**Degraded**	**Initial**	**Degraded**
J_{sc} ($mAcm^{-2}$)	15.24 ± 0.05	2.58 ± 0.03	14.55 ± 0.01	14.26 ± 0.02
V_{oc} (V)	0.71 ± 0.05	0.58 ± 0.03	0.94 ± 0.01	0.91 ± 0.01
FF	0.37 ± 0.04	0.11 ± 0.02	0.58 ± 0.01	0.56 ± 0.01
PCE (%)	4.03 ± 0.1	0.17 ± 0.05	7.83 ± 0.01	7.3 ± 0.02

The backward PCE scan of both type of PSCs indicated that a suitable metal oxide (mp-TiO_2) could indeed slow down the photodegradation process under dry air and visible light. The superoxide

evolution yield within the photoactive layer of TiO_2-$MAPbI_3$ based solar cell devices took place on a much slower pace compared with Al_2O_3-$MAPbI_3$ based devices. Photocurrent (J_{sc}) of the alumina devices suffered severely only when the devices were bathed under constant light-dry air degradation conditions. This corresponded with the rapid reduction in TAS decays shown previously. The mass lost in $MAPbI_3$ coverage and PbI_2 cluster formations shown on the top view SEM images of photo-degraded perovskite films shown in Figure 26, explained the reduction of V_{oc} and FF of the PSCs when the devices were photo-degraded continuously. Even though the one JV curve of the Al_2O_3 and TiO_2 based device were shown in Figure 27 and Table 4, six device of were tested and exhibited identical JV behaviours after being oxygen-light degraded continuously for two hours.

It was noted that the light intensity used in the JV experiment was nearly five times brighter than the tungsten halogen lamp used in TAS experiments. Therefore, it was not a big surprise when the solar cells ceased to function in the JV experiment much earlier than when they were reflected in TAS. On the other hand, the presence of the gold electrode which was deposited on top of the spiro-OMeTAD, acted as a physical barrier that slowed down superoxide evolution rate with the $MAPbI_3$ photoabsorber. Therefore, TAS experiment should not be considered as an extension of JV experiments.

Soon after, another set of extensive PCE experiment was undertaken and plotted in Figure 28 in order to establish the direct relation between superoxide generation yield and a drop in PCE of $MAPbI_3$ bulk heterojunction solar cells.

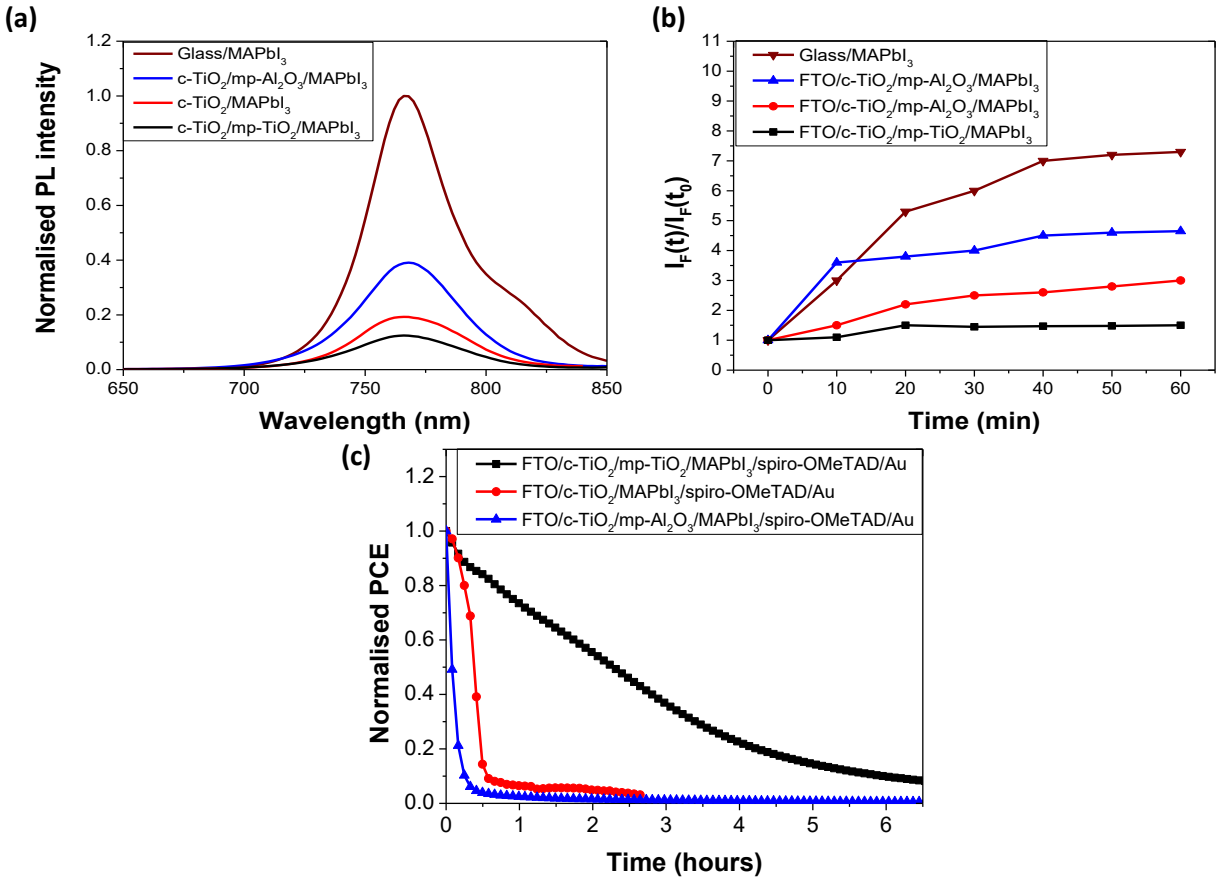


Figure 28: (a) Steady-state photoluminescence spectra of $MAPbI_3$ based films along with a $MAPbI_3$ reference sample (with 485 nm excitation wavelength) (b) Normalised fluorescence intensity at 610 nm (with 520 nm excitation) of HE probe solution to detect the relative amount of superoxide generation within one hours. $I_F(t)$ is the probe fluorescence intensity maximum at time t whereas $I_F(t_0)$ is the background fluorescence intensity of the probe at t = 0. The $I_F(t)$: $I_F(t_0)$ hereafter refers to relative yield of superoxide generation (c) Normalised power conversion efficiencies (PCE) of $MAPbI_3$ based solar cells are measured under different conditions (see legends). The samples are measured under AM 1.5 G powered by equivalent white LED array equipped with UV blocking filter. Dry air comprised of approximately 20.95 % O_2 and 78.09 N_2. This data is adapted from the paper published by Bryant et al. [134].

In 2016, Bryant et al. reported a drop in PCE of three $MAPbI_3$ based solar cell devices : (1) fluorine doped tin oxide (FTO)/ compact TiO_2 (c-TiO_2)/ mesoporous TiO_2 (mp-TiO_2)/$MAPbI_3$/spiro-OMeTAD/Au (2) FTO/c-TiO_2/$MAPbI_3$/spiro-OMeTAD/Au (3) FTO/c-TiO_2/mp-Al_2O_3/$MAPbI_3$/spiro-OMeTAD/Au when they were subjected to a constant AM 1.5 G illumination and dry air flow. The author also contributed to the discussion in this paper via steady state photoluminescence spectra and superoxide measurements of the corresponding pseudo- $MAPbI_3$ solar cell device configuration (without the Au counter electrode) shown in Figure 28-a and b in order to rationalise this observation. In particular, Figure 28-a suggested that electron extraction capability at the perovskite-ETL interfaces can be adjusted manually by using mp-TiO_2 over planer c-TiO_2 or mp-Al_2O_3 which is considered to be an

electron insulating layer. It was shown in Figure 28-b that the degree of instability of the tested devices correlated well with the relative yield of superoxide generation when these pseudo devices (device (1)-(3) without Au counter electrode) were immersed into HE probe solution and exposed to visible light and oxygen for one hour. All these observations pinpoint that superoxide formation is indeed responsible for $MAPbI_3$ degradation.

In addition, Bryant et al. induced the degradation reaction by manually injecting electons into the $MAPbI_3$ based devices [134] (shown in Figure 28-c). Mainly, an additional test was performed to the FTO /c-TiO_2/mp-TiO_2/$MAPbI_3$/spiro-OMeTAD/Au devices while being subjected to injected electrons and oxygen [134]. The $MAPbI_3$ based solar cells were tested in the dark under forward bias (V_{bias} = 0.9, J= 20 $mAcm^{-2}$) while exposed to either N_2 gas or dry air [134]. In between, the devices were PCE measured under light and oxygen while the environmental exposure was kept to a minimum. It was found that devices could degrade in the dark with a combination exposure of excess injected electrons and oxygen [134]. On the other hand, the devices remained relatively stable when both conditions were not met [134].

4.5. Conclusions

Chapter four established interrelation between oxygen-light stability, superoxide generation yield and charge recombination lifetime of the $MAPbI_3$ films. This interrelation was made possible by comparing the absorbance spectra, PL spectra and microsecond TAS decay as a function of oxygen-light aging time. As the $MAPbI_3$ film oxygen-light degraded, its UV-vis absorbance dropped, superoxide formed which in turn decreased its charge recombination lifetime. In particular, the perovskite films started to lose their charge generation properties even before any optical changes to the films began to surface visually. The degradation sign was confirmed via EDX, XRD patterns and top view SEM images of each $MAPbI_3$ before and after the oxygen-light degradation. Afterward, JV measurements were employed to compare the difference between alumina and titiania based $MAPbI_3$ solar cells. It was shown that within two hours of constant light and oxygen ageing, the J_{sc} of alumina based devices dropped sharply while its FF and V_{oc} exhibited some substantial drop during this experimental period. The enhancement in oxygen-light stability of the titiania-$MAPbI_3$ based device was observed because the suitable energy alignments for TIO_2 devices allowed highly energetic charges to be extracted. This retained their photodiode performances under the light-oxygen photodegradation within the test duration. Chapter four was concluded by implementing the method to minimise superoxide formation within $MAPbI_3$ based solar cells during the oxygen-light degradation process. This was made possible by increasing TiO_2-$MAPbI_3$ interfacial areas of the PSCs.

5. Establishment of an Electron Transporting Layer Design Guideline to Enhance Oxygen-light Stability for Lead Triiodide Perovskite Films and Solar Cells

5.1. Abstract

In recent years, the recorded photovoltaic performances of perovskite solar cells (PSCs) has risen rapidly from a few percent to over 22 % [148]. However, there has been very little study regarding photo stability of PSCs which impedes their practical applications and mass industrialisations. Based on the background knowledge that a combination of oxygen and visible light establishes two of the environmental factors that causes perovskite solar cells to cease to function as photodiodes [133,134].

In chapter four, it was shown that superoxide was responsible for the oxygen-light degradation of $MAPbI_3$. In fact, the superoxide generation yield of each can be estimated by performing PL emission of the hydroethedine probe solution. In addition, the superoxide generation yield at ETL-$MAPbI_3$ interface was minimised when the suitable electron extraction layer such as mesoporous-titiania was implemented.

Therefore, an electron transporting layer (ETL) design guideline is established in this chapter in order to maximise operational lifetime of the PSCs without affecting their overall photovoltaic performances. Here, the proposed ETL guideline is made for methyl lead triiodide perovskite ($CH_3NH_3PbI_3$ or $MAPbI_3$) photoactive layers. This chapter consists of three main methods to enhance air and light stability of the $MAPbI_3$ films and bulk heterojunction solar cell devices: 1.) Select suitable electron extraction layers 2.) Maximise the $MAPbI_3$-mesoporous metal oxide interfacial area 3.) Select more air stable absorber layers. The most optimum $MAPbI_3$ based solar cell (ITO/c-SnO_2/mp-TiO_2/CsFAPbI_3/spiro-OMeTAD/Au) can last over 80 hours under constant exposure of illumination of AM 1.5 G and a dry air environment, while the non-optimized ITO/c-TiO_2/mp-TiO_2/$MAPbI_3$/spiro-OMeTAD/Au reference solar cell device ceases to function as a working solar cell in less than an hour.

5.2. Introduction

There are a number of environmental factors that affect the operational lifetime of lead trihalide perovskite solar cells, namely moisture [120,125,126], temperature [120,128–130] and UV illumination [121–123]. In chapter four, it was shown that moisture content from 20 ppm to 60 %RH did not play an important role in to $MAPbI_3$ visual stability. A combination of oxygen and light on the other hand, presented the two key components required to photo-degrade lead trihalide perovskite readily. The mechanism of

this oxygen and light degradation mechanism involved three main steps [133]. The visible light generates photo-excited electrons upon contract with $MAPbI_3$. Then, these highly energetic electrons interact with oxygen in the open atmosphere and form superoxide. Finally, this superoxide is shown to attack the material by deprotonation of the methylammonium cation which leads to the formation of lead trihalide by-products such as lead iodide, iodine and methylamine. Furthermore, the PCE comparison study between titiania-$MAPbI_3$ and alumina-$MAPbI_3$ bulk heterojunction solar cells at the end of chapter four showed us that by increasing electron extraction rate at metal oxide-perovskite interfaces, air-light stability of $MAPbI_3$ films and solar cells improve dramatically. The electron extraction was performed physically by replacing an electron insulating layer (Al_2O_3) with an electron conductive layer (TiO_2). This metal oxide substitution further enhanced extraction of photo-generated electrons from the photoabsorber layer before they could interact with oxygen in the atmosphere to form superoxide, thus it subdued superoxide formation and deprotonation of organic cation.

These observations and conclusions in chapter four indicated highly light-air stable perovskite films and solar cells can be achieved by maximising the electron extraction rate from the photoabsorber to the electron transporting layer and enhancing the intermolecular attraction between cation ions and lead ions. These two concepts can be implemented in a number of ways. Based on these 2 concepts, this chapter presents three main approaches to create ETL design guidelines to achieve more air-light stable methyl lead trihalide films and working solar cells.

1.) **Selecting an appropriate metal oxide electron extraction layer** – the PCE comparison study between Al_2O_3 and TiO_2-$MAPbI_3$ based solar cells made in chapter four lead me to believe that a suitable metal oxide extractor plays an important role which results in highly air-light stable solar cell devices. In chapter five, three different metal oxide extractor were selected and compared namely zinc oxide (ZnO), tin oxide (SnO_2) and titiania (TiO_2). This metal oxide replacement offers the direct benefit of fine tuning the conducting band of metal oxide-$MAPbI_3$ in which it will maximise electron extraction capability between the ETL and the perovskite photoabsorber layer.
2.) **Maximising interfacial area at $MAPbI_3$-mp-TiO_2 interfaces** – This study involved varying an interfacial area between mp-TiO_2 and $MAPbI_3$. This was practically achieved by increasing the metal scaffold thickness while maintaining the same volume of the perovskite photoabsorber. As the interfacial area increased, the electron extraction rate from the absorber also escalated which in turn subdued superoxide formation.
3.) **Applying 1.) and 2.) to caesium formamidinium lead triiodide perovskite films and solar cells** – By substitution of monovalent organic cation (MAI) with inorganic cation such as Cs^+ and

formamidinium (FA), stronger intermolecular attraction between cation and lead ions [139]. As a result, the absorber operational lifetime was maximised under constant exposure of dry air and light. This is considered as a stepping stone in order to reach the radiative PV efficiency limit.

After each individual factor is optimised, a highly stable lead trihalide solar cell was achieved. At the end of this chapter, a PCE comparison study of non-optimized and optimized bulk hetero junction PSCs will be made.

5.3. Experimental

As in chapter four, UV-vis was also used in order to track and access any visual variation in each $MAPbI_3$ film while TAS was used to observe the change in charge kinetic as each perovskite based film started to photo-degrade. Without the combination of oxygen and light, it was shown that there would be no change in both UV-vis and TAS. The rate of signal reduction became vivid as the film was subjected to both visible light and oxygen constantly. The reduction in microsecond TAS decays started to show much earlier than any visual change had started to surface on $MAPbI_3$ films.

The superoxide formation of each $MAPbI_3$ perovskite film was accessed via photoluminescence (PL) of the hydroethedine (HE) probe at 610 nm with an excitation wavelength of 520 nm. Each perovskite sample was submerged in a mixture of dry toluene and HE solution, as stated in chapter three while exposed under a constant halogen light source (20 $mWcm^{-2}$) under dry environment (less than 10 ppm H_2O). The solution was tested with PL at ten minute intervals over a course of one hour. The PL signal growth relative to its background represents superoxide formation of each perovskite sample.

At the end of chapter five, a PCE comparison study among the reference $MAPbI_3$ bulk heterojunction solar cells (ITO/c-TiO_2/mp-TiO_2/$MAPbI_3$/spiro-OMeTAD/Au) and two other $CsFAPbI_3$ based solar cells (ITO/c-TiO_2/mp-TiO_2/$CsFAPbI_3$/spiro-OMeTAD/Au) and (ITO/c-SnO_2/mp-TiO_2/$CsFAPbI_3$/spiro-OMeTAD/Au) was made. Each JV curved for each specimen was plotted while they were being subjected to a constant A.M 1.5 G illumination and dry air (less than 10 ppm H_2O) simultaneously.

5.4. Results and discussions

In this chapter, three main approaches were implemented to this ETL design guidelines for PSCs to optimise their operational lifetime under constant exposure of visible light and dry air.

1.) Selecting an appropriate metal oxide electron extraction layer (ETL)

Three candidates were selected to maximise the electron extraction capability at the electron transporting layer (ETL)-$MAPbI_3$ interfaces after the photoexcitation reaction had taken place. Compact layers of ZnO, SnO_2 and TiO_2 were used individually to alter their energy offset between the photoabsorber and each ETL. Intrinsically, these three ETLs have a different HOMO-LUMO levels as illustrated in Figure 29.

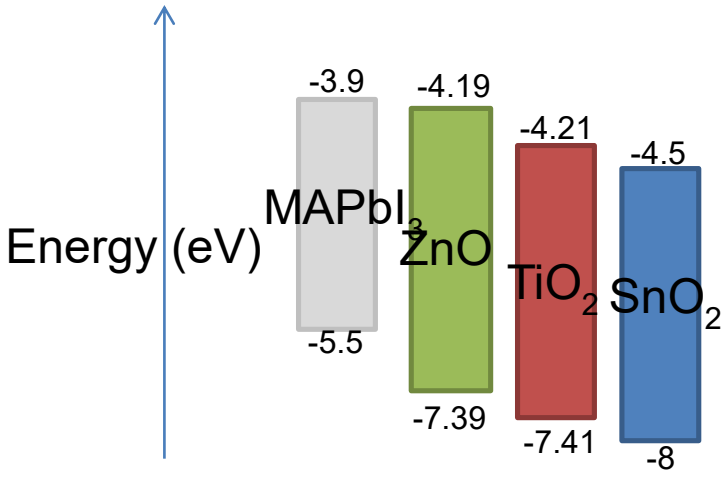


Figure 29: Energy level of $MAPbI_3$ as well as the HOMO and LUMO of three different compact electron transporting layer; namely zinc oxide (ZnO), titanium dioxide (TiO_2), tin oxide (SnO_2).

The different energy offset between each ETL and $MAPbI_3$ altered its photo-generated electron extraction capability as $MAPbI_3$ absorbed light. Deeper LUMO localisation in the electron extraction layer with respect to the $MAPbI_3$ equated to a larger driving force for the electron extraction reaction to become more energetic and feasible, thus decreasing their superoxide evolution. In turn, this enhanced the PSCs operational lifetime under constant exposure of dry air and light. To confirm this rationalisation, UV-vis, superoxide evolution comparison experiments via PL emission and TAS were performed and plotted in Figure 30-32, respectively. In addition, the spectra traces of each ETL-$MAPbI_3$ film was plotted and overlaid as the electron extraction layer varied (Figure 33).

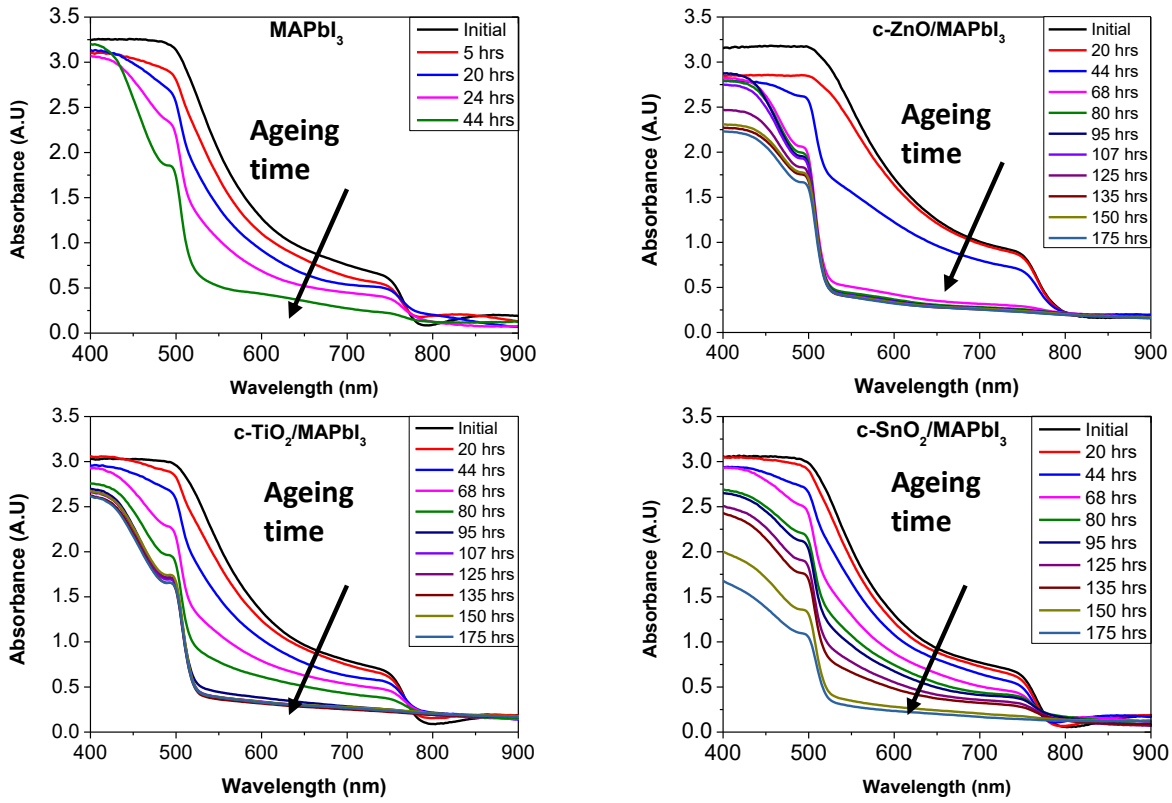


Figure 30: Absorbance spectra of glass/with and without ETL/$MAPbI_3$ samples (see labels) under constant exposure of a halogen tungsten lamp (~ 20 $mWcm^{-2}$) and dry air (less than 10 ppm H_2O). Three different ETLs were tested namely c-ZnO, c-TiO_2 and c-SnO_2.

The absorbance spectra of a reference $MAPbI_3$ sample along with three glass/ETL/$MAPbI_3$ samples were plotted side by side when all samples were subjected to a constant exposure of halogen light source (20$mWcm^{-2}$) and dry air (less than 10 ppm H_2O). As the energy offset at ETL-$MAPbI_3$ started to increase (ZnO, TiO_2 and SnO_2, respectively), less alteration in its absorbance over ageing time was observed. This effect implied that the c-SnO_2/$MAPbI_3$ film exhibited a better visual stability than c-TiO_2/$MAPbI_3$ and c-ZnO/$MAPbI_3$, respectively. To prove that c-SnO_2/$MAPbI_3$ generated less superoxide species as hypothesized earlier, a superoxide evolution test was performed on identical set of samples via comparing their PL emissions (Figure 31).

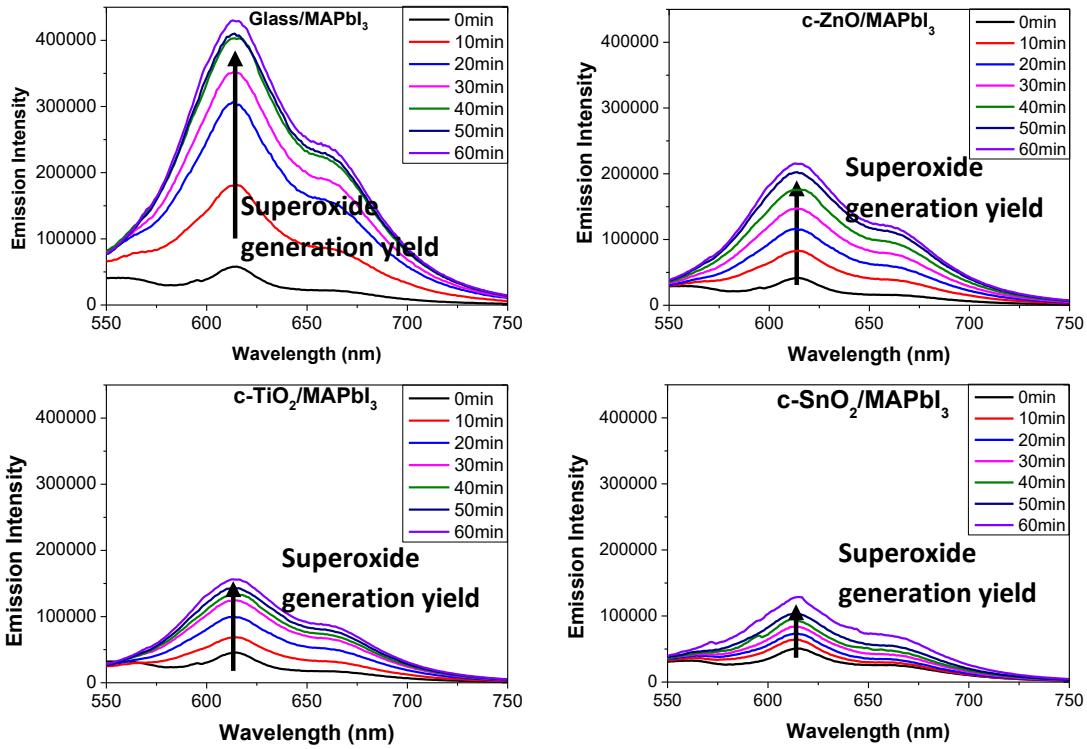


Figure 31: PL emissions as a function of ageing time. Both reference and glass/ETL/$MAPbI_3$ samples were submerged in a mixture of dry toluene and hydroethedine (HE) probe solution (31.7 µM) under constant exposure of halogen light and excess dry air individually. Each PL emission of the toluene solution was measured at 10 minute interval over the course of one hour.

For the next step in order to compare the recombination lifetime of the hole species, TAS spectra of these three tested samples (glass/ ETL/$MAPbI_3$/spiro-OMeTAD) were plotted and compared in Figure 32. Here, each TAS signal on each tested sample was probed at 1,600 nm. In order to track recombination lifetime in spiro-OMeTAD, the laser photo pulses excitation that was at 510 nm with an energy density of approximately 25 μJcm^{-2}. The full experimental conditions were stated back in chapter three.

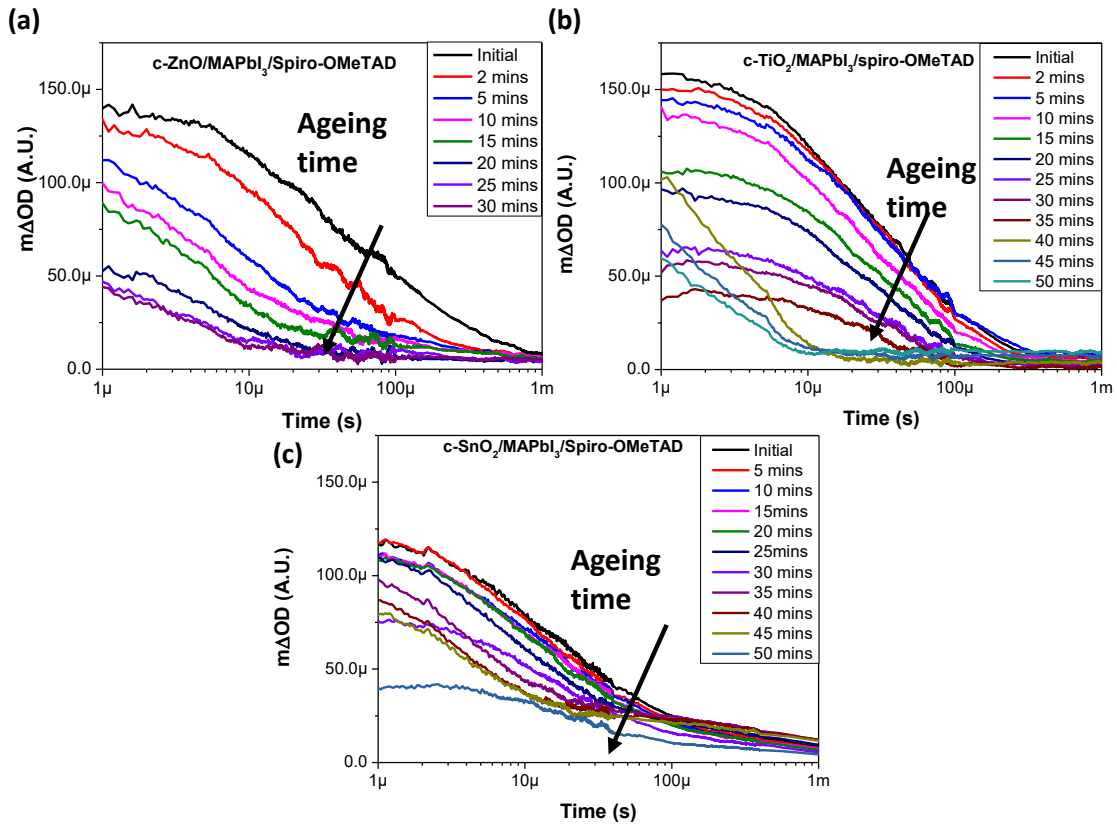


Figure 32: Microsecond transient absorption kinetic as a function of ageing time when each specimen (c-ETL/$MAPbI_3$/spiro-OMeTAD) was probed at 1,600 nm to trace the recombination lifetime of hole species in spiro-OMeTAD that deposited on each $MAPbI_3$ photoabsorber (see label). All samples were aged under constant 20 $mWcm^{-2}$ illumination of a halogen lamp and excess flow of dry air (~1 lpm). The signal was probed at 1,600 nm for spiro-OMeTAD and the laser photo pulses excitation was at 510 nm with an energy density of approximately 25 μJcm^{-2}.

After UV-vis (Figure 30), PL emission (Figure 31) and TAS spectra (Figure 32) on each tested sample with different ETL was obtained. The vertical traces were normalised and overlaid for the sake of comparison (Figure 33). Here, oxygen-light stability of $MAPBI_3$ deposited on top of each ETL was reflected.

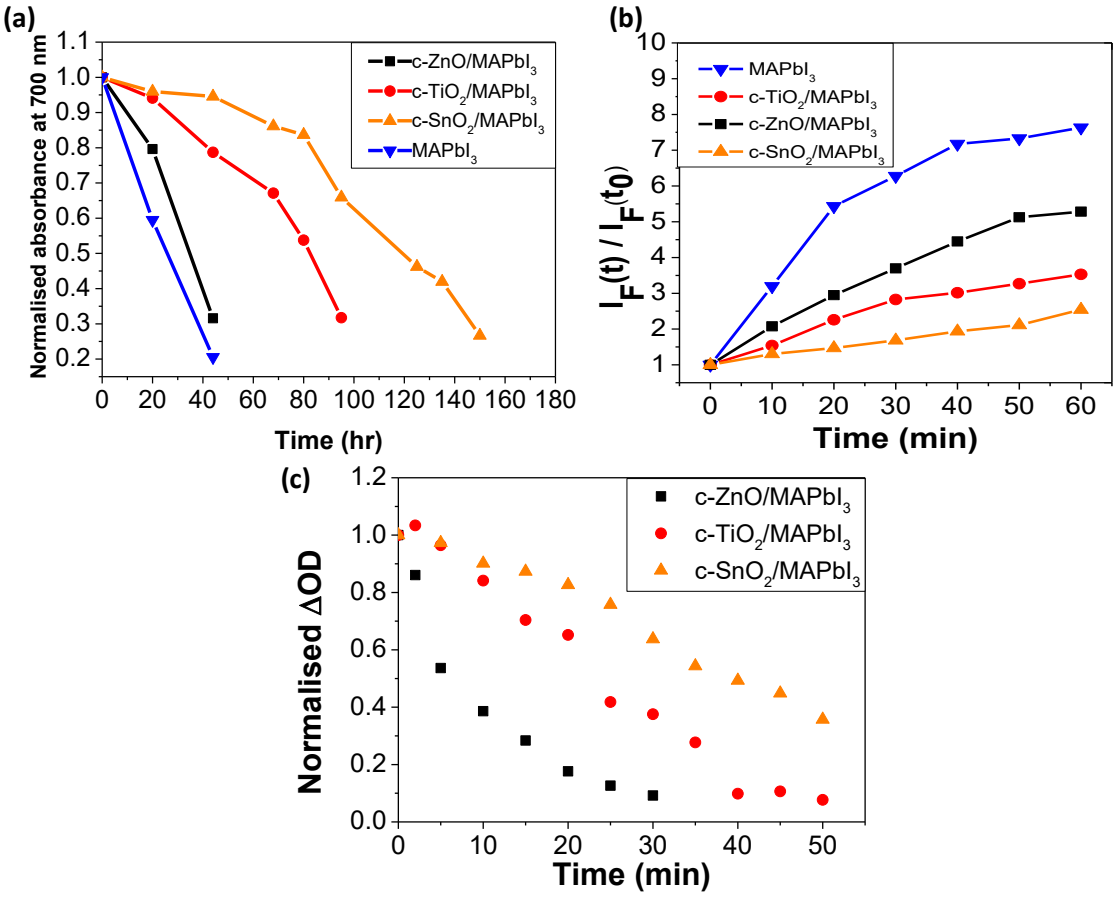


Figure 33: (a) 700 nm UV-vis trace of $MAPbI_3$ samples deposited on three different electron extraction layer (ETL) (see legend). (b) Superoxide measurement of hydroethedine probe (HE) which was highly emissive at 610 nm via excitation wavelength of 520 nm. $I_F(t)$ was the maximum PL intensity at time t while $I_F(t_0)$ was the background fluorescence intensity at the probe at t = 0. The ratio between the two represented the superoxide generation yield. Each specimen degraded under a dry environment and constant halogen light source (~20 $mWcm^{-2}$). (c) Normalised Transient absorption spectra trace at 10 µs as electron extraction layers are differed (see legend). All samples were aged under constant 20 $mWcm^{-2}$ illumination of a halogen lamp and an excess flow of dry air (~1 lpm). The signal was probed at 1,600 nm for spiro-OMeTAD and the laser photo pulses excitation was at 510 nm with an energy density of approximately 25 μJcm^{-2}.

Figure 33-a clearly shows that c-SnO_2/$MAPbI_3$ retained a better visual stability, while it produced relatively less superoxide generation yield than c-TIO_2/$MAPbI_3$ and c-ZnO/$MAPbI_3$, respectively. The drop in absorbance spectra was due to the conversion of $MAPbI_3$ (black) to PbI_2 (yellow) along with other by-products. This effect can be explained with the trend observed on the PL emission traces at 610 nm of each tested toluene/HE probe solution. The relative ratio of PL emission ($I_F(t)$:$I_F(t_0)$) increased according to the relative amount that the HE probe captures the generated superoxide molecules. This ratio also implied that relatively more superoxide was formed in systems such as c-ZnO/$MAPbI_3$ and c-TiO_2/$MAPbI_3$ than the c-SnO_2/MAPbI3 sample. Therefore, c-ZnO and c-TiO_2 cannot

extract photogenerated electrons as efficiently and as quickly as c-SnO_2. As a result, these two systems exhibited a much lower degree of oxygen-light stability compared to the c-SnO_2/$MAPbI_3$.

The 10 µs trace in TAS spectra of each tested sample provided an additional insight regarding the recombination lifetime of the hole species within spiro-OMeTAD for each specimen. Any rapid signal drop in both lifetime and yield often indicated a sign of oxygen-light instability on that tested subject. The PCE trends shown in Figure 33-c corresponded well with both the UV-vis and PL-emission trends shown in Figure 33-a and Figure 33-b. Here, the lifetime of the hole species in the c-SnO_2/$MAPbI_3$/spiro-OMeTAD sample was altered at a much slower pace compared with the lifetime of the c-TiO_2/$MAPbI_3$/spiro-OMeTAD and c-ZnO/$MAPbI_3$/spiro-OMeTAD samples. In addition, the change in TAS signal often occurred much earlier compared to the two other trends observed via UV-vis and PL: This indicated that $MAPbI_3$ could cease to function as a working photovoltaic devices before any visual instability could be observed.

All results shown section 5.4 led to the same conclusion: that c-SnO_2 is the most efficient electron extraction layer out of the three tested candidates. Its low lying LUMO caused any relatively extra photo-generated electrons at $MAPbI_3$-metal oxide interfaces to be most energetic and feasible, thus stabilising the absorber layer the most compared with c-TiO_2 or c-ZnO based samples.

2.) Maximising interfacial area at $MAPbI_3$-mp-TiO_2 interfaces

An additional solution to maximise electron extraction capability at the ETL-$MAPbI_3$ interface was utilised to maximise the photoabsorber-metal oxide interfacial areas. In section 5.4, four different pseudo solar cell devices were tested and compared. Practically, the metal oxide-$MAPbI_3$ interfaces were enhanced by varying the degree of porosity of a mesoporous titiania (TiO_2) thickness while relatively retaining similar overall thickness among these four specimens. Each pseudo-solar cell architecture of a $MAPbI_3$ is shown in Figure 34.

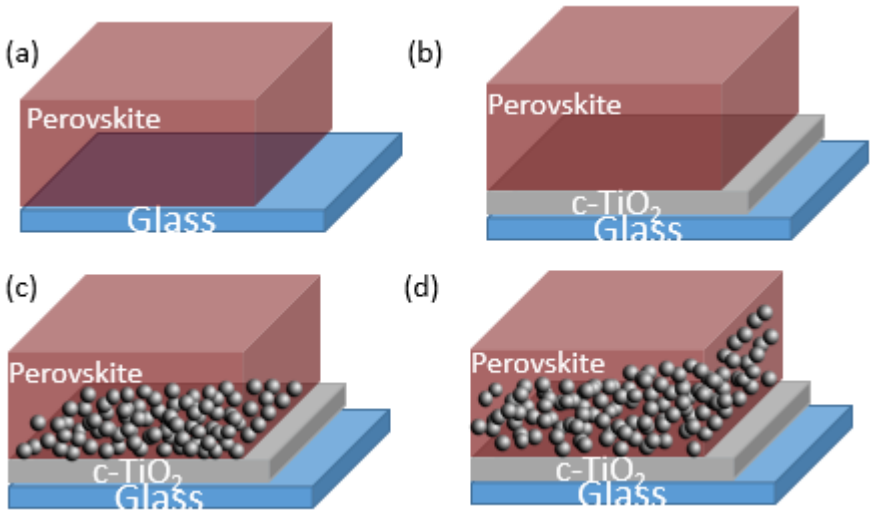


Figure 34: Schematic shows (a) $MAPbI_3$ (b) c-TiO_2/$MAPbI_3$ (c) c-TiO_2/mp-TiO_2/$MAPbI_3$ with overlayer (d) c-TiO_2/mp-TiO_2/$MAPbI_3$ without the overlayer. The absence of excess $MAPbI_3$ overlayer indicated that interfacial area between the absorber and mesoporous titiania was maximised.

Similarly to chapter three and four, the UV-vis PL emission and TAS spectra of these four tested samples were plotted and compared in Figure 35, Figure 36 and Figure 37, respectively.

Approximately, a 20 $mWcm^{-2}$ halogen lamp and excess dry air was exposed to all specimens. At fixed intervals, each UV-vis absorbance graph was measured for each individual sample (Figure 35). Since for absorbance of the photoabsorber for each sample was directly proportional to its thickness, these relatively similar UV-vis signals on all four samples clearly indicated that their overall thickness must also be similar.

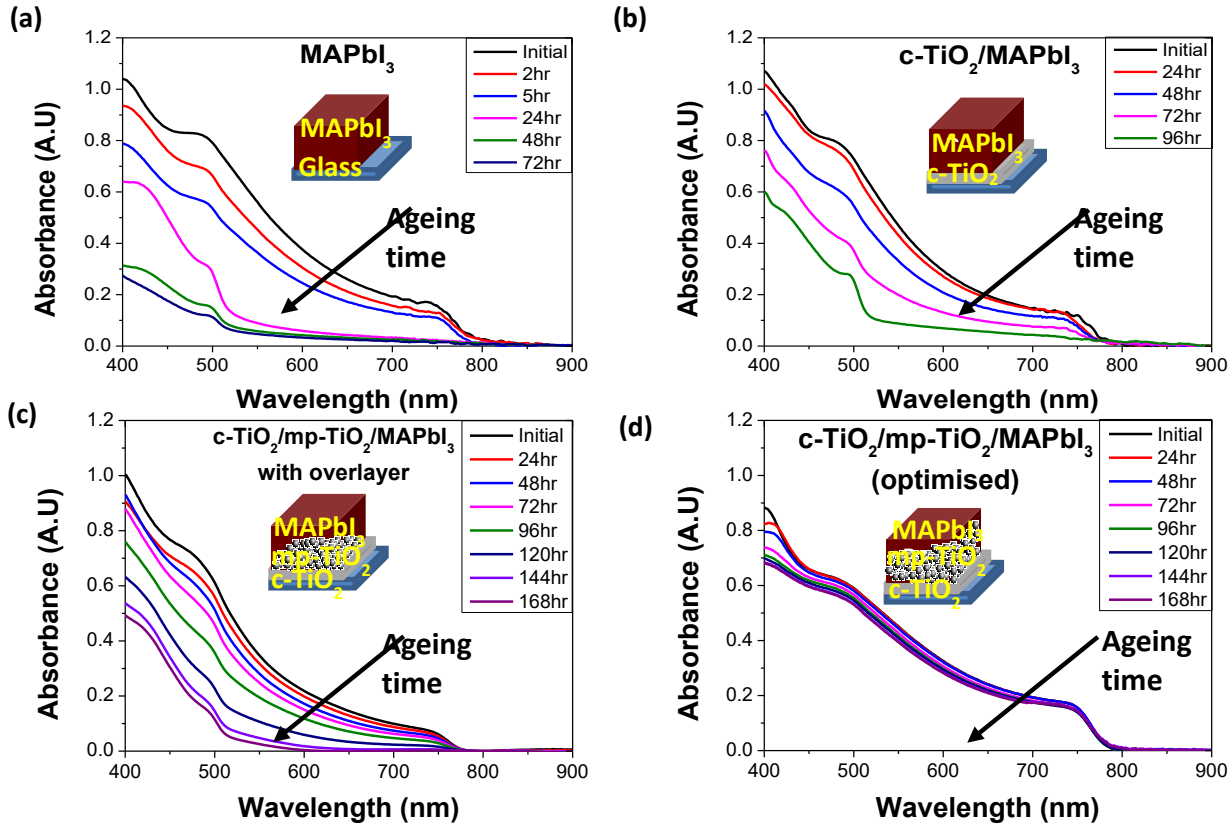


Figure 35: Absorbance curves of four $MAPbI_3$ based specimens as each metal oxide-photoabsorber interfacial area (between $MAPbI_3$ and mp-TiO_2) increased (a) $MAPbI_3$ (b) c-TiO_2/$MAPbI_3$ (c) c-TiO_2/mp-TiO_2/$MAPbI_3$ with an excess overlayer (d) c-TiO_2/mp-TiO_2/$MAPbI_3$ without excess overlayer (optimised). The absence of $MAPbI_3$ overlayer indicated that the interfacial area between the absorber and mp-TiO_2 was maximised. All 4 specimens were under constant exposure of a halogen lamp (20 $mWcm^{-2}$) and dry air (less than 10 ppm H_2O).

Superoxide measurements shown in Figure 36 was also performed in similar fashion as described in Figure 31 in order to relate superoxide generation yield with reduction in UV-vis absorbance spectra.

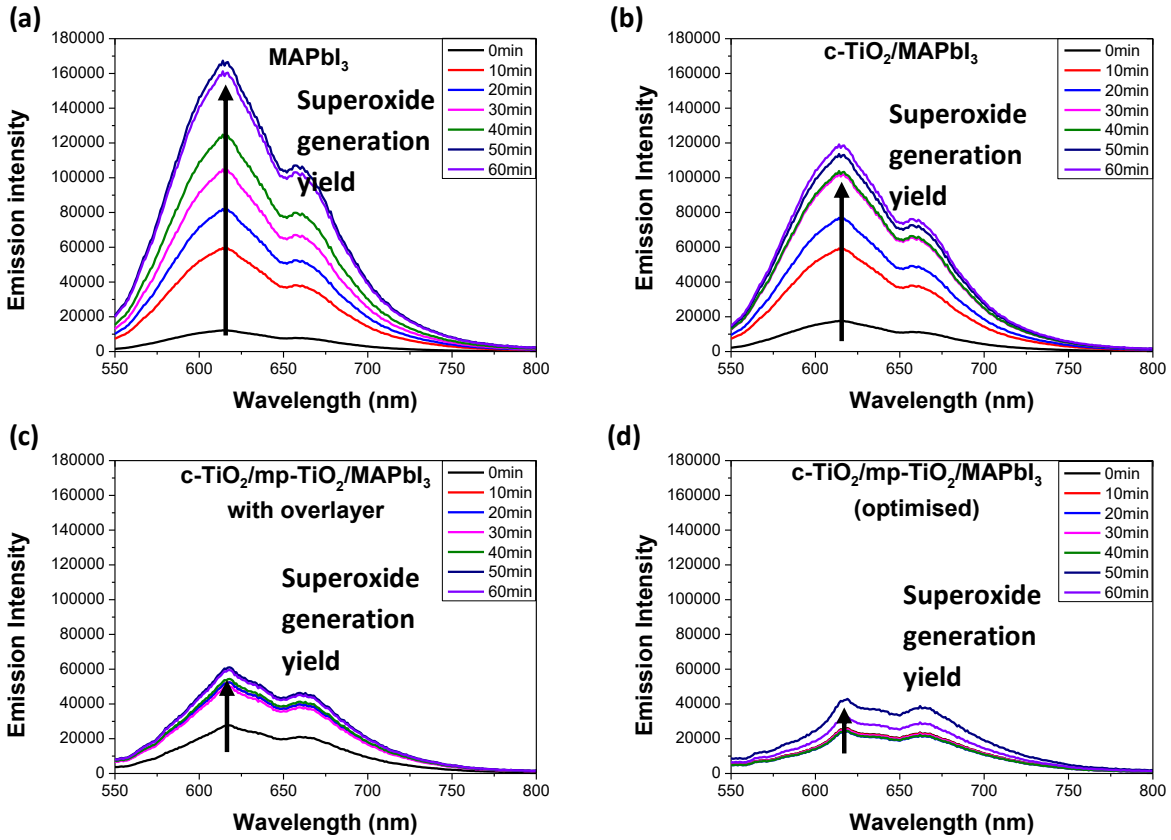


Figure 36: Superoxide measurements of toluene and hydroethedine probe solution which was highly emissive at 610 nm via the excitation wavelength of 520 nm. $I_F(t)$ was the maximum PL intensity at time t while $I_F(t_0)$ was the background fluorescence intensity at probe at t = 0. The ratio between the two represents the superoxide evolution yield as the absorber film degraded under a combination of constant halogen light (~20 $mWcm^{-2}$) and a dry environment (less than 10 ppm H_2O).

By increasing mp-TiO_2-$MAPbI_3$ interfacial areas to the $MAPbI_3$ samples, more stable absorbance spectra were retained while each sample was subjected to constant light and dry air exposure (Figure 37a). In addition, the relative superoxide evolution yield in the $MAPbI_3$ sample containing highly mesoporous titiania was massively supressed compared to that for a bilayer sample (c-TiO_2/$MAPbI_3$) or a reference sample (glass/$MAPbI_3$) as shown in Figure 37b.

Figure 37c strongly indicates that photo generated electrons were extracted at a much faster pace when the ETL-$MAPbI_3$ interfacial areas were maximised. Approximately ten times less superoxide concentration was detected in the HE probe solution for the optimised sample compared with the reference sample (glass/$MAPbI_3$). Steady state PL was also performed for all four samples before the superoxide test was carried out. The lower PL intensity often related to the fact that the most photo generated excitons were quenched more efficiently from the perovskite to the titiania when the metal oxide-photoabsorber was maximised.

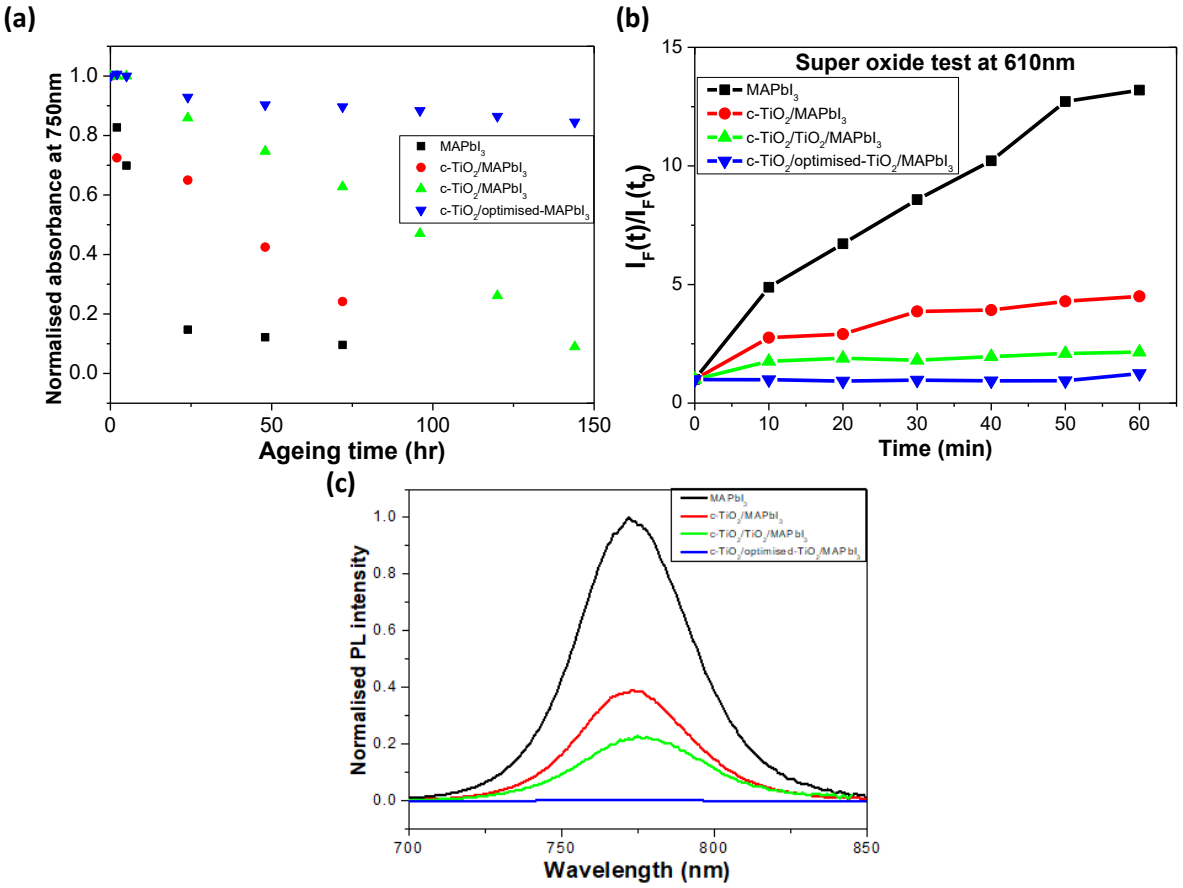


Figure 37: (a) absorbance trace at 750 nm of 4 different $MAPbI_3$ samples with different interfacial area between the $MAPbI_3$ and the mp-TiO_2 (see legend) (b) Superoxide generation traces at 610 nm of the mixture of toluene and hydroethedine probe (31.7 µM) with a 520 nm excitation wavelength (c) a steady state PL emission curves as the mp-TiO_2-$MAPbI_3$ interfaces was enhanced.

By using microsecond-TAS (Figure 38), much earlier signs of hole recombination occurred in the bilayer $MAPbI_3$ sample and reference sample compared with the bulk heterojunction $MAPbI_3$ based sample. After constant exposure to dry air and a halogen lamp, the hole recombination lifetime for the optimised $MAPbI_3$ sample was still relatively similar while signs of photo-instability occurred on the other two non-optimised samples at a much faster pace (a few minutes compared with 24 hours).

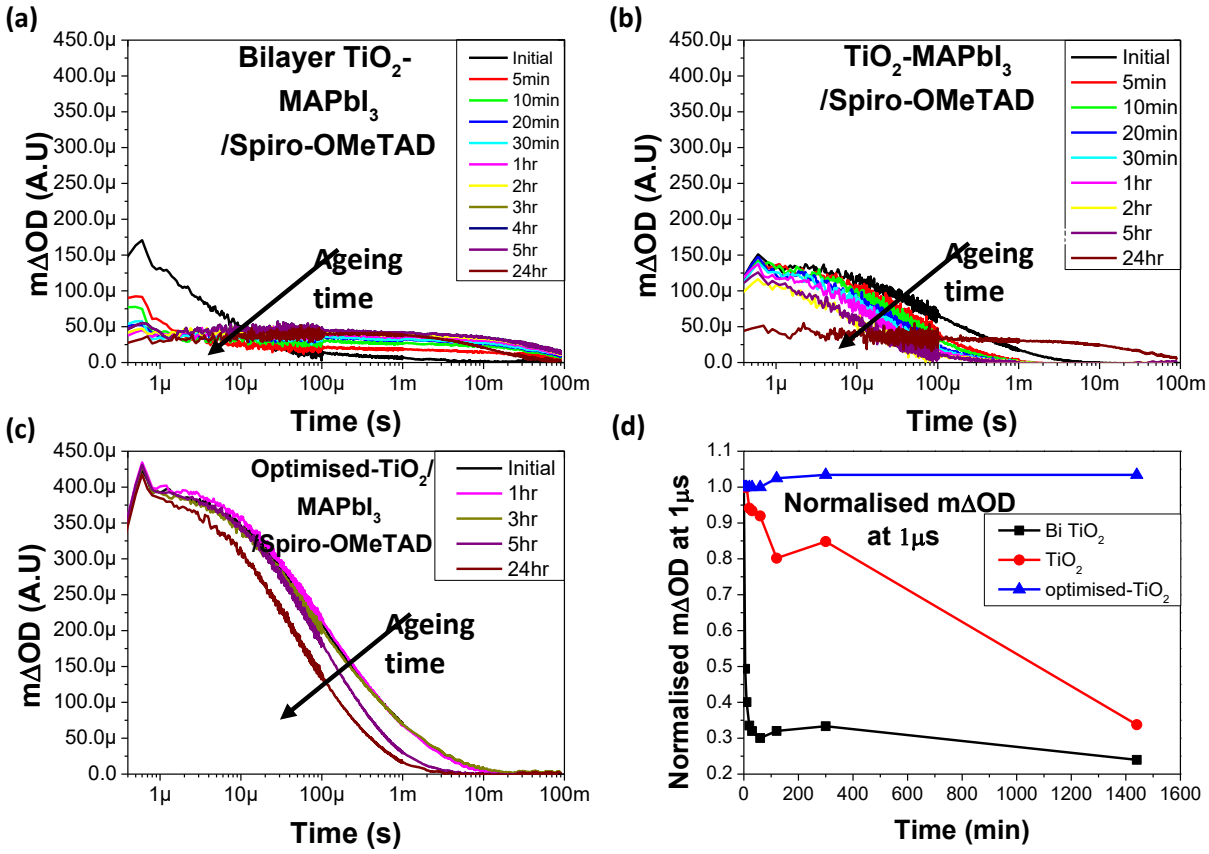


Figure 38: Transient charge kinetic of $MAPbI_3$ based films (a) c-TiO_2/$MAPbI_3$/spiro-OMeTAD (b) c-TiO_2/mp-TiO_2/$MAPbI_3$-with excess overlayer/spiro-OMeTAD (c) c-TiO_2/$MAPbI_3$-without overlayer/spiro-OMeTAD (d) Normalised TAS decay at 1 µs versus oxygen-light ageing time .All samples are aged under constant 20 $mWcm^{-2}$ illumination from a halogen lamp and an excess flow of dry air or open air. The signal was probed at 1600 nm for spiro-OMeTAD. Laser photo excitation was at 510 nm with an energy density of approximately 25 μJcm^{-2}.

To confirm the presence of the $MAPbI_3$ excess overlayer, top view and cross sectional SEM images were performed (Figure 39).

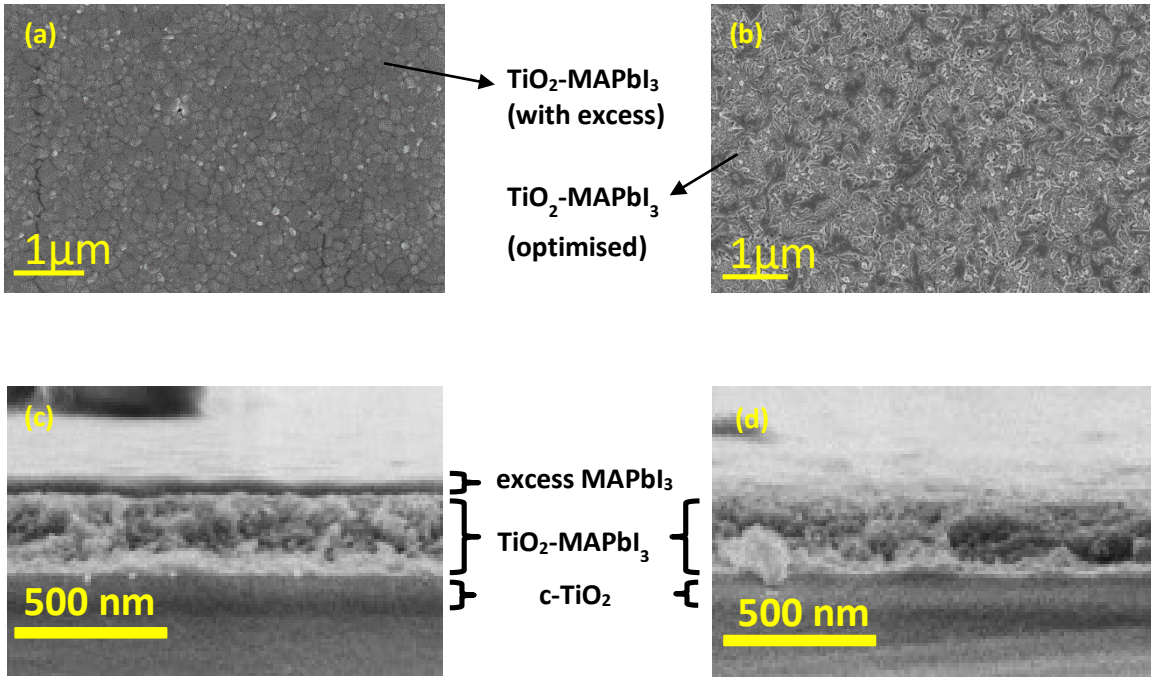


Figure 39: (a) top view and (c) cross sectional SEM images of c-TiO_2/mp-TiO_2/$MAPbI_3$ with the excess overlayer. (b) top view (d) cross sectional SEM of the optimised c-TiO_2/mp-TiO_2/$MAPbI_3$.

From this additional information, it was hypothesised that existence of an overly thick $MAPbI_3$ overlayer which was not in contact with mp-TiO_2 might impede any photogenerated electrons to transport back to the ETL. On the other hand, in terms of the PV performance aspect, some excess overlayer of $MAPbI_3$ was still essential and required to prevent the working solar cells from short circuiting. Therefore, it was important to optimise the overall thickness of the mp-TiO_2 as well as the photoabsorber thickness to maximise both the device operational lifetime and its overall photovoltaic performances.

3.) Applying 1.) and 2.) to caesium formamidinium lead triiodide perovskite films and solar cells

This approach focused on enhancing intermolecular attraction between cations and the lead ions within the perovskite structure. The weakest link components within $MAPbI_3$ crystals that often detached first was the organic group ($MeNH_3^+$). Many literatures reported that the average bond length between lead ions and cation/halide ions became shorter when Cs^+ or FA^+ were to replace MA^+ component [149–151]. For example, Cs-X (halide) average bond length of $CsPbI_3$ and $MAPbI_3$ 3.9 Å and 4.5 Å, respectively [149–151]. This was attributed to the considerably smaller ionic radius of Cs ion when compared with MA ions (1.81 Å in Cs^+ compared with 2.70 Å in MA or 2.79 Å for FA) [140,152]. As a result, by replacing the relatively weak-linked organic group of $MANH_3^+$ with a stronger bonded organic $Cs_{0.17}FA_{0.83}NH_3^+$ component, the superoxide generation yield of the photoabsorber should reduce dramatically [139,140]. Here, MA^+ ions was substituted with a stronger bond inorganic ion (Cs^+). This effect

should in turn stagnate the conversion reaction of a lead trihalide perovskite photoabsorber to its subsequent by-products upon constant exposure to light and oxygen. Therefore, $CsFAPbI_3$ perovskite film was hypothesized to resist the oxygen-light degradation better than $MAPbI_3$ photoabsorber.

In a similar fashion to the first ETL optimisation guideline where three different compact layers were studied (c-ZnO, c-TiO_2 and c-SnO_2), four different types of $Cs_{0.17}FA_{0.83}PbI_3$ (which will be referred to as $CsFAPbI_3$ from now on) based perovskite films were investigated: namely 1.) reference $CsFAPbI_3$ 2.) c-ZnO/$CsFAPbI_3$ 3.) c-TiO_2/$CsFAPbI_3$ 4.) C-SnO_2/$CsFAPbI_3$. Firstly, UV-vis trace was plotted in Figure 40 followed by superoxide generation yield measurement as shown in Figure 41.

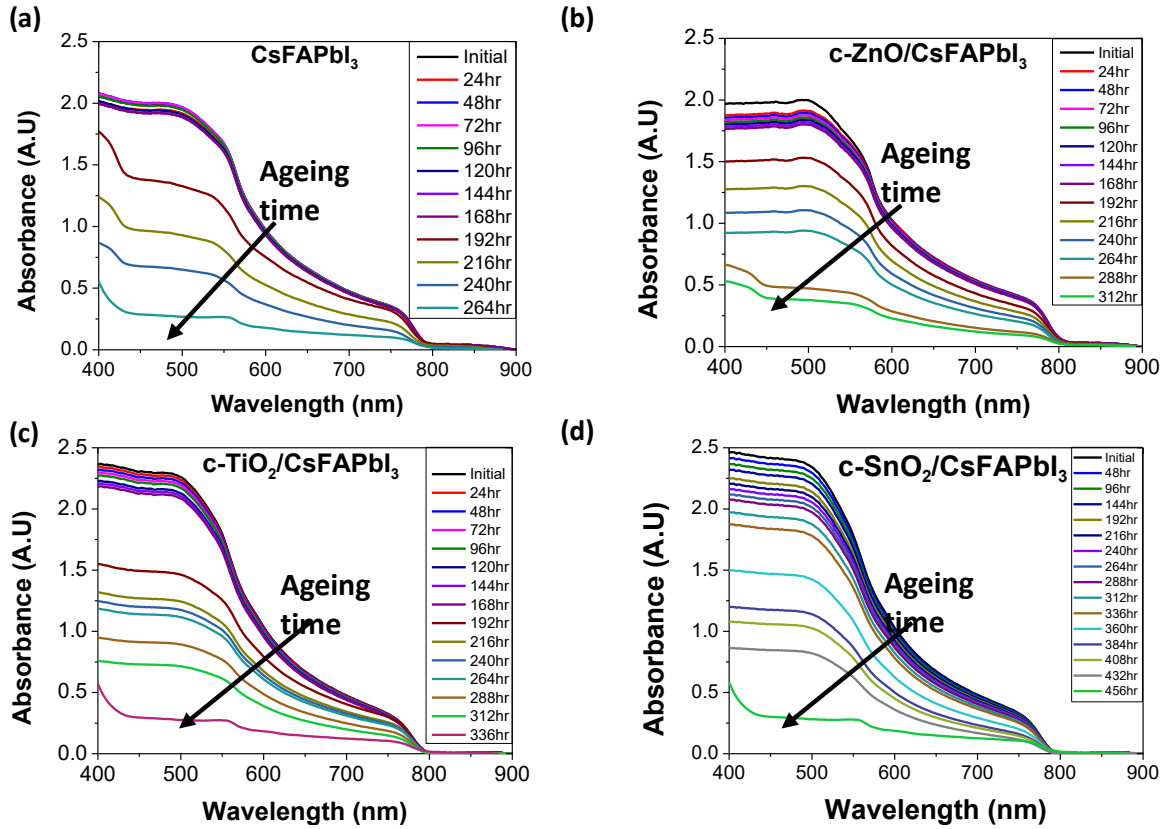


Figure 40: Absorbance curves of (a) $CsFAPbI_3$ (b) c-ZnO/$CsFAPbI_3$ (c) TiO_2/$CsFAPbI_3$ (d) c-SnO_2/$CsFAPbI_3$. All the samples were aged under constant illumination of halogen light (20 $mWcm^{-2}$) and dry air exposure (less than 10 ppm H_2O).

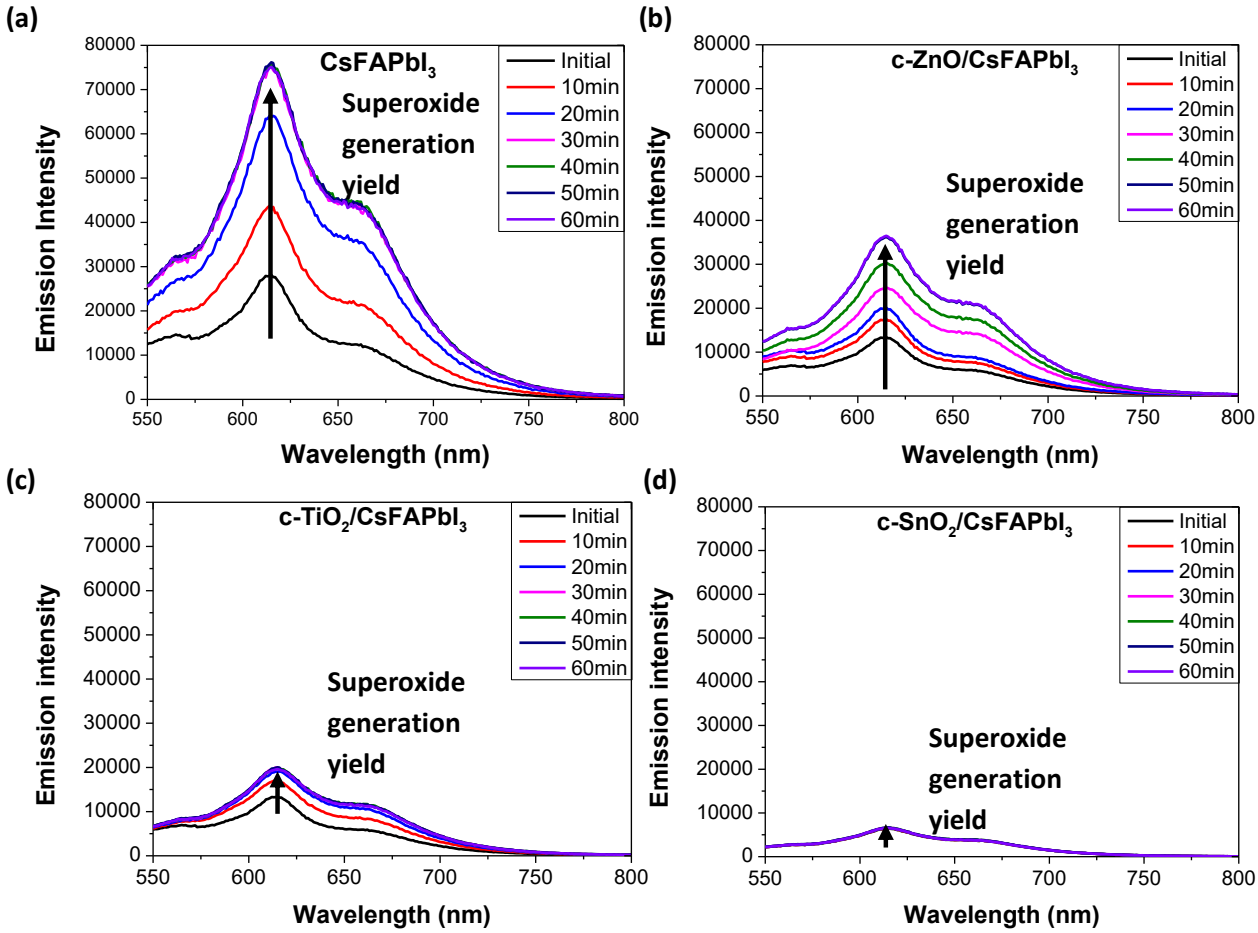


Figure 41: Superoxide measurement of mixture of dry toluene and hydroethedine (HE) probe solution (31.7 µM) after submerging each $CsFaPbI_3$ sample while each sample was exposed to a constant exposure of halogen light and excess dry air. The tested solution was highly emissive at 610 nm via an excitation wavelength of 520 nm upon superoxide formation. $I_F(t)$ is the maximum PL intensity at time t while $I_F(t_0)$ is the background fluorescence intensity at probe at t = 0. The ratio between the two is the superoxide yield as the absorber film degrades under a constant light-oxygen environment.

The absorbance spectra of superoxide generation yield of four $CsFAPbI_3$ based samples were plotted in Figure 40 and 41, respectively. Afterwards, the absorbance trace at 750 nm of each ETL/$CsFAPbI_3$ sample along with the reference $CsFAPbI_3$ film was plotted side by side with superoxide generation trace at 610 nm for each case of metal oxide-$CSFAPbI_3$ in Figure 42.

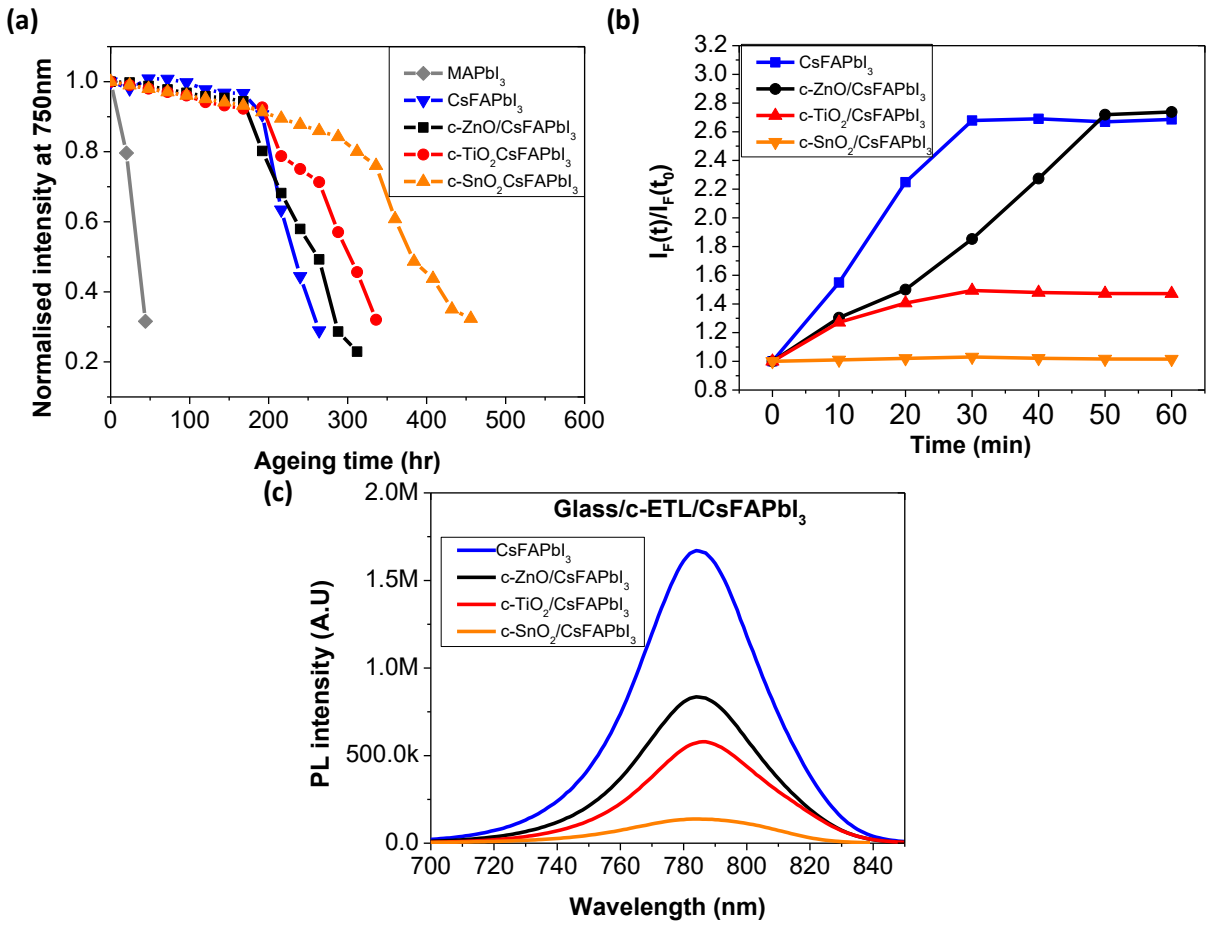


Figure 42: (a) absorbance traces at 750 nm of $MAPbI_3$ and $CSFAPbI_3$ deposited on three difference compact layers of metal oxide (see legend) (b) Superoxide generation traces of the tested toluene mixed with HE probe solution (31.7 µM) at 610 nm with 520 nm excitation wavelength. Each c-ETL/$CsFAPbI_3$ contain three different compact metal oxides along with a reference $CsFAPbI_3$ sample (see legend) (c) raw steady state PL emission intensity of four different c-ETL/$CsFAPbI_3$.

In general, the much slower drop in absorbance of c-ETL/$CsFAPbI_3$ as a function of oxygen-light ageing time indicated that a stronger cation bonding between caesium formamidinium cation and lead ions prolong visual stability of the photoabsorber. Figure 42a also compares a different degree of light-oxygen stability between a $MAPbI_3$ and a $CsFAPbI_3$ sample. The $CsFAPbI_3$ film remained as a photoabsorber roughly six times longer than the $MAPbI_3$ reference sample when they were exposed to nearly identical testing conditions. Similar to the first guideline, the oxygen-light stability of the $CsFAPbI_3$ based sample differed according to which compact metal oxide was inserted underneath the photoabsorber.

Figure 42 also shows that with appropriate compact metal oxide and appropriate photoabsorber, its air-stability can be enhanced dramatically (c-SnO, c-TiO_2 and c-ZnO_2/$CsFAPbI_3$, respectively). The superoxide generation yield in the $CsFAPbI_3$ absorber was minimised while its electron extraction

capability at the absorber-metal oxide interface was enhanced. These two effects complimented each other and resulted in an even greater oxygen-light stable sample.

The next focus on section 5.4 is about combining all three established ETL design guidelines together in order to maximise the operational lifetime of the lead trihalide perovskite films and working solar cells while still retaining relatively high PV performances. Here, UV-vis absorbances, PL emission spectra of the toluene and HE probe solution along with TAS signals of three different c-ETLs/mp-ETLs/$CsFAPbI_3$ films and the $CsFAPbI_3$ reference sample were measured in the same manner as chapter four (Figure 43, 44 and 45, respectively). Lastly, the vertical trace of each individual spectra obtained from three separate experiments was plotted and compared side by side in Figure 46 in order to observed the effect of charges kinetic in the optimised structure.

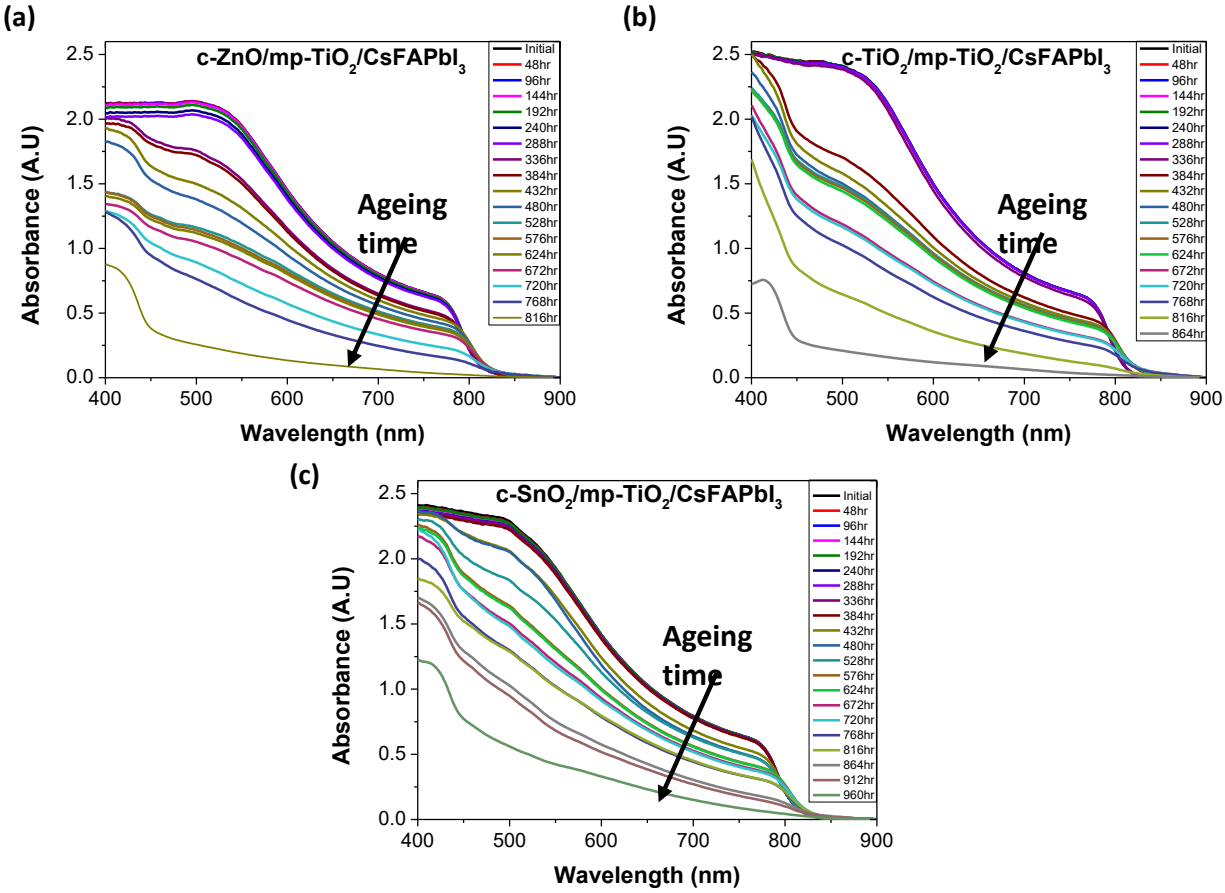


Figure 43: Absorbance curves over ageing time of (a) c-ZnO/mp-TiO_2/$CsFAPbI_3$ (b) c-TiO_2/mp-TiO_2/$CsFAPbI_3$ (c) c-SnO_2/mp-TiO_2/$CsFAPbI_3$ .All the samples were aged under constant illumination of light (~20 $mWcm^{-2}$) and dry air exposure (less than 10 ppm H_2O).

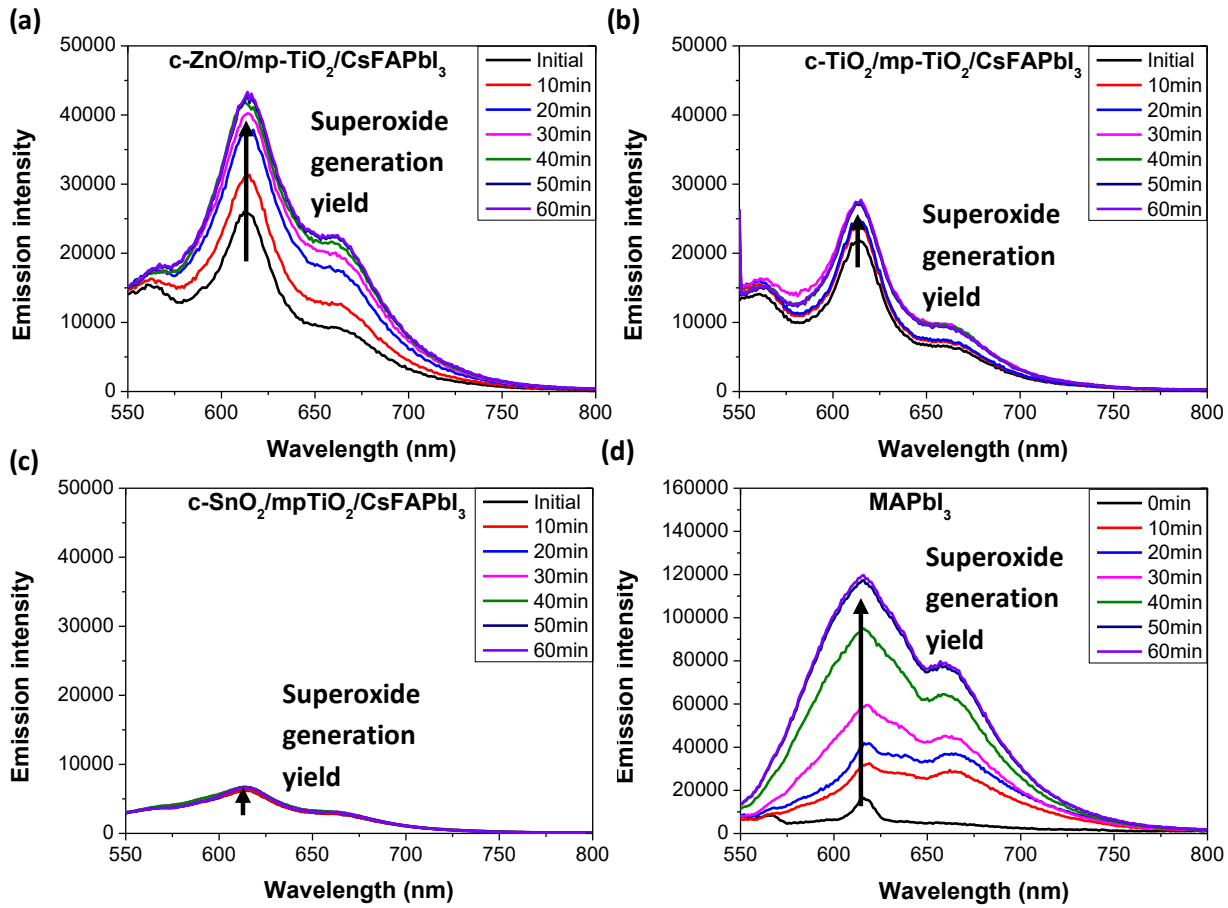


Figure 44: Superoxide measurement of hydroethedine probe solution which was highly emissive at 610 nm while excitation wavelength was at 520 nm for each $CsFAPbI_3$ based samples (see legends). $I_F(t)$ is the maximum PL intensity at time t while $I_F(t_0)$ is the background fluorescence intensity at probe at t = 0. The ratio between the two is the superoxide yield as the absorber film degrades under a dry environment. Superoxide measurement of $MAPbI_3$ sample was included in (d) for comparison.

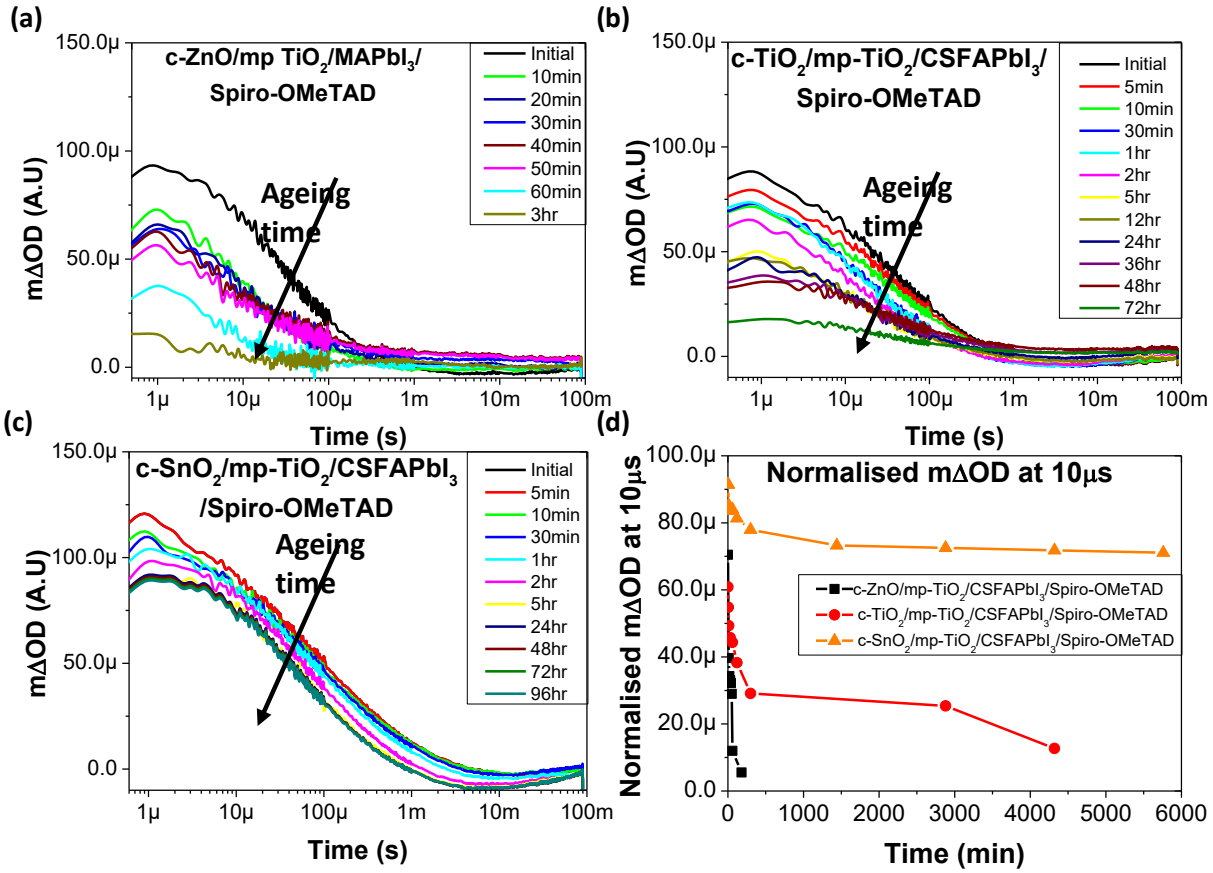


Figure 45: Transient charge kinetic of $MAPbI_3$ based films (a) c-ZnO/mp-TiO_2/$CsFAPbI_3$/spiro-OMeTAD (b) c-TiO_2/mp-TiO_2/$CsFAPbI_3$/spiro-OMeTAD /spiro-OMeTAD (c) c-SnO_2/mp-TiO_2/$CsFAPbI_3$/spiro-OMeTAD (d) TAS vertical trace at 10µs of its optical density of $CsFAPbI_3$ deposited on 3 different compact metal oxides. All samples were aged under constant 20 $mWcm^{-2}$ illumination of a halogen lamp and excess flow of dry air (less than 20 ppm H_2O). The signal was probed at 1,600 nm to track hole recombination lifetime in spiro-OMeTAD. Laser photo excitation was undertaken at 510 nm with an energy density of approximately 25 μJcm^{-2}.

From this, UV-absorbance vertical traces at 750 nm, superoxide generation yield trace at 610nm and PL emission peak is plotted next to each other for the sake of valid comparison as shown in Figure 46.

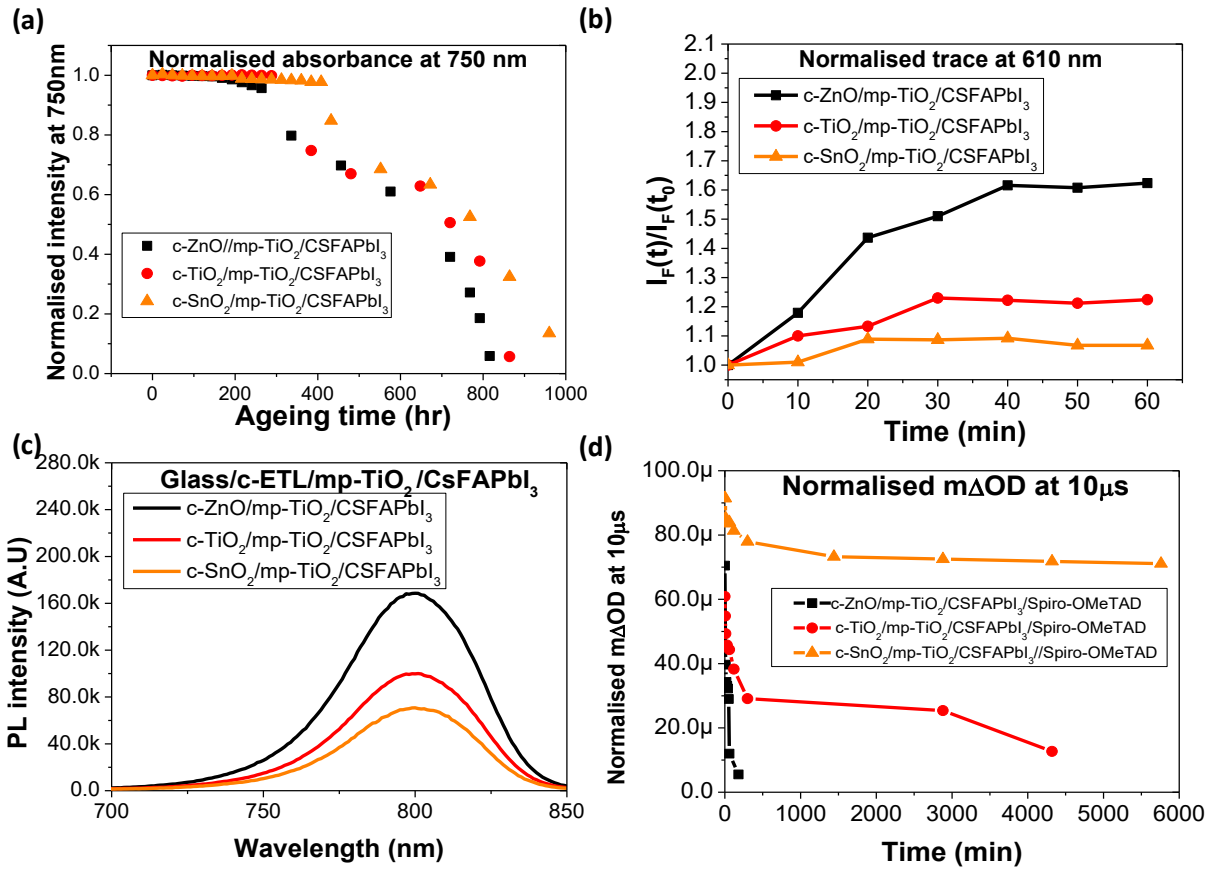
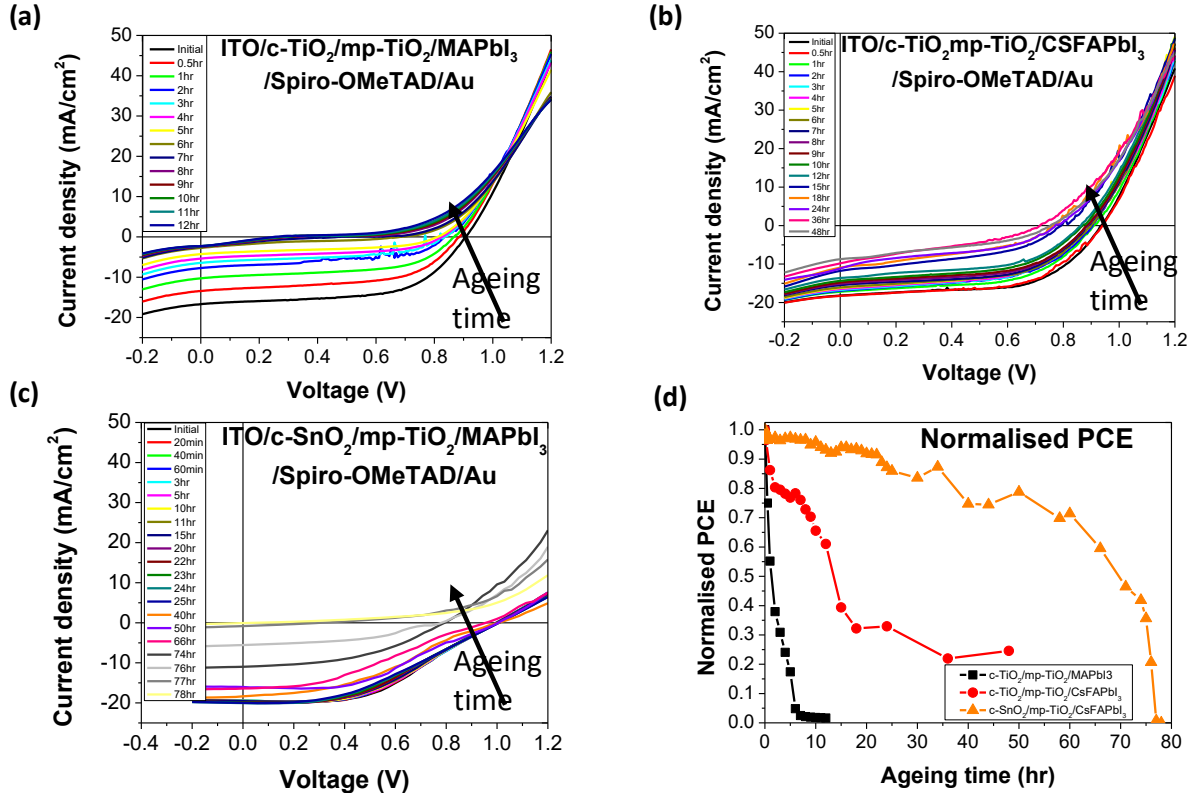


Figure 46: (a) Normalised of UV-vis absorbance trace at 750 nm of c-ETLs/mp-TiO_2/$CsFAPbI_3$ (where ETL were namely ZnO, TiO_2 and c-SnO_2) (b) relative superoxide generation yield ($I_F(t)$:$I_F(t_0)$)at 610 nm of c-ETLs/mp-TiO_2/$CsFAPbI_3$ (c) raw steady state emission peak of c-ETLs/mp-TiO_2/$CsFAPbI_3$ (d) Transient absorption trace at 10 µs of of c-ETLs/mp-TiO_2/$CsFAPbI_3$/spiro-OMeTAD where each sample consisted of a different compact metal oxide (see legend). All of the optimised photoabsorbers were deposited on mesoporous titiania in order to maximise electron extraction at the absorber-mesoporous metal oxide interfaces.

By following all three of the ETL design guidelines in order to create a highly air-light stable solar cell, the optimised solar cell was constructed. The optimum bulk heterojunction solar cell devices that were solution processable consisted of ITO/c-SnO_2/mp-TiO_2/$CsFAPbI_3$/spiro-OMeTAD/Au. The optimum conditions were reached by maximising photo-electron extraction capability at the metal oxide-perovskite photoabsorber and minimising superoxide generation within the photoabsorber layer. Evidently, ITO/c-SnO_2/mp-TiO_2/$CsFAPbI_3$ film has the least drop in its absorbance trace at 750 nm compared with other test specimens, while its superoxide generation yield stayed at minimum when the sample was submerged in toluene and HE probe solution with a constant exposure to light and oxygen. In addition, the most stable sample retain the longest hole recombination lifetime.

As shown in Figure 47 and Table 5, the most light-air stable lead trihalide perovskite device under a constant exposure of constant dry oxygen and AM 1.5 G xenon light still lived as a working photodiode

over six to eight times longer than the heterojunction reference solar cell (ITO/c-TiO_2/mp-TiO_2/$MAPbI_3$/Spiro-OMeTAD/Au) (roughly 80 hours compared with 10 hours for the optimised and the reference solar cell, respectively). It was speculated that a drop in FF of the ITO/c-SnO_2/mp-TiO_2/$CsFAPbI_3$ sample due to the porosity optimization effect could be regarded as a compromise to trade a slight drop in its PV performances to gain a massive improvement for air-light stability. After each solar cell sample was bathed under an AM 1.5 G xenon lamp and dry air continuously, J_{sc} values of all tested samples tended to drop drastically over time as the superoxide species started to form at the absorber layer. Since one of the light-oxygen degradation by-products is water molecules, this will cause a self-catalytic reaction to occur. Therefore, each perovskite sample could absorb less light and



generate a lesser amount of exciton overtime under the test conditions. Thus, a rapid fallout in PCE in PSCs tends to take place eventually.

Figure 47: JV curves of (a) ITO/c-TiO_2/mp-TiO_2/$MAPbI_3$/spiro-OMeTAD/Au (b) ITO/c-TiO_2/mp-ITO/TiO_2/$MAPbI_3$/spiro-OMeTAD/Au (c) ITO/c-SnO_2/mp-TiO_2/$CsFAPbI_3$/spiro-OMeTAD/Au (d) Normalised PCE for perovskite derived from (a), (b) and (c). Both samples are exposed under AM 1.5 G with approximately 100 $mWcm^{-2}$ irradiance powered by equivalent white LED array equipped with UV blocking.

Table 5: PV parameters of three different bulk heterojunction solar cells: ITO/c-TiO_2/mp-TiO_2/$MAPbI_3$/spiro-OMeTAD/Au, ITO/c-TiO_2/mp-TiO_2/$CsFAPbI_3$/spiro-OMeTAD/Au and ITO/c-SnO_2/mp-TiO_2/$CsFAPbI_3$/spiro-OMeTAD/Au. The total of six devices from each category were being measured simultaneously.

	ITO/c-TiO_2/mp-TiO_2/$MAPbI_3$/Spiro-OMeTAD/Au	ITO/c-TiO_2/mp-TiO_2/$CsFAPbI_3$/Spiro-OMeTAD/Au	ITO/c-SnO_2/mp-TiO_2/$CsFAPbI_3$/Spiro-OMeTAD/Au
PCE	9.07 ± 0.05	10.15 ± 0.1	9.16 ± 0.05
J_{sc}	16.70 ± 0.03	18.18 ± 0.05	19.45 ± 0.01
V_{oc}	0.91± 0.01	0.93 ± 0.02	0.99 ± 0.04
FF	0.59 ± 0.01	0.60 ± 0.02	0.47 ± 0.03

5.5. Conclusions

Chapter five introduced three ETL design guidelines of the perovskite photoabsorber films in order to suppress its superoxide generation yield during the oxygen-light degradation process: 1.) select a suitable electron extraction layer 2.) maximise interfacial areas at the absorber-mesoporous metal oxide 3.) apply 1.) and 2.) to caesium formamidinium lead triiodide perovskite films and solar cells which tolerate oxygen-light degradation much better than $MAPbI_3$ perovskite. Figure 48 summarised and compared visual stability of organo/inorgano-lead triiodide perovskite. The reduction in absorbance of each lead perovskite film sample was directly related with superoxide generation yield as the oxygen-light degradation process took place shown in Figure 48a and 48b, respectively. In particular, when appropriate ratio of Cs^+ and FA^+ was implemented in the perovskite crystal structure over the MA^+ ions, a stronger intermolecular attractions between cation ions and lead/halide ions was formed which in turn reduced superoxide generation in the perovskite photoabsorber films during oxygen-light degradation. Chapter five concluded that c-SnO_2/mp-TiO_2/$CsFAPbI_3$/spiro-OMeTAD/Au was the most oxygen-light stable solar cell device going forward. This was made possible by following the three design guidelines that were established previously.

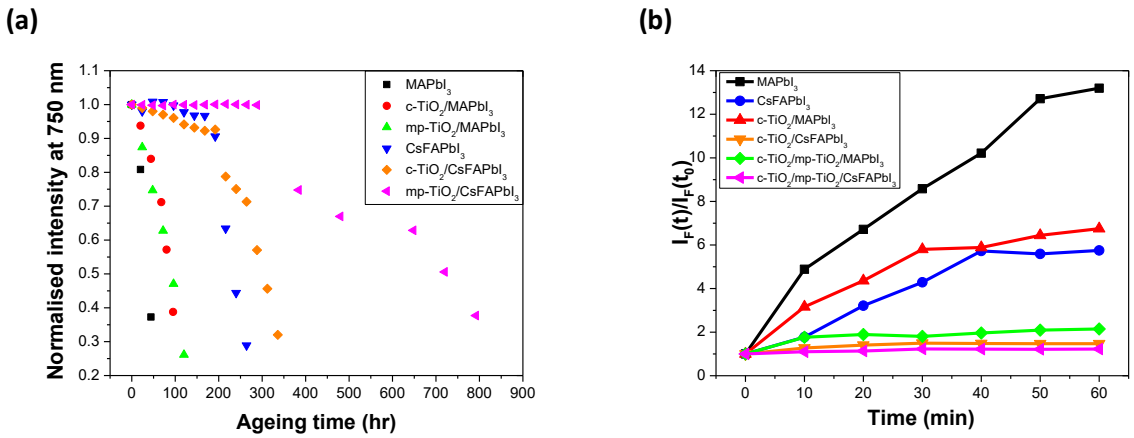


Figure 48: (a) absorbance spectra trace at 750 nm of lead trihalide perovskite films (see legends) (b) Superoxide generation yield trace at 610 nm (with 520 nm excitation wavelength) of HE probe solution.

6. Oxygen-light Stability Enhancement of $CsFAMAPbI_3$ Based Perovskite Films and Working Solar Cells with $PC_{70}BM$ Dopant

6.1. Abstract

In chapter five, the ETL design guideline set out how to maximise oxygen and light stability of $MAPbI_3$ and $CSPAPbI_3$ perovskite films and solar cells. Predominantly, the main concepts in chapter five revolved around maximising photo-generated electrons extraction capability at ETL-perovskite interface during the light harvesting process by adjusting the conduction band edge of the ETL with respect to the perovskite photoabsorber. In addition, the intermolecular attraction within the organo-lead perovskite crystal structure was raised by replacing a weak-linked $MANH_3^+$ with $FANH_3^+$ and Cs^+ ions. The most oxygen-light stable perovskite solar cells remained in operational condition as a working photodiode approximately six to eight times longer than the titiania based reference device. In chapter six, the oxygen-light stability of $CsFAPbI_3$ perovskite films and bulk heterojunction solar cells are investigated. An alternative method to further extract any photo-generated electrons at the perovskite/ETL interfaces is to dope the photoabsorber $CsFAPbI_3$ solution with a solution containing an appropriate amount PCBM. Both $PC_{60}BM$ and $PC_{70}BM$ doped perovskite films were investigated and compared to undoped $CsFAPbI_3$ perovskite films. $PC_{70}BM$ doped $CsFAPbI_3$ films showed a higher degree of oxygen-light tolerance when an appropriate amount of the electron acceptor was incorporated into the perovskite structure. Practically, the most optimal $PC_{70}BM$ concentration was found by doping the perovskite precursor solution with 40 µl of 0.2 $mgml^{-1}$ of $PC_{70}BM$: DMSO doping solution. The UV-vis and PL emission spectra of the most optimised $PC_{70}BM$ doped $CsFAPbI_3$ perovskite sample indicated that $PC_{70}BM$ acted as an additional source to extract photo-generated electrons from the perovskite to the ETL layer. The recombination lifetime of hole species of spiro-OMeTAD that deposited on top of the doped sample shown with TAS transfer kinetic were almost identical to a non-$PC_{70}BM$ doped film. Therefore, the presence of $PC_{70}BM$ did not hinder or alter the photogenerated charge transportation processes. At the end of this chapter, bulk heterojunction solar cells consisting of $PC_{70}BM$ doped $CsFaPbI_3$ as a photoabsorber were fabricated. The doped devices resisted oxygen-light degradation approximately two times longer than the un-doped bulk heterojunction $CsFaPbI_3$ reference device. The photoabsorber $PB_{70}BM$ doped $CsFAPbI_3$ films in particular exhibited a much higher oxygen-light stability. Much less relative superoxide generation yield was detected with the $PC_{70}BM$-doped $CsFAPbI_3$ films.

Therefore, the further oxygen-light stability enhancement of the $CsFAPbI_3$ absorber layer was implemented by doping the absorber layer with an appropriate amount of $PC_{70}BM$ dopant. The dopant

was hypothesized to migrate to any available vacancy sites (for examples. grain boundaries), and increase highly energetic charge from the absorber to the dopant. This can further reduce the superoxide formation yield within the absorber and results a high tolerant oxygen-light photoabsorber film. In this chapter, $CsFAPbI_3$ absorber solution was doped with an appropriate amount of $PC_{60}BM$ and $PC_{70}BM$ solution. $PC_{70}BM$ doped-$CsFAPbI_3$, in particular, exhibited outstanding oxygen-light stability. It is noted that appropriate $PC_{70}BM$ doped $CsFAPbI_3$ does not change the crystal structure of the absorber or its degradation pathway or obstruct its charge transfer after photo absorption.

6.2. Introduction

Phenyl-C61-Butyric acid methyl ester ($PC_{60}BM$) and *[6,6]-Phenyl-C71-butyric acid* methyl ester ($PC_{70}BM$) are widely used as electron acceptors in OPVs [153–156]. As explained previously in chapter two, $PC_{60}BM$ and $PC_{70}BM$ have many desirable properties when incorporated with P3HT (and many other electron donor polymers) to create sufficient energy offset in order to separate excitons after the photoexcitation process in P3HT:PCBM OPV systems. Here, PCBM also acted as electron accepting material to transfer the separated charges to the designated electrode. In this chapter, PCBM was incorporated as an additional electron accepting source in order to maximise the PSCs operational lifetime under constant exposure of visible light and oxygen. In general, PCBM has many desirable properties when used as a doping agent material for the perovskite system: 1.) The PCBM molecule is quite bulky, thus it does not alter the perovskite crystal structure (901.9 $gmol^{-1}$ and 1030.99 $gmol^{-1}$ for $Pc_{60}BM$ and $Pc_{70}BM$, respectively [157]) 2.) PCBM itself has an appropriate LUMO and HOMO level to act as an intermediate source to extract any excess photogenerated electrons (-6.1 eV and -3.7 eV for HOMO and LUMO level of $Pc_{60}BM$ while-5.9 and -3.9 eV are HOMO and LUMO energy level for $PC_{70}BM$, respectively [92]) 3.) PCBM molecules do not aggregate when it is heated below 100 ^{o}C [158,159] 4.) PCBM can be dissolved in DMSO mixture solution which is one of the solvents used to dissolve $CsFAPbI_3$ perovskite precursor solution (~0.2 mg of PCBM in 1 ml of DMSO[93,160]). According to all four desirable traits of PCBM, both $PC_{60}BM$ and $PC_{70}BM$ were used as a dopant for the $CsFAPbI_3$ perovskite solution before the annealing step of the photoabsorber layer. Therefore in this chapter, a different amount of PCBM dopant solution (0.2 $mgml^{-1}$ in DMSO) for each $CsFAPbI_3$ precursor solution from 0 µl to 100 µl with 20 µl interval increment was investigated and compared. The aim of chapter six is to find the optimal amount of PCBM dopant which will enhance light-oxygen stability of $CsFAPbI_3$ films and solar cells without altering the crystal structure of the perovskite.

6.3. Experimental

UV-vis, steady state PL measurement and TAS transfer kinetic spectra were also plotted and compared as each $CsFAPbI_3$ precursor solution was doped with a different amount of PCBM (0.2 mg in 1 ml of DMSO solution) from 0 µl to 100 µl with 20 µl increments. All $CsFAPbI_3$ based films were subjected to constant halogen lamp illumination (~20 $mWcm^{-2}$) and excess dry air flow throughout the entire experimental period. The superoxide measurement were not made possible in this part of the thesis due to the fact that PCBM is soluble in toluene solution.

Other characterisation techniques namely XRD, EDX and SEM, were performed for all fresh and air-light aged $CsFAPbI_3$ based samples to ensure that all lead trihalide films/solar cells underwent the same degradation pathway. In addition, there should not be any major initial crystal or phase change as the PCBM dopant was added to the photoabsorber films.

This chapter concludes with a PCE measurement comparison study between a reference $CsFAPbI_3$ (ITO/mp-TiO_2/$CsFAPbI_3$/spiro-OMeTAD/Au) and the most optimally PCBM doped bulk heterojunction solar cells (ITO/mp-TiO_2/PCBM-$CsFAPbI_3$/spiro-OMeTAD/Au).

6.4. Results and Discussions

In chapter six, 0.2 mg of either $PC_{60}BM$ or $PC_{70}BM$ was added in 1 ml DMSO solution in order to make a dopant solution. Firstly, the effect of dopant addition of $PC_{60}BM$ to the oxygen-light stability of $CsFAPbI_3$ was monitored via UV-vis absorbance (Figure 49 and 50a) and steady state PL (Figure 50b) comparison studies.

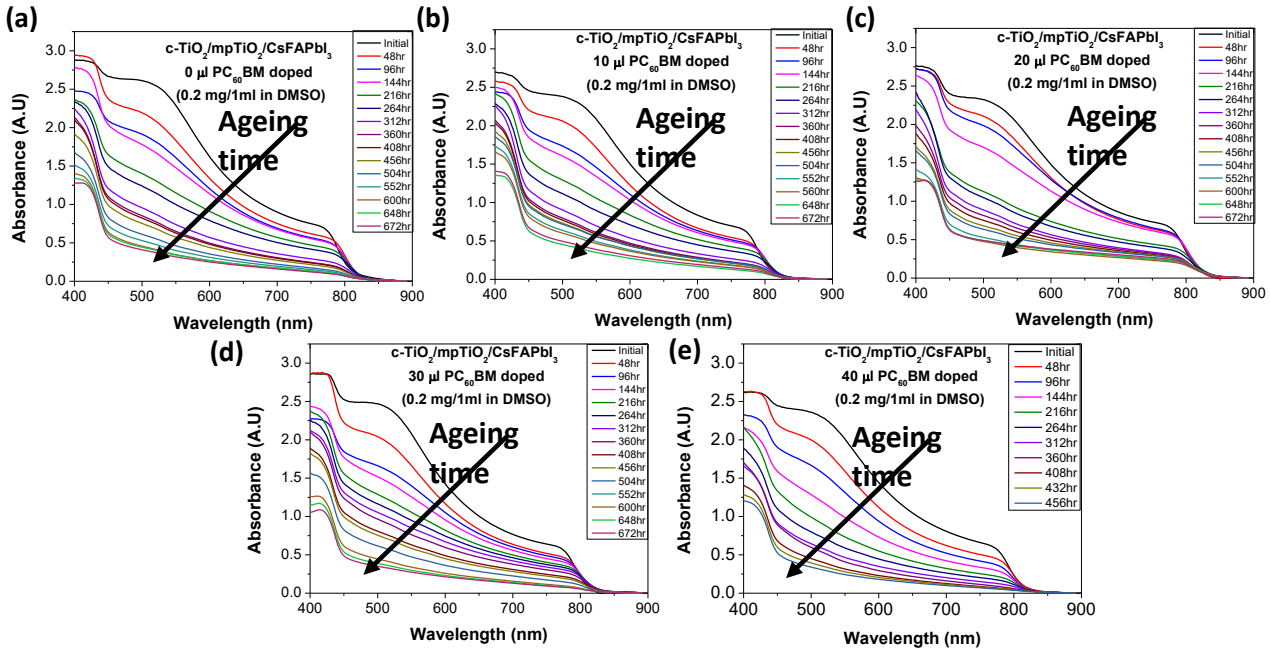


Figure 49: Absorbance spectra of c-TiO_2/mp-TiO_2/$CsFAPbI_3$ with and without $PC_{60}BM$/DMSO solution dopant (0.2 mg of $PC_{60}BM$ in 1 ml of DMSO). Each sample was doped with (a) 0 µl $PC_{60}PM$ (b) 10 µl $PC_{60}PM$ (c) 20 µl $PC_{60}PM$ (d) 30 µl $PC_{60}PM$ (e) 40 µl $PC_{60}PM$ doped dopant solution.

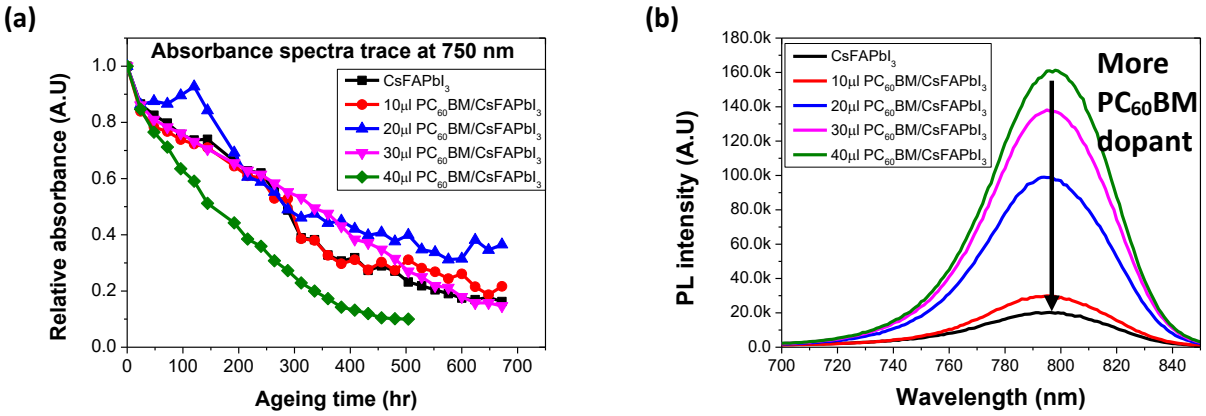


Figure 50: (a) UV-vis absorbance trace at 750 nm of c-TiO_2/$PC_{60}BM$-$CsFAPbI_3$ (b) steady state PL emission of c-TiO_2/PC60BM-$CsFAPbI_3$. Each CsFAPbI3 based film was doped with a different volume of the $PC_{60}BM$ DMSO solution.

Figure 50-a was derived from using an absorbance trace at 750 nm on each $CsFAPbI_3$ specimen. Figure 49-50 showed that the amount of the dopant does not help to remove any photo-generated electrons at the $CsFAPbI_3$-ETL interfaces. It was hypothesized that the $PC_{60}BM$ molecule is too bulky to fit in between the grain boundaries or other bulk defects within the $CsFAPbI_3$ structure. As a result, the $PC_{60}BM$ molecules impeded and stagnated any photogenerated electrons from transporting to the mp-TiO_2 layer. Therefore, the visual stability of $PC_{60}BM$ doped $CsFAPbI_3$ samples decreased as more dopant concentration was added into the $CsFAPbI_3$ precursor solution.

However, Kakavelakis et al. reported the air stable planer invert perovskite solar cell with reduced graphene oxide doped PCBM that could function as an electron transporting layer [161]. Here, the 5 % reduced graphene oxide-PCBM exhibited approximately 38 % more PL quenching compared to pristine PCBM films [161]. Perhaps, the reason why the $PC_{60}BM$ molecules did not assist the $CsFAPbI_3$ photo-generated electron to be quenched in this case was because the LUMO level in $PC_{60}BM$ was slightly higher than that for $PC_{70}BM$ (-3.9 eV compared with -3.7 eV).

On the other hand, $PC_{70}BM$ molecules could efficiently extract photogenerated electrons from the $CsFAPbI_3$ to the mp-TiO_2 layer. In order to pinpoint the optimum $PC_{70}BM$ dopant concentration, a wider dopant variation range was performed via UV-vis and steady-state PL emission which are shown in Figure 51.

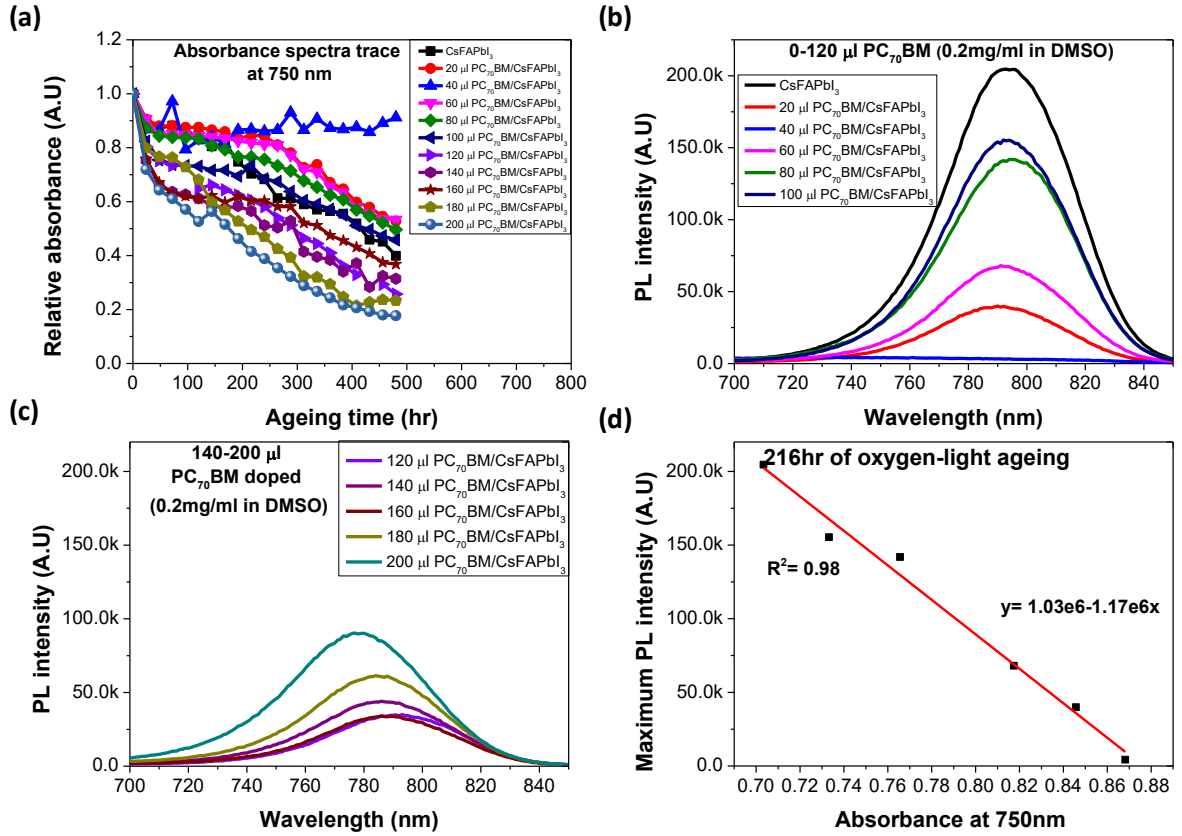


Figure 51: (a) absorbance traces of c-TiO_2/mp-TiO_2/$CsFAPbI_3$ films doped with different amounts of $PC_{70}BM$ at 750 nm (see legend). All samples were degraded under constant exposure of illumination and dry air (less than 10 ppm H_2O). (b) steady state PL emission of 0-100 µl $PC_{70}BM$ doped $CsFAPbI_3$ based samples. Here, the amount of the dopant concentration corresponded with the photo-generated electron extraction capability at the $CsFAPbI_3$-mp-TiO_2 interfaces. (c) steady state PL emission of 120-200 µl $PC_{70}BM$ (0.2 mg in 1ml of DMSO) doped $CsFAPbI_3$ based samples. Here, the peak of PL emission of the heavily $PC_{70}BM$ doped sample started to become blue-shifted. (d) maximum PL intensity vs the normalised absorbance linier relation graph after 216 hours of a constant tungsten halogen light (~20 $mWcm^{-2}$) and oxygen ageing. The Raw UV-vis absorbance data is supplemented in the SI sections.

The trends of absorbance instability were clearly separated into two groups. The appropriate amount of 40 µl $PC_{70}BM$ dopant into a $CsFAPbI_3$ precursor solution was found to be an optimal amount that retained the visual stability of the perovskite film via maximisation of photogenerated electron extraction capability at $CsFAPbI_3$-mp-TiO_2 interfaces. Figure 51-b and Figure 51-c clearly display an opposite trend in photo-generated electron quenching ability for each sample. In addition the blue-shifted in steady state PL emission took place when too much $PC_{70}BM$ dopant solution was added into the perovskite precursor solution. In this particular case, this effect induced more light and oxygen-instability to the $CsFAPbI_3$ films. In particular, 40 µl of $PC_{70}BM$ dopant (0.2 mg in 1 ml of DMSO) was concluded to be an appropriate amount of $PC_{70}BM$ that assists ETL to further enhance photo-generated electron to be extracted from the perovskite photoabsorber layer. From all these findings, the TAS transfer kinetics of 0-100 µl doped $PC_{70}BM$ –$CsFAPbI_3$ based samples were measured and compared in Figure 52.

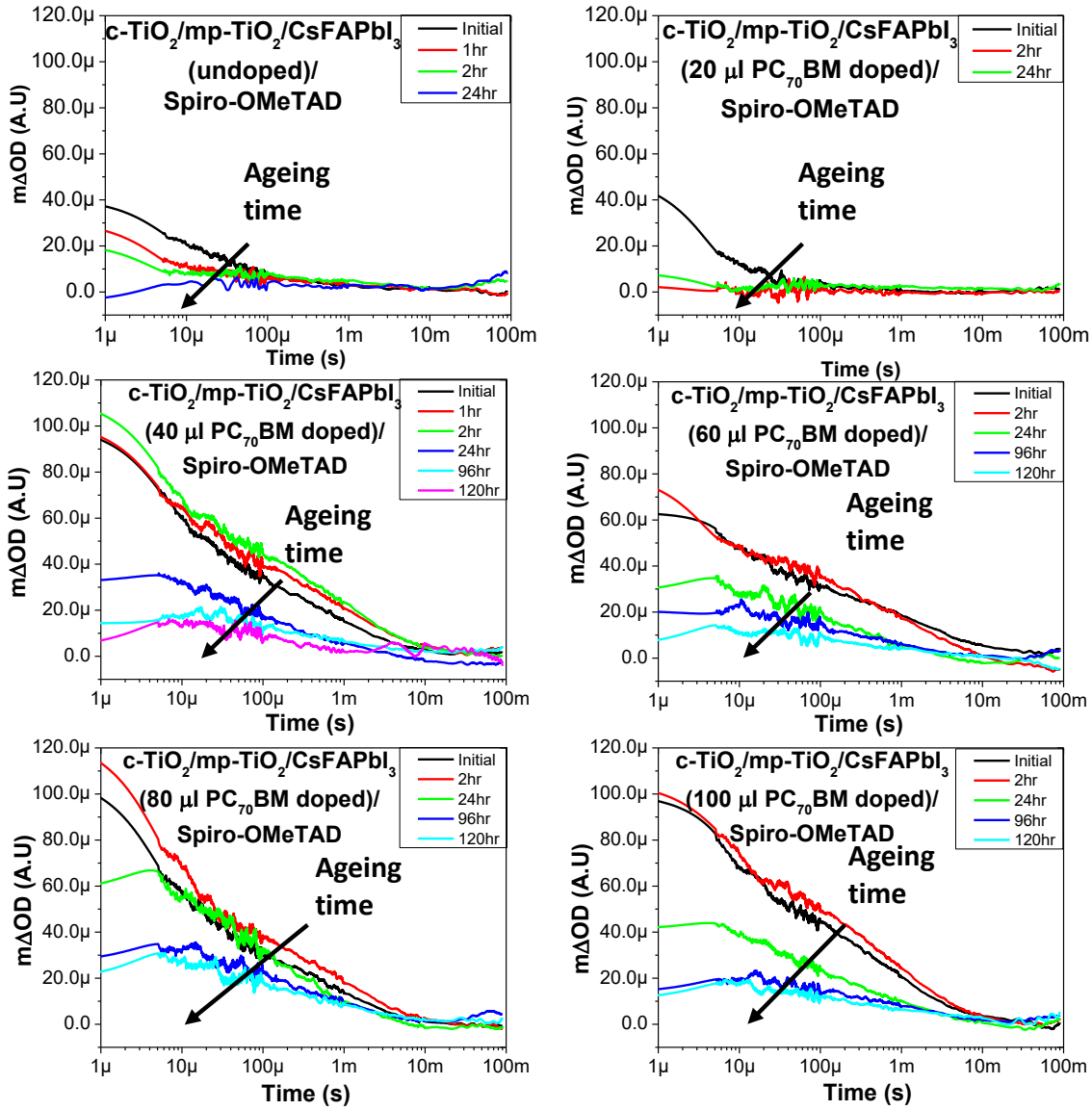


Figure 52: Transient charge kinetic of c-TiO_2/mp-TiO_2/$PC_{70}BM$ doped $CsFAPbI_3$spiro-OMeTAD as the dopant amount and oxygen-light ageing time was varied (see labels). All $CsFAPbI_3$ based samples were aged under constant 20 $mWcm^{-2}$ illumination with a halogen lamp and an excess flow of dry air. The signal was probed at 1,600 nm to track the hole recombination interaction in spiro-OMeTAD. Laser photo excitation was set at 510 nm with an energy density of approximately 25 μJcm^{-2}

Figure 52 clearly shows the hole recombination lifetime increased by approximately one order of magnitude after the appropriate amount of $PC_{70}BM$ was added into the perovskite precursor solution. In fact, a greater presence of $PC_{70}BM$ molecules within the $CsFAPbI_3$ film reduced the probability of the hole species to recombine with photogenerated electrons being transported from the $CsFAPbI_3$ to mp-TiO_2 layer. This experiment also indicated that the presence of $PC_{70}BM$ molecules within the $CsFAPbI_3$ did not impede charge extraction and the transportation process. In contrast, the dopant helped improve electron extraction capability at the photoactive-ETL interfaces which in turn helped

extend hole recombination lifetime when an appropriate volume of dopant solution was added into the $CsFAPbI_3$ based samples.

The XRD patterns for fresh and 648 hours of constant light-oxygen ageing on c-TiO_2/mp-TiO_2/$PC_{70}BM$-$CsFAPbI_3$ samples doped with different amounts of $PC_{70}BM$ were measured and overlaid (Figure 53). The identical XRD patterns of the undoped and doped $PC_{70}BM$ samples ensured that the incorporation of $PC_{70}BM$ did not alter the crystal structure of the $CsFAPbI_3$ perovskite. In addition, Figure 53 also reinforces the previous findings via the UV-vis and PL experiment that 40 µl of $PC_{70}BM$ dopant solution (0.2 mg in 1 ml DMSO) was the optimal dopant concentration. An additional XRD peaks from 20 to 40 °2Θ indicated various oxygen-light by-products of $CsFAPbI_3$ such as PbI_2, CsI and $CsPbI_3$.

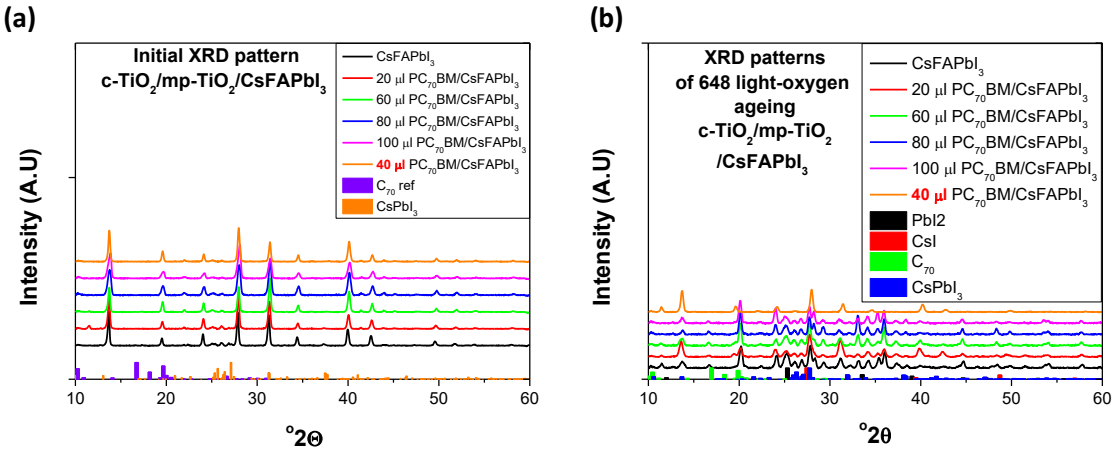


Figure 53: XRD patterns of (a) initial c-TiO_2/ mp-TiO_2/$CsFAPbI_3$ with different $Pc_{70}BM$ dopant content (see legend) (b) 648 hours light-oxygen aged c-TiO_2/ mp-TiO_2/$CsFAPbI_3$ under constant exposure of dry air and illumination (~20 $mWcm^{-2}$).

The top view SEM images (Figure 54) were carried out on fresh c-TiO_2/ mp-TiO_2/$CsFAPbI_3$ samples that were either undoped or doped with a different concentration of the $PC_{70}BM$ (from 0 µl to 100 µl) in order to rationalise and reinforce the previous UV-vis, TAS and XRD findings. In addition, the average crystal size of the $MAPbI_3$ grains were recorded in Table 6.

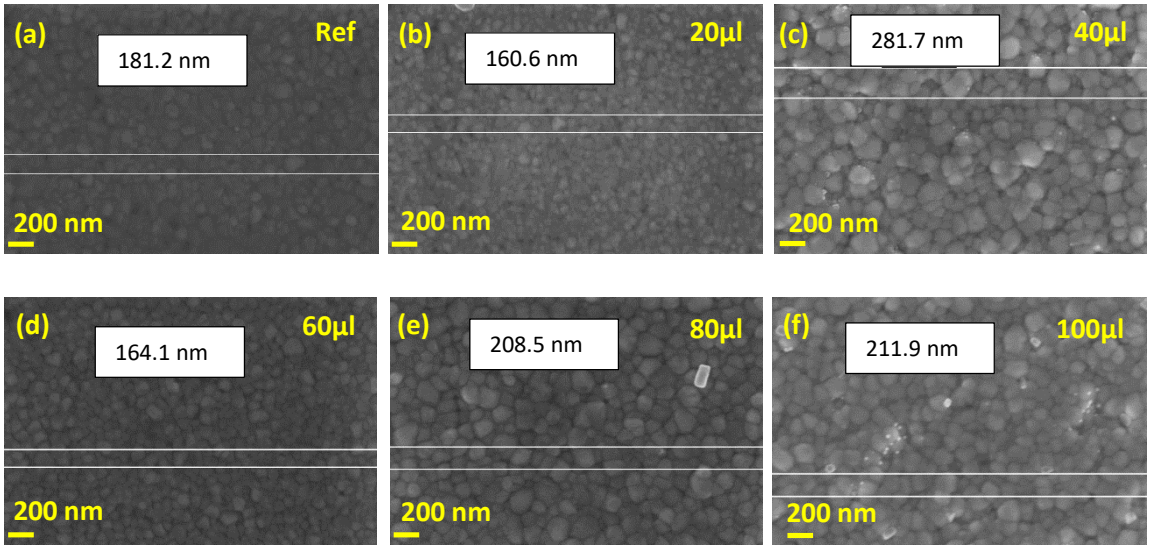


Figure 54: Top view SEM images of c-TiO_2/mp-TiO_2/$CsFAPbI_3$ while $PC_{70}BM$ dopant solution (0.2 mg of $PC_{70}BM$ in 1 ml of DMSO) is varied (see legend). The dopant is dissolved in DMSO solution at 0.2 $mgml^{-1}$. The crystal size increases upon dopant addition.

Table 6: Average crystal size of the $CsFAPbI_3$ upon $PC_{70}BM$ dopant addition (0.2 mg in 1 ml of DMSO). The average crystal sizes were maximised with 40 µl of the $PC_{70}CM$ dopant solution put into the $CsFAPbI_3$ precursor solution prior to the spin coating process of the photoactive layer.

$PC_{70}BM$ dopant volume in DMSO (0.2mg/ml)	Average crystal size (nm)
Reference	181.4 ± 2.09
20 µl	161.0 ± 1.93
40 µl	**287.0 ± 1.42**
60 µl	164.7 ± 1.60
80 µl	207.9 ± 1.79
100 µl	211.5 ± 0.99

The average crystal size on the $CsFAPbI_3$ perovskite samples was obtained by taking an average of 10 different measurements of each top view SEM image for $PC_{70}BM$ doped and undoped $PC_{70}BM$ $CsFAPbI_3$ samples. 40 µl – (0.2 $mgml^{-1}$ in DMSO)-$CsFAPbI_3$ displayed largest average crystal size within the tested top surface compared to other doped samples. The increment in average $CsFAPbI_3$ crystal sizes reflected the relative light-oxygen stability of the $CsFAPbI_3$perovskite layer. It was hypothesized that the presence of $PC_{70}BM$ molecules might assist $CsFAPbI_3$ to grow relatively larger compared with the undoped $CsFAPbI_3$ sample.

Chapter six is concluded by comparing optimally $PC_{70}BM$ doped-$CsFAPbI_3$ with an undoped $CsFAPbI_3$ bulk heterojunction solar cell (Figure 55). The reference $CsFAPbI_3$ solar cell consisted of ITO/c-TiO_2/mp-TiO_2/$CsFAPbI_3$/spiro-OMeTAD/Au while the optimally $PC_{70}BM$ doped-$CsFAPbI_3$ consisted of ITO/c-TiO_2/mp-TiO_2/40 µl $PC_{70}BM$ (0.2 mg/ml in DMSO)-$CsFAPbI_3$/spiro-OMeTAD/Au. Both specimens were subjected to a constant light exposure xenon lamp powered by equivalent white LED array

equipped with UV blocking filter with A.M 1.5 G illumination (100 mWcm-^{2}) and dry air continuously and simultaneously.

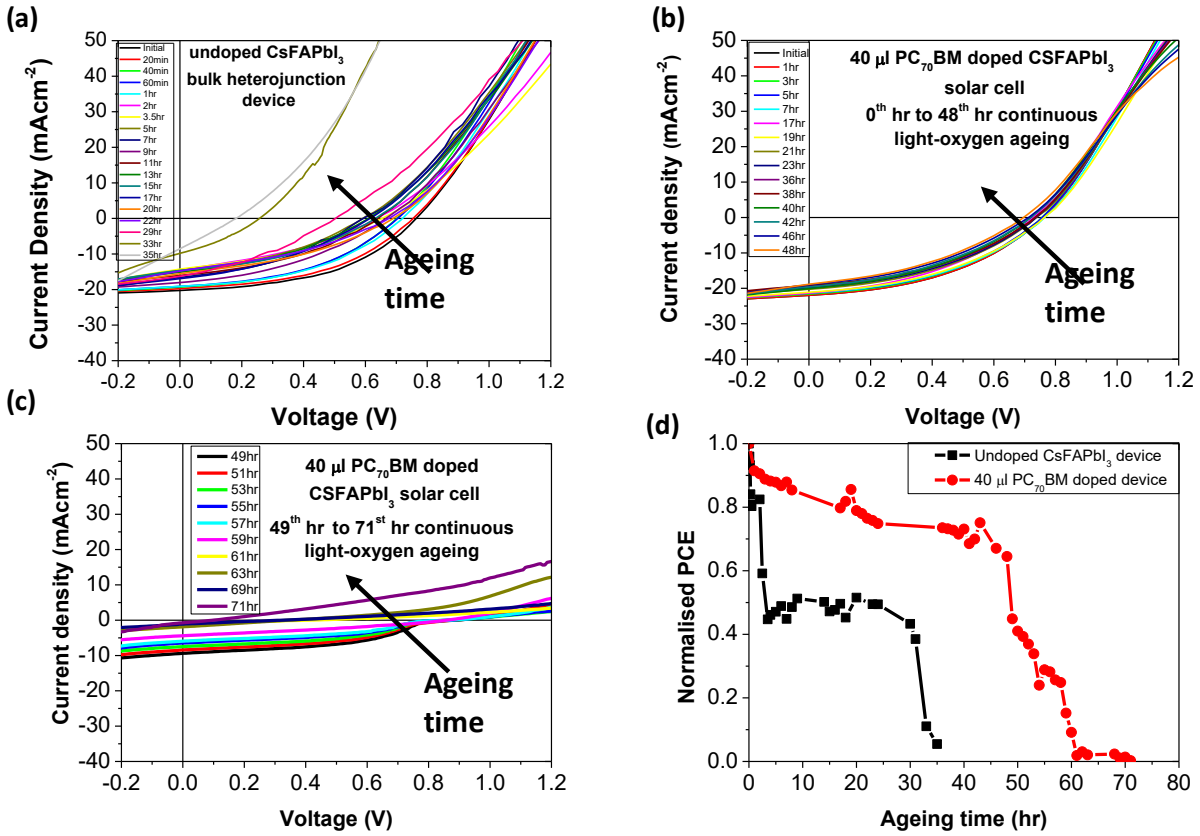


Figure 55 : (a) JV curves of ITO/c-TiO_2/mp-TiO_2/$CsFAPbI_3$/spiro-OMeTAD/Au reference solar cells (b) ITO/c-TiO_2/mp-TiO_2/$CsFAPbI_3$-40 µl doped $PC_{70}BM$ (0.2 mgml^{-1} in DMSO)/spiro-OMeTAD/Au from 0th hour to 48th hour under the testing conditions (c) The continuation of JV measurement over ageing time of the optimally doped $PC_{70}BM$-$CsFAPbI_3$ based solar cell under testing conditions from 49th hour to 71th hour (d) Normalised PCE traces of the undoped and optimally $PC_{70}BM$ doped-$CsFAPbI_3$ solar cells over ageing conditions. Both samples were exposed under constant exposure of dry air and AM 1.5 G with approximately 100 mWcm^{-2} irradiance powered by equivalent white LED array equipped with UV blocking filter. Each JV curve was obtained via a backward JV scan from 1.2 V to -0.2 V.

For the PCE comparison measurements between an undoped and optimally $PC_{70}BM$ doped (40 µl of 0.2 mg $PC_{70}BM$ in 1 ml of DMSO)-$CsFAPbI_3$ samples, the normalised PCE trace were plotted in Figure 55. Figure 55-d indicates that $PC_{70}BM$ dopant could indeed preserve overall PV performance of the perovskites while helping to prolong the operational lifetime of the device under constant light and oxygen exposure by approximately two times (38 hours and 71 hours for an optimally $PC_{70}BM$ doped-$CsFAPbI_3$ devices). Table 7 compared PCE, J_{sc} Voc and FF of the reference solar cell device and 40 µl $PC_{70}BM$ doped (0.2 mg/ml in DMSO) $CsFAPbI_3$ devices.

Table 7: Relevant PV parameters for ITO/c-TiO_2/mp-TiO_2/$CsFAPbI_3$/spiro-OMeTAD/Au reference solar cell device and ITO/c-TiO_2/mp-TiO_2/$CsFAPbI_3$-40 µl doped $PC_{70}BM$ (0.2 mg/ml in DMSO)/spiro-OMeTAD/Au devices. Total of six identical devices from each category were being measured simultaneously.

Initial PV parameters	Reference (undoped)	40 µl $PC_{70}BM$ doped (0.2 mg/ml in DMSO) solar cell
PCE (%)	7.34 ± 0.05	7.74 ± 0.04
J_{sc} ($mAcm^{-2}$)	20.25 ± 0.03	22.62 ± 0.03
V_{oc} (V)	0.76 ± 0.05	0.78 ± 0.07
FF	0.47± 0.06	0.43 ± 0.03

The initial PCE parameters of both the undoped and 40 µl $PC_{70}BM$ doped (0.2 mg in 1 ml DMSO)-$CsFAPbI_3$ bulk heterojunction solar cell device were shown in Table 7. The presence of an appropriate concentration of $PC_{70}BM$ molecules that were imbedded within the $CsFAPbI_3$ layer helped photogenerated electrons to be successfully extracted from $CsFAPbI_3$ to mp-TiO_2 more efficiently. Hence, J_{sc} of the optimally $Pc_{70}BM$ doped sample showed an increase from 20.25 to 22.62 $mAcm^{-2}$. In addition, the V_{oc} and FF value of the doped $CsFAPbI_3$ sample showed no significant shift which reinforced the previous finding from their XRD and TAS experiment that the existence of PCBM not only retains crystal structure of the perovskite photoabsorber but also helps extend harvested charge recombination lifetime after the photoexcitation process had taken place.

6.5. Conclusions

Chapter six continued to uphold the three ETL design guidelines that were established in Chapter five. In addition, chapter six provided the additional method in order to supress superoxide generation yield during the oxygen-light degradation of the $CsFAPbI_3$ films. This was made possible by mixing $PC_{70}BM$ dopant solution to the perovskite precursor before the perovskite film was spin-coated on the designated substrate. 40 µl of $PC_{70}BM$ dopant solution (0.2 $mgml^{-1}$ DMSO) in particular assisted the $CsFAPbI_3$ photoactive layer to extend its visual and charge transport capability. In addition, The XRD patterns and TAS kinetic spectra of the PCBM doped sample also provided a confirmation that the $PC_{70}BM$ dopant did not either alter crystal structure or hinder the charge transportation processes to the $CsFAPbI_3$ layer. The information provided by using top view SEM images of the $PC_{70}BM$ doped samples confirmed that the 40 µl $PC_{70}BM$ dopant (0.2 $mgml^{-1}$ DMSO) played an important role to increase average crystal sizes of the $CsFAPbI_3$ layer which potentially helped minimise the contacts of oxygen molecules surrounding the samples. It was hypothesized that $PC_{70}BM$ migrated and imbed themselves at any available bulk detects such as grain boundaries and act as an additional photo-electron acceptor sources.

7. Oxygen-light Stability Enhancement with Post Annealing Temperature Effect on Lead Trihalide Perovskite Films and Solar Cells

7.1. Abstract

In chapter six, the photogenerated electron extraction capability at the lead trihalide perovskite-mesoporous titiania interfaces was assisted by incorporating $PC_{70}BM$ molecules, which hypothesized to act as an additional electron acceptor source located at the grain boundaries of the photoactive layer in order to stagnate the oxygen-light degradation. In chapter seven, the core principle is to maximise intermolecular attraction of cations and anions within the perovskite crystal that surrounded each lead ion. By partially replacing some iodide ions with bromide ions to the lead trihalide photoabsorber molecule, the crystal integrity of the perovskite photoabsorber increased substantially; thus this led to more efficient PV devices with a better oxygen-light stability.

In addition, the effect of post annealing temperature to lead trihalide perovskite samples was investigated due to the fact that a continuous light exposure to a photodiode often caused the its inner temperature to rise to some extent. This phenomenon was replicated practically by varying post annealing temperature (from room temperature to 100 ^{o}C with 20 ^{o}C increments) of the lead perovskite trihalide tested samples while fixing all of their post annealing time to 30 minutes. Then the optical and electrical properties of each perovskite sample was compared individually. Here, an insight comparison of oxygen-light stability with post annealing temperature effect taken into account on the structural, optical and electrical properties of three different lead trihalide perovskite samples namely; $MAPbI_3$, $Cs_{0.17}FA_{0.83}PbI_3$, and $Cs_{0.17}FA_{0.83}Pb\ (I_{0.8}Br_{0.2})_3$, was made throughout this chapter. The oxygen-light stability comparison of each lead perovskite sample was assessed via three different spectroscopy techniques: ultraviolet-visible light absorbance spectra, photoluminescence emission of the superoxide HE probe solution and microsecond-transient absorption spectra of perovskite/spiro-OMeTAD. All spectra comparisons from three different experiments clearly indicated that $Cs_{0.17}FA_{0.83}Pb\ (I_{0.8}Br_{0.2})_3$ perovskite based films exhibited a higher degree of oxygen-light stability and tolerate a higher degree of the post annealing effect than $Cs_{0.17}FA_{0.83}PbI_3$ and $MAPbI_3$ based films, respectively. The chapter concludes by comparing the drop of PCE for all three bulk heterojunction lead trihalide perovskite devices. It was shown that $Cs_{0.17}FA_{0.83}Pb\ (I_{0.8}Br_{0.2})_3$ devices exhibited higher initial and more constant of power conversion efficiency values compared to $Cs_{0.17}FA_{0.83}PbI_3$ and $MAPbI_3$ devices.

7.2. Introduction

It is widely accepted that organic-inorganic perovskite solar cells (PSCs) have attracted significant research attention for their high PV performance in converting solar energy into electrical power with a Power conversion efficiency (PCE) exceeding 20 % [118]. However, there are many external factors that can diminish the PV performances of PSCs overtime such as moisture [120,125,126], UV illumination [121–123], and elevated temperature [120,128–130] and lastly, the combination of oxygen and visible light. Some of these factors such as UV light and moisture can be excluded or minimised during the upscaling fabrication process. Unfortunately, it has proven impossible to completely exclude all oxygen and visible light to be absent during the PSC mass production processes. Thus far, the effect of oxygen-light towards the optical and electrical stability of lead trihalide perovskite films and solar cells have been made throughout this thesis. Here, many oxygen-light stability enhancements to lead trihalide perovskite films/solar cells were employed. Two core principles used to maximise lead trihalide perovskite oxygen-light stability are: 1.) Maximising photo-generated electron extraction capability at the perovskite-ETL interfaces. 2.) Enhancing the intermolecular attractions between cations and lead ions by replacing methylammonium lead triiodide perovskite photoabsorber with caesium formamidinium lead trihalide perovskite photoabsorbers.

In this chapter, the effect of elevated temperature to the operational lifetime of lead trihalide perovskite films and solar cells was also taken into account alongside the oxygen-light induced degradation processes. During the past power conversion efficiency measurements of $CsFAPbI_3$ and $MAPbI_3$ based solar cells, the overall temperature within each device started to increase whenever they were being continuously exposed to AM 1.5 G illumination for long period of time. In order to simulate this effect and gain a better understanding on how it actually affects the optical and electrical stability of lead trihalide perovskite films/solar cells, an additional annealing step was implemented to three different lead trihalide perovskite films, namely MAPbI3, $Cs_{0.17}FA_{0.83}PbI_3$ and $Cs_{0.17}FA_{0.83}Pb(I_{0.8}Br_{0.2})_3$ after each photoactive layer was deposited. Each perovskite sample was subjected to a range of post annealing temperature from room temperature up to 100 °C with 20 °C increments for 30 minutes. Then the extent of optical and electrical stability of all perovskite samples was reflected by comparing their UV-vis absorbance trace, superoxide formation yield and the recombination lifetime of hole species in transfer kinetic spectra during the oxygen-light degradation process on each perovskite sample. The most oxygen-light stable and thermal-stable perovskite film was found to be $Cs_{0.17}FA_{0.83}Pb(I_{0.8}Br_{0.2})_3$ film. When the $Cs_{0.17}FA_{0.83}Pb(I_{0.8}Br_{0.2})_3$ samples were exposed to halogen light and oxygen, the films showed substantially less change in UV-vis absorbance, superoxide formation yield and TAS decay over 120 hours compared with those spectra changes observed in $Cs_{0.17}FA_{0.83}PbI_3$ and $MAPbI_3$, films, respectively.

Ultimately, the bulk heterojunction solar cells with each of three different perovskite photoactive layers were PCE measured and compared over time under a constant exposure of A.M 1.5G illumination and excess dry air flow as post annealing on each perovskite sample varies. In particular, $Cs_{0.17}FA_{0.83}Pb(I_{0.8}Br_{0.2})_3$ solar cells ($CsFAPb(I_{0.2}Br_{0.8})_3$ or $CsFAPb(IBr)_3$ in short) exhibited higher initial and better oxygen-light stability than $Cs_{0.17}FA_{0.83}PbI_3$ ($CsFAPbI_3$ in short) and $MAPbI_3$. It was shown that the optical and electrical stability was maximised with appropriate cation and halide substitutions.

7.3. Experimental

Perovskite based films and working bulk heterojunction solar cells consisting of one of the three photoactive lead perovskite layers: $MAPbI_3$, $CsFAPbI_3$ and $CsFAPb(I_{0.8}Br_{0.2})_3$ were oxygen-light degraded simultaneously under the identical degradation conditions. In chapter seven, three main spectroscopy techniques were employed in order to compare visual, electrical and thermal stability of these lead trihalide perovskite films and working solar cells: UV-vis, PL and TAS. The changes in absorbance, PL emission and TAS decay reflecting the operational lifetime of the perovskite samples were plotted and overlaid among each other after all perovskite samples were subjected to constant exposure of a tungsten halogen lamp (~20 $mWcm^{-2}$) and dry air. The thermal stability aspect in each perovskite sample was practically simulated by introducing an additional post annealing step after each photoactive film was deposited and cooled down for 30 minutes. This post annealing temperature range for all 3 perovskite photoactive layers varied from 0 ^oC to 100 ^oC with 20 ^oC interval. Each perovskite sample was post annealed for a fixed period of 30 minutes before taking each of the sample off the hotplate and letting it cool down. The subsequent layers such as spiro-OMeTAD and/or Au electrode were then deposited normally afterwards for the samples used for the TAS and PCE experiment, respectively.

The exact details regarding how each lead perovskite photoactive precursor solution was prepared and deposited on the mp-TiO_2 layers was stated back in chapter three.

Other characterisation methods such as XRD, EDX, and top view SEM were employed as the tools to rationalise the visual, electrical and thermal stability for all three types of lead trihalide perovskite films.

Chapter seven will be summarised by comparing PV performances among three different sets of the bulk heterojunction solar cells consisting of one of the three perovskites as a photoabsorber layer : 1.) ITO/mp-TiO_2/$MAPbI_3$/spiro-OMeTAD/Au 2.) ITO/mp-TiO_2/$CsFAPbI_3$/spiro-OMeTAD/Au 3.) ITO/mp-TiO_2/$CsFAPb(I_{0.8}Br_{0.2})_3$/spiro-OMeTAD/Au. Additionally, the perovskite photoactive layer in 1.), 2.) and 3.) were also being subjected to post annealing temperature at room temperature, 60 ^oC or 100 ^oC for

30 minutes during the solar cell fabrication processes. All tested solar cell devices were oxygen- AM 1.5 G light degraded continuously and their PCE values were tracked and compared.

7.4. Results and Discussions

The visual stability comparison of $MAPbI_3$, $CsFAPbI_3$ and $CSFAPb\ (I_{0.8}Br_{0.2})_3$ based films was made possible via tracking the drop in the UV-vis absorbance spectra under the subjection of post annealing and the oxygen-light degradation effect (SI section chapter seven). The films configuration composed of a glass/c-TiO_2/mp-TiO_2/lead trihalide perovskite photoactive layer. After the samples were completely degraded, each UV-vis absorbance was overlaid. Then, the vertical UV-vis trace at each absorption band edge (either 700 nm or 750 nm) was plotted in Figure 56 for all three types of lead trihalide perovskites.

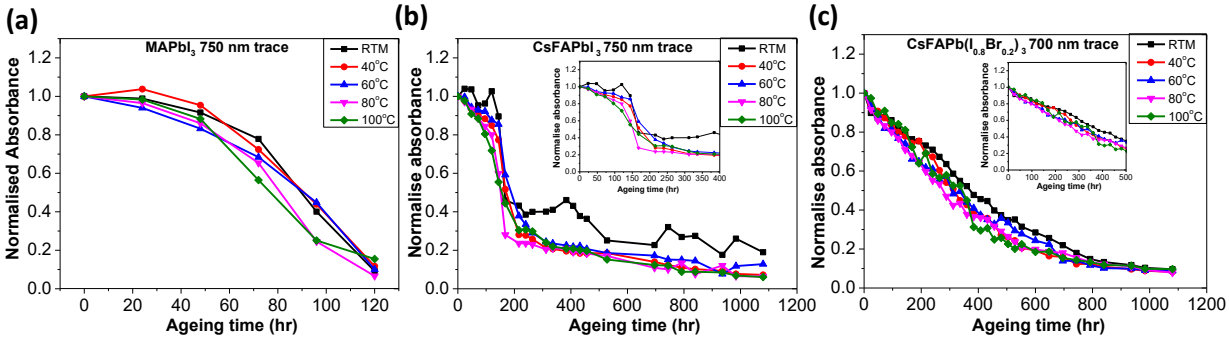


Figure 56: (a) 750 nm of UV-vis absorbance traces of glass/c-TiO_2/mp-TiO_2/$MAPbI_3$ with a different post annealing temperature (see labels) for 30 minutes (b) 750 nm of UV-vis absorbance traces of glass/c-TiO_2/mp-TiO_2/$CsFAPbI_3$ with a different post annealing temperature (see labels) for 30 minutes (c) 750 nm of UV-vis absorbance traces of glass/c-TiO_2/mp-TiO_2/$CsFAPb\ (I_{0.8}Br_{0.2})_3$ with different post annealing temperature (see labels) for 30 minutes. All samples were subjected to constant exposure of a tungsten halogen lamp (20 $mWcm^{-2}$) and excess dry air flow (less than 10 ppm of H_2O). The insets shown in (b) and (c) emphasize the initial oxygen-light degradation period. The raw absorbance data of each individual perovskite sample is located at the SI section.

The absorbance trace for $CsFAPb\ (I_{0.8}Br_{0.2})_3$ based samples exhibited a better oxygen-light stability and thermal stability compared with $CsFAPbI_3$ and $MAPbI_3$ based samples. This effect was attributed to the stronger intermolecular force of cation ions (Cs^+ and $FANH_3^+$) and halide (Br^- and I^-) to the lead ion. As a result, the crystal integrity of $CsFAPb\ (I_{0.8}Br_{0.2})_3$ photoabsorber was enhanced which ultimately led to a higher tolerance of oxygen-light degradation.

Unsurprisingly, the effect of post annealing for each perovskite sample for 30 minutes did not majorly affect the colour alteration or UV-absorbance shift of the perovskite photoactive layer. However, the yield of superoxide formation within each set of lead trihalide perovskite samples measured via PL

spectra was altered differently when the effect of post annealing temperature was implemented on the sample.

By comparing the increment of PL spectra (SI section chapter seven) at 610 nm of the HE solution probe of all lead trihalide perovskite samples (with 520 nm excitation wavelength), different superoxide evolution yields were detected for each set of perovskite photoabsorbers after an additional effect of post annealing temperature was to be implemented (Figure 57).

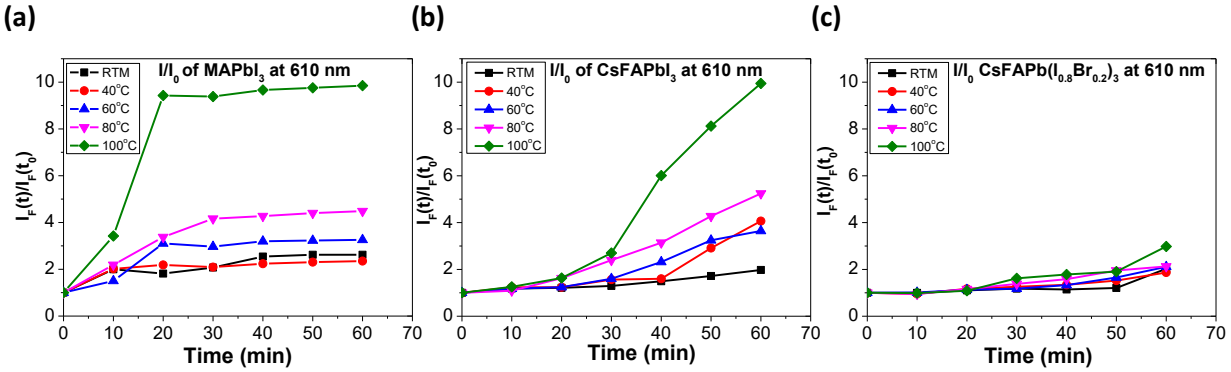


Figure 57: Superoxide measurement of three different set of lead trihalide perovskite based films: (a) glass/c-TiO_2/mp-TiO_2/$MAPbI_3$ (b) glass/c-TiO_2/mp-TiO_2/$CsFAPbI_3$ (c) glass/c-TiO_2/mp-TiO_2/CsFAPb $(I_{0.8}Br_{0.2})_3$. The superoxide generation yield on each sample was derived by tracking the evolution of luminescence hydroethedine (HE) probe solution that was highly emissive at 610 upon exposing it to the excitation wavelength of 520 nm. $I_F(t)$ was the maximum PL intensity at time t while $I_F(t_0)$ was the background fluorescence intensity at probe at t = 0. The ratio between the two represented the superoxide generation yield in each perovskite photoabsorber layer. Each perovskite film was subjected to a different post annealing temperature for 30 minutes (see labels). All perovskite samples were submerged in HE probe solution while being exposed to a constant tungsten halogen light (20 $mWcm^{-2}$) and oxygen over the course of one hour. The raw data within this figure is supplemented in the SI section.

Figure 57 compares superoxide generation yield of $MAPbI_3$, $CsFAPbI_3$ and CsFAPb $(I_{0.8}Br_{0.2})_3$ perovskite samples when each individual sample was subjected to a different post annealing temperature for 30 minutes from room temperature to 100 °C with 20 °C increments. It clearly indicated that CsFAPb $(I_{0.8}Br_{0.2})_3$ films generated a relatively lower amount of superoxide species at room temperature than $CsFAPbI_3$ and $MAPbI_3$, films over the course of one hour, respectively (black trace in Figure 57-a,b and c). In addition, CsFAPb $(I_{0.8}Br_{0.2})_3$ based films exhibited much higher thermal stability when the post annealing effect was implemented than $CsFAPbI_3$ and $MAPbI_3$, films, respectively. Here, the growth in superoxide formation yield upon increasing post annealing temperature to the CsFAPb $(I_{0.8}Br_{0.2})_3$ sample was found to be much less than the superoxide formation yield in $CsFAPbI_3$ and $MAPbI_3$ cases. This observation from the superoxide HE probe experiment indicated a sign of visual and thermal instability in the photoabsorber which consisted of weak link of cation components. The effect of post annealing temperature of oxygen-light lead trihalide perovskite became significantly clearer when the

TAS experiment was employed (Figure 58). Here, hole recombination lifetime was tracked via microsecond TAS spectra as each perovskite sample was subjected to constant light illumination, dry oxygen and the post annealing effect.

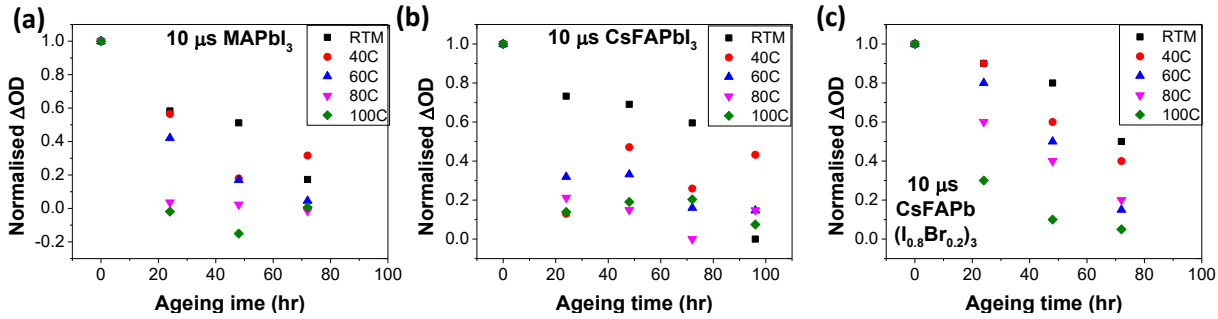


Figure 58: 10 µs of vertical trace of transient absorption spectra as a function of oxygen-light ageing time of (a) glass/c-TiO_2/mp-TiO_2/$MAPbI_3$ (b) glass/c-TiO_2/mp-TiO_2/$CsFAPbI_3$ (c) glass/c-TiO_2/mp-TiO_2/CsFAPb $(I_{0.8}Br_{0.2})_3$. Each perovskite film was subjected to a different post annealing temperature for 30 minutes (see labels). In addition, each sample was subjected to a constant tungsten halogen light (~20 $mWcm^{-2}$) and excess dry air flow (1 lpm). The signal was probed at 1,600 nm to track the hole recombination interaction in spiro-OMeTAD. Laser photo excitation was set at 510 nm with an energy density of approximately 25 μJcm^{-2}. Raw TAS data for every point is located in the SI sections.

Figure 58 shows the vertical trace at 10 µs of each microsecond TAS decay. The comparison of hole recombination lifetime in spiro-OMeTAD which was deposited on top of $MAPbI_3$, $CsFAPbI_3$ or CsFAPb $(I_{0.8}Br_{0.2})_3$ perovskite is displayed in this figure. CsFAPb $(I_{0.8}Br_{0.2})_3$ in particular tolerates oxygen-light as well as the post annealing effect much better than other samples which contained either $CsFAPbI_3$ or $MAPbI_3$ as its photoabsorber. This effect was attributed to a stronger intermolecular force between cation and anion ions within CsFAPb $(I_{0.8}Br_{0.2})_3$ perovskite structure. Thus, this increase intermolecular attraction within the perovskite crystal structure. As a result, both oxygen-light and thermal stability of CsFAPb $(I_{0.8}Br_{0.2})_3$ was found to be much higher than $CsFAPbI_3$ and $MAPbI_3$, respectively.

To ensure that all three types of lead trihalide perovskite were subjected to the same oxygen-light degradation pathways, SEM/EDX spectra was employed for each sample (data was plotted in SI section chapter 7). Table 8 to 10 summaries I:Pb atomic ratio of $MaPbI_3$, $CsFAPbI_3$ and CsFAPb $(I_{0.8}Br_{0.2})_3$ perovskite samples before and after oxygen-light degradation (120 hours) from room temperature to 100 ^oC, respectively.

Table 8: Relative atomic ratio of I:Pb for c-TiO_2/mp-TiO_2/$MAPbI_3$ samples before and after oxygen-light degradation (120 hours). Each EDX spectra is plotted in the SI section.

$MAPbI_3$	Initial			120 hr aged			
Temperature (°C)	I (at. %)	Pb (at. %)	I/Pb	I (at. %)	Pb (at. %)	I/Pb	**Difference between I/Pb**
RTM	76.1	23.9	3.18	68.28	31.72	2.15	**1.03**
40 °C	76.16	23.84	3.19	67.04	32.96	2.03	**1.16**
60 °C	76.8	23.2	3.31	68.91	31.09	2.22	**1.09**
80 °C	77.16	22.84	3.38	68.59	31.41	2.18	**1.19**
100 °C	74.2	25.8	2.88	66.63	33.37	2.00	**0.88**

Table 9: Relative atomic ratio of I:Pb for c-TiO_2/mp-TiO_2/$CsFAPbI_3$ samples before and after oxygen-light degradation (840 hours). Each EDX spectra is plotted in the SI section.

	Initial			840 hr aged			
Temperature (°C)	I (at. %)	Pb (at. %)	I/Pb	I (at. %)	Pb at. %)	I/Pb	**Difference between I/Pb**
RTM	78.15	21.85	3.58	72.29	27.71	2.61	**0.97**
40 °C	78.29	21.71	3.61	70.65	29.35	2.41	**1.20**
60 °C	78.21	21.79	3.59	74.21	25.79	2.88	**0.71**
80 °C	78.11	21.89	3.57	71.44	28.56	2.50	**1.07**
100 °C	78.11	21.89	3.57	70.83	29.17	2.43	**1.14**

Table 10: Relative atomic ratio of I:Pb for c-TiO_2/mp-TiO_2/CsFAPb $(I_{0.8}Br_{0.2})_3$ samples before and after oxygen-light degradation (840 hours). Each EDX spectra is plotted in the SI section

CsFAPb $(I_{0.8}Br_{0.2})_3$	Initial				840 hr aged				
Temperature (°C)	Br	I	Pb	I/Pb	Br	I	Pb	I/Pb	**Difference between I/Pb**
RTM	23.58	55.07	21.35	2.58	29.18	42.38	28.44	1.49	**1.09**
40 °C	22.56	56.07	21.37	2.62	24.58	48.42	27	1.79	**0.83**
60 °C	23.52	55.22	21.27	2.60	24.12	48.73	27.14	1.80	**0.80**
80 °C	23.36	55.99	21.66	2.58	25.96	47.3	26.74	1.77	**0.82**
100 °C	23.38	55.43	21.19	2.62	25.2	49.6	25.19	1.97	**0.65**

Table 8, 9 and 10 summarise the changes in EDX spectra when each lead triiodide perovskite sample was subjected to oxygen-light degradation until the sample coloration altered from black to yellow completely. This indicated a sign of the photoabsorber degradation process. The difference between I:Pb ratio and before and after the oxygen-light degradation process clearly confirmed a formation of the oxygen-light by-products such as PbI_2, Cs_xPbI_{3-x}, CsBr (which will be confirmed via XRD plotted in Figure 59. In general, a lower value of ΔI/Pb ratio was found when higher post annealed temperature

was imposed to all three types of the lead trihalide samples. This observation suggested that some of the oxygen-light degradation by-products are volatised and have already dissipated from the photoabsorber films after the photoabsorber was oxygen-light degraded completely.

In the next step, XRD patterns were obtained from the same set of perovskite samples consisting of one of the three lead trihalide perovskites as a photoabsorber. The existence of non-volatile by-products after oxygen-light degradation such as $CsPbI_3$, CsI, PbBr were detected by comparing the XRD patterns of each degraded film to the reference XRD patterns of all by-products (Figure 59).

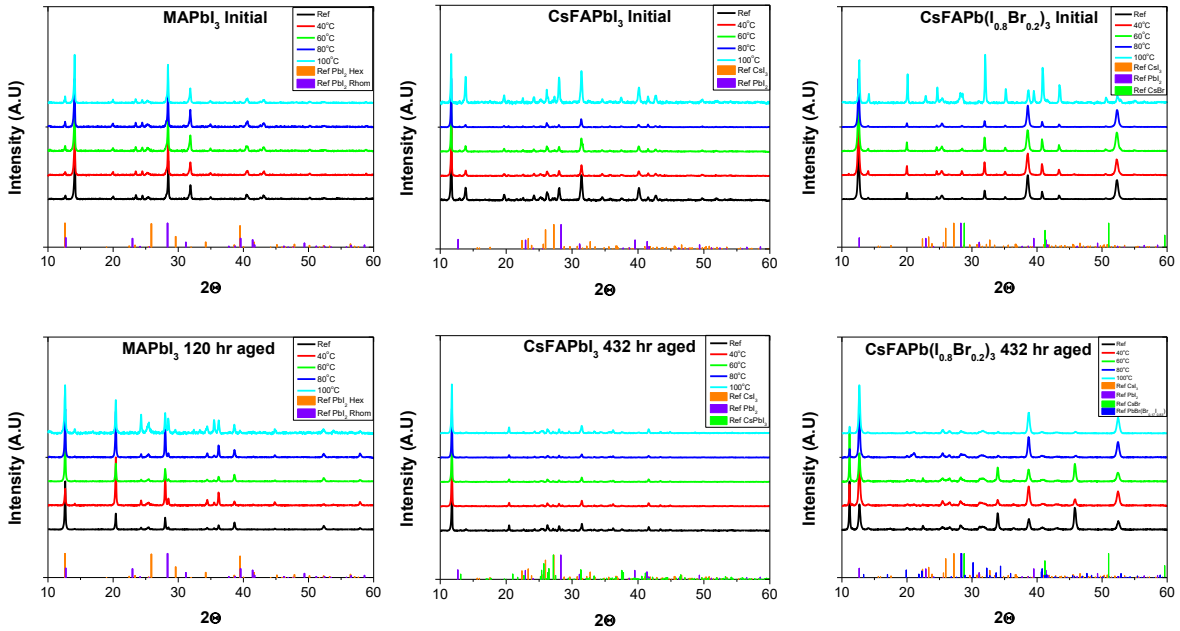


Figure 59: XRD patterns of initial and fully oxygen-light aged c-TiO_2/mp-TiO_2/perovskite samples (see labels). All $MAPbI_3$, $CsFAPbI_3$ or CsFAPb $(I_{0.8}Br_{0.2})_3$ samples were subjected to constant exposure of a tungsten halogen lamp (~20 $mWcm^{-2}$) and dry air. In addition, 30 minutes of post annealing was imposed on each lead perovskite sample for 30 minutes from RTM to 100 ^oC (see legends).

XRD patterns of fresh and fully oxygen-light degraded $MAPbI_3$, $CsFAPbI_3$ and CsFAPb $(I_{0.8}Br_{0.2})_3$ samples are shown in Figure 59. The initial XRD patterns of all perovskites samples were mostly identical when post annealing temperature of less than 60-80 ^oC was imposed on the perovskite samples. The additional peaks of $CsFAPbI_3$ and CsFAPb $(I_{0.8}Br_{0.2})_3$ sample with 100 ^oC thermal annealing located from 20-30 $^o2\Theta$ signified the formation of the meta-stable, non-volatile by-products such as CsI or PbI_2. The XRD patterns of the fully oxygen-light degraded perovskites samples indicate that post annealing temperature did not alter the oxygen-light degradation pathways but in fact assisted formation of the by-products when the input thermal energy was sufficient.

In order to visualise the damage caused by post annealing temperature, top view SEM were employed to all three lead trihalide perovskite samples (Figure 60-65).

c-TiO_2/mp-TiO_2/$MAPbI_3$

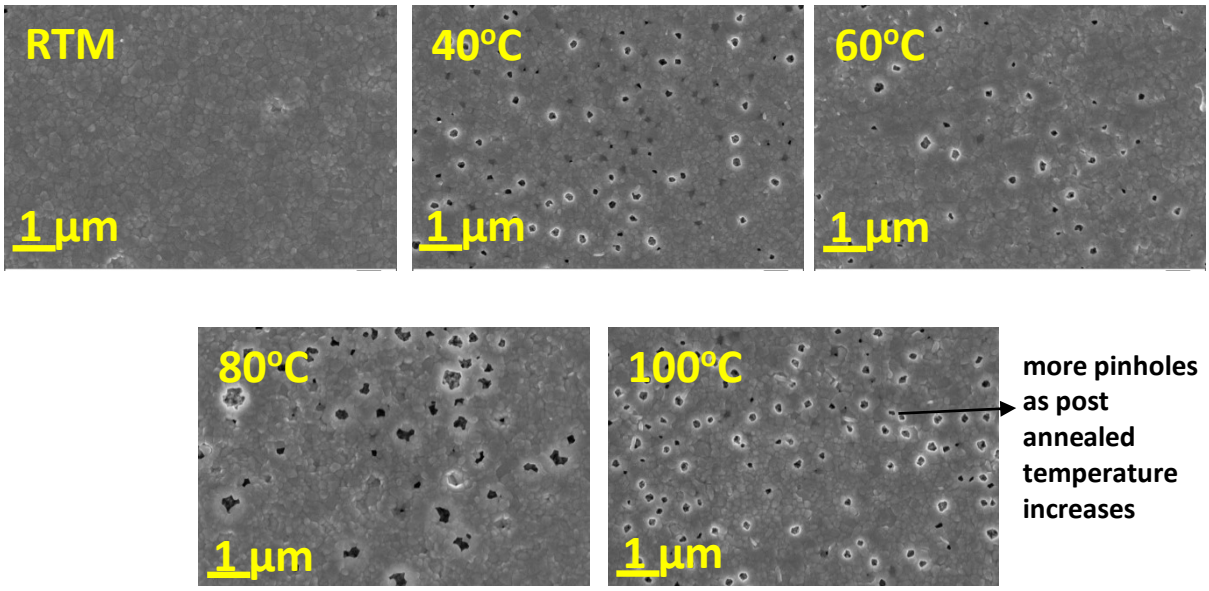


Figure 60: Top view SEM images of c-TiO_2/mp-TiO_2/$MAPbI_3$ before subjecting to oxygen-light degradation. Each sample was post annealed at different temperature (see labels) for 30 minutes.

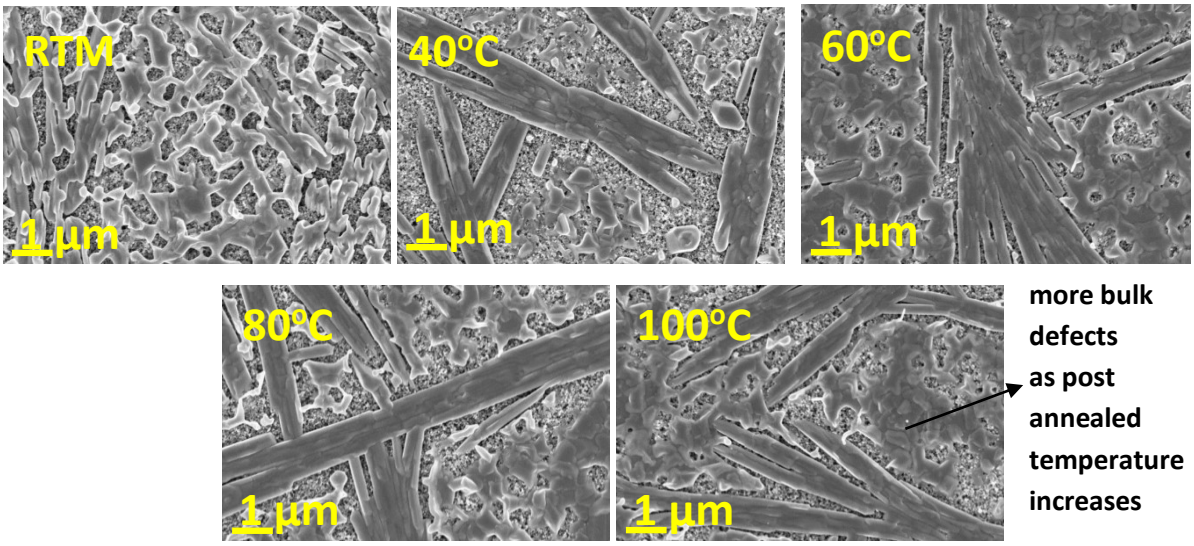


Figure 61: Top view SEM images of c-TiO_2/mp-TiO_2/$MAPbI_3$ after subjecting to oxygen-light degradation (120 hours). Each sample was post annealed at different temperatures (see labels) for 30 minutes.

Figure 60 and Figure 61 compare top view SEM images of the $MAPbI_3$ before and after the oxygen-light degradation process reached completion. An additional post annealing introduced pin-holes and bulk defects to the perovskite layers. As a result, both oxygen-light stability of $MAPbI_3$ decreased dramatically after a higher post annealing temperature was imposed on the sample.

c-TiO_2/mp-TiO_2/$CsFAPbI_3$

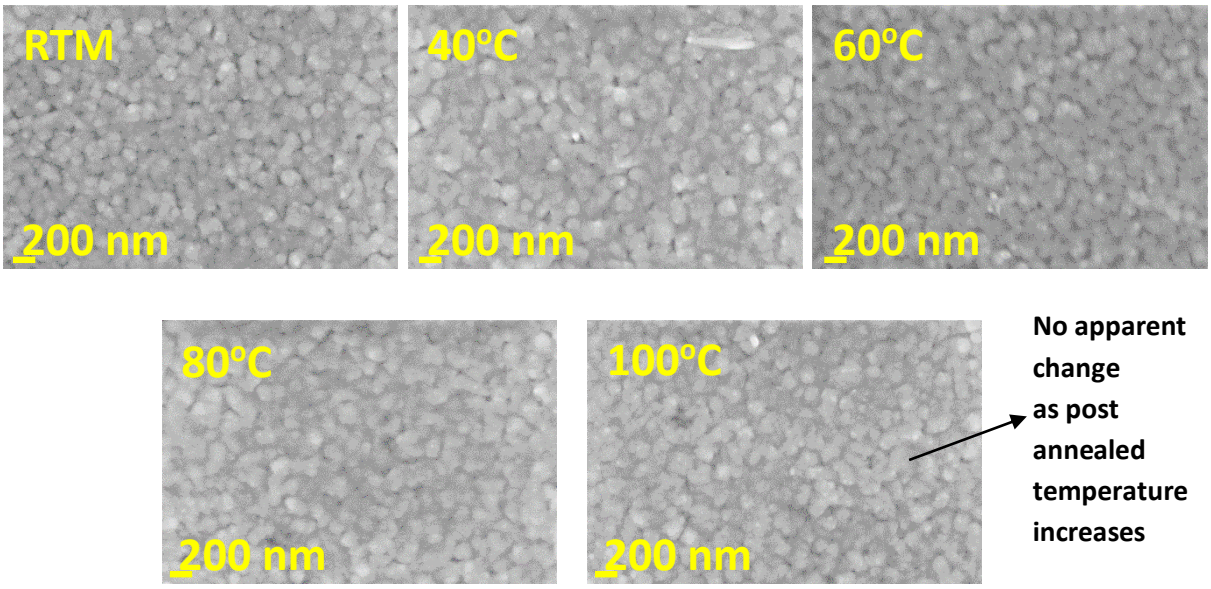


Figure 62: Top view SEM images of c-TiO_2/mp-TiO_2/$CsFAPbI_3$ before subjecting to oxygen-light degradation. Each sample was post annealed at a different temperature (see labels) for 30 minutes**.**

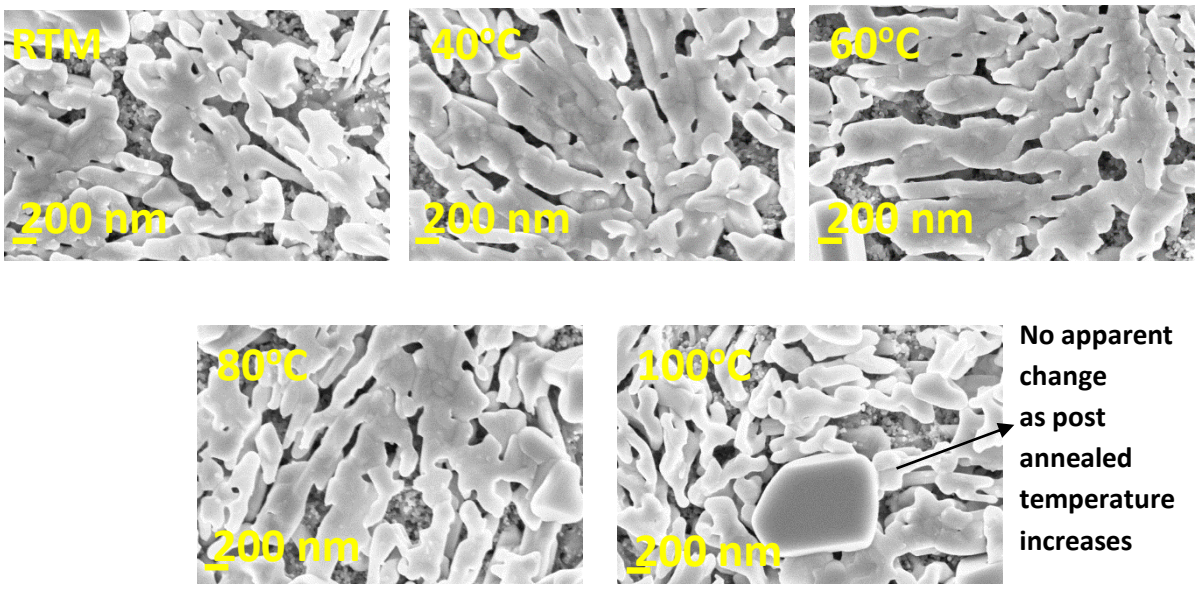


Figure 63: Top view SEM images of c-TiO_2/mp-TiO_2/$CsFAPbI_3$ after subjecting to oxygen-light degradation (696 hours). Each sample was post annealed at a different temperature (see labels) for 30 minutes.

The comparison between Figure 62 and Figure 63 indicated that $CsFAPbI_3$ did tolerate oxygen-light degradation and thermal annealling much better than $MAPBI_3$ perovskite photoabsorbers. However, the effect of post annealing temperature still introduceed noticable suface defects to $CsFAPbI_3$ layers. Hence, the oxygen-light degraded $CsFAPbI_3$ film with 100 °C post thermal annealing were much more rough than any other $CsFAPbI_3$ degraded samples.

c-TiO_2/mp-TiO_2/CsFAPb$(I_{0.8}Br_{0.2})_3$

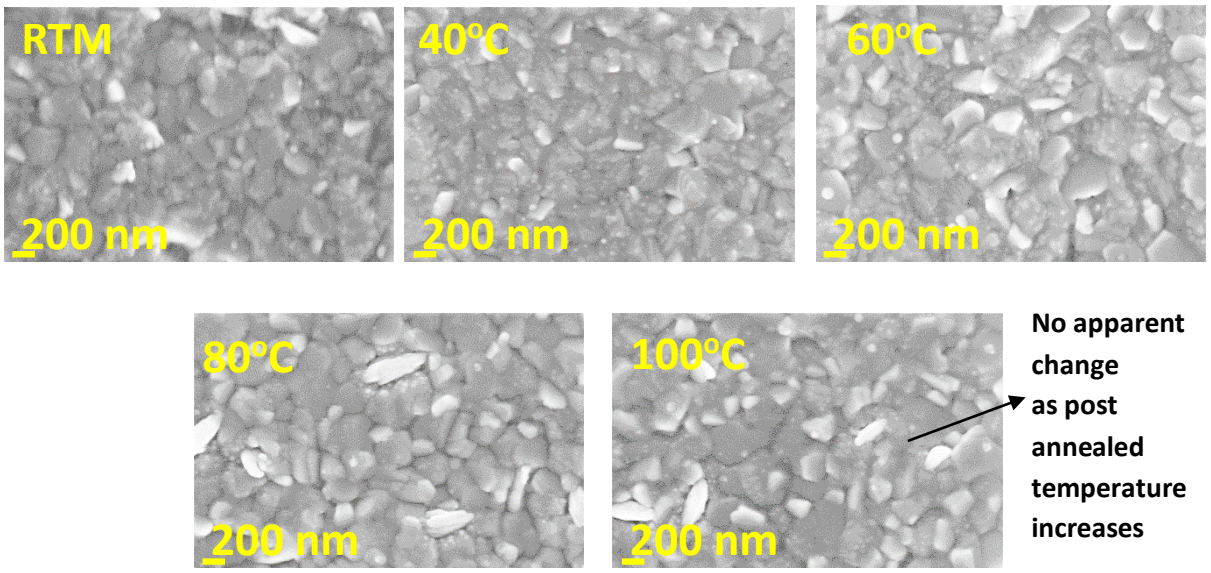


Figure 64: Top view SEM images of c-TiO_2/mp-TiO_2/CsFAPb $(I_{0.8}Br_{0.2})_3$ before subjecting to oxygen-light degradation. Each sample was post annealed at a different temperature (see labels) for 30 minutes**.**

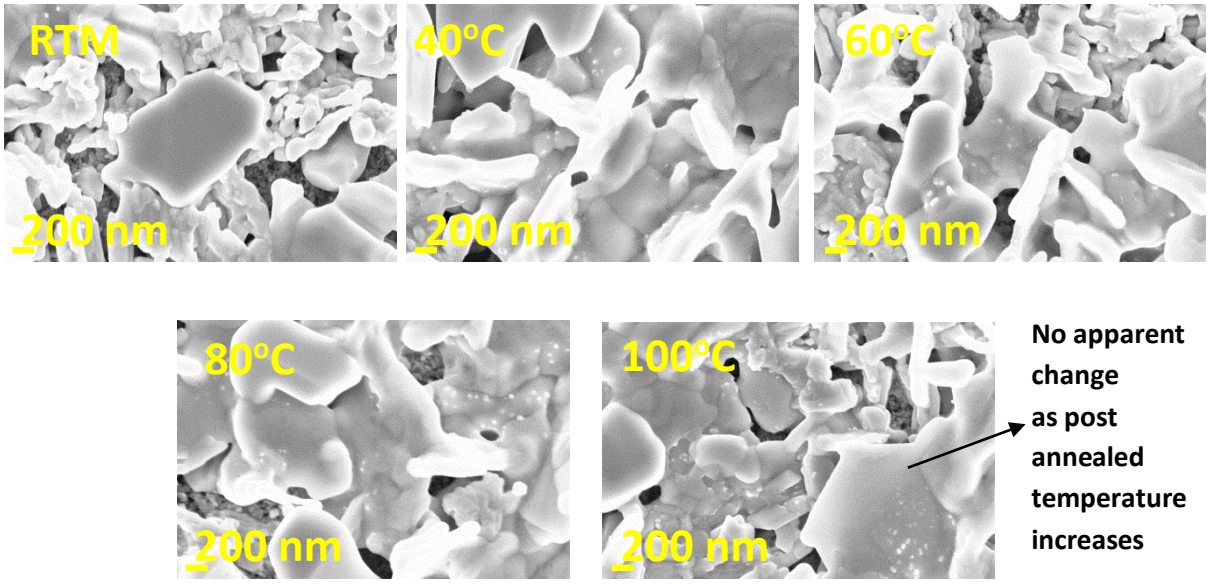


Figure 65: Top view SEM images of c-TiO_2/mp-TiO_2/ CsFAPb $(I_{0.8}Br_{0.2})_3$ after subjecting to oxygen-light degradation (696 hours). Each sample was post annealed at a different temperature (see labels) for 30 minutes.

Figure 64 and Figure 65 showed that the superoxide formation yield was kept at minimum for CsFAPb $(I_{0.8}Br_{0.2})_3$ samples. The top view of initial and oxygen-light fully degraded CsFAPb $(I_{0.8}Br_{0.2})_3$ films looked almost identical to each other as post annealing effect was taken into account during the perovskite fabrication process.

Chapter seven is enclosed by comparing JV curves of bulk heterojunction solar cells with three different lead trihalide perovskite photoabsorbers that were subjected to both oxygen-light degradation and post annealing effect. Their PCE values were tracked individually as a function of oxygen-light ageing time as shown in Figure 66.

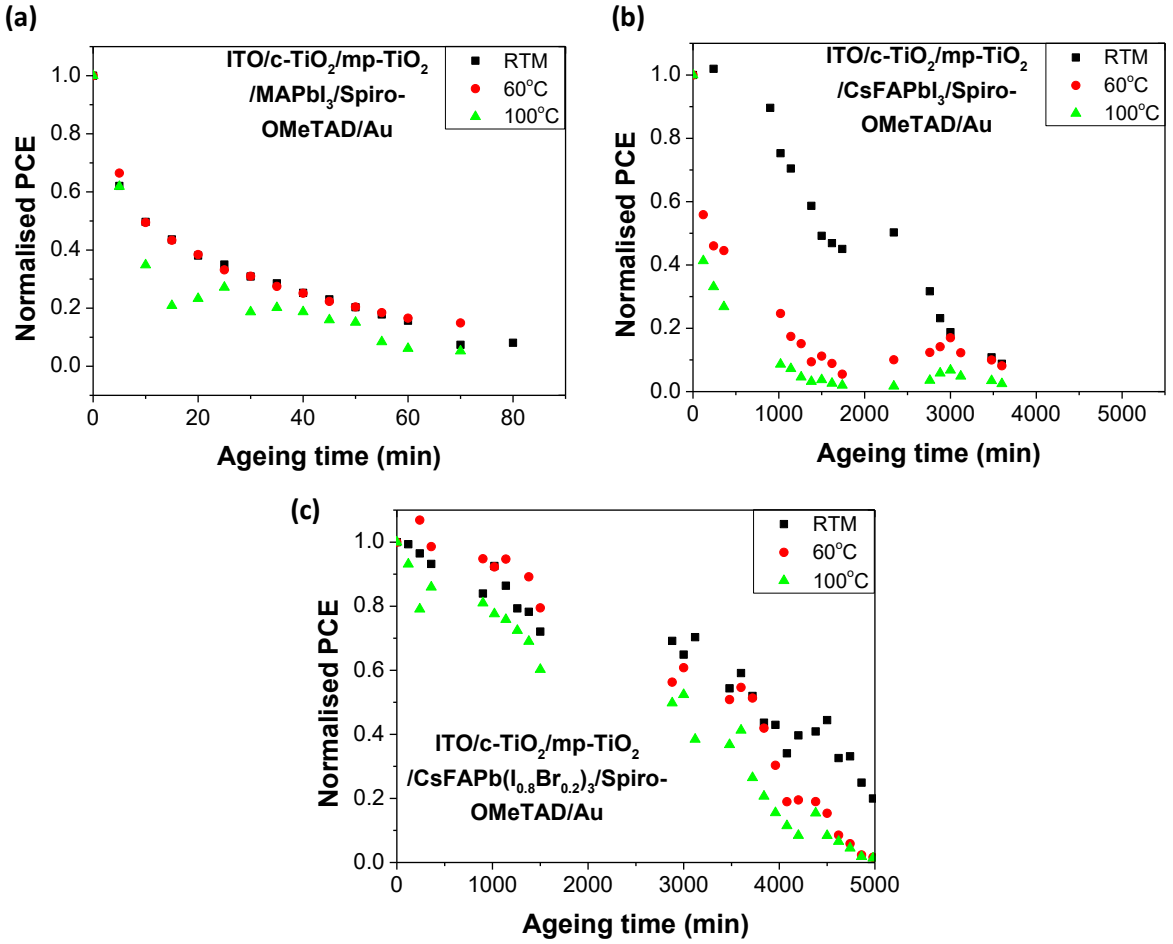


Figure 66: Normalised PCE traces over ageing conditions of (a) ITO/c-TiO_2/mp-TiO_2/$MAPbI_3$/spiro-OMeTAD/Au (b) ITO/c-TiO_2/mp-TiO_2/$CsFAPbI_3$/spiro-OMeTAD/Au (c) ITO/c-TiO_2/mp-TiO_2/ c-TiO_2/mp-TiO_2/ CsFAPb $(I_{0.8}Br_{0.2})_3$ /spiro-OMeTAD/Au. In addition, 30 minutes of post annealing to the perovskite photoabsorber was implemented during the device fabrication process (see legends). All samples were exposed under constant exposure of dry air and AM 1.5 G with approximately 100 $mWcm^{-2}$ irradiance powered by equivalent white LED array equipped with UV blocking filter. Each JV curve was obtained via a backward JV scan from 1.2 V to -0.2 V. Each JV curve which represents each point for all lead trihalide bulk heterojunction devices, is plotted in the SI section.

Then the important PV parameters such as J_{sc}, Voc, FF, PCE along with half life on each lead trihalide perovskite solar cells are summarised in Table 11.

Table 11: PV parameters for three lead trihalide perovskite bulk heterojunction solar cells. Six identical devices from each category were measured simultaneously however only the best performing devices from each category were being shown.

Samples		Initial				Final				
	Post annealing T (°C)	J_{sc}	V_{oc}	FF	PCE	J_{sc}	V_{oc}	FF	PCE	Half life (min)
ITO/c-TiO_2/mp-TiO_2/$MAPbI_3$/spiro-OMeTAD/Au	rtm	16.35	0.78	0.56	7.20	5.06	0.42	0.26	0.54	8
	60	18.03	0.77	0.54	7.51	3.31	0.35	0.28	0.33	8
	100	18.26	0.81	0.63	9.35	4.83	0.43	0.23	0.47	7
ITO/c-TiO_2/mp-TiO_2/$CsFAPbI_3$/spiro-OMeTAD/Au	rtm	16.30	0.87	0.56	7.90	6.77	0.42	0.25	0.70	1500
	60	7.71	0.76	0.47	2.79	3.12	0.31	0.23	0.23	240
	100	10.25	0.82	0.45	3.82	1.98	0.20	0.24	0.09	120
ITO/c-TiO_2/mp-TiO_2/ c-TiO_2/mp-TiO_2/ CsFAPb $(I_{0.8}Br_{0.2})_3$ /spiro-OMeTAD/Au	rtm	18.70	1.07	0.56	11.22	5.28	0.58	0.24	0.75	3720
	60	19.70	1.07	0.53	11.24	0.66	0.27	0.26	0.05	3480
	100	19.19	1.05	0.60	12.14	1.89	0.23	0.24	0.10	1620

Figure 65 and Table 11 compare three oxygen-light and thermal stability of three different lead halide bulk heterojunction solar cells : (a) ITO/c-TiO_2/mp-TiO_2/$MAPbI_3$/spiro-OMeTAD/Au (b) ITO/c-TiO_2/mp-TiO_2/$CsFAPbI_3$/spiro-OMeTAD/Au (c) ITO/c-TiO_2/mp-TiO_2/ c-TiO_2/mp-TiO_2/ CsFAPb $(I_{0.8}Br_{0.2})_3$ /spiro-OMeTAD/Au. These solar cells were subjected to a constant A.M 1.5 G illumination and excess dry air flow in between their PCE measurements. In particular, CsFAPb $(I_{0.8}Br_{0.2})_3$ perovskite devices which consisted of the strongest intermolecular bonding within their structure compared with $CsFAPbI_3$ and $MaPbI_3$ photoabsorber, respectively. Subsequently, better oxygen-light and thermal stability was attained for CsFAPb $(I_{0.8}Br_{0.2})_3$ based solar cells compared to the other two perovskite photoabsorbers. In addition, the suitable bromide substitution in CsFAPb $(I_{0.8}Br_{0.2})_3$ and post-thermal annealing induced a better morphology to the photoactive layer which resulted in its higher value of V_{oc}. However, excess post-thermal annealing temperature beyond 60 °C led to a substantially lower oxygen-light stability of the lead trihalide perovskite.

7.5. Conclusions

Chapter seven introduced the effect of post annealing effect alongside the oxygen-light degradation process to the $MAPbI_3$, $Cs_{0.17}FA_{0.83}PbI_3$ and $Cs_{0.17}FA_{0.83}Pb\ (I_{0.8}Br_{0.2})_3$ samples. During the fabrication process of the photoactive layer, an additional post annealing step with a range of temperature, varied from room temperature to 100 ^oC (with 20 ^oC increment) was imposed to the perovskite samples for 30 minutes. All spectroscopic results pointed to the same conclusion, that $Cs_{0.17}FA_{0.83}Pb\ (I_{0.8}Br_{0.2})_3$ film tolerated oxygen-light and post annealing effect much better than $Cs_{0.17}FA_{0.83}PbI_3$ and $MAPbI_3$ film, respectively. The data obtained from the PCE measurements of all three type of PSCs samples suggested that the effect of the post annealing improve the initial PCE of lead trihalide perovskite solar cells to some extent, however at the cost of lower long term oxygen-light stability.

8. Conclusions

During the past two decades, the solid state bulk heterojunction solar cell has been developed as a promising technology to conventional photovoltaics (PV). Recently, organic-inorganic lead halide perovskite solar cells (PSCs) have generated considerable research interest because of their rapid growth in power conversion efficiency. To date, the world record efficiency of PSCs has been updated from under 10 % to over 20 %. However, their poor operational stability impedes any further outdoor applications. PSCs tend to malfunction under exposure of many external factors such as moisture, temperature, UV-visible light, and oxygen, even though some of these external factors can be excluded relatively easy. For example, encapsulating PSCs under an inert atmosphere using glass as a barrier layer or using UV-coating on a glass surface. Unfortunately, it is almost impossible to completely separate oxygen, visible light and moisture from the actual fabrication processes of PSCs, especially where a high degree of production flexibility is needed and glass encapsulations are not viable. Therefore, the sensitivity of PSCs to environmental exposure, specifically to water and (or) oxygen, is still a main concern. In this doctoral thesis, the effect of atmospheric stability of organo-inorgano lead perovskite based films and solar cells under subjection to constant exposure of visible light and oxygen was thoroughly studied. One of the main aim of this thesis has been to enhance oxygen-light stability of these lead trihalide based perovskite films and solar cells.

It has been established that lead trihalide perovskite films required a combination of oxygen and visible light in order to degrade and cease to function as a photoabsorber material. The proposed oxygen-light degradation reaction involved three main steps: 1.) Photoexcitation reaction within the lead trihalide perovskite film 2.) Superoxide formation via the interaction between oxygen molecules and the photogenerated electrons that were yet to be harvested from the lead trihalide perovskite film 3.) Apply~~ing~~ the ETL design guideline 1.) and 2.) to caesium formamidinium lead triiodide perovskite films and solar cells which exhibit a higher degree of oxygen-light tolerant. The thesis started off by solidifying the foundation of these oxygen-light degradation reactions via three spectroscopic techniques, namely ultraviolet-visible light (UV-vis) absorption spectroscopy, photoluminescence (PL) emission of Hydroethedine probe solution and microsecond transient absorption (TAS) spectroscopy. The spectroscopic changes of UV-vis, PL and TAS caused by this oxygen-light degradation of $MAPbI_3$ based films were seen to be interrelated. It was also found that the change in these three spectra types was at minimum when superoxide formation has been supressed. Practically, this effect was achieved by selecting a suitable electron extraction layer (ETL) in order to efficiently extract more photogenerated electrons from $MAPbI_3$ layer after photoexciation reaction took place.

Based on earlier findings and established oxygen-light degradation mechanisms, the ETL design guidelines to fabricate lead trihalide perovskite based films and solar cells was made. The two core principles of this ETL design guideline involved maximising electron extraction at perovskite-ETL interfaces and enhancing intermolecular attraction between cation ions and lead ions by replacing a methylammonium lead triiodide perovskite photoabsorber to a caesium formamidinium lead trihalide perovskite film. The design guideline consisted of three main approaches: 1.) selecting suitable ETL such as SnO_2 over TiO_2 and ZnO, respectively; this being due to the lower conduction band edge in SnO_2 2.) maximising mesoporous titiania (mp-TiO_2) – $MAPbI_3$ 3.) applying ETL designing guideline 1.) and 2.) to a more oxygen-light stable lead trihalide perovskite, namely caesium formamidinium lead triiodide perovskite in order to maximise the oxygen-light operational lifetime of the PSC films and solar cells. The most oxygen-light stable lead trihalide perovskite films/solar cells were found when all three design guidelines were incorporated. The most optimal lead trihalide perovskite bulk heterojunction solar cells were found to resist oxygen-light degradation six times longer than the non-optimised $MAPbI_3$ reference solar cell.

An alternative approach to maximise photo-generated electrons extraction was to introduce during the lead trihalide perovskite spin-coating process. Here, Phenyl-C61-Butyric acid methyl ester ($PC_{60}BM$) or [6,6]-Phenyl-C71-butyric acid methyl ester ($PC_{70}BM$) dopant solution (0.2 $mgml^{-1}$ in Dimethyl Sulfoxide, DMSO) was added appropriately. In particular, it was found that 40 µl of this $PC_{70}BM$ dopant solution resulted in much better oxygen-light stable lead trihalide perovskite films and solar cells. It was hypothesized that $PC_{70}BM$ molecules sit at the bulk defect sites such as grain boundaries within the photoabsorber and act as an alternate electron accepter source when the photoexcitation process takes place within the photoabsorber layer. As a result, superoxide formation of the $PC_{70}BM$-lead halide perovskite films/solar cells was kept at minimum. The most optimally $PC_{70}BM$ doped-lead trihalide perovskite solar cell remained in operational condition as a photodiode roughly two times longer than the undoped reference lead trihalide perovskite devices (~70 hours compared with ~30 hours, respectively).

Lastly, the effect of the post annealing was taken into account along with the oxygen-light degradation process for a more realistic degradation profile. Inevitably, the inner thermal temperature within bulk heterojunction lead trihalide perovskite solar cells will rise after being subjected to an extend period of light conversion processes. This effect was simulated to the photoactive film by post annealing each lead perovskite sample from room temperature to 100 ^oC with 20 ^oC intervals. three types of lead trihalide perovskite photoactive layers were compared, which were $MAPbI_3$, $Cs_{0.17}FA_{0.83}PbI_3$ and $Cs_{0.17}FA_{0.83}Pb\ (I_{0.8}Br_{0.2})_3$. Specially, $Cs_{0.17}FA_{0.83}Pb\ (I_{0.8}Br_{0.2})_3$ based films displayed a much lower drop in

UV-vis absorbance, lower superoxide formation rate and longer hole recombination lifetime when the photoabsorber was subjected to constant oxygen-light degradation compared with $Cs_{0.17}FA_{0.83}PbI_3$ and $MAPbI_3$ based samples, respectively. As a result, the solar cell consisting of $Cs_{0.17}FA_{0.83}Pb(I_{0.8}Br_{0.2})_3$ resisted post-thermal annealing and oxygen-light degradation effects much better than solar cells with photoabsorbers made from either $Cs_{0.17}FA_{0.83}PbI_3$ or $MAPbI_3$ (~80 hours, ~60 hours and ~2 hours, respectively).

9. Outlooks

Up until this point, a direct correlation has been established between superoxide generation yield of lead trihalide perovskite films and theirs oxygen-light stability. From this correlation, the oxygen-light stability of the lead trihalide perovskite solar cell can be enhanced based on number of techniques such as $PC_{70}BM$ doping or crystal structure manipulation via the partial substitution of cadmium and bromide within the lead trihalide perovskite. However, there are still rooms for improvement for the studies of perovskite solar cells that are yet to be explored in the thesis due to the lack of time. For future work, there are three main topics that should be investigated in order to elevate the studies of atmospheric stability of the PSCs.

The first point being that lead trihalide perovskite films and solar cells should be fabricated on bigger glass substrates. Throughout the thesis, each perovskite film and solar cell was spin-coated on the 1.2 cm x 1.2 cm instead of 1 inch x 1 inch glass substrate. In order to made the concept of upscaling the production of perovskite solar cells more realistic, the oxygen-light degradation of lead trihalide perovskite should be explored with the biggest substrate available in the lab.

The second point being that the atmospheric moisture content should be varied as oxygen-light degradation of the lead trihalide perovskite took place. This concept could be made possible by integrating the moisture vapour monitoring unit when oxygen-light degradation is happening. This will make the degradation processes of lead trihalide perovskite more realistic.

The third point being that the atmospheric stability of alternate non-toxic PSCs material such as tin or bismuth based perovskite solar cells should be explored. The big advantage of using more environmental friendly based perovskite solar cells translates to a reduction of the production cost of PSCs. It would be interesting to compare the oxygen-light stability of lead trihalide perovskite solar cells to these alternative PSCs.

10. References

1. Statista 2018. Primary energy consumption worldwide from 2005 to 2016, by fuel type (in million tons oil equivalent). *2016* 1 (2016). doi:https://www.statista.com/statistics/265619/primary-energy-consumption-worldwide-by-fuel/

2. Birol, F. Key World Energy Statistics 2017. *Int. Energy Agency* 80 (2017).

3. ITCA. The Sun As A Source Of Energy. *Itaca* 4 (2008). Available at: http://www.itacanet.org/the-sun-as-a-source-of-energy/part-2-solar-energy-reaching-the-earths-surface/.

4. World Energy Council. Energy Resources: Solar. *World Energy Counc. 2013 World Energy Resour. Sol.* 1–28 (2013). doi:https://www.worldenergy.org/wp-content/uploads/2013/10/WER_2013_8_Solar_revised.pdf

5. Ma, Y. *et al.* Recent Research Developments of Perovskite Solar Cells. *Chinese J. Chem.* (2014). doi:10.1002/cjoc.201400435

6. National Renewable Energy Laboratory. Research Cell Record Efficiency Chart. *Best Research Cell Efficiencies* (2016).

7. Feynman, R. Semiconductor. *1963* 1 (1963). doi:https://en.wikipedia.org/wiki/Semiconductor

8. Massimi, M. *Pauli's Exclusion Principle*. *Pauli's Exclusion Principle* **9780521839**, (2005).

9. Condon, E. U. & MacK, J. E. An interpretation of Pauli's exclusion principle. *Phys. Rev.* **35**, 579–582 (1930).

10. T. Cazenave1 and P. L. Lions. Orbital Stability of Standing Waves for Some Nonlinear Schrodinger Equations Ml. *Commun. Math. Phys.* **85**, 549–561 (1982).

11. Atkins, P. & Paula, J. De. Atkins' Physical chemistry 9th edition. *Chemistry (Easton).* 430–468 (2009). doi:10.1021/ed056pA260.1

12. B. Van Zeghbroeck. Chapter 2: Semiconductor Fundamentals. 1 (2011). doi:http://ecee.colorado.edu/~bart/book/book/chapter2/ch2_3.htm

13. Stirling, U. 2.5.5. Derivation of the Fermi-Dirac distribution function. 1 doi:https://ecee.colorado.edu/~bart/book/book/chapter2/ch2_5.htm#2_5_1

14. Kittel, C., Kroemer, H. & Scott, H. L. Thermal physics - Kittel.pdf. 473 (1980).

15. Tung, R. T. The physics and chemistry of the Schottky barrier height. *Appl. Phys. Rev.* **1**, (2014).

16. Singh, J. Semiconductor Devices: Basic Principles. in *Semiconductor Devices: Basic Principles* 51 (2001).

17. Singh, J. *Electronic and optoelectronic properties of semiconductor structures*. *Arbor Ciencia Pensamiento Y Cultura* (2003). doi:10.1017/CBO9780511805745

18. Singh, J. *Semiconductor optoelectronics: physics and technology*. *McGraw-Hill series in electrical and computer engineering.$pElectronics and VLSI circuits* (1995).

19. Chapin, D. M., Fuller, C. S. & Pearson, G. L. A new silicon p-n junction photocell for converting solar radiation into electrical power [3]. *Journal of Applied Physics* **25**, 676–677 (1954).

20. Deshayes, Y. & Béchou, L. State-of-the-Art of Infrared Technology. *Reliab. Robustness Fail. Mech. LED Devices* 1–44 (2016). doi:10.1016/b978-1-78548-152-9.50001-8

21. Sood, A. K. *et al.* Development of low dark current SiGe-detector arrays for visible-NIR imaging sensor. *Proc. SPIE - Int. Soc. Opt. Eng.* **7660**, 76600L-76600L–7 (2010).

22. Smets, A., Jäger, K., Isabella, O., Van Swaaij, R. & Zeman, M. Solar Cell Parameters and Equivalent Circuit. *Sol. Energy Phys. Eng. Photovolt. conversion, Technol. Syst.* 111–124 (2016).

23. Ii, P. & Cell, P. Photovoltaic Cell I-V Characterization Theory and LabVIEW Analysis Code. *Power* 1–7 (2009).

24. Atwater, H. A. Paths to high efficiency low-cost photovoltaics. *Conf. Rec. IEEE Photovolt. Spec. Conf.* 000001–000003 (2011). doi:10.1109/PVSC.2011.6185830

25. Green, M. A., Emery, K., Hishikawa, Y., Warta, W. & Dunlop, E. D. Solar cell efficiency tables (version 39). *Prog. Photovoltaics Res. Appl.* (2012). doi:10.1002/pip.2163

26. Green, M. A., Ho-Baillie, A. & Snaith, H. J. The emergence of perovskite solar cells. *Nature Photonics* (2014). doi:10.1038/nphoton.2014.134

27. Razeghi, M. *et al.* High-purity GaAs layers grown by low-pressure metalorganic chemical vapor deposition. *Appl. Phys. Lett.* **55**, 1677–1679 (1989).

28. Sugiyama, M. *et al.* Kinetics of GaAs metalorganic chemical vapor deposition studied by numerical analysis based on experimental reaction data. *Japanese J. Appl. Physics, Part 1 Regul. Pap. Short Notes Rev. Pap.* **39**, 1642–1649 (2000).

29. Liu, C. H., Lin, T. K. & Chang, S. J. GaAs MOS capacitors with photo-CVD SiO2 insulator layers. *Solid. State. Electron.* **49**, 1077–1080 (2005).

30. Babichev, A. V., Gasumyants, V. E., Egorov, A. Y., Vitusevich, S. & Tchernycheva, M. Contact properties to CVD-graphene on GaAs substrates for optoelectronic applications. *Nanotechnology* **25**, (2014).

31. Yasui, K., Ishibashi, M., Taima, Y. & Akahane, T. Hot-mesh CVD for growth of GaN films on (100) GaAs. *Thin Solid Films* **464**–**465**, 116–119 (2004).

32. Reep, D. H. & Ghandhi, S. . Deposition of GaAs Epitaxial Layers by Organometallic CVD. *J. Electrochem. Soc.* **130**, 675 (1983).

33. Fujisaki, Y. Control of the GaAs/SiO2 interface through sulfur passivation and a photo-CVD process. *Appl. Surf. Sci.* **54**, 95–98 (1992).

34. Thompson, A. G. MOCVD technology for semiconductors. *Mater. Lett.* **30**, 255–263 (1997).

35. Molodyk, A., Novozhilov, M., Street, S., Castellani, L. & Ignatiev, A. All-MOCVD technology for coated conductor fabrication. *IEEE Trans. Appl. Supercond.* **21**, 3175–3178 (2011).

36. Yan, J. *et al.* High quality AlGaN grown on a high temperature AIN template by MOCVD. *J. Semicond.* **30**, (2009).

37. Blaauw, C., Shepherd, F. R., Miner, C. J. & Springthorpe, A. J. Silicon incorporation in InP during LP-MOCVD using disilane. *J. Electron. Mater.* **19**, 1–6 (1990).

38. Ingle, N. K., Theodoropoulos, C., Mountziaris, T. J., Wexler, R. M. & Smith, F. T. J. Reaction kinetics and transport phenomena underlying the low-pressure metalorganic chemical vapor deposition of GaAs. *J. Cryst. Growth* **167**, 543–556 (1996).

39. Pawlowski, R. P. *et al.* Fundamental models of the metalorganic vapor-phase epitaxy of gallium nitride and their use in reactor design. *J. Cryst. Growth* **221**, 622–628 (2000).

40. Sasaki, K. *et al.* Device-Quality β-Ga$_{2}$O$_{3}$ Epitaxial Films Fabricated by Ozone Molecular Beam Epitaxy. *Appl. Phys. Express* **5**, 035502 (2012).

41. Park, J. *et al.* Epitaxial graphene growth by carbon molecular beam epitaxy (CMBE). *Adv. Mater.* **22**, 4140–5 (2010).

42. Coleman, J. J. Metalorganic chemical vapor deposition for optoelectronic devices. *Proc. IEEE* **85**, 1715–1729 (1997).

43. Soga, T., Kato, T., Yang, M., Umeno, M. & Jimbo, T. High efficiency AlGaAs/Si monolithic tandem solar cell grown by metalorganic chemical vapor deposition. *J. Appl. Phys.* **78**, 4196–4199 (1995).

44. Rimada, J. C., Hern??ndez, L., Connolly, J. P. & Barnham, K. W. J. Conversion efficiency enhancement of AlGaAs quantum well solar cells. *Microelectronics J.* **38**, 513–518 (2007).

45. Wheeldon, J. F. *et al.* GaAs, AlGaAs and InGaP tunnel junctions for multi-junction solar cells under concentration: Resistance study. in *AIP Conference Proceedings* **1277**, 28–31 (2010).

46. Fraas, L. M. *et al.* GaSb booster cells for over 30% efficient solar-cell stacks. *J. Appl. Phys.* **66**, 3866–3870 (1989).

47. Laghumavarapu, R. B. *et al.* GaSb/InGaAs quantum dot-well hybrid structure active regions in solar cells. *Sol. Energy Mater. Sol. Cells* **114**, 165–171 (2013).

48. Sasaki, A., Ishio, K., Noda, S. & Fujita, S. Gap, algaas/gaas, algaassb/gasb photovoltaic devices and characteristics. *Jpn. J. Appl. Phys.* **21**, 93–98 (1982).

49. Takamoto, T., Kaneiwa, M., Imaizumi, M. & Yamaguchi, M. InGaP/GaAs-based multijunction solar cells. *Prog. Photovoltaics Res. Appl.* **13**, 495–511 (2005).

50. Takamoto, T., Ikeda, E., Kurita, H. & Ohmori, M. High efficiency InGaP solar cells for InGaP/GaAs tandem cell\napplication. *Proc. 1994 IEEE 1st World Conf. Photovolt. Energy Convers. - WCPEC (A Jt. Conf. PVSC, PVSEC PSEC)* **2**, 1729–1732 vol.2 (1994).

51. Wu, Z. H., Sun, M., Mei, X. Y. & Ruda, H. E. Growth and photoluminescence characteristics of AlGaAs nanowires. *Appl. Phys. Lett.* **85**, 657–659 (2004).

52. Burton, J. D., Culkin, F. & Riley, J. P. The abundances of gallium and germanium in terrestrial materials. *Geochim. Cosmochim. Acta* **16**, 151–180 (1959).

53. Schiff, E. A., Hegedus, S. & Deng, X. Amorphous Silicon-Based Solar Cells. in *Handbook of Photovoltaic Science and Engineering* 487–545 (2011). doi:10.1002/9780470974704.ch12

54. Matsui, T. *et al.* High-efficiency amorphous silicon solar cells: Impact of deposition rate on metastability. *Appl. Phys. Lett.* **106**, (2015).

55. Rech, B. & Wagner, H. Potential of amorphous silicon for solar cells. *Appl. Phys. A Mater. Sci. Process.* **69**, 155–167 (1999).

56. Chopra, K. L., Paulson, P. D. & Dutta, V. Thin-film solar cells: an overview. *Prog. Photovoltaics Res. Appl.* **12**, 69–92 (2004).

57. Carlson, D. E. & Wronski, C. R. Amorphous silicon solar cell. *Appl. Phys. Lett.* **28**, 671–673 (1976).

58. Luo, G. Successes and failures of China's golden-sun program. *Renew. Energy China* **129**, 131–148 (2014).

59. UCILIA WANG. Greentech Media Amorphous Silicon : Staking a Claim in Solar Market. 2010 (2010). Available at: https://www.greentechmedia.com/articles/read/amorphous-silicon-staking-a-claim-in-solar-market. (Accessed: 11th December 2009)

60. Park, S. H. *et al.* Tandem solar cells made from amorphous silicon and polymer bulk heterojunction sub-cells. *Adv. Mater.* **27**, 298–302 (2015).

61. Matsui, T. *et al.* High-efficiency thin-film silicon solar cells realized by integrating stable a-Si:H absorbers into improved device design. in *Japanese Journal of Applied Physics* **54**, (2015).

62. Meillaud, F. *et al.* Limiting factors in the fabrication of microcrystalline silicon solar cells and microcrystalline/amorphous ('micromorph') tandems. *Philos. Mag.* **89**, 2599–2621 (2009).

63. Staebler, D. L. & Wronski, C. R. Reversible conductivity changes in discharge-produced amorphous Si. *Appl. Phys. Lett.* **31**, 292–294 (1977).

64. Masuko, K. *et al.* Achievement of More Than 25%: Conversion Efficiency With Crystalline Silicon Heterojunction Solar Cell. *Photovoltaics, IEEE J.* **4**, 1433–1435 (2014).

65. Yoshikawa, K. *et al.* Silicon heterojunction solar cell with interdigitated back contacts for a photoconversion efficiency over 26%. *Nat. Energy* **2**, (2017).

66. Energy, N. World 's Highest Conversion Efficiency of 26.33% Achieved in a Crystalline Silicon Solar Cell - A World First in a Practical Cell Size -. *New Energy Ind. Technol. Dev. Organ. Kaneka Corp.* **5**, 1–3 (2016).

67. Deng, W. *et al.* 20.8% efficient PERC solar cell on 156 mm×156 mm p-type multi-crystalline silicon substrate. in *2015 IEEE 42nd Photovoltaic Specialist Conference, PVSC 2015* (2015). doi:10.1109/PVSC.2015.7356221

68. Huang, H. *et al.* 20.8% industrial PERC solar cell: ALD Al2O3rear surface passivation, efficiency loss mechanisms analysis and roadmap to 24%. *Sol. Energy Mater. Sol. Cells* **161**, 14–30 (2017).

69. Major, J. D., Treharne, R. E., Phillips, L. J. & Durose, K. A low-cost non-toxic post-growth activation step for CdTe solar cells. *Nature* **511**, 334–337 (2014).

70. Chang, L. Y., Lunt, R. R., Brown, P. R., Bulovi??, V. & Bawendi, M. G. Low-temperature solution-processed solar cells based on PbS colloidal quantum dot/CdS heterojunctions. *Nano Lett.* **13**, 994–999 (2013).

71. Hicks, W. Claims for solar cell efficiency put to test at NREL. 1–8 (2016). doi:10.1002/pip.2728/full

72. Geisthardt, R. M., Topič, M. & Sites, J. R. Status and Potential of CdTe Solar-Cell Efficiency. *IEEE J. Photovoltaics* **5**, 1217–1221 (2015).

73. Reinhard, P. *et al.* Review of progress toward 20% efficiency flexible CIGS solar cells and manufacturing issues of solar modules. *IEEE J. Photovoltaics* **3**, 572–580 (2013).

74. Green, M. A., Emery, K., Hishikawa, Y., Warta, W. & Dunlop, E. D. Solar cell efficiency tables (Version 45). *Prog. Photovoltaics Res. Appl.* **23**, 1–9 (2015).

75. Green, M. A. *et al.* Solar cell efficiency tables (version 49). *Prog. Photovoltaics Res. Appl.* **25**, 3–13 (2017).

76. Chiang, C. K. *et al.* Conducting polymers: Halogen doped polyacetylene. *J. Chem. Phys.* **69**, 5098–5104 (1978).

77. Chiang, C. K. *et al.* Electrical conductivity in doped polyacetylene. *Phys. Rev. Lett.* **39**, 1098–1101 (1977).

78. You, J., Dou, L., Hong, Z., Li, G. & Yang, Y. Recent trends in polymer tandem solar cells research. *Progress in Polymer Science* (2013). doi:10.1016/j.progpolymsci.2013.04.005

79. Krebs, F. C. Fabrication and processing of polymer solar cells: A review of printing and coating techniques. *Solar Energy Materials and Solar Cells* (2009). doi:10.1016/j.solmat.2008.10.004

80. Cheng, Y. J., Yang, S. H. & Hsu, C. S. Synthesis of conjugated polymers for organic solar cell applications. *Chem. Rev.* (2009). doi:10.1021/cr900182s

81. Nielsen, T. D., Cruickshank, C., Foged, S., Thorsen, J. & Krebs, F. C. Business, market and intellectual property analysis of polymer solar cells. *Sol. Energy Mater. Sol. Cells* (2010). doi:10.1016/j.solmat.2010.04.074

82. Li, G., Zhu, R. & Yang, Y. Polymer solar cells. *Nature Photonics* (2012). doi:10.1038/nphoton.2012.11

83. Siddiki, M. K., Li, J., Galipeau, D. & Qiao, Q. A review of polymer multijunction solar cells. *Energy Environ. Sci.* (2010). doi:10.1039/b926255p

84. Carlé, J. E. & Krebs, F. C. Technological status of organic photovoltaics (OPV). *Sol. Energy Mater. Sol. Cells* **119**, 309–310 (2013).

85. Krebs, F. C., Espinosa, N., Hösel, M., Søndergaard, R. R. & Jørgensen, M. 25th anniversary article: Rise to power - OPV-based solar parks. *Advanced Materials* **26**, 29–39 (2014).

86. Wright, M. & Uddin, A. Organic-inorganic hybrid solar cells: A comparative review. *Solar Energy Materials and Solar Cells* **107**, 87–111 (2012).

87. Nielsen, T. D., Cruickshank, C., Foged, S., Thorsen, J. & Krebs, F. C. Business, market and intellectual property analysis of polymer solar cells. *Sol. Energy Mater. Sol. Cells* **94**, 1553–1571 (2010).

88. Krebs, F. C., Nielsen, T. D., Fyenbo, J., Wadstrøm, M. & Pedersen, M. S. Manufacture, integration and demonstration of polymer solar cells in a lamp for the "Lighting Africa" initiative. *Energy Environ. Sci.* **3**, 512 (2010).

89. Heliatek sets new organic photovoltaic world record efficiency of 13.2%. *Renewable Energy Focus* **17**, 84–89 (2016).

90. Wright, M. & Uddin, A. Organic-inorganic hybrid solar cells: A comparative review. *Solar Energy Materials and Solar Cells* (2012). doi:10.1016/j.solmat.2012.07.006

91. Do, K., Huang, D. M., Faller, R. & Moulé, A. J. A comparative MD study of the local structure of polymer semiconductors P3HT and PBTTT. *Phys. Chem. Chem. Phys.* **12**, 14735 (2010).

92. Zhang, F. *et al.* Influence of PC60BM or PC70BM as electron acceptor on the performance of polymer solar cells. in *Solar Energy Materials and Solar Cells* **97**, 71–77 (2012).

93. Wang, C. I. & Hua, C. C. Solubility of C60 and PCBM in Organic Solvents. *J. Phys. Chem. B* **119**, 14496–14504 (2015).

94. Moulé, A. J., Chang, L., Thambidurai, C., Vidu, R. & Stroeve, P. Hybrid solar cells: basic principles and the role of ligands. *J. Mater. Chem.* (2012). doi:10.1039/C1JM14829J

95. SES research. Carbon 60 99.5%. *2017* 1 (2017). doi:https://www.sesres.com/fullerene/

96. Moser, J. Notiz ??ber Verst??rkung photoelektrischer Str??me durch optische Sensibilisirung. *Monatshefte f??r Chemie* **8**, 373 (1888).

97. Gerischer, H. & Willig, F. Reaction of excited dye molecules at electrodes. in *Physical and Chemical Applications of Dyestuffs* 31–84 (1976). doi:10.1007/BFb0046057

98. O'Regan, B. & Gratzel, M. A Low-Cost, High-Efficiency Solar-Cell Based on Dye-Sensitized Colloidal TiO_2 Films. *Nature* **353**, 737–740 (1991).

99. Mathew, S. *et al.* Dye-sensitized solar cells with 13% efficiency achieved through the molecular engineering of porphyrin sensitizers. *Nat. Chem.* **6**, 242–247 (2014).

100. Gong, J., Sumathy, K., Qiao, Q. & Zhou, Z. Review on dye-sensitized solar cells (DSSCs): Advanced techniques and research trends. *Renewable and Sustainable Energy Reviews* **68**, 234–246 (2017).

101. Bach, U. *et al.* Solid-state dye-sensitized mesoporous TiO2 solar cells with high photon-to-electron conversion efficiencies. *Nature* **395**, 583–585 (1998).

102. Wang, D., Wright, M., Elumalai, N. K. & Uddin, A. Stability of perovskite solar cells. *Solar Energy Materials and Solar Cells* **147**, 255–275 (2016).

103. Eperon, G. E., Burlakov, V. M., Docampo, P., Goriely, A. & Snaith, H. J. Morphological control for high performance, solution-processed planar heterojunction perovskite solar cells. *Adv. Funct. Mater.* **24**, 151–157 (2014).

104. Yang, Y. *et al.* Ammonium-iodide-salt additives induced photovoltaic performance enhancement in one-step solution process for perovskite solar cells. *J. Alloys Compd.* **684**, 84–90 (2016).

105. Chen, C.-C. *et al.* Perovskite/polymer monolithic hybrid tandem solar cells utilizing a low-temperature, full solution process. *Mater. Horiz.* **2**, 203–211 (2015).

106. Chen, C. C. *et al.* Visibly transparent polymer solar cells produced by solution processing. *ACS Nano* (2012). doi:10.1021/nn3029327

107. Roldán-Carmona, C. *et al.* Flexible high efficiency perovskite solar cells. *Energy Environ. Sci.* **7**, 994 (2014).

108. Schmidt, T. M., Larsen-Olsen, T. T., Carlé, J. E., Angmo, D. & Krebs, F. C. Upscaling of Perovskite Solar Cells: Fully Ambient Roll Processing of Flexible Perovskite Solar Cells with Printed Back Electrodes. *Adv. Energy Mater.* **5**, (2015).

109. King, R. R. *et al.* Band gap-voltage offset and energy production in next-generation multijunction solar cells. *Prog. Photovoltaics Res. Appl.* **19**, 797–812 (2011).

110. Park, N. G. Perovskite solar cells: An emerging photovoltaic technology. *Materials Today* (2015). doi:10.1016/j.mattod.2014.07.007

111. Yin, W.-J., Yang, J.-H., Kang, J., Yan, Y. & Wei, S.-H. Halide perovskite materials for solar cells: a theoretical review. *J. Mater. Chem. A* (2015). doi:10.1039/C4TA05033A

112. Stranks, S. D. *et al.* Electron-hole diffusion lengths exceeding 1 micrometer in an organometal trihalide perovskite absorber. *Science (80-.).* **342**, 341–344 (2013).

113. Kojima, A., Teshima, K., Shirai, Y. & Miyasaka, T. Organometal halide perovskites as visible-light sensitizers for photovoltaic cells. *J. Am. Chem. Soc.* **131**, 6050–6051 (2009).

114. Im, J.-H., Lee, C.-R., Lee, J.-W., Park, S.-W. & Park, N.-G. 6.5% efficient perovskite quantum-dot-sensitized solar cell. *Nanoscale* **3**, 4088 (2011).

115. Kim, H. S. *et al.* Lead iodide perovskite sensitized all-solid-state submicron thin film mesoscopic solar cell with efficiency exceeding 9%. *Sci. Rep.* **2**, (2012).

116. Lee, M. M., Teuscher, J., Miyasaka, T., Murakami, T. N. & Snaith, H. J. Efficient Hybrid Solar Cells Based on Meso-Superstructured Organometal Halide Perovskites. *Science (80-.).* **338**, 643–647 (2012).

117. Park, N.-G. Methodologies for high efficiency perovskite solar cells. *Nano Converg.* **3**, 15 (2016).

118. Yang, W. S. *et al.* SOLAR CELLS. High-performance photovoltaic perovskite layers fabricated through intramolecular exchange. *Science* **348**, 1234–7 (2015).

119. Roesch, R. *et al.* Procedures and practices for evaluating thin-film solar cell stability. *Adv. Energy Mater.* **5**, (2015).

120. Niu, G., Guo, X. & Wang, L. Review of recent progress in chemical stability of perovskite solar cells. *J. Mater. Chem. A* **3**, 8970–8980 (2015).

121. Osterwald, C. R. *et al.* Degradation in weathered crystalline-silicon PV modules apparently caused by UV radiation. *Proc. 3rd World Conf. Photovolt. Energy Conversion, Vols a-C* 2911–2915 (2003).

122. Jørgensen, M., Norrman, K. & Krebs, F. C. Stability/degradation of polymer solar cells. *Solar Energy Materials and Solar Cells* (2008). doi:10.1016/j.solmat.2008.01.005

123. Hinsch, A. *et al.* Long-term stability of dye-sensitised solar cells. *Prog. Photovoltaics Res. Appl.* **9**, 425–438 (2001).

124. Leijtens, T. *et al.* Overcoming ultraviolet light instability of sensitized TiO2 with meso-superstructured organometal tri-halide perovskite solar cells. *Nat. Commun.* **4**, (2013).

125. Frost, J. M. *et al.* Atomistic origins of high-performance in hybrid halide perovskite solar cells. *Nano Lett.* **14**, 2584–2590 (2014).

126. Yang, J., Siempelkamp, B. D., Liu, D. & Kelly, T. L. An Investigation of CH3NH3PbI3 Degradation Rates and Mechanisms in Controlled Humidity Environments Using in situ Techniques. *ACS Nano* Advance (2015). doi:10.1021/nn506864k

127. Christians, J. A., Miranda Herrera, P. A. & Kamat, P. V. Transformation of the excited state and photovoltaic efficiency of CH3NH3PbI3 perovskite upon controlled exposure to humidified air. *J. Am. Chem. Soc.* **137**, 1530–1538 (2015).

128. Philippe, B. *et al.* Chemical and electronic structure characterization of lead halide perovskites and stability behavior under different exposures-A photoelectron spectroscopy investigation. *Chem. Mater.* **27**, 1720–1731 (2015).

129. Dualeh, A. *et al.* Effect of annealing temperature on film morphology of organic-inorganic hybrid pervoskite solid-state solar cells. *Adv. Funct. Mater.* **24**, 3250–3258 (2014).

130. Conings, B. *et al.* Intrinsic Thermal Instability of Methylammonium Lead Trihalide Perovskite. *Adv. Energy Mater.* **5**, (2015).

131. Leguy, A. M. A. *et al.* Reversible Hydration of CH3NH3PbI3 in Films, Single Crystals, and Solar Cells. *Chem. Mater.* **27**, 3397–3407 (2015).

132. O'Mahony, F. T. F. *et al.* Improved environmental stability of organic lead trihalide perovskite-based photoactive-layers in the presence of mesoporous TiO_2. *J. Mater. Chem. A* **3**, 7219–7223 (2015).

133. Aristidou, N. *et al.* The Role of Oxygen in the Degradation of Methylammonium Lead Trihalide Perovskite Photoactive Layers. *Angew. Chemie - Int. Ed.* **54**, 8208–8212 (2015).

134. Bryant, D. *et al.* Light and oxygen induced degradation limits the operational stability of methylammonium lead triiodide perovskite solar cells. *Energy Environ. Sci.* **9**, 1655–1660 (2016).

135. Ham, J. The Spectra of Iodine Solutions. III. The [formula-omitted] Transition of the Iodine Molecule in Solution. *J. Am. Chem. Soc.* **76**, 3886–3887 (1954).

136. Bhachu, D. S. *et al.* Scalable Route to CH3NH3PbI3 Perovskite Thin Films by Aerosol Assisted Chemical Vapor Deposition. *J. Mater. Chem. A* **00**, 1–3 (2014).

137. Baikie, T. *et al.* Synthesis and crystal chemistry of the hybrid perovskite (CH3NH3)PbI3 for solid-state sensitised solar cell applications. *J. Mater. Chem. A* **1**, 5628 (2013).

138. Jeon, N. J. *et al.* Solvent engineering for high-performance inorganic-organic hybrid perovskite solar cells. *Nat. Mater.* **13**, 897–903 (2014).

139. Lee, J. W. *et al.* Formamidinium and cesium hybridization for photo- and moisture-stable perovskite solar cell. *Adv. Energy Mater.* **5**, (2015).

140. Saliba, M. *et al.* Cesium-containing triple cation perovskite solar cells: improved stability, reproducibility and high efficiency. *Energy Environ. Sci.* **9**, 1989–1997 (2016).

141. Wang, Q. *et al.* Large fill-factor bilayer iodine perovskite solar cells fabricated by a low-temperature solution-process. *Energy Environ. Sci.* **7**, 2359–2365 (2014).

142. Hau, S. K. *et al.* Air-stable inverted flexible polymer solar cells using zinc oxide nanoparticles as an electron selective layer. *Appl. Phys. Lett.* **92**, 253301 (2008).

143. Murugadoss, G. *et al.* An efficient electron transport material of tin oxide for planar structure perovskite solar cells. *J. Power Sources* **307**, 891–897 (2016).

144. Ponseca, C. S. *et al.* Organometal halide perovskite solar cell materials rationalized: Ultrafast charge generation, high and microsecond-long balanced mobilities, and slow recombination. *J. Am. Chem. Soc.* **136**, 5189–5192 (2014).

145. Leijtens, T. *et al.* Carrier trapping and recombination: the role of defect physics in enhancing the open circuit voltage of metal halide perovskite solar cells. *Energy Environ. Sci.* **9**, 3472–3481 (2016).

146. Deschler, F. *et al.* High photoluminescence efficiency and optically pumped lasing in solution-processed mixed halide perovskite semiconductors. *J. Phys. Chem. Lett.* **5**, 1421–1426 (2014).

147. O'Mahony, F. T. F., Lutz, T., Guijarro, N., Gómez, R. & Haque, S. A. Electron and hole transfer at metal oxide/Sb2S3/spiro-OMeTAD heterojunctions. *Energy Environ. Sci.* (2012). doi:10.1039/c2ee23037b

148. Chen, Q. *et al.* Under the spotlight: The organic-inorganic hybrid halide perovskite for optoelectronic applications. *Nano Today* (2015). doi:10.1016/j.nantod.2015.04.009

149. Rakita, Y., Cohen, S. R., Kedem, N. K., Hodes, G. & Cahen, D. Mechanical Properties of APbX3 (A=Cs or CH3NH3; X=I or Br) Perovskite Single Crystals. *Arxiv Prepr.* **3**, 1–20 (2015).

150. Zhao, P. *et al.* Large-Size CH3NH3PbBr3 Single Crystal: Growth and in Situ Characterization of the Photophysics Properties. *J. Phys. Chem. Lett.* **6**, 2622–2628 (2015).

151. Stoumpos, C. C., Malliakas, C. D. & Kanatzidis, M. G. Semiconducting tin and lead iodide perovskites with organic cations: Phase transitions, high mobilities, and near-infrared photoluminescent properties. *Inorg. Chem.* **52**, 9019–9038 (2013).

152. Amat, A. *et al.* Cation-induced band-gap tuning in organohalide perovskites: Interplay of spin-orbit coupling and octahedra tilting. *Nano Lett.* **14**, 3608–3616 (2014).

153. Chen, D., Nakahara, A., Wei, D., Nordlund, D. & Russell, T. P. P3HT/PCBM bulk heterojunction organic photovoltaics: Correlating efficiency and morphology. *Nano Lett.* **11**, 561–567 (2011).

154. Ge, N. An overview on P3HT : PCBM , the most efficient organic solar cell material so far . *Solid State Phys.* 1–11 (2009).

155. Cook, S. *et al.* A photophysical study of PCBM thin films. *Chem. Phys. Lett.* **445**, 276–280 (2007).

156. Liao, H. C. *et al.* Nanoparticle-tuned self-organization of a bulk heterojunction hybrid solar cell with enhanced performance. *ACS Nano* (2012). doi:10.1021/nn204654h

157. Berriman, G. A., Holdsworth, J. L., Zhou, X., Belcher, W. J. & Dastoor, P. C. Molecular versus crystallite PCBM diffusion in P3HT:PCBM blends. *AIP Adv.* **5**, (2015).

158. Treat, N. D., Mates, T. E., Hawker, C. J., Kramer, E. J. & Chabinyc, M. L. Temperature dependence of the diffusion coefficient of PCBM in poly(3-hexylthiophene). *Macromolecules* **46**, 1002–1007 (2013).

159. Treat, N. D. *et al.* Interdiffusion of PCBM and P3HT reveals miscibility in a photovoltaically active blend. *Adv. Energy Mater.* **1**, 82–89 (2011).

160. Lee, C.-K. & Pao, C.-W. Solubility of PCBM and Optimal Blending Ratio of Bulk Heterojunction Polymer Solar Cells. *J. Phys. Chem. C* **116**, 120523033714004 (2012).

161. Kakavelakis, G. *et al.* Efficient and Highly Air Stable Planar Inverted Perovskite Solar Cells with Reduced Graphene Oxide Doped PCBM Electron Transporting Layer. *Adv. Energy Mater.* **7**, (2017).

SI sections

SI for Chapter 6

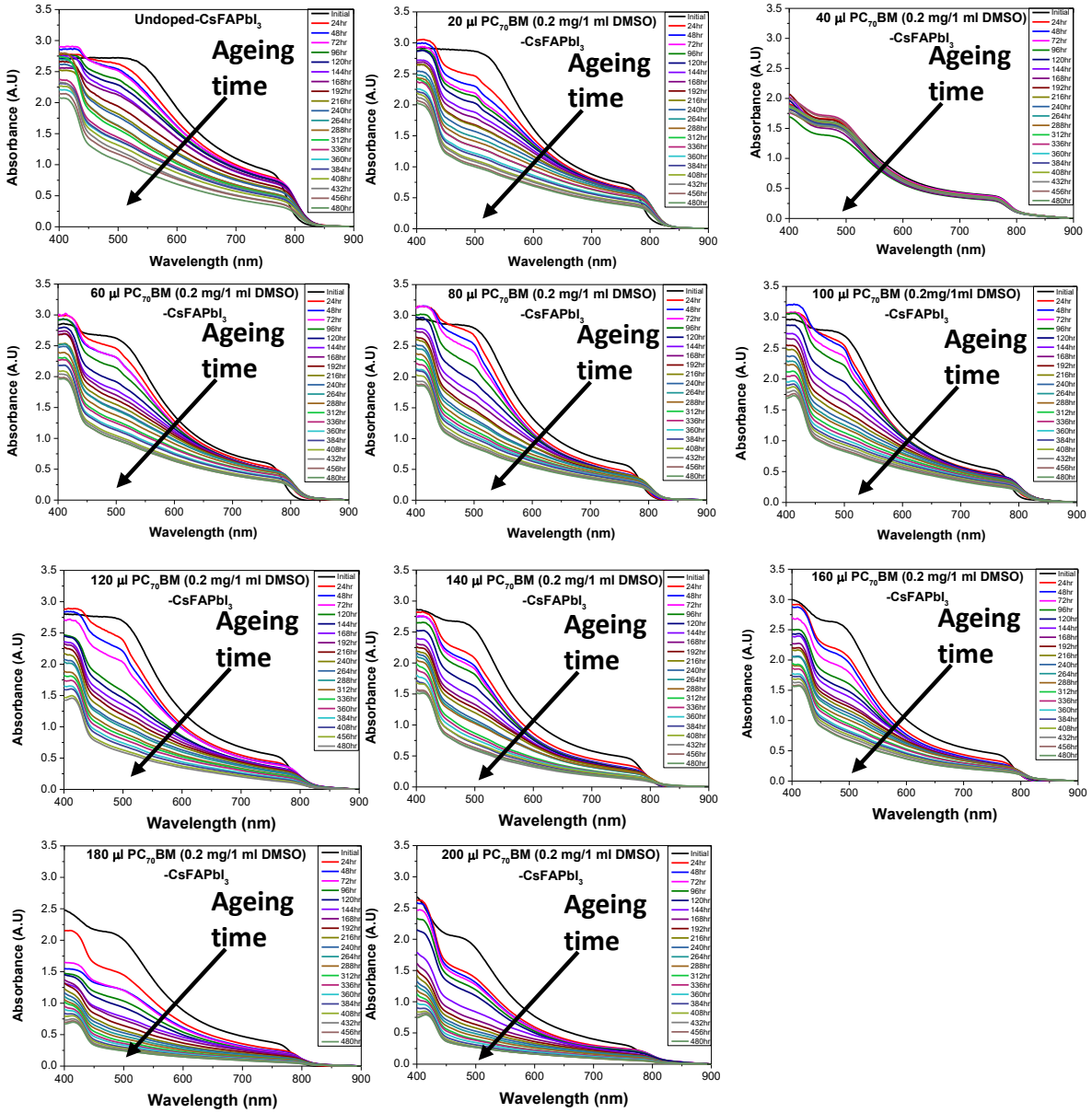


Figure 51-a: Absorbance curves of c-TiO_2/mp-TiO_2/$CsFAPbI_3$ films doped with different amounts of $PC_{70}BM$ at 750 nm (see legends). All samples were degraded under constant exposure of illumination and dry air (less than 10 ppm H_2O)

SI for Chapter 7

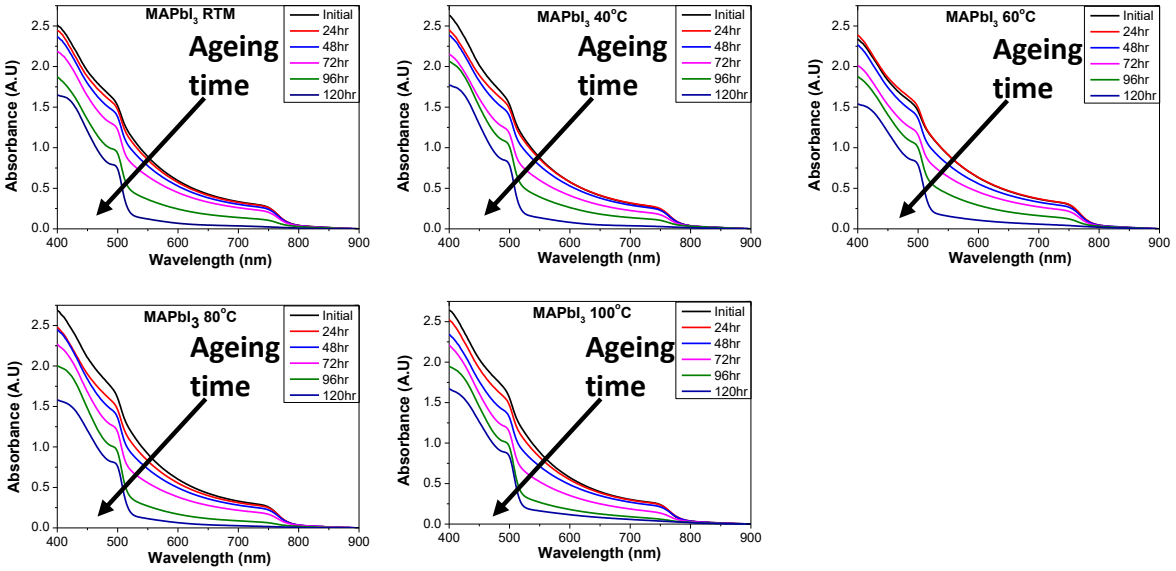


Figure 56-a: UV-vis absorbance spectra of glass/c-TiO_2/mp-TiO_2/$MAPbI_3$ samples with a different post annealing temperature (see labels) for 30 minutes. All samples were subjected to constant exposure of a tungsten halogen lamp (20 $mWcm^{-2}$) and excess dry air flow (less than 10 ppm of H_2O).

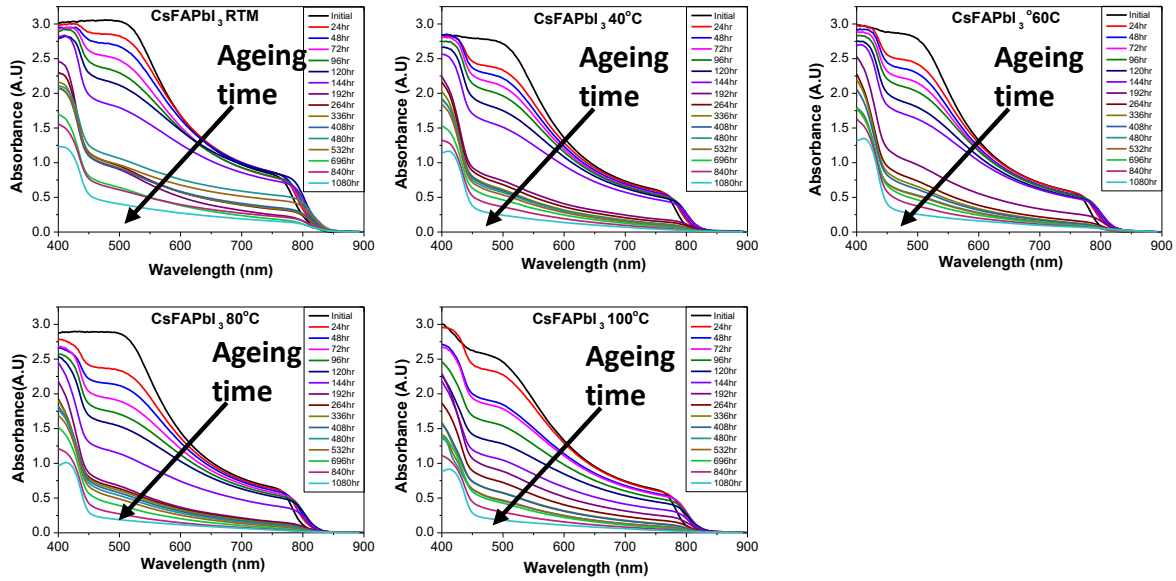


Figure 56-b: UV-vis absorbance spectra of glass/c-TiO_2/mp-TiO_2/$CsFAPbI_3$ samples with a different post annealing temperature (see labels) for 30 minutes. All samples were subjected to constant exposure of a tungsten halogen lamp (20 $mWcm^{-2}$) and excess dry air flow (less than 10 ppm of H_2O).

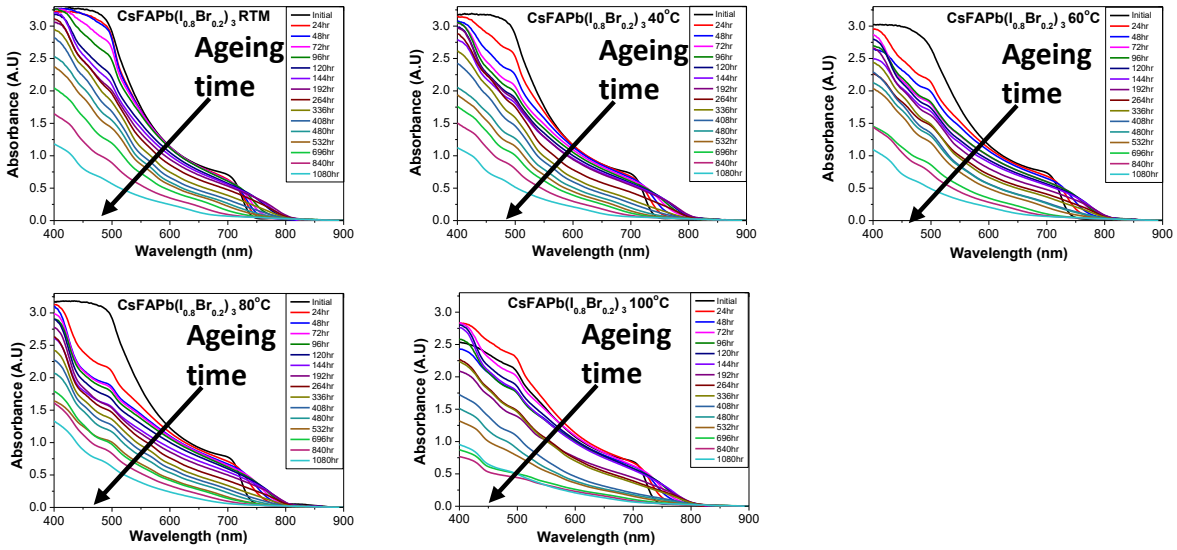


Figure 56-c: UV-vis absorbance spectra of glass/c-TiO_2/mp-TiO_2/CsFAPb $(I_{0.2}Br_{0.8})_3$ samples with a different post annealing temperature (see labels) for 30 minutes. All samples were subjected to constant exposure of a tungsten halogen lamp (20 $mWcm^{-2}$) and excess dry air flow (less than 10 ppm of H_2O).

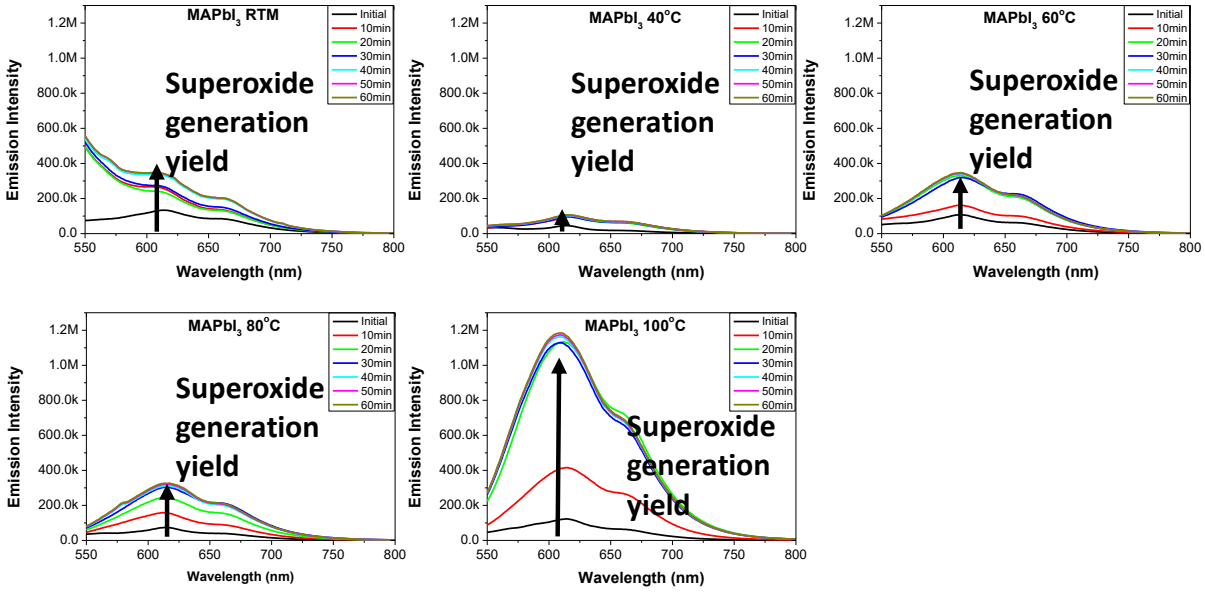


Figure 57-a: Superoxide measurement of of glass/c-TiO_2/mp-TiO_2/$MAPbI_3$ samples with a different post annealing temperature (see labels) for 30 minutes. All perovskite samples were submerged in HE probe solution that was highly emissive at 610 upon exposing it to the excitation wavelength of 520 nm. All samples were subjected to the constant exposure of tungsten halogen lamp (20 $mWcm^{-2}$) and excess dry air flow (less than 10 ppm of H_2O) over the course of one hour.

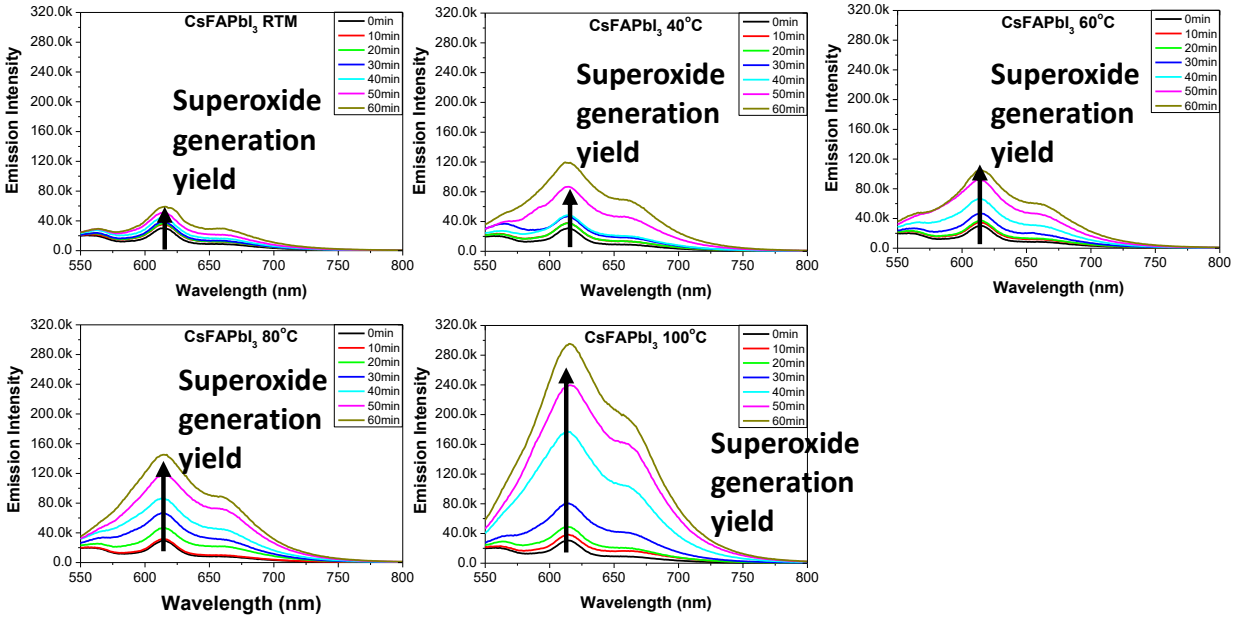


Figure 57-b: Superoxide measurement of glass/c-TiO_2/mp-TiO_2/$CsFAPbI_3$ samples with a different post annealing temperature (see labels) for 30 minutes. All perovskite samples were submerged in HE probe solution that was highly emissive at 610 upon exposing it to the excitation wavelength of 520 nm. All samples were subjected to the constant exposure of a tungsten halogen lamp (20 $mWcm^{-2}$) and excess dry air flow (less than 10 ppm of H_2O) over the course of one hour.

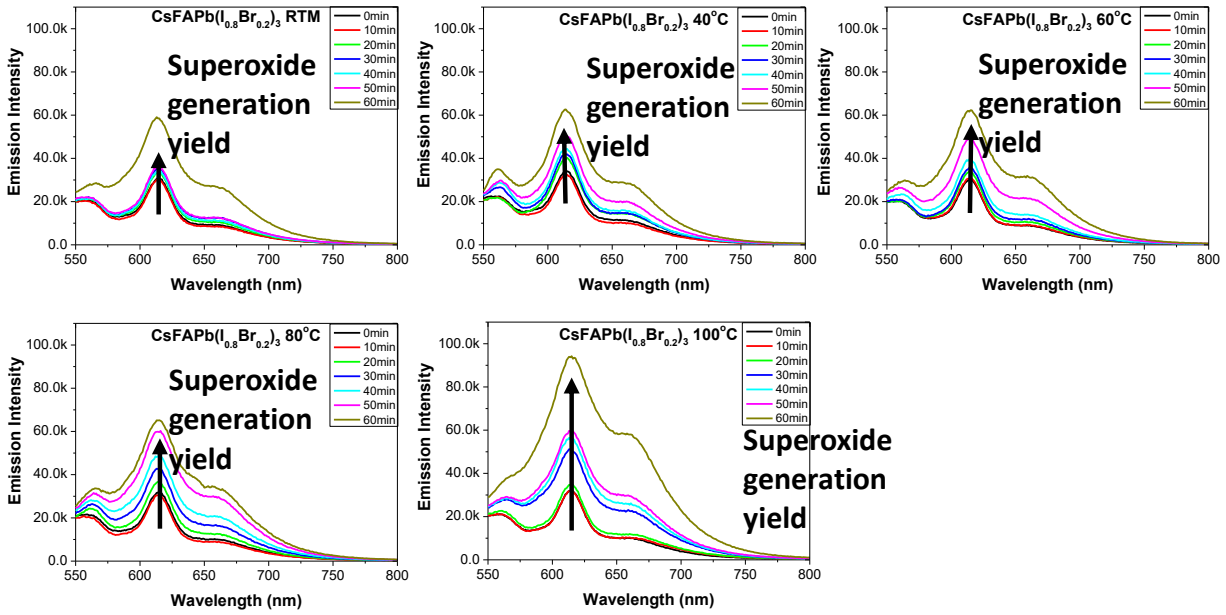


Figure 57-c: Superoxide measurement of glass/c-TiO_2/mp-TiO_2/ $CsFAPb(I_{0.2}Br_{0.8})_3$ samples with a different post annealing temperature (see labels) for 30 minutes. All perovskite samples were submerged in HE probe solution that was highly emissive at 610 upon exposing it to the excitation wavelength of 520 nm. All samples were subjected to a constant exposure of a tungsten halogen lamp (20 $mWcm^{-2}$) and excess dry air flow (less than 10 ppm of H_2O) over the course of one hour.

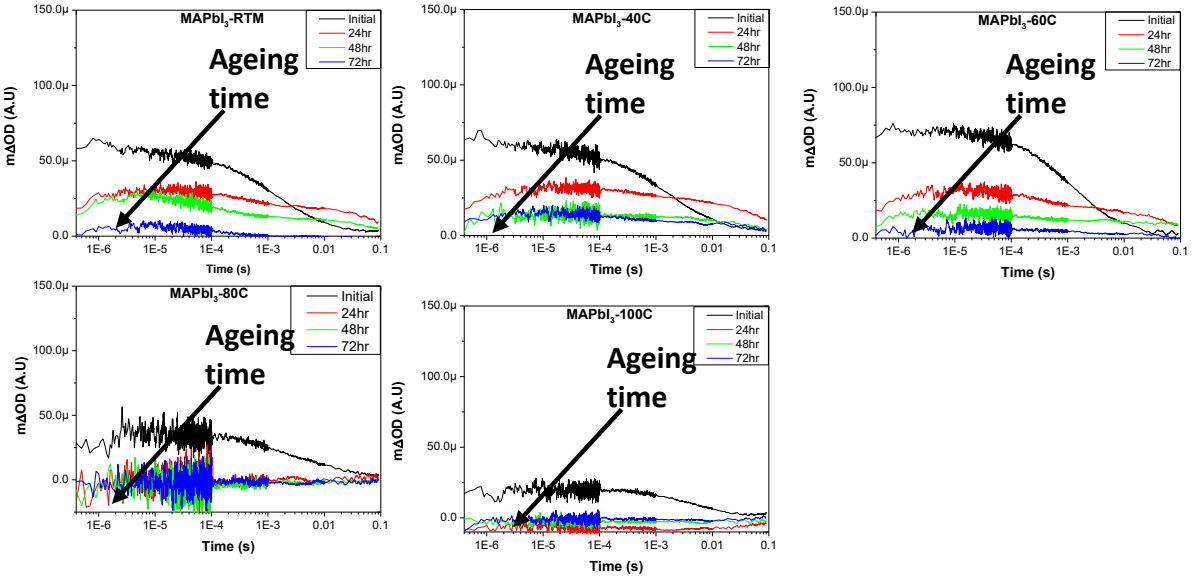


Figure 58-a: Transient absorption spectra as a function of oxygen-light ageing time of glass/c-TiO_2/mp-TiO_2/$MAPbI_3$. Each perovskite film was subjected to a different post annealing temperature for 30 minutes (see labels). In addition, each sample was subjected to constant tungsten halogen light (~20 $mWcm^{-2}$) and excess dry air flow (1 lpm). The signal was probed at 1,600 nm to track the hole recombination interaction in spiro-OMeTAD. Laser photo excitation was set at 510 nm with an energy density of approximately 25 μJcm^{-2}.

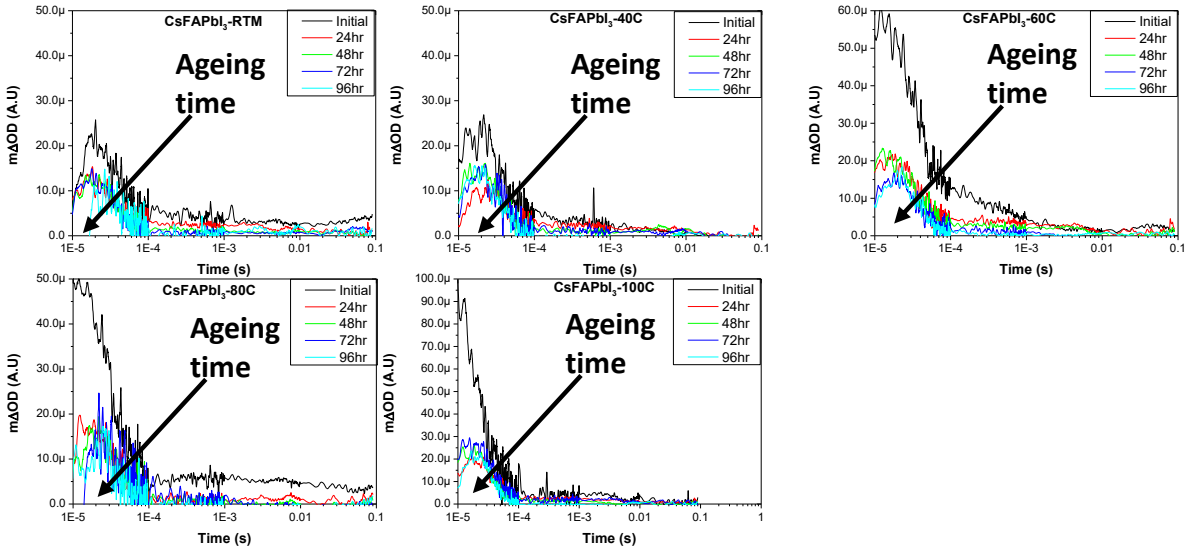


Figure 58-b: Transient absorption spectra as a function of oxygen-light ageing time of glass/c-TiO_2/mp-TiO_2/$CsFAPbI_3$. Each perovskite film was subjected to a different post annealing temperature for 30 minutes (see labels). In addition, each sample was subjected to constant tungsten halogen light (~20 $mWcm^{-2}$) and excess dry air flow (1 lpm). The signal was probed at 1,600 nm to track the hole recombination interaction in spiro-OMeTAD. Laser photo excitation was set at 510 nm with an energy density of approximately 25 μJcm^{-2}.

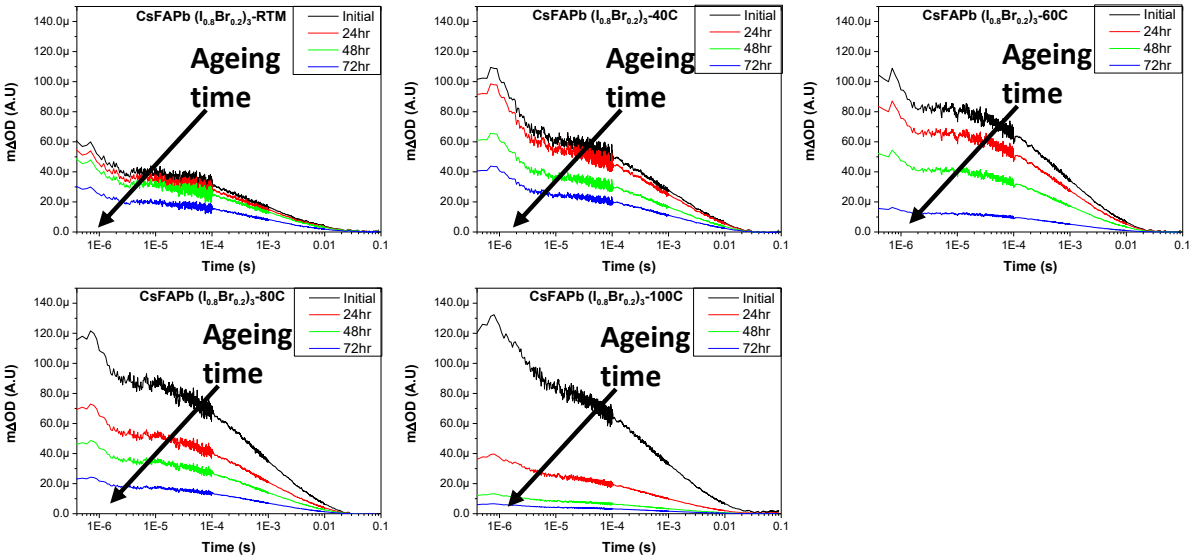


Figure 58-c: Transient absorption spectra as a function of oxygen-light ageing time of glass/c-TiO_2/mp-TiO_2/CsFAPb $(I_{0.8}Br_{0.2})_3$. Each perovskite film was subjected to a different post annealing temperature for 30 minutes (see labels). In addition, each sample was subjected to constant tungsten halogen light (~20 $mWcm^{-2}$) and excess dry air flow (1 lpm). The signal was probed at 1,600 nm to track the hole recombination interaction in spiro-OMeTAD. Laser photo excitation was set at 510 nm with an energy

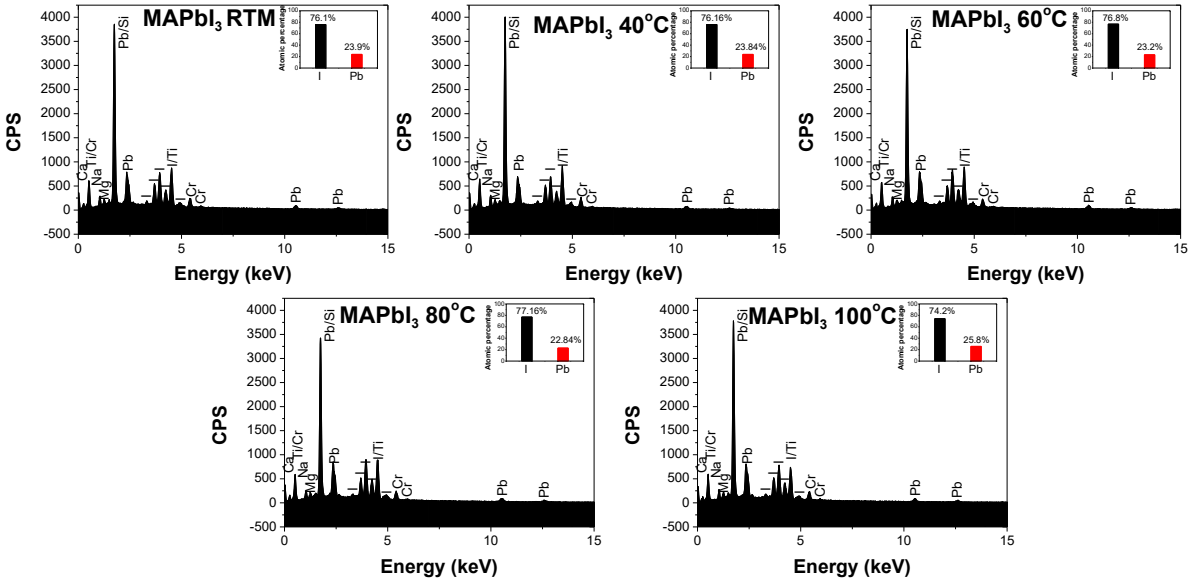


Table 8-1: EDX spectra of c-TiO_2/mp-TiO_2/$MAPbI_3$ samples before oxygen-light degradation took place with different post annealing temperature for 30 minutes (see labels). The inset in EDX spectra highlight relevant relative atomic ratio such as Pb and I on each sample.

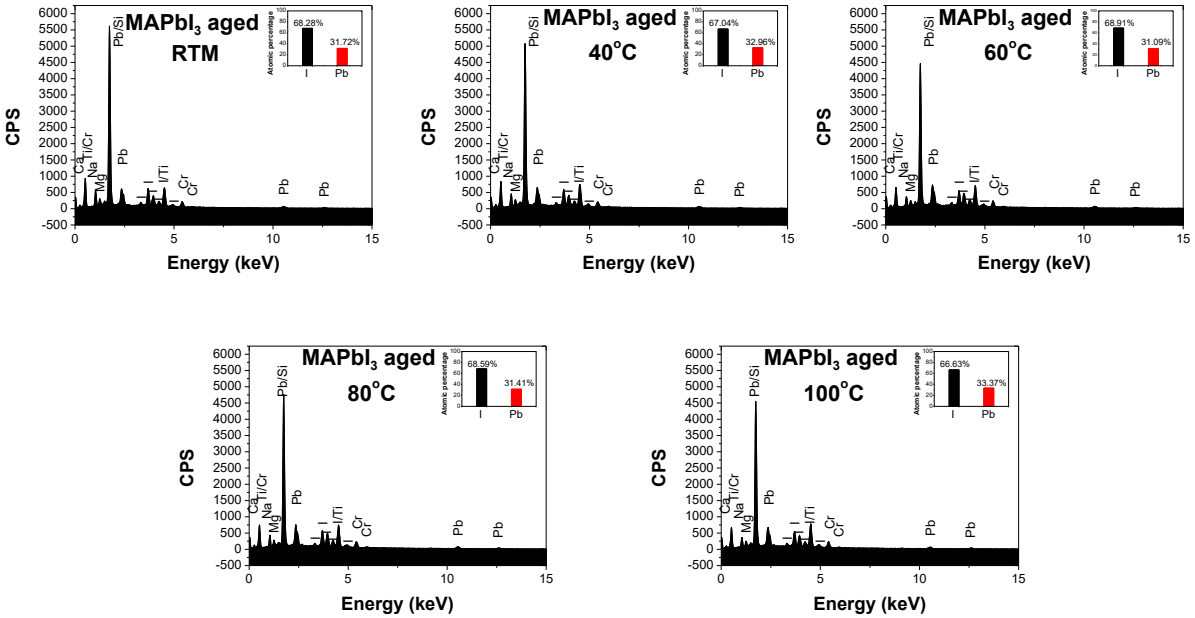


Table 8-2: EDX spectra of c-TiO_2/mp-TiO_2/$MAPbI_3$ samples after oxygen-light degradation (120 hours) with different post annealing temperature for 30 minutes (see labels). The inset in EDX spectra highlight relevant relative atomic ratio such as Pb and I on each sample.

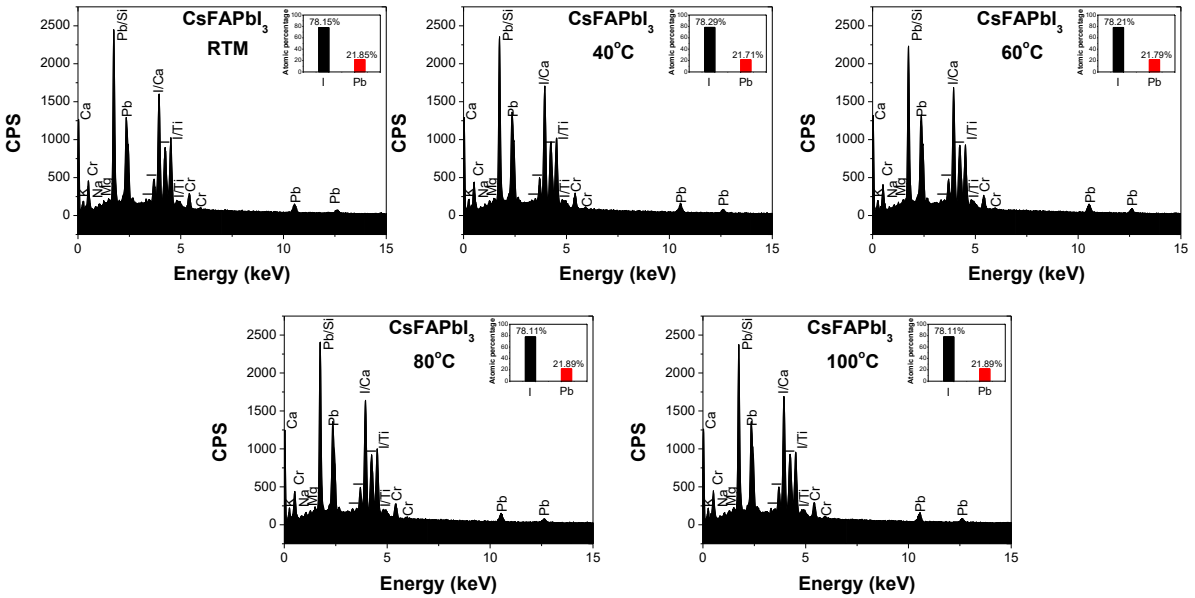


Table 9-1: EDX spectra of c-TiO_2/mp-TiO_2/$CsFAPbI_3$ samples before oxygen-light degradation took place with different post annealing temperature for 30 minutes (see labels). The inset in EDX spectra highlight relevant relative atomic ratio such as Pb, I and Br on each sample.

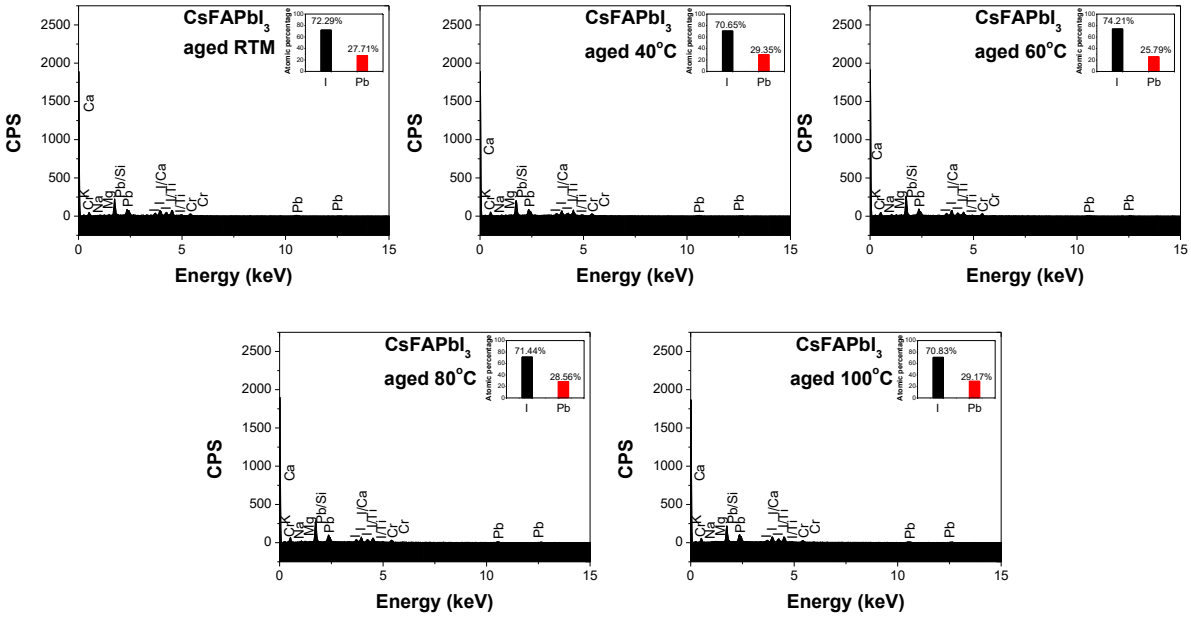


Table 9-2: EDX spectra of c-TiO_2/mp-TiO_2/$CsFAPbI_3$ samples after oxygen-light degradation took place (840 hours) with different post annealing temperature for 30 minutes (see labels). The inset in EDX spectra highlight relevant relative atomic ratio such as Pb, I and Br on each sample.

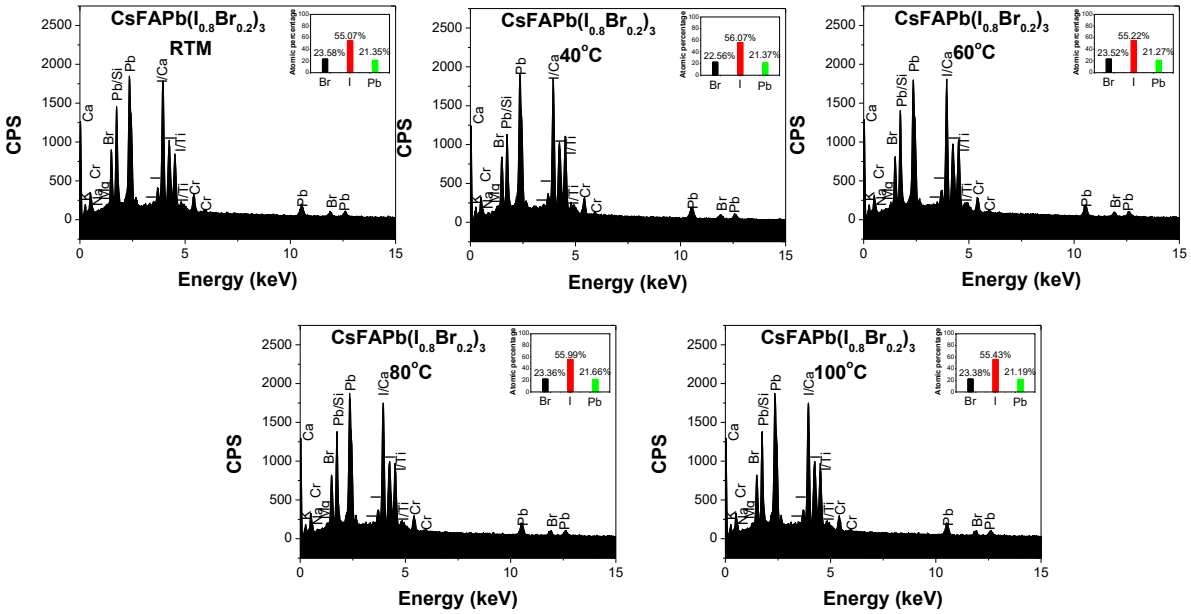


Table 10-1: EDX spectra of c-TiO_2/mp-TiO_2/CsFAPb $(I_{0.8}Br_{0.2})_3$ samples before oxygen-light degradation took place with different post annealing temperature for 30 minutes (see labels). The inset in EDX spectra highlight relevant relative atomic ratio such as Pb, I and Br on each sample.

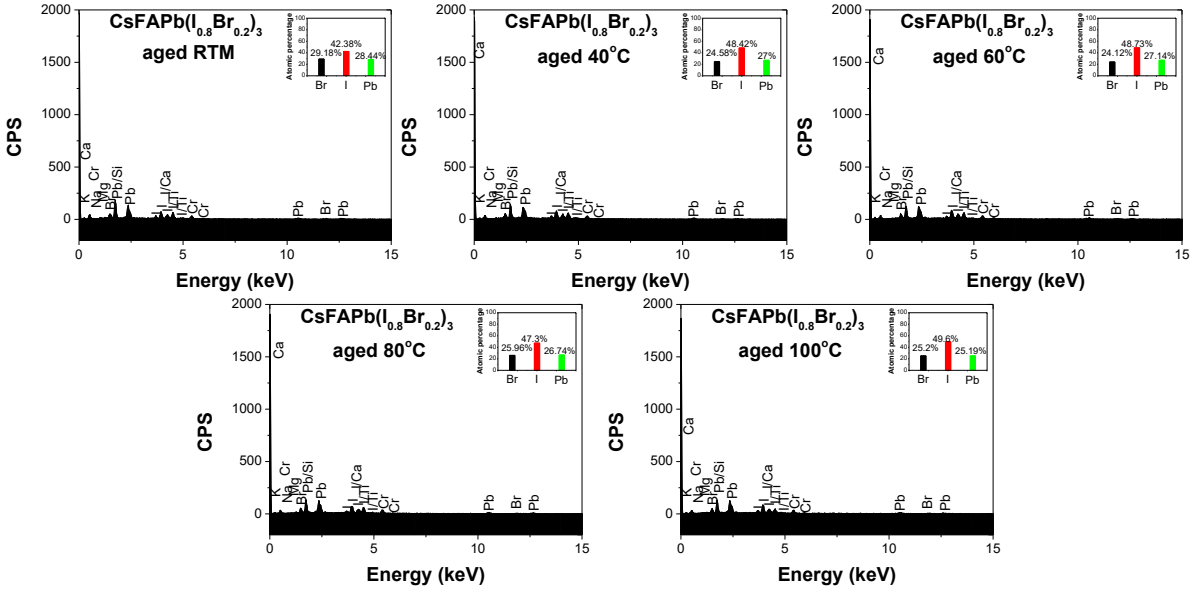


Table 10-2: EDX spectra of c-TiO_2/mp-TiO_2/CsFAPb $(I_{0.8}Br_{0.2})_3$ samples after oxygen-light degradation took place (840 hours) with different post annealing temperature for 30 minutes (see labels). The inset in EDX spectra highlight relevant relative atomic ratio such as Pb, I and Br on each sample.

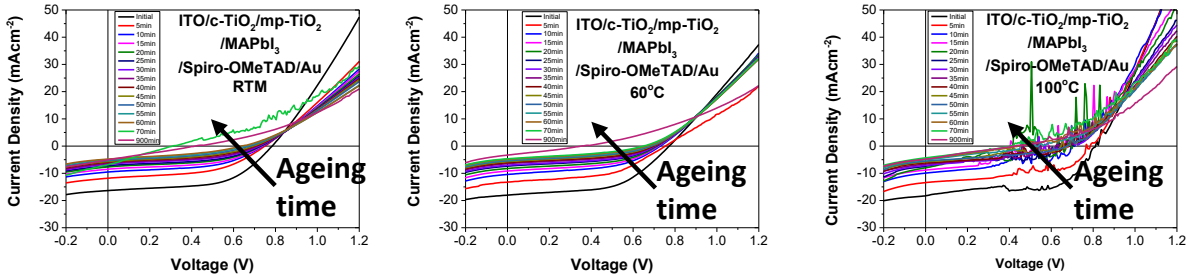


Figure 66-a: JV curves over ageing conditions of the ITO/c-TiO_2/mp-TiO_2/$MAPbI_3$/spiro-OMeTAD/Au device. In addition, 30 minutes of post annealing to the perovskite photoabsorber were implemented during the device fabrication process (see legends). All samples were exposed under constant exposure of dry air and AM 1.5 G with approximately 100 $mWcm^{-2}$ irradiance powered by equivalent white LED array equipped with UV blocking filter. Each JV curve was obtained via backward JV scan from 1.2 V to -0.2 V.

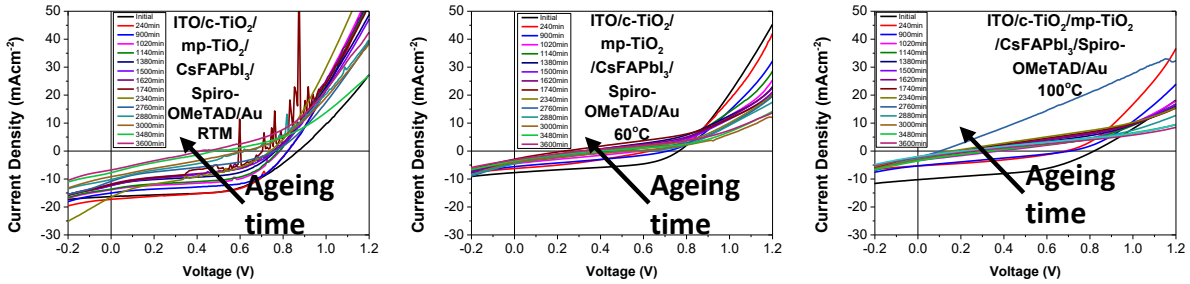


Figure 66-b: JV curves over ageing conditions of the ITO/c-TiO_2/mp-TiO_2/$CsFAPbI_3$/spiro-OMeTAD/Au device. In addition, 30 minutes of post annealing to the perovskite photoabsorber were implemented during the device fabrication process (see legends). All samples were exposed under constant exposure of dry air and AM 1.5 G with approximately 100 $mWcm^{-2}$ irradiance powered by equivalent white LED array equipped with UV blocking filter. Each JV curve was obtained via backward JV scan from 1.2 V to -0.2 V.

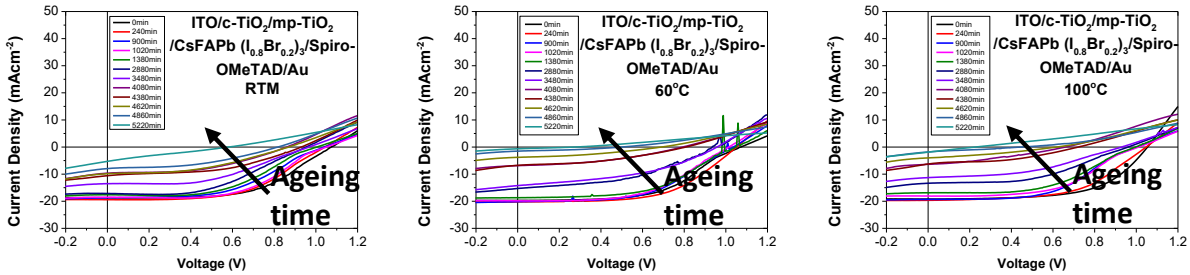


Figure 66-c: JV curves over ageing conditions of the ITO/c-TiO_2/mp-TiO_2/ c-TiO_2/mp-TiO_2/ CsFAPb $(I_{0.8}Br_{0.2})_3$ /spiro-OMeTAD/Au device. In addition, 30 minutes of post annealing to the perovskite photoabsorber were implemented during the device fabrication process (see legends). All samples were exposed under constant exposure of dry air and AM 1.5 G with approximately 100 $mWcm^{-2}$ irradiance powered by equivalent white LED array equipped with UV blocking filter. Each JV curve was obtained via backward JV scan from 1.2 V to -0.2 V.